UNIVERSITAT POLITÈCNICA DE VALÈNCIA

Toward a new generation of photonic devices based on the integration of metal oxides in silicon technology

Jorge Parra Gómez

Supervisor:
Prof. Dr. Pablo Sanchis Kilders

Doctoral thesis submitted for the degree of Doctor of Philosophy in Telecommunications Engineering

València, October 2022

A mi familia.

Acknowledgements

This work is supported in part by grants ACIF/2018/172 funded by Generaliltat Valenciana, and FPU17/04224 funded by MCIN/AEI/10.13039/501100011033 and by "ESF Investing in your future".

First and foremost, I would like to thank my supervisor Prof. Pablo Sanchis Kilders. Thank you Pablo for being such a great leader, researcher, and professor. I am very grateful for your trust and support.

I would like to express my sincere gratitude to the technical staff of the Nanophotonics Technology Center (Universitat Politècnica de València) for the fabrication of the samples, characterization of ITO and VO_2 materials, and their help with the setups of the lab. I would like to thank our collaborators of the Functional Nanosystems group (KU Leuven) led by Prof. Jean-Pierre Locquet, for providing VO_2 to our photonic chips. Also, I am grateful to Prof. Wolfram Pernice and his group members in the Center for NanoTechnology (WWU Münster) for allowing a pleasant research stay despite the COVID-19 pandemic.

Special thanks to all the coauthors of the papers and conferences we have published and presented during these four years. Most of them are part of this PhD Thesis. Their comments and suggestions were vital for the success of all the works.

Thank you very much to former and current Photonic Integrated Devices group members. I have been lucky to mentor several entry-research members in the exciting field of integrated photonics. Also, I cannot forget the more than 300 students from *Circuit Theory* lab course (2019-2022, ETSIT-UPV) for making my first steps as a teacher such an enriching experience.

Last but not least, outside the workplace, my most personal and warmest words are for my closest people. I would like to dedicate this work to my family and dearest people, who gave me the strength and unconditional support to carry out this project.

Resumen

La búsqueda de nuevas soluciones e ideas innovadoras en el campo de la fotónica de silicio mediante la integración de nuevos materiales con prestaciones únicas es un tema de alta actualidad entre la comunidad científica en fotónica y con un impacto potencial muy alto. Dentro de esta temática, esta tesis pretende contribuir hacia una nueva generación de dispositivos fotónicos basados en la integración de óxidos metálicos en tecnología de silicio. Los óxidos metálicos elegidos pertenecen a la familia de óxidos conductores transparentes (TCO), concretamente el óxido de indio y estaño (ITO) y el óxido de cadmio (CdO), y materiales de cambio de fase (PCM) como el dióxido de vanadio (VO_2). Dichos materiales se caracterizan especialmente por una variación drástica de sus propiedades optoelectrónicas, tales como la resistividad o el índice de refracción, frente a un estímulo externo ya sea en forma de temperatura, aplicación de un campo eléctrico o excitación óptica. De esta forma, nuestro objetivo es diseñar, fabricar y demostrar experimentalmente nuevas soluciones y dispositivos clave tales como dispositivos no volátiles, desfasadores y dispositivos con no linealidad óptica. Tales dispositivos podrían encontrar potencial utilidad en diversas aplicaciones que comprenden las comunicaciones ópticas, redes neuronales, LiDAR, computación, cuántica, entre otros. Las prestaciones clave en las que se pretende dar un salto disruptivo son el tamaño y capacidad para una alta densidad de integración, el consumo de potencia, y el ancho de banda.

Resum

La recerca de noves solucions i idees innovadores al camp de la fotònica de silici mitjançant la integració de nous materials amb prestacions úniques és un tema d'alta actualitat entre la comunitat científica en fotònica i amb un impacte potencial molt alt. D'aquesta temàtica, aquesta tesi pretén contribuir cap a una nova generació de dispositius fotònics basats en la integració d'òxids metàl·lics en tecnologia de silici. Els òxids metàl·lics elegits pertanyen a la família d'òxids conductors transparents (TCO), concretament l'òxid d'indi i estany (ITO) i l'òxid de cadmi (CdO), i materials de canvi de fase (PCM) com el diòxid de vanadi (VO_2). Aquests materials es caracteritzen especialment per una variació dràstica de les propietats optoelectròniques, com ara la resistivitat o l'índex de refracció, davant d'un estímul extern ja siga en forma de temperatura, aplicació d'un camp elèctric o excitació òptica. D'aquesta manera, el nostre objectiu és dissenyar, fabricar i demostrar experimentalment noves solucions i dispositius clau com ara dispositius no volàtils, desfasadors i dispositius amb no-linealitat òptica. Aquests dispositius podrien trobar potencial utilitat en diverses aplicacions que comprenen les comunicacions òptiques, xarxes neuronals, LiDAR, computació, quàntica, entre d'altres. Les prestacions clau en què es pretén fer un salt disruptiu són la grandària i la capacitat per a una alta densitat d'integració, el consum de potència i l'amplada de banda.

Abstract

The search for new solutions and innovative ideas in the field of silicon photonics through the integration of new materials featuring unique optoelectronic properties is a hot topic among the photonics scientific community with a very high potential impact. Within this topic, this thesis aims to contribute to a new generation of photonic devices based on the integration of metal oxides in silicon technology. The chosen metal oxides belong to the family of transparent conducting oxides (TCOs), namely indium tin oxide (ITO) and cadmium oxide (CdO), and phase change materials (PCMs) such as vanadium dioxide (VO_2). These materials are characterized by a drastic variation of their optoelectronic properties, such as resistivity or refractive index, in response to an external stimulus either in the form of temperature, application of an electric field, or optical excitation. Therefore, our objective is to design, fabricate and experimentally demonstrate new solutions and key devices such as non-volatile devices, phase shifters, and devices with optical nonlinearity. Such devices could find potential utility in several applications, including optical communications, neural networks, LiDAR, computing, and quantum. The key features in which we aim to take a leapfrog are footprint and capacity for high integration density, power consumption, and bandwidth.

Contents

List of tables

List of figures

List of acronyms

ALD Atomic layer deposition

ASIC Application-specific integrated circuit

AZO Aluminium-doped zinc oxide

AWG Arbitrary waveform generator

CMOS Complementary metal-oxide semiconductor

CNT Carbon nanotubes

CVD Chemical vapor deposition

CW Continuous wave

EDFA Erbium-doped fiber amplifier

ENZ Epsilon-near-zero

EOM Electro-optic modulator

ER Extinction ratio

FDTD Finite-difference time-domain

FEM Finite element method

FN Fowler-Nordheim

FOM Figure of merit

IL Insertion loss

IMT Insulator-metal transition

ITO Indium tin oxide

LiDAR Light detection and ranging

LMI Light-matter interaction

MAC Multiply accumulate

MBE Molecular beam epitaxy

MEM Micro-electro-mechanical system

MIT Metal-insulator transition

MMI Multimode interferometer

MOMOS Metal-oxide-metal-oxide

MOS Metal-oxide semiconductor

MRR Microring resonator

MZI Mach-Zehnder interferometer

NTC Nanophotonics Technology Center

NVMZI Non-volatile Mach-Zehnder interformeter

OPA Optical phased array

PC Polarization controller

PCM Phase-change material

PD Photodetector

PDE Plasma dispersion effect

PDK Process design kit

PECVD Plasma-enhanced chemical vapor deposition

PhCC Photonic crystal cavity

PhCW Photonic crystal waveguide

PIC Photonic integrated circuit

PML Perfectly matched layer

RRAM Resistive random access memory

RT Room temperature

RTE Radiative transport equation

SEM Scanning electron microscopy

SHG Second harmonic generation

SOI Silicon-on-insulator

SPT Structural phase transition

TCO Transparent conducting oxide

TE Transverse electric

TM Transverse magnetic

TMD Transition-metal dichalcogenide

TPA Two-photon absorption

UPV Universitat Politècnica de València

WDM Wavelength division multiplexing

1 Introduction

1.1 Silicon-based integrated photonics

Photonics enables the generation, processing, transmission, and detection of signals using photons. Lasers, optical fibers, the cameras and screens in our phones, optical tweezers, and lighting in our cars, homes, computer screens, and TVs are just a few examples of photonics. Given the current landscape and the potential that photonics has to enhance innovation in several industries, it has been recognized as one of Europe's key enabling technologies (KETs) of the 21^{st} Century [1].

Among the different applications, photonics has already had a major impact on telecommunications. Telecom networks are currently supported by optical fibers, which are the best media to transmit data over long distances. The main benefits of optical fibers over electrical cables or wireless transmission are the

ultra-high capacity (> Tb/s) and long transmission distances due to the low propagation loss (∼ 0.2 dB/km) and immunity against electromagnetic interferences. However, the growing demand for bandwidth in our connected society leads to ever-increasing energy consumption that is currently impacting our environment and economy. Moreover, the new technological paradigm of this century requires photonic devices that not only can transmit and receive ultra-fast signals through the fiber (i.e., sources, modulators, and detectors) but also have the potential for a broad number of applications encompassing health, energy savings, safety and security, and manufacturing, to name a few[1].

In this context, photonic integrated circuits (PICs) hold promises to fulfill such demands since they offer many advantages compared to discrete and bulky fiber-based devices, such as miniaturization, higher speed, low thermal effects, large integration capacity, and compatibility with existing fabrication processing flows that allow for high yield, volume manufacturing, and lower prices.

1.1.1 Silicon technology

Silicon (Si) photonics has emerged as the best approach for enabling large-scale and low-cost production of PICs. Silicon is transparent at telecom wavelength and has a high refractive index ($n \approx 3.47$ at $\lambda = 1550$ nm), which allows the implementation of photonic waveguides where the optical light can be highly confined (see Fig. 1.1a), leading to compact devices (see Fig. 1.1b), and thereby enabling high-density PICs with and large-scale manufacturing (see Fig. 1.1c).

The distinctive benefit of silicon photonics is the compatibility of the fabrication processes with the well-proven and extended complementary metal-oxide-semiconductor (CMOS) processes that are used by the micro/nano electronics industry. Such an advantage enables the monolithic co-integration of photonics and electronics on a single chip fabricated using the same infrastructure. This is a crucial feature because it simultaneously achieves the required levels of performance, scalability, and complexity for electronic-photonic systems; it substantially accelerates system-level innovation by enabling a cohesive design environment and device ecosystem to realize entire systems on a chip [2]. Figure 1.2 shows a recent experimental demonstration of monolithic integration of photonics and electronics in the same 65-nm bulk CMOS platform [3]. Therefore,

[1] https://photonhub.eu

the combination of both CMOS-compatible fabrication and high index contrast results in the enormous potential of silicon photonics for manufacturing PICs at a large scale, with low cost and high integration density. Currently, silicon photonics-based products are already in the market provided by leading companies like Intel or Cisco, and many foundries offer large-scale silicon PICs manufacturing.

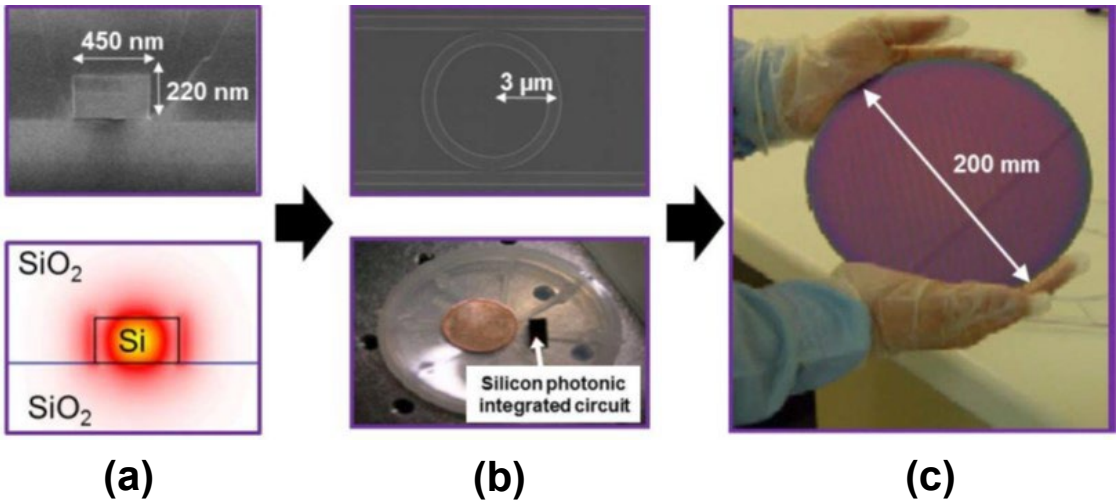

Fig. 1.1. **(a)** Scanning electron microscope (SEM) image of a typical silicon waveguide (top image) and fundamental mode profile for TE polarization (bottom image). **(b)** Photonic structure made by a bent silicon waveguide with a radius of 3 µm and silicon PIC used for testing at the laboratory. **(c)** 8-inch (200 mm) silicon wafer fabricated in a CMOS foundry containing more than 2000 PICs.

1.1.2 Applications

Driven by the impressive technological development in recent years, silicon photonics is expanding its frontiers toward new applications beyond optical communications, such as artificial intelligence and neuromorphic computing, laser imaging detection and ranging (LiDAR), and signal processing and computing, to name a few.

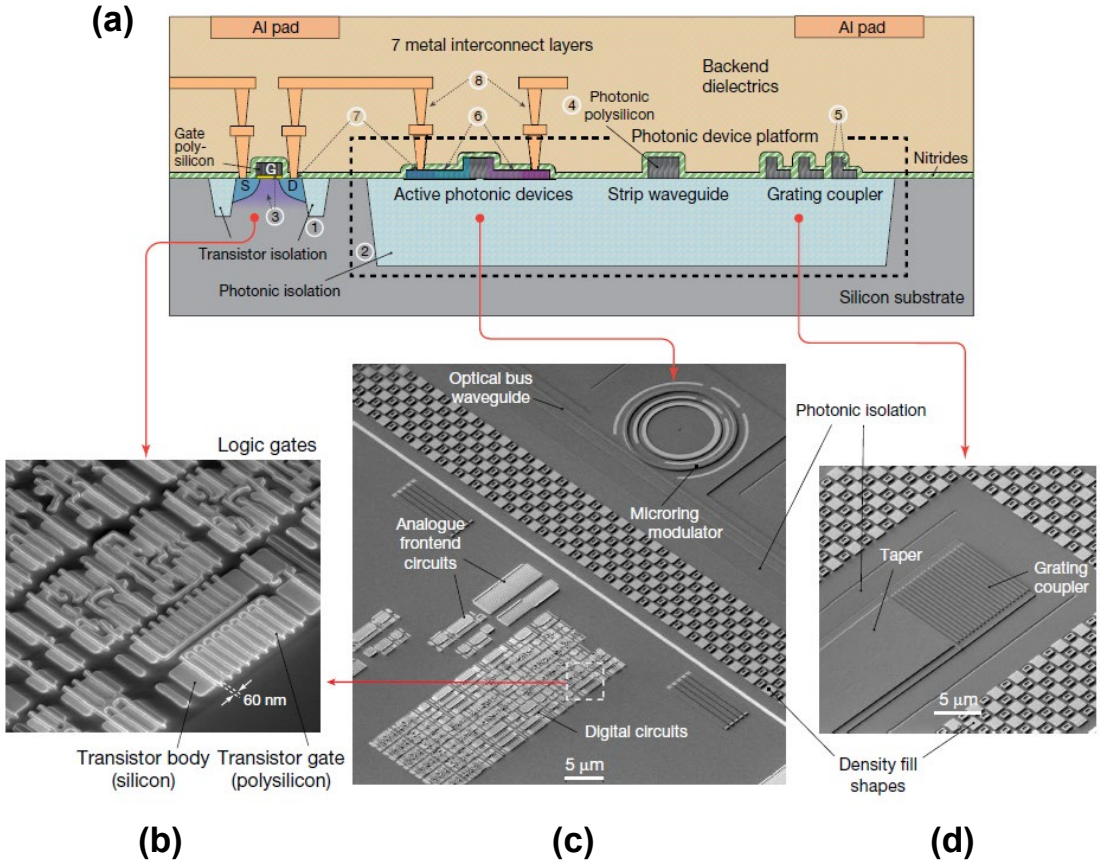

Fig. 1.2. **(a)** Cross-sectional drawing of the monolithic integration of a photonic circuit and nanoscale transistors into planar bulk CMOS process. **(b)**-**(d)** SEM images of the electronic and photonic blocks: **(b)** Digital electronic circuits, **(c)** active photonic devices and electronics, and **(d)** grating structure used for fiber-to-chip coupling [3].

Optical communications

The main application of silicon photonics is currently the development of ultra-fast transceivers for optical interconnectivity in telecom networks and data centers. Optical transceivers are already in the market for high-speed data communications by exploiting the large capacity provided by optical fiber. Current efforts are focused on extending photonics inside the racks of data centers for data switching and routing data at higher speed and lower energy consumption by mitigating the bottleneck introduced by electronic-photonic conversions [4].

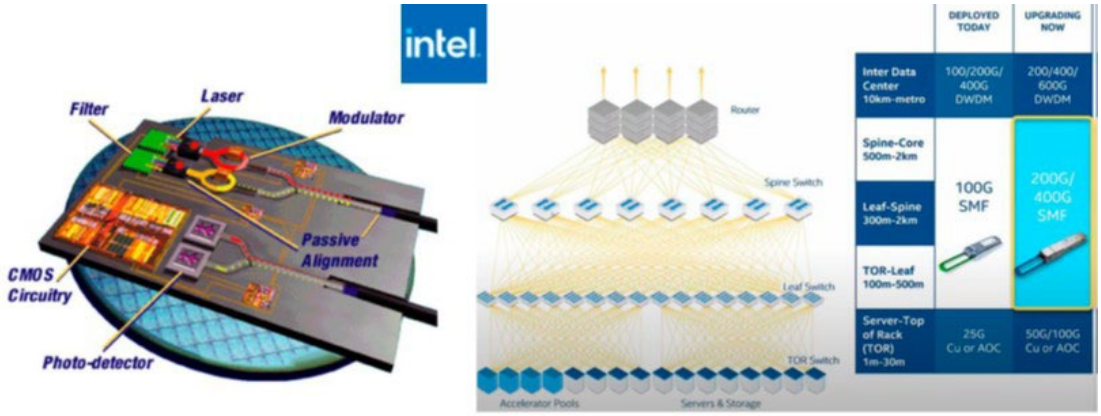

(a) **(b)**

Fig. 1.3. **(a)** Schematic of a photonic transceiver and **(b)** architecture of today's hyper-scale data-centers optical interconnected with photonics transceivers. On the right are commercial silicon photonic transceivers supplied by Intel (100 Gb/s inside the data center) and upgrading plans.

Figure 1.3a shows a silicon photonic integrated transceiver schematic. The transmitter (lasers, modulators, combiner/multiplexer) and the receiver (photodetectors, splitters/demultiplexers) are integrated on a single photonic chip with the driving electronics and connected to the input/output optical fibers. Remarkably, silicon photonics is the only technology that allows the monolithic integration of electronics and photonics. Figure 1.3b shows the typical architecture of today's hyper-scale data-centers. Such mega-scale data centers have been developed to meet the demand of the continuous increase in global internet traffic produced by a nearly exponential growth in cloud-based applications, social media, and big data analytics. Actually, most of this internet traffic is not between data centers and users or between data centers. Most of the traffic, above 70% of the total data center traffic, occurs within the data center between servers and switches. Silicon photonic transceivers, shown in the right part of Fig. 1.3b, are currently supplied by Intel with data rates up to 400 Gb/sto to provide optical interconnectivity inside the data center.

However, as data center networking speed and capacity increase, power consumption increases because more energy is required to transmit the electric signals between the transceivers and electrical switches. That energy creates heat;

thus, additional power is needed to keep the data center cool. In fact, data centers account for around 1% of global electricity demand despite great efficiency improvements that have helped to limit energy demand growth [5]. Therefore, co-packaged solutions, where photonics is much closer to electronics, are being developed [2]. In addition, optical switching has also been identified as a potential enabler due to the low energy requirements of optical switches compared to their electronic counterparts.

Artificial intelligence and neuromorphic computing

Artificial intelligence is an attempt to approach human-level accuracy in tasks that are challenging for traditional computers but easy for humans. A subset of artificial intelligence is machine learning which allows machines to learn from data without being programmed explicitly. Machine learning is implemented in our daily practices, such as finding the fastest path to reach a destination, medical diagnosis, language translation, and many others. Faster and more energy-efficient information processing is obtained by implementing software machine-learning algorithms into hardware. In this regard, neuromorphic computing is partly an attempt to move elements of machine learning and artificial intelligence algorithms to hardware that reflects their massively distributed nature. Massively distributed hardware relies heavily on massively parallel interconnections between the neural elements, i.e., neurons. However, most modern computers are based on the von Neumann architecture, which is suited to running sequential, digital, procedure-based programs but inefficient for neural networks.

Photonic circuits are well suited to high-performance implementations of neural networks for two principal reasons: interconnectivity and linear operations [8]. Optical signals can be multiplied by transmission through tunable waveguide elements. Indeed, the silicon photonics platform can host high-quality passive components combined with high-speed active optoelectronics, all available with competitive integration density. Figure 1.4 shows some examples of neural networks implemented in silicon photonics. Therefore, neuromorphic photonic processors can enable applications that are unreachable at present by conventional electronics –those requiring low latency, high bandwidth, and low energies – such as fundamental physics problems [9], nonlinear programming [10], or accelerated learning [11].

However, although photonics provides advantages in connectivity and linear

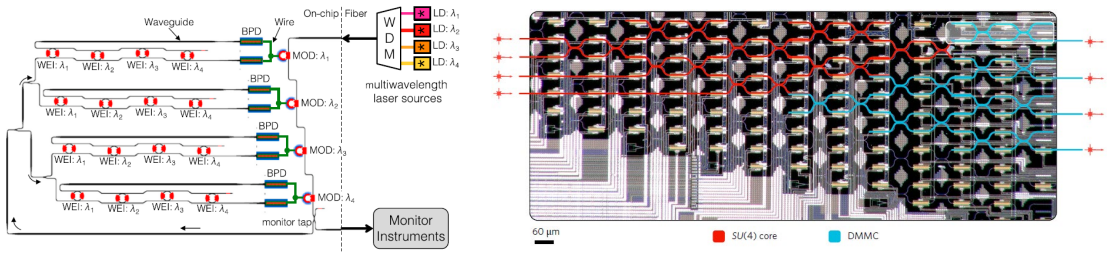

(a) (b)

Fig. 1.4. **(a)** Schematic of a multiwavelength broadcast-and-weight photonic neural network [6]. **(b)** Coherent all-optical feed-forward network configured to implement a matrix using singular value decomposition: red meshes implement a unitary matrix, and blue meshes implement a diagonal matrix [7].

operations over electronics, other aspects, such as storing and accessing neuron weights in on-chip memory, present new challenges. Therefore, future scalable neuromorphic photonic processors will need to have a tight co-integration of electronics with potentially hybrid electronic and optical memory architectures.

Free-space optics systems

Although PICs are built on waveguides, integrated photonics can enable the next generation of space communications systems [12], the autonomous vehicle using LiDAR (Light Detection and Ranging) [13], or three-dimensional holography [14]. Those applications rely on generating a narrow, low divergence laser beam, known as optical beam shaping or optical beam steering, when there is a dynamic pointing or scanning of such beams. For instance, beam steering can compensate for the relative displacements between transmitter and receiver in space communications systems or make a 3D mapping of the environment. Currently, systems that can generate, shape, and steer a narrow optical beam tend to be rather bulky, as they often consist of mechanical assemblies based on optomechanical systems. Such systems are expensive, relatively slow, and sensitive to temperature changes and mechanical shocks, which limit their use typically to static, ground-based deployment. In this context, PICs offer such systems a drastic reduction in their size, weight, and power consumption, thus enabling their mounting on, for example, autonomous cars, drones, or smartphones [15].

Optical beam steering is usually achieved using optical phased arrays (OPAs).

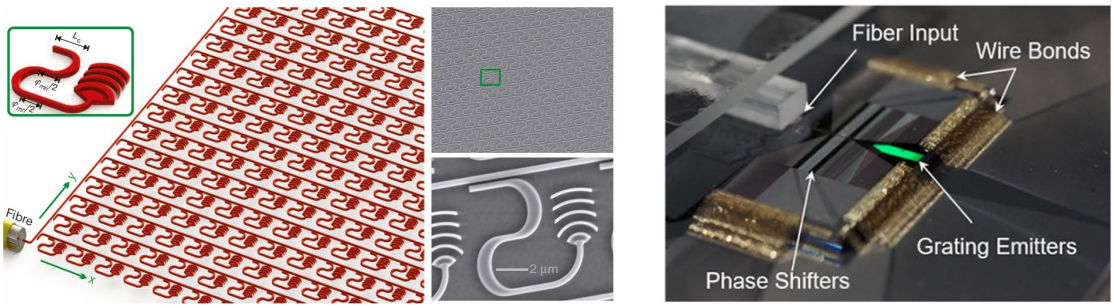

(a) (b)

Fig. 1.5. **(a)** Schematic illustration of a 64×64 silicon-based phased array system (left image), and SEM image of the fabricated chip [16]. **(b)** Optical phased array containing 512 active silicon antennas. Tha package devices consists of a 8 mm × 15 mm phased array chip wire-bonded to a silicon interposer, along with an optical fiber input [17].

Like phased array antennas for microwaves, OPAs are basically arrays of coherent optical antennas. Similarly, the radiation pattern of an OPA is controlled by adjusting the phase and/or amplitude of the optical antenna. Compared to microwave phased arrays, the short wavelength of light offers the potential for silicon-based OPAs to greatly exceed the number of elements found in their radiofrequency counterparts, with thousands or even millions of elements in a compact, low-cost chip. Figure 1.5a shows an illustration of an OPA in a silicon chip consisting of a total of 4,096 nanoantennas, each of one with a dimension of just 9 μm × 9 μm [16]. In order to achieve a widely steerable and low-divergence output, a large number of tunable optical antennas is required. Tunability is usually achieved by incorporating active devices, such as phase shifters, into the emitters (see Fig. 1.5b) [17]. Therefore, a major challenge of tunable OPAs is to keep the power consumption as low as possible, even for thousands or hundreds of thousands of tunable emitters. In this regard, the main quest is how to build low-loss, low-power, and compact phase shifters that meet the demands of OPA applications.

Signal processing and computing

Microwave photonics Current analog signal processors suffer from low bandwidth, are complex, bulky, and/or offer limited functionalities. Photonic tech-

niques provide many advantageous features over their electronic counterpart for generating, processing, controlling, and distributing microwave and mm-wave signals for applications such as broadband wireless access networks, sensor networks, radar, satellite communications, instrumentation, and warfare systems [18]. A microwave photonic (MWP) signal processor is a photonic counterpart of an analog RF signal processor, wherein optical signal processing enables high frequency and ultra-broadband operation (easily into the THz range) with electromagnetic interference immunity. The major functions of microwave photonics systems include photonic generation, processing, control, and distribution of microwave and millimeter-wave (mm-wave) signals. In general, the topics covered by microwave photonics include the photonic generation of microwave and mm-wave signals, photonic processing of microwave and mm-wave signals, optically controlled phased array antennas, radio-over-fiber systems, and photonic analog-to-digital conversion.

Therefore, integrated microwave photonics (IMWP) based processors, wherein the sub-system is entirely integrated on a chip, can provide the performance specifications that are desired for practical applications, in terms of reduced power consumption, compactness, and low-cost [19]. IMWP signal processors are composed of several components, such as passive components, optical sources, modulators, and photodetectors. Many of these components require continuous tuning to allow reconfigurability. Hence, a significant challenge to address is the power consumption of these tuning elements. In this regard, ultra-low power switches and phase shifters would be highly desired.

Photonic tensor cores Photonic tensor cores are photonic hardware accelerators capable of operating at speeds of more than billions of multiply-accumulate (MAC) operations per second. They are considered the optical analog of an application-specific integrated circuit (ASIC). Such type of hardware is needed in neural networks since they rely on vector-matrix math operations, in which large matrices of data and weights are multiplied. Integrated photonics can indeed provide parallel, power-efficient, and low-latency computing, which is possible because analog wave chips can (a) perform the dot product inherently using light-matter interactions such as via a phase shifter or modulator, (b) enable signal accumulation (summation) by either coherent electromagnetic interference or incoherent accumulation through detectors, and (c) enable parallelism strategies

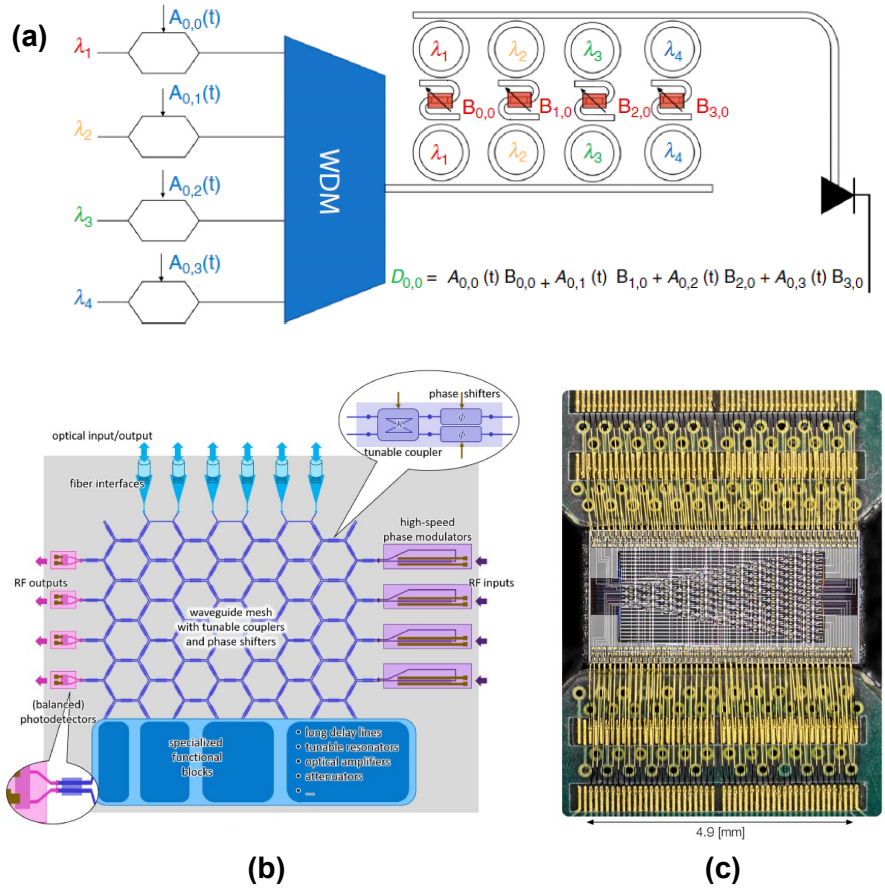

Fig. 1.6. **(a)** Implementation schematic of a photonic tensor core constituted by a 16-dot product engine that inherently and independently performs row-by-column pointwise multiplication and accumulation. [20]. **(b)** Basic concept of a programmable photonic circuit, where a reconfigurable linear circuit connects the optical fiber ports, the modulators (RF inputs), and balanced photodetectors (RF outputs) with the other functional blocks. The central mesh consists of electrically actuated 2×2 couplers, and phase shifters [21]. **(c)** Optical micrograph of programmable silicon-based processor for quantum application. The processor consists of 26 inputs/outputs, and 176 phase shifters [22].

and higher throughput using multiplexing schemes [20].

Figure 1.6a shows an example of a 4×4 integrated photonic tensor core implementation to multiply and input matrix $\boldsymbol{A}$ by a stored kernel $\boldsymbol{B}$. The i^{th} row of the input matrix is given by wavelength-division-multiplexed (WDM) signals, which are modulated by high-speed modulators. The kernel matrix's j^{th} column

is loaded in the photonic memory by properly setting its weight states. Exploiting the light-matter interaction with the memory, the inputs, opportunely spectrally filtered by microring resonators (MRR), are weighted in a seemingly quantized electroabsorption scheme (i.e., amplitude modulation), thus performing element-wise multiplication. The element-wise multiplications are thence incoherently summed up using a photodetector, which amounts to a MAC operation (D_{ij}).

Recently, integrated photonic tensor cores have been demonstrated in the silicon nitride platform operating at 10^{12} MACs per second [23]. Moreover, the authors of that work predict that such values could even exceed 1 Peta-MAC operation per second (10^{15} MAC operations per second) by scaling up the matrix size by leveraging the smaller footprint of the silicon photonics platform. Therefore, Si-based non-volatile devices would be highly appealing to enable such promising results.

Programmable photonics Integrated photonic circuits designed for specific applications leverage the benefits of a photonics platform to obtain the best performance for such an application. However, sometimes universality and run-time reconfigurability for multifunctional applications is desired with a certain penalty on the hardware performance. In this regard, programmable integrated photonics has emerged as a pivotal topic. Programmable PICs are based on the idea that the flow of light on the chip can be manipulated at run-time, for example, by electrically controlling tunable beam couplers connected by optical waveguides. This way, light is distributed and spatially rerouted under software control [24]. Figure 1.6c illustrates the basic concept of a programmable photonic circuits. Optical reconfigurability occurs in the waveguide mesh using tunable couplers and phase shifters, also known as "universal unitary gate" (see top right inset of Fig. 1.6c) [21]. In this regard, programmable integrated photonics can be considered the optical analog of field-programmable gate arrays (FPGAs), with applications encompassing from microwave photonics to neural networks or quantum information processing. However, the main limitation of current programmable photonic circuits is the footprint and power consumption of the tunable building block. Therefore, compact, low-loss, and low-power devices to build a "universal unitary gate" would be highly appealing to the programmable integrated photonics community.

Quantum information processing Photons can be exploited as quantum information carriers. By using optical waveguides to guide and route photons, integrated quantum photonics provides phase-stable quantum circuitry with core functionalities, including entangled state generation, quantum state manipulation, and single-photon detection [25]. Re-programming photonic chips allow the processing of multiple quantum tasks and algorithms in a single chip. Investigation of the role of environmental noise in quantum transport has been demonstrated using a nanophotonic processor comprised of a mesh of 88 generalized beamsplitters programmable on microsecond timescales (see Fig. 1.6c) [22]. Like programmable photonics, one of the basic building blocks of PICs for quantum functionalities are switches with ultra-low losses [26]. Therefore, fast and ultra-low loss switches will be required to continue the development of quantum applications.

1.1.3 Beyond silicon: Hybrid material integration

Although Si is an excellent material for building passive devices, its active properties are relatively modest. For instance, there are no silicon-based on-chip light sources due to the Si indirect bandgap. On the other hand, modulators ready to be used for commercial devices are based on the plasma dispersion effect. High speeds above 40 Gb/s may be achieved. However, the weak physical effect leads to devices with a very large footprint. Modulation lengths are typical of several millimeters, which are various orders of magnitude higher than the nanoscale size of transistors achieved by current CMOS electronics. Hence, the size mismatch between photonics and electronics hinders the electro-optical co-integration for developing PICs with advanced functions.

Therefore, aiming to meet the requirements of these emerging applications, the Si photonics community is exploring the hybrid integration of alternative CMOS-compatible materials with high-performance optoelectronic properties to improve the performance and footprint drastically. Figure 1.7 shows a timeline with a subjective view of some of the major milestones in the field of silicon photonic devices encompassing from the first passive devices made in silicon-on-insulator to more advanced optoelectronic devices thanks to the integration of other materials. One clear success example is the integration of group IV materials such as germanium with silicon to develop ultra-compact photodetectors

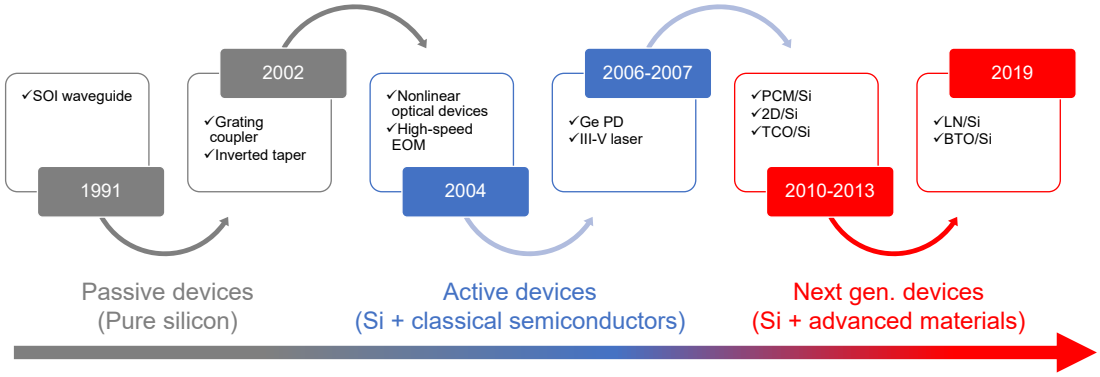

Fig. 1.7. Timeline of some of the major milestones in the field of silicon photonic devices. Passive devices: Silicon-on-insulator (SOI) waveguide [27], grating coupler [28], and inverted taper [29]. Active devices based on silicon and group IV materials: Nonlinear optical devices [30, 31], high-speed electro-optic modulator (EOM) [32], III-V laser [33], and Ge photodetector (PD) [34]. Next generation of devices based on the integration of advanced materials in a silicon waveguide: Phase-change materials (PCMs) [35, 36], two-dimensional (2D) materials [37], transparent conducting oxides (TCOs) [38], lithium niobate (LN) [39], and barium titanate (BTO) [40].

with an active length below 10 µm and competitive performance for real applications. Over the last decade, various advanced materials with unique optoelectronic properties have been proposed to integrate into the silicon photonics platform, such as phase-change materials (PCMs), transparent conducting oxides (TCOs), 2D materials, ferroelectrics, among many others. Among these, metal oxides such as TCO compounds and vanadium dioxide (VO_2) are very appealing to meet the device requirements of the applications mentioned above.

As described in the next section, TCOs can provide extraordinary tuning and modulation of their complex refractive indices by changing the carrier concentration by applying an electric field. Therefore, TCOs provide an excellent platform for enabling ultra-compact photonic devices with active lengths in the micrometer range and electro-optical activity. On the other hand, VO_2 features a dramatic (unitary) and hysteretic change in its refractive index that can be induced by different external stimuli such as heat, electric field, or light. Therefore, the integration of this material can enable both electro-optic and all-optical compact

devices with active lengths in the micrometer range.

1.2 Metal oxides for hybrid integrated photonics

1.2.1 Transparent conducting oxides (TCOs)

Transparent conducting oxides are a family of electrically conductive metal oxides but have low absorption at visible wavelengths [41]. Thus, the most used application for TCOs is as transparent electrodes. Apart from such properties, compared to conventional noble metals, TCOs have high melting points and are chemically stable [42]. Moreover, the optical properties of TCOs can be adjusted via doping and/or fabrication processes [43]. Therefore, in recent years, TCOs have gained significant attention as an alternative to conventional metals. In this regard, TCOs films have been widely investigated for optoelectronic applications such as solar cells, transistors, or consumer electronics due to the advent of touch-screen devices [44].

There are many TCO compounds, and the most popular are indium tin oxide (ITO), aluminum-doped zinc oxide (AZO), cadmium oxide (CdO), gallium zinc oxide (GZO), and indium gallium zinc oxide (IGZO). ITO is the most used TCO since it has been employed in the industry for the fabrication of transparent electrodes for over two decades due to its high transparency at visible wavelengths [45]. The composition of ITO is usually 90 %wt indium oxide (In_2O_3) and 10 %wt tin oxide (SnO_2). However, indium is a scarce material, and ITO can be potentially toxic to the people exposed during the fabrication. Therefore, the optoelectronics community is seeking other alternative TCOs. In particular, AZO is an attractive TCO because it posses similar electrical and optical properties like ITO [46], but is made of abundant natural elements while being nontoxic [47].

Free carrier tunability and epsilon-near-zero (ENZ) regime

Materials that are both transparent and electrically conductive may be seen as a contradiction since, to be conductive, a material should have high carrier mobility and carrier concentration. Typically, these two conditions lead to a material with high optical loss. However, TCOs overcome this problem due to their wide bandgap (3-5 eV) that ensures almost no interband transition losses. TCOs are a class of highly-doped degenerate semiconductors capable of accepting high doping concentrations without a fundamental change of the material structure [48]. Typically, the extra doping of TCOs is n-type, in which extra free carriers, typi-

cally between 10^{19} and 10^{21} cm^{-3}, are injected into the conduction band. The increase in the carrier concentration pushes the Fermi level up into the conduction band, which widens the bandgap via the Moss-Burstein shift. Therefore, both electrical conductivity and optical transparency can be enhanced at the same time [49].

Because TCOs are conductive, the free carrier concentration determines their permittivity in the near-infrared regime. Hence, like for metals, the Drude model is usually employed to retrieve the dielectric function, $\varepsilon = \varepsilon' + j\varepsilon''$, of TCOs at telecom wavelengths [50]. Therefore, the expressions of the electrical resistivity ρ and optical permittivity at the near-infrared are

$$\rho = \frac{\Gamma m^*}{N q^2} \tag{1.1}$$

and

$$\varepsilon = \varepsilon_\infty \left(1 - \frac{\omega_p^2}{\omega^2 + j\omega\Gamma} \right), \tag{1.2}$$

where ε_∞ is the high-frequency permittivity, ω is the angular frequency, Γ is the damping factor, and ω_p is the plasma frequency, which can be expressed as:

$$\omega_p = \sqrt{\frac{N q^2}{\varepsilon_\infty \varepsilon_0 m^*}}. \tag{1.3}$$

The parameter N stands for the free carrier concentration, q is the electron charge, ε_0 is the vacuum permittivity, and m^* is the effective electron mass.

Importantly, compared to metals, TCOs have a significantly lower free carrier concentration. This feature enables TCOs to have the unique property of crossing between being dielectric ($\varepsilon' > 0$) and metallic ($\varepsilon' < 0$) around telecom wavelengths (see Fig. 1.8a) together with a low value of $|\varepsilon|$ caused by the small value of ε'' (see Fig. 1.8b). Such near-zero permittivity, known as the epsilon-near-zero (ENZ) regime, is very interesting because the light-matter interaction (LMI) is dramatically enhanced [51] around the crossing wavelength (λ_{ENZ}). In order to achieve the ENZ regime at telecom wavelengths, TCOs require a free carrier concentration of the order of $10^{20} - 10^{21}$ cm^{-3}. To this end, such values could be obtained by adjusting the fabrication parameters, doping level, or stoichiometry [42].

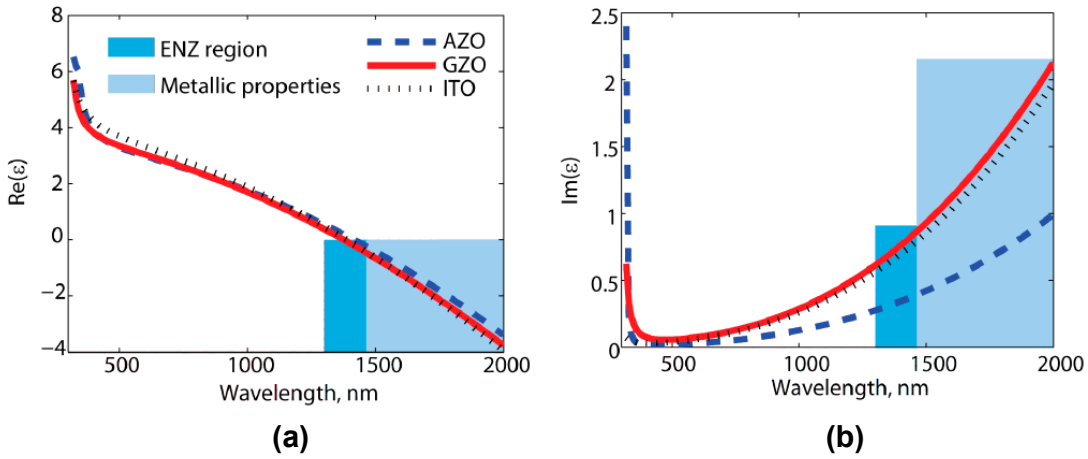

Fig. 1.8. Optical properties of different TCOs (AZO, GZO, and ITO): **(a)** real and **(b)** imaginary parts of permittivity [52].

Thin film fabrication

TCOs thin films can be deposited and patterned by standard fabrication procedures and integrated with many other standard technologies. Typical fabrication processes encompass sputtering [53], laser ablation [54], chemical vapor deposition (CVD) [55], or solution processing [56]. Deposition schemes such as laser ablation or sputtering are more suitable when stoichiometry needs to be controlled. For instance, ITO is a non-stoichiometric compound whose optical properties largely depend on the deposition process and annealing conditions [57, 53]. Performing post-annealing in nitrogen has been shown to produce more conductive and less transparent ITO films, whereas less conductive and more transparent films are achieved by annealing the ITO in oxygen [58]. Also, for this latter, the influence of the annealing temperature and sputtering power has been investigated [59], showing that as the annealing temperature increases, the optical losses decrease, and the λ_{ENZ} shifts to higher wavelengths. On the other hand, as the sputtering power is increased, both λ_{ENZ} and optical loss decrease, which is attributed to a decreased oxygen content in the ITO.

Applications in integrated photonics

Extraordinary tuning and modulation of the TCOs refractive index can be achieved by changing the carrier concentration by applying an external electri-

cal field. Hence, TCOs have become promising candidates for building electro-optic devices [60] and, particularly, for developing electro-optic modulators in the silicon photonics platform featuring optical broadband response in ultra-compact footprints [61, 52]. Figure 1.9a illustrates the concept of TCO-based silicon electro-optic devices. To this end, the TCO is embedded in a MOS structure as shown in Fig. 1.9b, where a charge accumulation or depletion occurs in the TCO layer (see Fig. 1.9c) which in turn changes the plasma frequency (see Eq. (1.3)), and thereby its permittivity (see Eq. (1.2)) [52]. In this regard, in the recent years, numerous TCO-based modulators have been experimentally demonstrated [38, 62–74] (Fig. 1.10 shows a selection of these devices), featuring in ultra-compact footprints of few micrometers high-speeds in the gigahertz range [67, 70, 71, 73], and beyond 40 GHz [74], with energy consumptions as low as 18.3 fJ [73], and broad spectral response at telecom wavelengths.

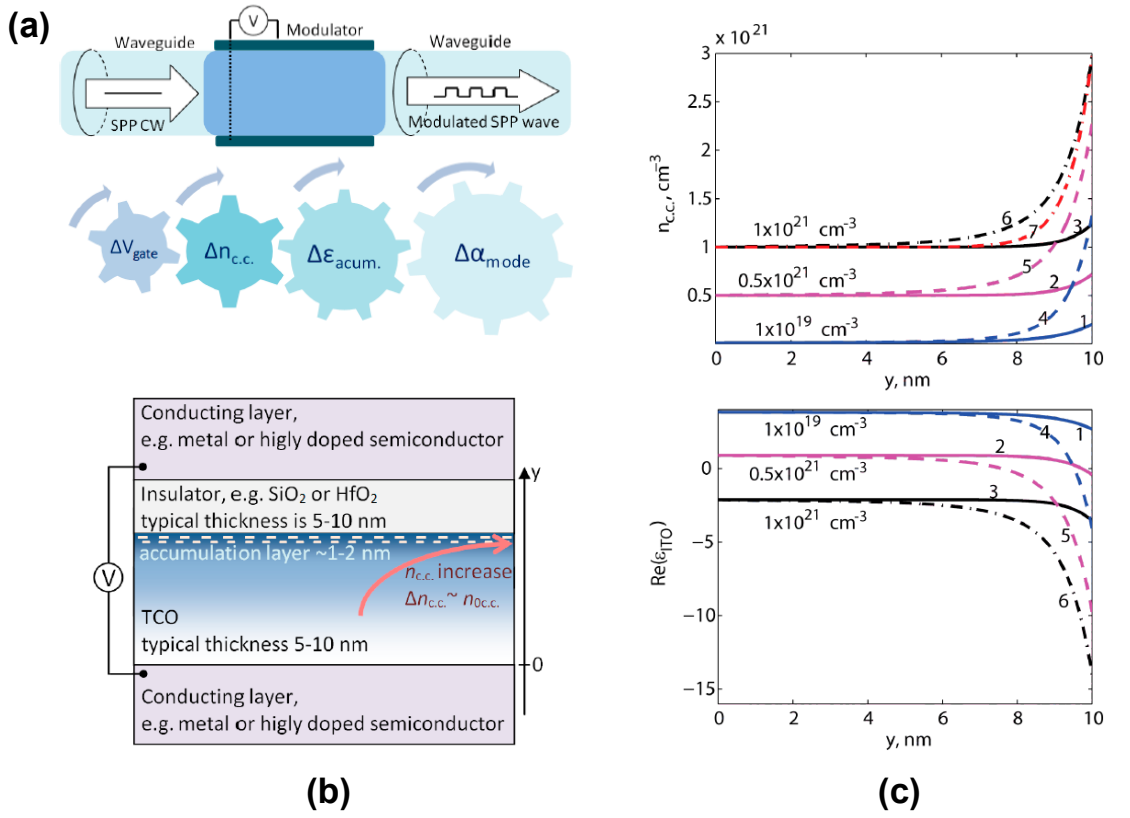

Fig. 1.9. **(a)** General concept of a TCO modulator integrated with a waveguide and utilized in hybrid photonic/electronic circuits: electrical bias V changes properties of sandwiched TCO and thus controls the absorption of the light. The voltage ΔV_{gate} changes the free carrier concentration of the TCO $\Delta n_{\text{c.c}}$, which results in a change in the permittivity in the region where the accumulation/depletion layer occurs $\Delta\varepsilon_{\text{acum}}$, and thereby there is a change in the propagation loss of the optical mode $\Delta\alpha_{\text{mode}}$. **(b)** Schematic view of a typical MOS structure with the TCO sandwiched. **(c)** Typical distribution in the MOS structure of the carrier concentration (top image) and TCO permittivity (bottom image) according to the Thomas-Fermi screening theory and for different initial carrier concentrations in the TCO layer. Images reproduced from [52].

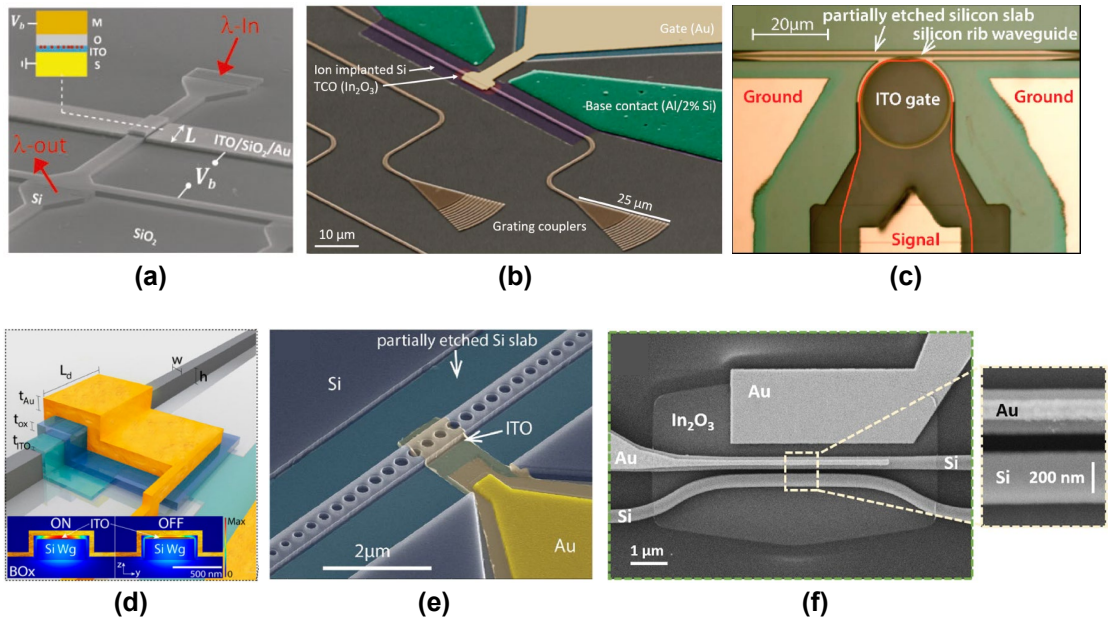

Fig. 1.10. **(a)** SEM image of a 5-μm-long ITO/Si modulator formed by a MOS capacitor (ITO-SiO_2-Au) [38]. **(b)**False colored SEM image of a 4-μm-long TCO/Si modulator based on In_2O_3 and working up to 2.5 Gb/s [67]. Optical image of a tunable silicon ring resonator using ITO [69]. **(d)** Schematic of a broadband and gigahertz ITO-based phase shifter of only 1.4 μm long [70]. **(e)** False-color SEM image of 1-μm-long silicon nanocavity modulator driven by an ITO gate with energy efficiency as low as 18.3 fJ/bit. **(f)** SEM image of an ultra-fast (> 40 GHz) modulator based on a 3.5-μm-long In_2O_3/Si directional coupler [74].

1.2.2 Vanadium dioxide (VO_2)

Metal-insulator transition (MIT) –also known as insulator-metal transition (IMT), depending on which phase initiates the phase transition– in oxides is a half-century-old topic of intense research in condensed matter material sciences [75]. Typically, the MIT in such oxides is accessed by temperature. Figure 1.11a shows a list of a selected oxides and their MIT temperature (T_{MIT}). Among these oxides, the V-O system could be one of the most attractive materials caused by the great variety of compounds, such as VO, VO_2, V_2O_3, V_4O_7, and many others. Many of them exhibit a typical MIT with sharp changes in optical, electrical, thermal, and magnetic properties [76].

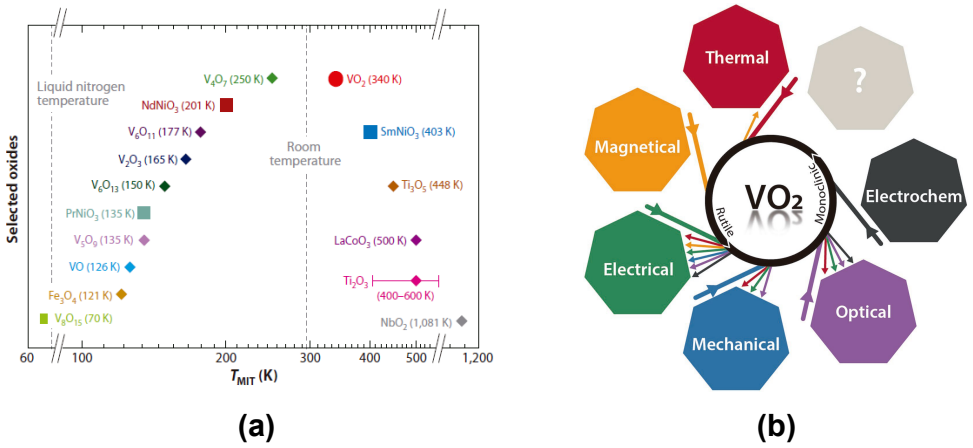

Fig. 1.11. **(a)** MIT temperature (T_{MIT}) of some selected oxides [77]. **(b)** Illustration of the demonstrated stimuli to induce the MIT and input-output conversion. The input arrow stands for the stimulus and the output for the response. The arrow color is the type of response. The "?" block represent future/undiscovered input/outputs [76].

Mainly, VO_2 is the most exciting compound because its transition temperature occurs near room temperature (~ 68 ºC, 340 K) [78]. In VO_2, the MIT is accompanied by a structural phase transition (SPT) between a first-order monoclinic (M) insulator phase and to rutile (R) metallic phase transition. On the other hand, the MIT in VO_2 can be driven by a broad number of stimuli, as shown in Fig. 1.11b, such as optical, electrical, thermal, mechanical, and magnetic signals [76]. Interestingly, VO_2 can work as a transducer by producing an input-output

conversion (see input-output arrows of Fig. 1.11b). For these reasons, VO_2 is usually coined to the family of PCMs among the photonics community [79]. PCMs can be defined as a group of materials whose optical properties can be modified by changing their atomic structure. Finally, such a powerful feature has enabled a plethora of different applications encompassing smart windows, camouflage, sensors, electro-optic/all-optical switching, memories, photodetectors, transistors, memristors, spintronics, and many others [76].

Metal-insulator transition (MIT): Electrical and optical properties

As mentioned above, the phase transition of VO_2 can be triggered using different approaches. Here, we focus on temperature excitation and the associated change in the electrical and optical properties of VO_2 for both states. For other stimuli, we refer the reader to these reviews [76, 80].

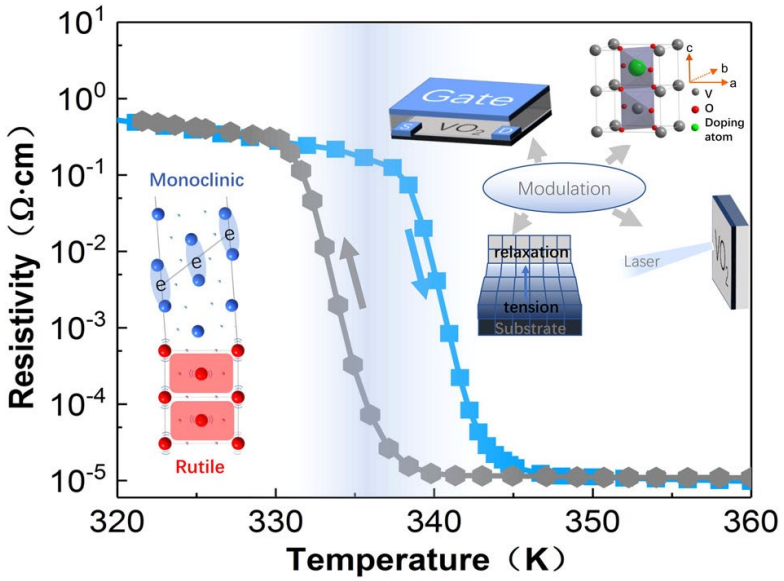

Fig. 1.12. VO_2 resistivity undergoing the IMT and MIT during a heating-cooling cycle. Insets show the phase transition between the metallic and insulating phase (lower left), and the different modulation methods (upper right) [81].

Typically, VO_2 films have a sharp change of 3-5 orders of magnitude in the resistivity between the insulating and metallic phase, as shown in Fig. 1.12. Moreover, the response has certain hysteresis, as noted in the different temperatures for the MIT and insulator-metal transition (IMT), which can be of interest

for some applications such as memories. The optical side accompanies such a change in the electrical properties. In this regard, the VO_2 also suffers a drastic change in the complex refractive index, as shown in Fig. 1.13. Both real parts and imaginary parts change in the order of unity. The typical values at 1550 nm are $\sim 3.2 + j0.2$ and $\sim 2 + j3$ for the insulating and metallic states, respectively. It should be underlined that both resistivity and refractive depend on various factors, including deposition conditions, substrate, stoichiometry, and grain size [81]. Therefore, it is recommended to characterize the electrical and optical properties of VO_2 thin films before their use in the application of interest. The optical modeling of the refractive index through the MIT is non-trivial, caused by the coexistence of different phases. Hence, several Lorentz oscillators are typically employed with a Drude oscillator to represent the free carriers in the metallic phase better [82].

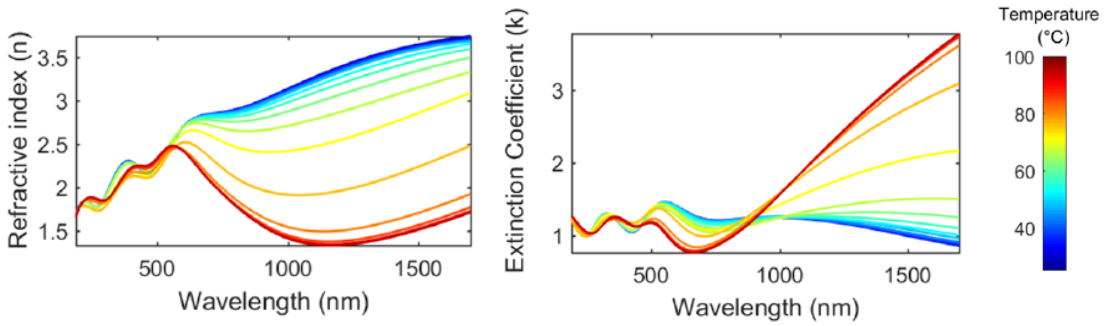

Fig. 1.13. **(a)** Real and **(b)** imaginary parts of the complex refractive index spectrum of VO_2 thin film deposited on sapphire for different temperatures. Adapted from [83] and [84] (original data).

Thin film fabrication

A key aspect of synthesizing high-quality VO_2 thin films is to achieve precise control of the stoichiometry to avoid the formation of oxygen defects and other stoichiometric phases, e.g., V_2O_3, by regulating the growth conditions [80]. The most common methods to grow thin films with pure VO_2 are CVD [85], sputtering [86], pulsed laser deposition (PLD) [87], sol-gel deposition [88], and molecular beam epitaxy (MBE) [89].

Applications in integrated photonics

As mentioned, VO_2 stands out for the ultra-large change in its complex refractive index between the insulating and metallic states. This feature enables hybrid tunable VO_2 waveguides with lengths down to hundreds of nanometers. Moreover, these waveguides are broadband since the changes in the VO_2 refractive index span a spectral range from the visible to the mid-infrared wavelength regions. The scheme of a commonly reported hybrid VO_2/Si waveguide is depicted in Fig. 1.14. The latter comprises a silicon waveguide with a patch of VO_2 on top. By triggering the IMT of VO_2 with an external excitation (heat, electric field, or light), the guided mode could experience a change in both phase and amplitude. Hence, several VO_2 integrated devices, mainly for switching operation, have been experimentally demonstrated in the last decade [35, 90–99, 97, 100]. Figure 1.15 gathers a selection of experimental switching devices having ultra-compact footprints (< 20 µm) and driven switching mechanisms.

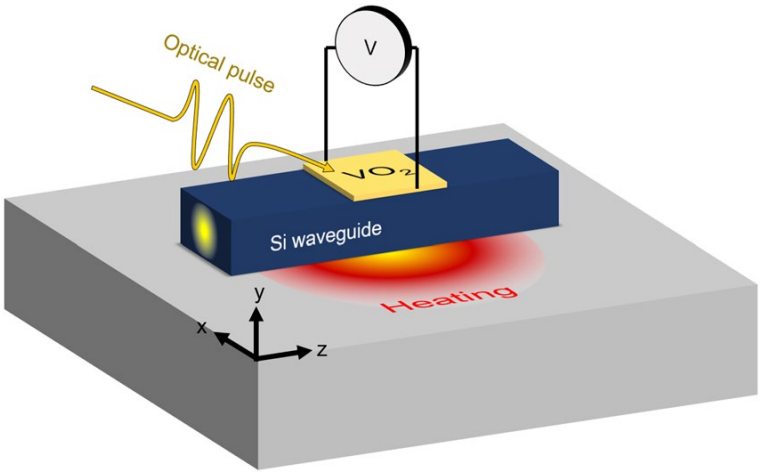

Fig. 1.14. Scheme of a hybrid VO_2/Si waveguide and different external excitations to control its properties.

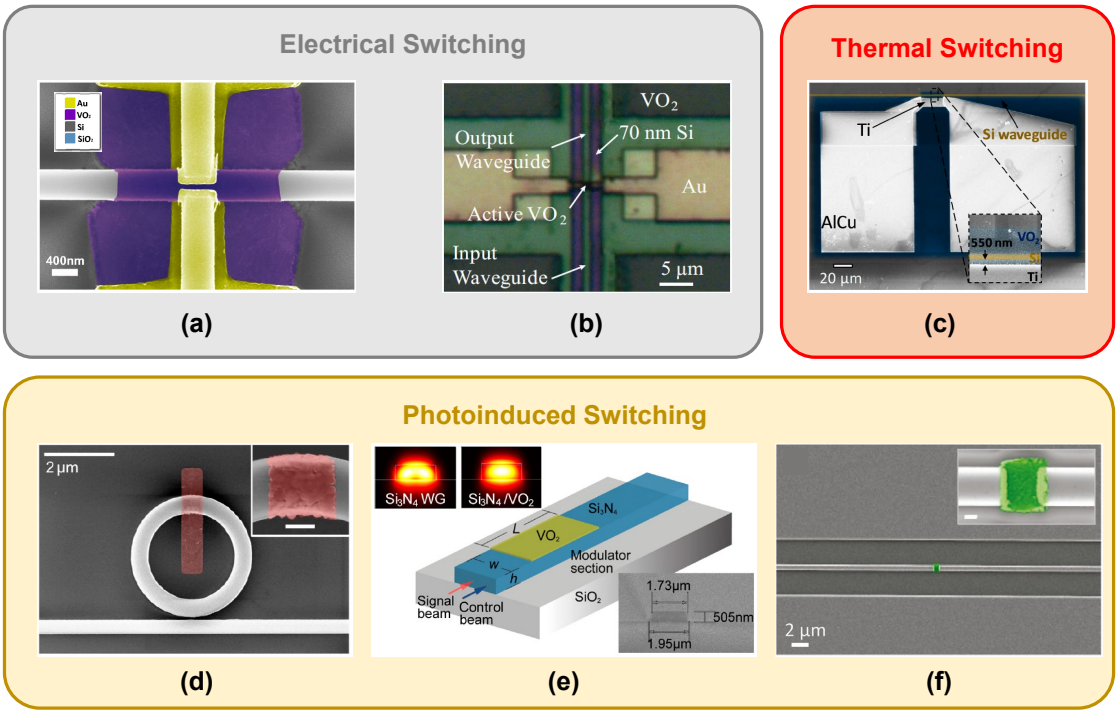

Fig. 1.15. **(a)** False-color SEM image of a VO2/Si electro-absorption switch [92]. Optical microscope image of a 500-nm-long VO_2/Si device that acts as an electro-optic switch and photodetector [93]. **(c)** SEM image of a thermal-driven VO_2/Si waveguide using a lateral microheater with the double Ti-AlCu metallization. The inset shows a zoom over the hybrid VO_2/Si area [95]. **(d)** SEM image of a Si microring resonator with a 560-nm-long VO_2 path on top photothermal modulated [90]. **(e)** Schematic of a VO_2/SiN modulator driven by evanescent coupling. Insets show the calculated E-field (top left), and SEM image of the fabricated SiN waveguide cross-section [99]. **(f)** False-color SEM image of a Si waveguide with a 700-nm-long VO_2 path embedded optically modulated at subpicosecond speeds [100].

1.3 Objectives, methodology, and outline of the thesis

The research presented hereinafter has been carried out within the Photonic Integrated Devices group led by Prof. Pablo Sanchis Kilders in the Nanophotonics Technology Center (NTC) of the UPV. A three-month research stay was done at the *Pernice's Lab* in the Center for Nanotechnology (CeNTech) under the supervision of Prof. Wolfram Pernice. This short stay aimed to investigate the utilization of ITO as a low-loss microheater for electro-thermal switching of GeTe –a phase-change material– on silicon nitride waveguides. On the other hand, we have worked closely with the Functional Nanosystems (FuN) group at the Katholieke Universiteit Leuven (KU Leuven), led by Prof. Jean-Pierre Locquet.

This thesis is mainly framed in two Spanish government-funded research projects: METALONIC TEC2016-76849-C2-2-R (*Development of transition metal oxides with silicon technology for green and efficient photovoltaic and (opto) electronic applications*) and NOVOPIC PID2019-111460GB-I00 (*Towards non-volatile photonic devices*).

Objectives

The main goal of our research is to bring new –and enhance current– functionalities to the silicon photonics platform to meet the requirements of current and emerging applications in integrated photonics. To achieve this objective, we aim to propose, design, and experimentally demonstrate new disruptive silicon photonic devices working at telecom wavelengths based on the CMOS-compatible metal oxides TCOs and VO_2. In particular, such materials' electrical and optical properties will be leveraged to build electro-optic/all-optical ultra-compact devices with particular emphasis on achieving broad spectral operation alongside low energy consumption. The specific objectives of this thesis are:

- To determine the optimal optoelectronic properties of the metal oxides for the target application.
- To propose and design new disruptive silicon photonic devices using the optimal metal oxides with application in mainstream and emerging applications.

- To study and define the fabrication steps for the designed hybrid devices.
- To characterize the fabricated devices and analyze their performance.

Methodology

To fulfill such goals, the methodology of this work covers mainly three stages: design and simulation, thin-film and device fabrication, and characterization. The relationship between the different phases and our contribution to each is described in Fig. 1.16.

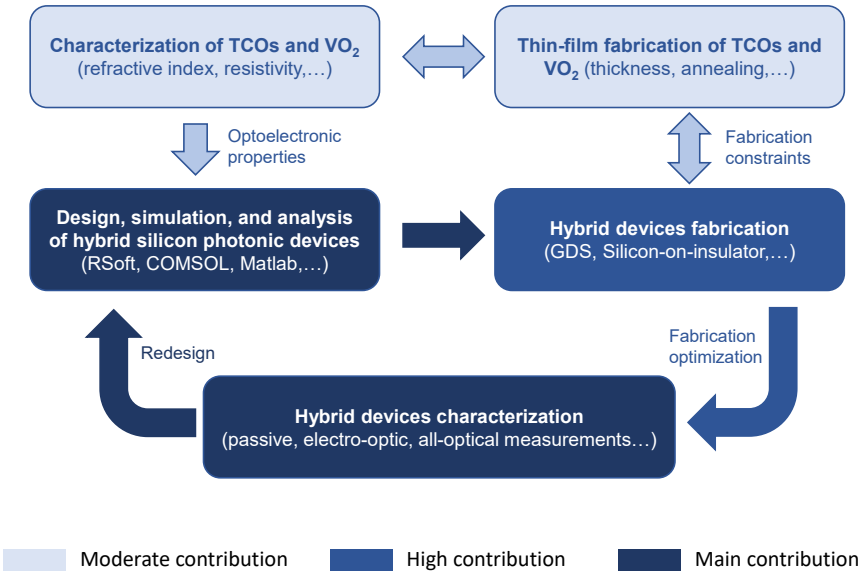

Fig. 1.16. Relationship between the stages carried out in this thesis and the author contribution.

To determine the optimal optoelectronic properties of the metal oxides, we will characterize and analyze the main electrical and optical properties, such as resistivity and refractive index, and investigate the influence of the fabrication parameters. To this end, the metal oxides will be fabricated in a thin film, and different deposition parameters, such as thickness and annealing, will be varied. The characterization measurements and thin-film deposition of the metal oxides will be done by technical staff in our research center[2] and collaborators. ITO will

[2]The NTC offers a rapid prototyping platform and is part of the *Red de Salas Blancas de Mi-*

be deposited at the NTC-UPV, whereas VO_2 will be synthesized by the group of Prof. Jean-Pierre Locquet (FuN-KUL). Our contribution to these two phases is moderate since our task will be restricted to assessing and analyzing the results derived from the characterization and providing feedback and guidelines to obtain the optimal performance for such materials.

Based on the metal oxides' optimal electrical and optical properties, we will design and analyze our hybrid silicon devices using numerical simulation using commercial tools such as RSoft, COMSOL, or Matlab. The design procedure will focus on specific metrics such as footprint, power consumption, speed, and bandwidth. This phase is one of our main contributions to this work. The designed hybrid devices will be fabricated on standard 220-nm-thick silicon-on-insulator chips. This task will be carried out by technical staff and at the NTC-UPV for ITO/Si devices and in joint collaboration with our collaborators for VO_2/Si devices. The utilization of metal oxides would impose some fabrication constraints but remain in the realm of CMOS compatibility. Moreover, we will need to bear in mind the available fabrication resources of our research center and collaborators to define the fabrication steps to ensure success. Hence, continuous feedback from the fabrication people will be needed. We consider that our contribution to the fabrication of the hybrid devices is high since we will create the maks layout (GDS file) of the samples and define the fabrication steps.

The fabricated devices will be characterized in our laboratories at the NTC-UPV. We will employ familiar characterization passive and active (electro-optic/all-optical) procedures and equipment such as optical sources, high-speed detectors, oscilloscopes, arbitrary waveform generators, and many others. We will compare the experimental performance of our devices with simulation results to redesign, if necessary, the device and optimize the fabrication process. This phase is another of our main contributions to this work.

The fabrication side can be considered the most critical stage because of the necessity of cutting-edge fabrication equipment and the dependence of metal oxides considered in this work (TCOs and VO_2) on the fabrication conditions. Therefore, several iterations are expected to be performed to demonstrate our devices' performance experimentally. On the other hand, it should be highlighted

cro y Nanofabricación together with the CNM (*Centro Nacional de Microelectrónica*) and the CT-ISOM (*Central de Tecnología del Instituto de Sistemas Opto-Electrónicos*) in the framework of the *Infraestructuras Científicas y Tecnológicas Singulares* (ICTS) supported by the Spanish Government.

that the methods employed here aim to reach a broad audience familiar with silicon photonics and microelectronic fabrication processes. To this end, we rely on well-known numerical simulation methods such as the finite-element method (FEM) or finite-difference time-domain (FDTD), CMOS-compatible fabrication processes, and typical testing techniques and equipment.

Outline of this work

Briefly, the thesis starts in Chapter 1 introducing the field of silicon photonics, the metal oxides used in this work (TCOs and VO_2), and the objectives and organization of the thesis. The main content is provided in Chapter 2, Chapter 3, and Chapter 4. Each chapter deals with a specific topic (non-volatility, thermo-optic phase shifting, and nonlinearities). The chapter starts with a review of the topic. Then, our contribution to the topic and results are presented, and the chapter closes by comparing our results with the literature. The main content of these chapters is conceived as a compilation of our results published in peer-reviewed journals [Paper A] - [Paper H]. We present our main conclusions in Chapter 5 and outline future hybrid silicon photonic devices. After the conclusions, a list of the journal papers and conferences given derived –directly and additionally– from this thesis is given in Authors' Merits. The description of the methods employed to carry out and reproduce our research is attached as Appendices.

A more detailed description of the main chapters is given as follows:

- Chapter 1 aims to provide a brief review of the benefits of the silicon technology for developing PICs, the current and emerging applications, and the increasing trend of integrating unique optoelectronic materials, which inspired the work developed in this thesis. Then, we overview the metal oxides employed in this thesis (TCOs and VO_2). In particular, we focus on the optoelectronic properties, the fabrication side, and their main application for building hybrid silicon photonic devices. Finally, the objectives and outline of the thesis are given.

- Chapter 2 deals with the topic of non-volatile switching in silicon photonics. We review the main current approaches to provide non-volatility to silicon waveguides [Paper A]. We report our contribution to non-volatile switching by proposing intensity [Paper B] and phase [Paper C] non-volatile devices using TCOs as the materials for the floating gate in a flash-like

structure, mimicking electronic memories. We end the chapter by discussing the performance of our devices in comparison with similar flash-like devices in the literature.

- Chapter 3 is devoted to the long-standing topic of thermo-optic phase shifters. We introduce the topic of phase shifters by briefly reviewing the mainstream and emerging approaches. This overview allows us to discuss why thermal-based phase shifters are preferred over other types. Afterward, we focus on the design strategies and configurations that have been reported to build thermo-optic phase shifters accessed by electrical and optical signals. We report our contribution to this topic by employing TCOs as transparent heaters, thereby achieving low power consumption. To this end, we tailor the optical properties of such heaters near or far the epsilon-zero condition. Specifically, we experimentally demonstrate epsilon-far-zero ITO-based electrical microheaters [Paper D], and propose epsilon-near-zero TCO-based optical heaters [Paper E]. Then, we compare the performance of our devices with the literature and discuss further optimization routes relying on previously reviewed strategies and configurations.

- Chapter 4 deals with nonlinear optical devices. The chapter starts by justifying the need for other materials with better nonlinear properties than silicon. Then, we overview the available functional materials, such as VO_2, that have been employed for developing nonlinear silicon devices to focus next on the state-of-the-art of all-optical VO_2/Si devices [Paper F]. We report our contribution to this topic by experimentally demonstrating an all-optical absorption switch [Paper G] and a low-threshold and tunable power limiter [Paper H] based on ultra-compact VO_2/Si waveguides. Finally, we discuss the performance of our devices by comparing their characteristics with previous work.

- Finally, in Chapter 5, we present the main conclusion and the potential utilization of our devices in PIC applications, and we end by outlining the guidelines to develop future hybrid silicon photonic devices based on TCOs and VO_2.

2 Toward non-volatile switching in silicon photonic devices

2.1 Review of non-volatile technologies for silicon photonics

In this section, we analyze and compare the existing emerging technologies for non-volatile switching that might be integrated into the silicon photonics platform. Although our results are focused on a specific technology in the following sections, given that non-volatile silicon photonic devices are in an infant stage of development, we consider that a thoughtful review of the available technologies would be valuable for the reader. The main results of this section correspond to the review made in [Paper A].

2.1.1 Introduction

Driven by the growing market demand, silicon PICs have reached unprecedented maturity [101]. Over the last decade, many photonic innovation ecosystems have emerged, mainly in the US, Europe, and Asia, making cutting-edge photonics technologies within reach of tech companies. Their emergence, sustainability, and growth largely rely on the fabless/foundry model that has already proved successful for electronics [102]. As a result, PICs with ever-increasing complexity can now be fabricated in well-established low-to-high-volume silicon microelectronics foundries using mature CMOS-compatible processes [3]. Each foundry holds a unique process design kit (PDK) encompassing standard and more advanced photonic building blocks. Despite a focused twenty-year-long research and development effort, which has allowed high-performance silicon photonic building blocks to become fully mature and commercially available, non-volatile functionalities are still missing from standard libraries [103].

An ideal PIC augmented with non-volatile capabilities would encompass an interconnected mesh of reconfigurable elements, where switching between stable and reversible photonic states is dynamically achieved by employing a certain kind of mechanism consuming an ultra-small amount of energy. Non-volatility implies that no static energy or holding power is required to retain any of the states once it is set. This ultra-low energy consumption coupled with an optimal switching performance opens up a wealth of possibilities wherever highly scalable non-volatile switching solutions would suppose a significant added value. In fact, due to the fast spread of photonics in many fields, access to non-

volatile functions is expected to become of high importance in countless current and emerging applications requiring energy efficiency and full-reconfigurability, namely, programmable integrated photonic [24], power-efficient switching in data centers [104, 4], photonic memories [105, 106], neural networks [107] or large-scale photonic phased arrays for LiDAR systems [16, 13, 108], to name a few.

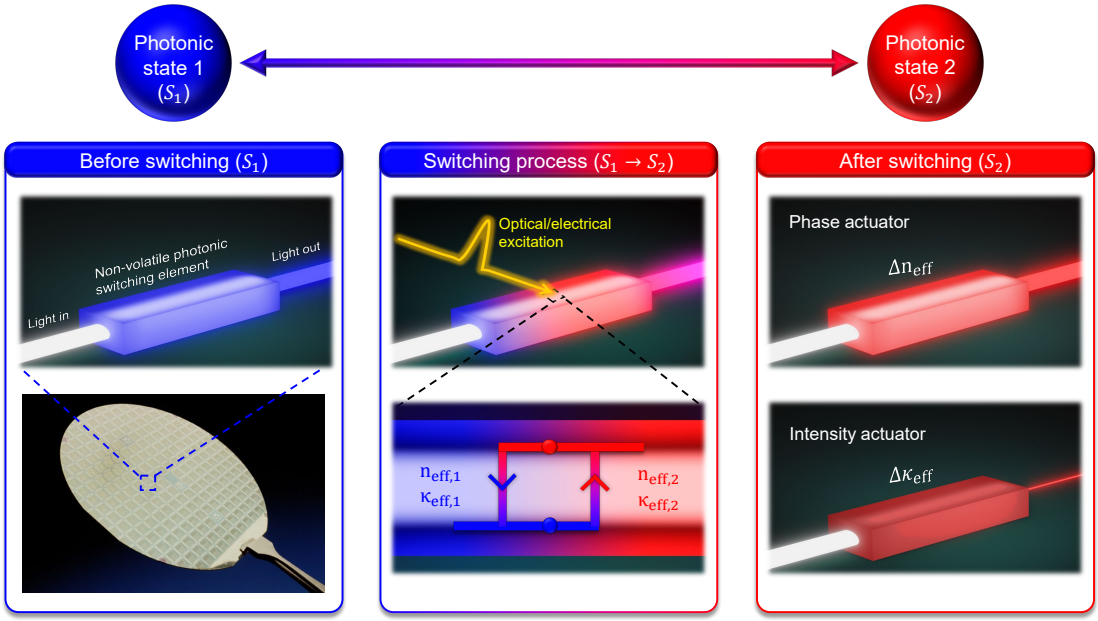

Fig. 2.1. Description of the fundamental performance of a generic non-volatile photonic switching element. Optical bistable performance is achieved by means of a looped hysteretic response that acts on the effective index of a silicon-based waveguide structure under optical or electrical excitation. The variation of the effective index, which can have a complex nature ($n_{\text{eff}} + j\kappa_{\text{eff}}$), yields control of the optical phase and absorption in a separate or coupled scheme depending on the underlying mechanism. Thereby, non-volatile switching between two (S_1 or S_2) or more photonic states is enabled.

Optical bistable performance is a necessary condition for building non-volatile photonic devices. Here, we focus on bistability based on a looped hysteretic response or latching operation that acts on the effective index of a photonic waveguide structure and allows to retain of two (bistable) or more (multi-level) states in a non-volatile way. Figure 2.1 describes the fundamental performance of a generic non-volatile photonic switching element. The variation of the effective

index, which can have a complex nature ($n_{\text{eff}} + j\kappa_{\text{eff}}$), yields control of the optical phase and absorption in a separate or coupled scheme depending on the underlying mechanism. An electrical or optical excitation can drive such control to enable non-volatile phase or intensity actuators. Different metrics can assess the optical switching performance. On one hand, for phase actuators, a large variation in the real part of the effective refractive index (Δn_{eff}) is desired together with low losses and the smallest variation of the imaginary part between photonic states ($\Delta\kappa_{\text{eff}} \approx 0$). On the other hand, large variations of the imaginary part ($\Delta\kappa_{\text{eff}}$) with minimum losses (minimum κ_{eff} for S_1 or S_2 in Fig. 2.1) are desired for intensity actuators. Such metrics will determine the insertion loss and extinction ratio of the non-volatile device. However, other metrics such as energy consumption, switching speed, retention time, footprint, or integration issues should not be forgotten. Ideally, the perfect non-volatile device would maximize all the metrics. In practice, trade-offs exist among them, and the most suitable non-volatile approach will be chosen by weighting such metrics. Thereby, a photonic device with access to non-volatile switching functions should be engineered to fulfill the requirements of a specific application.

The simplest way to achieve optical bistability on silicon is by exploiting its refractive index variation under a high optical power excitation combined with a photonic structure that provides optical feedback. However, the bistable response is volatile, although the holding power may be strongly reduced. Therefore, two main strategies are currently followed for providing non-volatility in silicon photonics devices. On one hand, non-volatile switching can be enabled by device engineering. The natural approach is staying within the realm of electronic memory-like device engineering in which non-volatile switching appears as a result of controlled dynamics of charge carriers or taking profit from the resistive switching effect. However, micro-mechanical systems (MEMS), which take advantage of the electrostatic and mechanical forces at the nanoscale to move and displace photonic waveguide structures, have become a promising alternative with quick progress in the last few years. The second main strategy for non-volatile switching is the hybrid integration of materials with unique optical properties on silicon waveguide structures. In particular, desirable materials are those in which the refractive index can change between two or more stable values. Chalcogenides, mainly germanium-antimony-tellurides, are the most mature candidates due to their intrinsically non-volatile response at room tem-

perature. However, VO_2 also deserves consideration because, despite its bistable response being shifted from room temperature at normal conditions, the possibility of a non-volatile switching performance is still in the spotlight. On the other hand, ferroelectric materials are emerging due to their unique ultra-fast and ultra-low energy electro-optical response. Finally, the use of liquids with different refractive index changes has also been proposed and demonstrated.

2.1.2 Optical bistability on silicon

Optical bistability can be achieved by combining an intensity-dependent refractive index change with a photonic structure, such as a ring resonator, providing optical feedback. The mechanisms for changing the refractive index have been based on the thermo-optic and plasma dispersion effects induced by optical absorption. Non-volatility cannot be achieved using those approaches. However, very low holding powers have been demonstrated by taking profit from the large refractive index of silicon and engineering photonic waveguide structures with high optical field confinement.

Thermo-optic effect

Optical bistability was first proven in silicon devices by using a microring resonator [109]. The microring resonator is shown in Fig. 2.2a. The bistable performance arises from the combined effect of the resonance wavelength shift when the input optical power increases and the dependence of the output power on the signal wavelength with respect to the resonance. Figure 2.2b shows the resulting hysteresis in the output versus input optical power response. Non-volatility is not achieved, so holding power is always required for exploiting the bistability. Furthermore, the hysteresis curve is highly dependent on the input wavelength, which could be an issue for implementing practical devices. On the other hand, the bistable performance may also be observed in the asymmetry and abrupt change in one of the edges of the ring resonance when the input signal is wavelength scanned, as it is shown in Fig. 2.2c. Such effects are accentuated when the input optical power increases.

The resonance wavelength shift is driven by thermal effects induced by optical absorption. The absorbed light is transformed into thermal energy that changes the refractive index of the silicon via its thermo-optic coefficient. Optical ab-

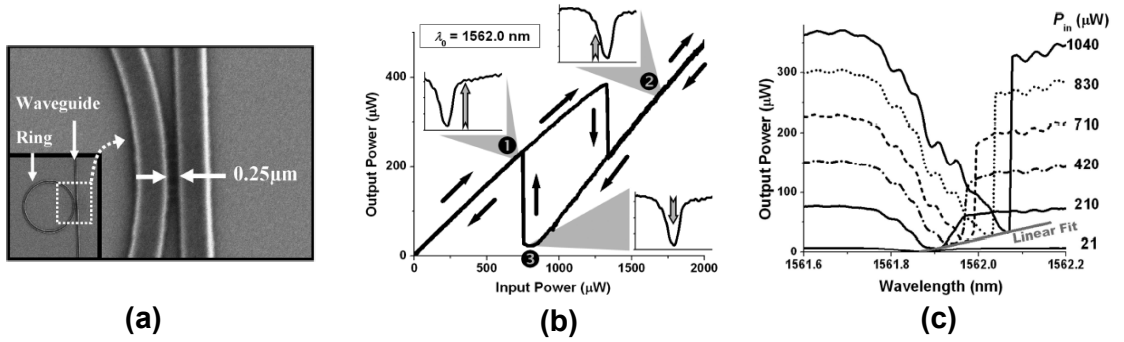

Fig. 2.2. **(a)** Silicon microring resonator employed for demonstrating optical bistability. **(b)** Hysteresis curve of output optical power as a function of the input optical power injected into the microring resonator. **(c)** Influence of the optical bistability on the transmission spectrum of the ring resonance when the input power is increased (wavelength is shifted from low to high) [109].

sorption may be originated from linear and non-linear contributions. The role of the different contributions will depend on the photonic structure, waveguide geometry, and fabrication process [110–112]. Linear optical losses are attributed to surface state absorption, which gets stronger in unpassivated waveguides. Optical bistability driven by predominantly linear losses was demonstrated with a holding power of 800 μW, switching energies above 400 pJ, and switching times in the microsecond range [109]. On the other hand, the non-linear absorption contributions arise from two-photon absorption (TPA) and the associated free-carrier absorption (FCA). Optical bistability driven by non-linear optical losses was achieved in an ultra-compact photonic crystal featuring holding powers as low as 40 μW, switching energies in the order of picojoules, and switching times of hundreds of nanoseconds [113]. The energy consumption is significantly reduced due to the high-quality factor and small cavity mode volume. The small size of the cavity also minimizes the switching time. However, the speed is ultimately limited by the slow response associated with thermal effects.

Plasma dispersion effect

Optical bistability based on carrier effects induced by TPA has been proposed to reduce the switching time in comparison with thermal-based approaches. In this case, the refractive index of silicon decreases as the input power is increased

due to the plasma dispersion effect. Switching times in the nanosecond range have been demonstrated by using a microring resonator but at the expense of high holding power of around 5.5 mW and high insertion losses of up to 12 dB [114]. On the other hand, thermal effects induced by optical absorption cannot be generally neglected. Therefore, the variation of the silicon refractive index is influenced by two opposite effects that degrade the bistable performance and, in particular, the stability of the high-power state. The influence of thermal effects has been minimized by modifying the fabrication process for achieving ultra-smooth Si/SiO_2 interfaces [115]. However, the carrier lifetime is also increased, leading to longer switching times. Ultra-high-quality nanocavities based on a photonic crystal structure have also been employed for reducing the switching energy [116]. Despite a more critical narrowband operation, the high optical confinement drastically reduced the switching energy to 100-200 fJ and the holding power to values between 1.6 and 7.9 μW [117]. On the other hand, the plasma dispersion effect can also be exploited by using more efficient p-i-n junctions integrated into the silicon waveguide. In this case, even lower switching energies down to a few femtoseconds and speeds up to 20 GHz have been predicted [118]. Nevertheless, it should be noted that, in all cases, the optical switching performance is volatile and highly wavelength-dependent because photonic cavities are required to provide optical feedback.

2.1.3 Non-volatile switching enabled by device engineering

Optical switching with a non-volatile response can stem from device engineering without the need for optical feedback. The main approaches rely on the adoption of non-volatile electronic configurations, such as flash memories or resistive switching devices or novel switching devices driven by micro-mechanical systems (MEMS) actuators.

Mimicking electronic memories

Microelectronics provides tools for fabricating PICs and knowledge regarding non-volatile devices. One of the most natural approaches to providing non-volatility to integrated photonic waveguides is the adaptation of the well-known and proven flash memory cell. In this case, the waveguide is combined with different CMOS-compatible materials such as oxides, doped semiconductors, and

metals. Therefore, such devices would come with the main advantage of maximum CMOS compatibility together with a non-volatile behavior. A bistable response at room temperature arises by utilizing a metal-oxide-silicon (MOS) structure in which a three-layer stack replaces the gate oxide. The stack comprises a charge storage layer sandwiched between tunneling and blocking oxide. The concept is schematically illustrated in Fig. 2.3a. Depending on the nature of the middle layer, the structure may be classified into two groups: floating gate and charge-trapping devices. Both approaches rely on the injection of carriers via the tunneling effect from the silicon substrate. The charge is stored in a conductor or a heavily doped semiconductor in a floating gate scheme. Charge trapping devices use a dielectric layer, such as silicon nitride, to retain the injected carriers, as shown in Fig. 2.3b.

The increase in the flatband voltage due to the trapped charges is taken advantage of to obtain non-volatility. A counter-clockwise hysteresis is obtained when performing capacitance-voltage measurements, as depicted in Fig. 2.3c. Charges are injected from silicon to the storage layer, whereas, for negative voltage, carriers are tunneled back to the substrate for negative voltages. There are three main physical effects used to inject carriers through the tunneling oxide: (i) direct and (ii) Fowler-Nordheim tunneling, and (iii) hot carrier injection. While the first two do not require the source and drain electrode to inject carriers, an applied voltage is needed for hot carrier injection to make the electrons gain kinetic energy through the channel. When they have enough energy to jump the oxide barrier, they are injected into the charge storage layer thanks to the vertical field created by the gate voltage. Finally, for charge-trapping devices, the Poole-Frenkel effect trap-assisted tunneling should be considered when modeling the current and carrier distribution across the trapping layer.

One of the main differences between floating gate and charge trapping schemes is found in their reliability. Due to the conducting nature of the floating gate, a single defect in the thin tunnel oxide causes the complete discharge of the device. This issue is avoided in charge-trapping devices, thus allowing for thinner tunneling oxides, lower programming, and erasing voltages. On the other hand, longer retention periods are more accessible to achieve in floating gate structures due to their larger detrapping barrier height. A balance must be generally established among speed, oxide thickness, and charge retention.

The integration of the flash memory with silicon photonics has been mainly

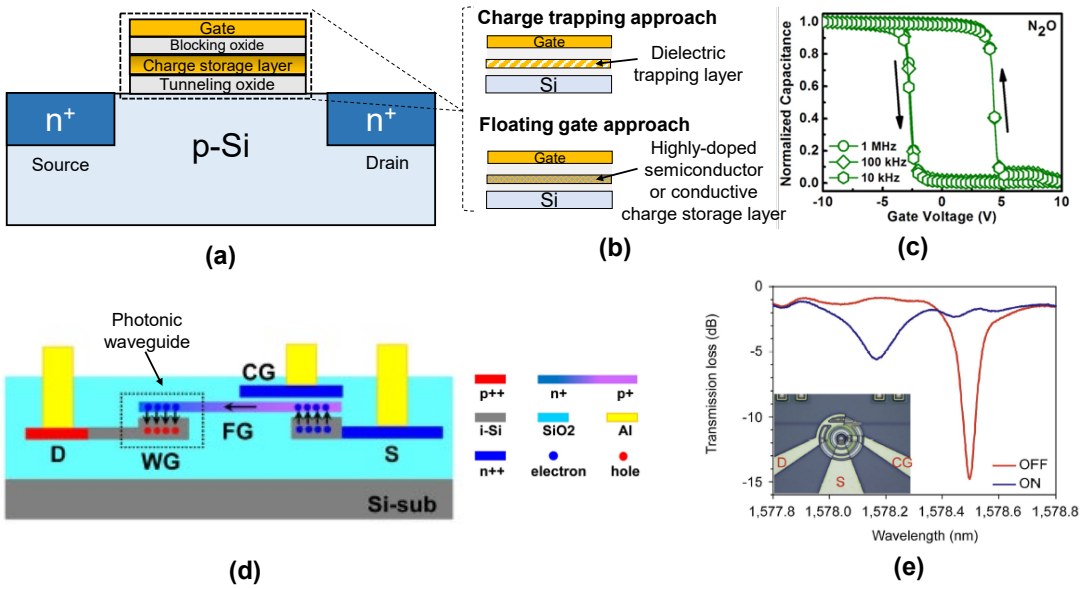

Fig. 2.3. **(a)** General scheme of an electronic non-volatile flash memory. **(b)** Detailed view of charge trapping (top) and floating gate (bottom) approaches. **(c)** Capacitance-voltage curves of a flash memory device in the frequency range of 10 kHz to 1 MHz. The hysteresis is due to the trapped charges in the stored layer [7]. **(d)** Photonic waveguide structure based on a floating gate approach and **(e)** experimental non-volatile change of the optical response in a microring resonator [119].

done by placing the charge store layer as near as possible to the waveguide structure [119–122]. The optical phase is then changed by means of the plasma dispersion effect due to the overlap of the guided mode either with the trapped carriers or with the screened charge inside the silicon waveguide. An additional interferometric or resonant photonic structure is required to transform the optical phase change into an optical intensity variation. The first photonic device following the flash memory approach was proposed in 2006 by integrating a charge-trapping structure based on silicon nitride into a silicon microring [120]. However, only simulations were provided. The carrier injection process was carried out with voltages below 10 V. One of the constraints of this configuration is the proximity of the metal control gate to the guiding structure. A thick blocking oxide is needed to avoid excessive optical losses; consequently, around 100 V is needed to discharge the device. A similar approach has been experimentally demonstrated

for trimming purposes [121]. In this case, the carrier injection from the silicon substrate was aided by exposing the device to ultraviolet light. More recently, a new configuration based on using hafnium oxide as a trapping layer has also been proposed by means of simulations to reduce the switching time to around 100 μs with gate voltages between 20-30 V [123].

A non-volatile performance has also been demonstrated by using the floating gate approach [119, 122]. The cross-section of the proposed waveguide structure is depicted in Fig. 2.3d. The carriers are injected into the floating gate using a typical floating gate memory structure during the charging process. Once injected, those carriers redistribute inside the charge storage layer and change the effective refractive index of the guided mode via the plasma dispersion effect. A microring structure was also employed to transform the optical phase change into an optical intensity variation. Figure 2.3e shows the experimental non-volatile change of the microring optical response. The transition between the uncharged to charged state is achieved in the millisecond range with a gate voltage of 20 V, demonstrating, in addition, a multi-level operation for intermediate injection times.

Graphene has been proposed through numerical simulation to be employed as a floating gate for such flash memory structures. However, although graphene exhibits stronger free-carrier dispersion than silicon, the weak interaction of the optical mode with the atomically thin material results in large footprint devices. Phase actuators with a length of around 650 μm for a π phase shift together with ∼3 dB of loss, and intensity actuators with around 330 μm of length to attenuate 20 dB, have been reported [124]. Such long lengths have been reduced down to ∼ 30 μm in recent designs [125, 126]. However, the switching energy is significantly increased from the few picojoules up to ∼ 10 μJ. On the other hand, the main pending challenge of all these proposed devices using advanced materials is their experimental demonstration.

Resistive switching devices

Resistive switching has been largely investigated for enabling resistive random access memories (RRAMs) based on the bistable behavior present in the electric response [127]. Basically, the electrical resistance is changed between a low and high resistive state following a pinched current-voltage hysteresis loop. Here, we focus on resistive switching based on the formation and destruction of conductive nanofilaments across an active material sandwiched between two electrodes [128,

129]. For photonic applications, the resistance change may give rise to a variation of the optical losses with also a hysteretic response [130]. However, the optical switching performance will depend on the active material and the surrounding materials and device structure.

The resistive switching effect was first demonstrated in hybrid plasmonic waveguides by using amorphous silicon as active material [131]. Figure 2.4a shows the hybrid plasmonic waveguide. Plasmonic waveguides allow high optical mode confinement on the ultra-thin active layer, as is depicted in Fig. 2.4b. When a positive voltage is applied, metal filaments are formed in the amorphous silicon layer by silver ions injected from the top silver electrode. The formation of metal filaments increases optical losses. The associated optical transmission variation is depicted in Fig. 2.4c. The maximum extinction ratio is not achieved at 0 V, which penalizes the non-volatile performance. Such behavior is because the bistability of the electrical switching is usually shifted at positive voltages, as can also be seen in Fig. 2.4c. Nevertheless, a switching power as low as 0.15 μW is achieved. On the other hand, the insertion loss is around 4.2 dB. The propagation losses of the plasmonic waveguide and the coupling losses to the connecting silicon waveguides must be considered to minimize the insertion loss.

Resistive switching in amorphous silicon has also been exploited for optical bistable switching at an atomic scale [132]. The device is shown in Fig. 2.4d-2.4e. The active region is driven as a plasmonic nanocavity in which a single nanofilament is created or erased. The resulting optical bistable response is shown in Fig. 2.4f. Non-volatility switching is not achieved, but the ultra-small scale of the active region allows for reducing the holding power to a few nanowatts and achieving switching energies as low as 12.5 fJ. However, the switching bandwidth is limited to 1 MHz. Further work is also required to investigate the influence of quantum effects on the optical switching mechanism.

Resistive switching has also been demonstrated in hybrid plasmonic waveguides with silicon dioxide as active material [133]. Figure 2.4g shows the waveguide cross-section based on a layer stack made of gold, silicon dioxide, and ITO on top of the silicon waveguide. The optical mode is depicted in Fig. 2.4h. The photonic structure was initially intended for carrier modulating in the ITO layer. Instead, a non-volatile optical switching performance was achieved due to a resistive switching effect in the silica layer. The silica layer was deposited by RF sputtering, which is expected to originate many defects. Metal filaments are formed

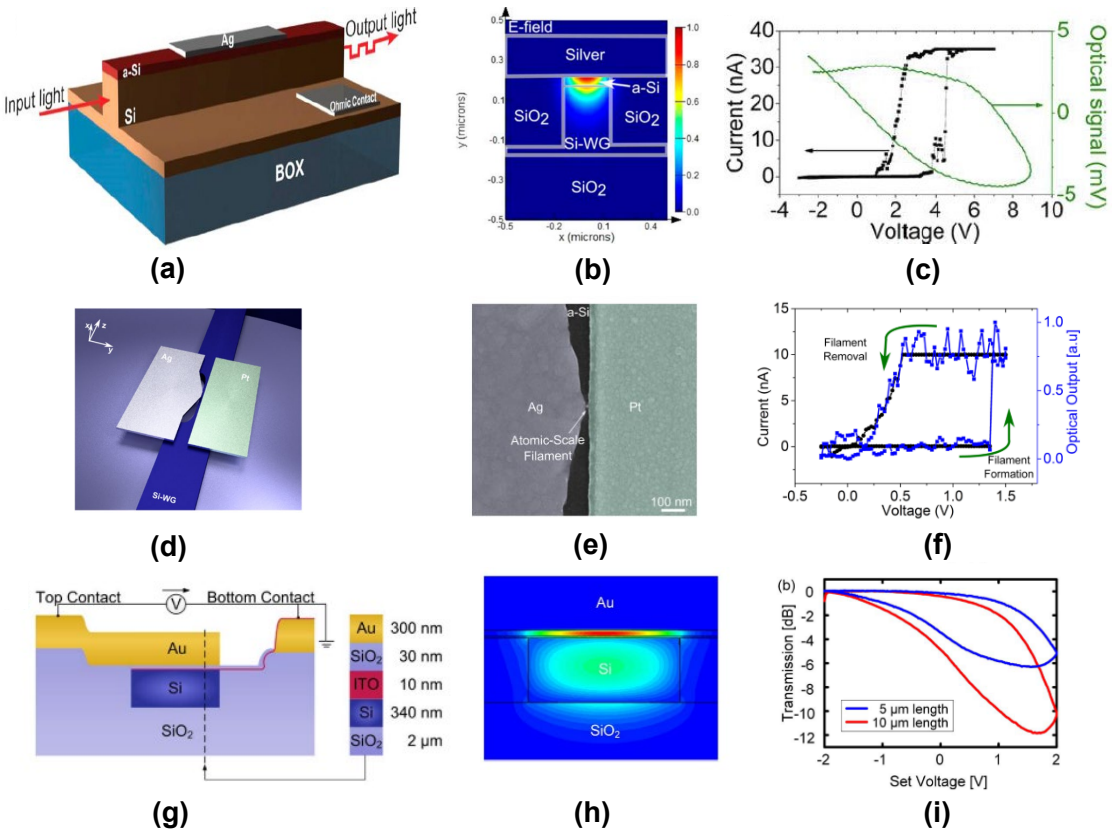

Fig. 2.4. **(a)** Non-volatile optical switching based on resistive switching in amorphous silicon: hybrid plasmonic waveguide device, **(b)** optical mode showing the light confinement at the amorphous silicon layer, and **(c)** measured electrical and optical switching performance [131]. **(d)** Plasmonic device based on resistive switching on amorphous silicon at an atomic scale, **(e)** SEM image of the fabricated device and **(f)** measured optical switching response [132]. **(g)** Hybrid plasmonic waveguide for non-volatile optical switching based on resistive switching in silica, **(h)** simulated optical mode, and **(i)** measured optical switching response for two different waveguide lengths [133].

in the silica by ions injected from the top gold electrode. The formation of filaments is expected to be facilitated by a large number of defects in the silica. Figure 2.4i depicts the optical transmission as a function of the applied electrical voltage for different lengths of the plasmonic waveguide. Non-volatile switching with an extinction ratio of around 5 dB and a switching power of 200 nW was achieved. However, a dependency of the extinction ratio with the duration

of the applied electrical pulses was found when studying the dynamic performance. Hence, the switching energy was between 60 μJ and 1 nJ, depending on the switching duration. Furthermore, a frequency response of 30 MHz and high insertion losses above 10 dB were reported.

The resistive switching effect has also been proved in many materials and layer stacks that could give rise to new approaches for non-volatile optical switching. However, there is not yet a clear material candidate, and there are still challenges to developing reliable devices [129]. For photonics, oxides compounds such as HfO_2 [134], TiO_2 [135], ZnO [136], or silicon rich-oxides [137, 138] could be good alternatives due to their low optical losses at telecom wavelength and CMOS compatibility. Electrical memory devices may be built relatively easily, relying on a simple layer stack. However, the integration in silicon photonic waveguide devices remains an open challenge. On the other hand, a good understanding and control of the underlying physics are also of paramount importance. The formation and destruction of the conductive nanofilaments have been mainly attributed to electrochemical metallization, valence change, and thermochemical mechanisms. However, the most suitable mechanism or combination of mechanisms for optical switching and their influence on the device performance is still unclear [139]. Electrochemical metallization is based on the diffusion from ions of a metal electrode, and it has been the mechanism used in photonic waveguide devices featuring resistive switching. The valence change mechanism usually dominates on materials with oxygen-related defects. Conductive filaments are formed by oxygen vacancies induced by ion migration. Electro-optical switching has been demonstrated with ZnO in the mid and large infrared (from 5-18 μm) but on a simple layer stack device [140]. Concerning the last mechanism, thermochemical reactions and Joule heating dominate the forming and destruction of the filaments. In this case, unipolar switching is more effective, but the influence of the thermal processes on the device speed would need to be carefully analyzed. Furthermore, electro-optical switching has not been demonstrated to the best of our knowledge.

Silicon MEMS devices

The integration of MEMS in photonic devices for enabling novel designs of tunable components has emerged as a very promising field in the last years [141, 142]. Tunability is achieved by a mechanical actuation mechanism that

changes the optical properties of a photonic waveguide or structure. One of the simplest ways to achieve optical switching is by lateral displacement of a movable photonic waveguide between two fixed waveguides, as can be seen in Fig. 2.5a [143]. The movable waveguide is suspended in air and driven by an electrostatic comb actuator, but the optical switching performance is volatile. The waveguide is moved by the electrostatic force induced by the actuation voltage. In contrast, the original position is restored when the voltage is no longer applied due to the resulting spring force originating in the suspended structure. Figure 2.5b shows the measured optical transmittance as a function of the applied voltage and induced lateral displacement. An experimental extinction ratio of 15 dB was achieved for a displacement of 540 nm using 65 V. The measured switching time was around 10 µs. Despite the high actuation voltages required, the switching energy consumption is low due to the capacitive operation of the electrostatic actuator.

Non-volatile optical switching can be achieved by modifying the MEMS actuator to enable a non-volatile bistable movement. This fact has been experimentally demonstrated by using a precompressed microspring structure that can be switched between two stable positions [144]. The switching device is shown in Fig. 2.5c. The precompression is only obtained after fabrication by locking a hook structure located at the center of the device. The non-volatile optical switching performance is obtained by a lateral displacement of the central movable photonic waveguide section by switching between the precompressed states of the microspring structure by means of the electrostatic comb actuators, as depicted in Fig. 2.5d. A switching voltage above 36 V was required, while the measured switching time was around 0.5 ms. On the other hand, insertion losses of 3 dB of the whole assembly, including fiber-to-waveguide coupling losses, were reported.

A similar concept has been proposed for enabling a non-volatile optical switching performance, but on a silicon coupler structure with movable waveguides in the vertical direction [145]. The cross-section of the coupler structure is shown in Fig. 2.6a. The movable waveguide is fabricated in an additional suspended polysilicon layer with residual compressive stress. Thereby, two stable mechanical states can be achieved by taking advantage of such precompressed stress and proper design of the geometry of the suspended structure. The movement is driven by two vertical comb electrostatic actuators, as depicted in Fig. 2.6b, which generate the required electrostatic force to exceed the critical bend-

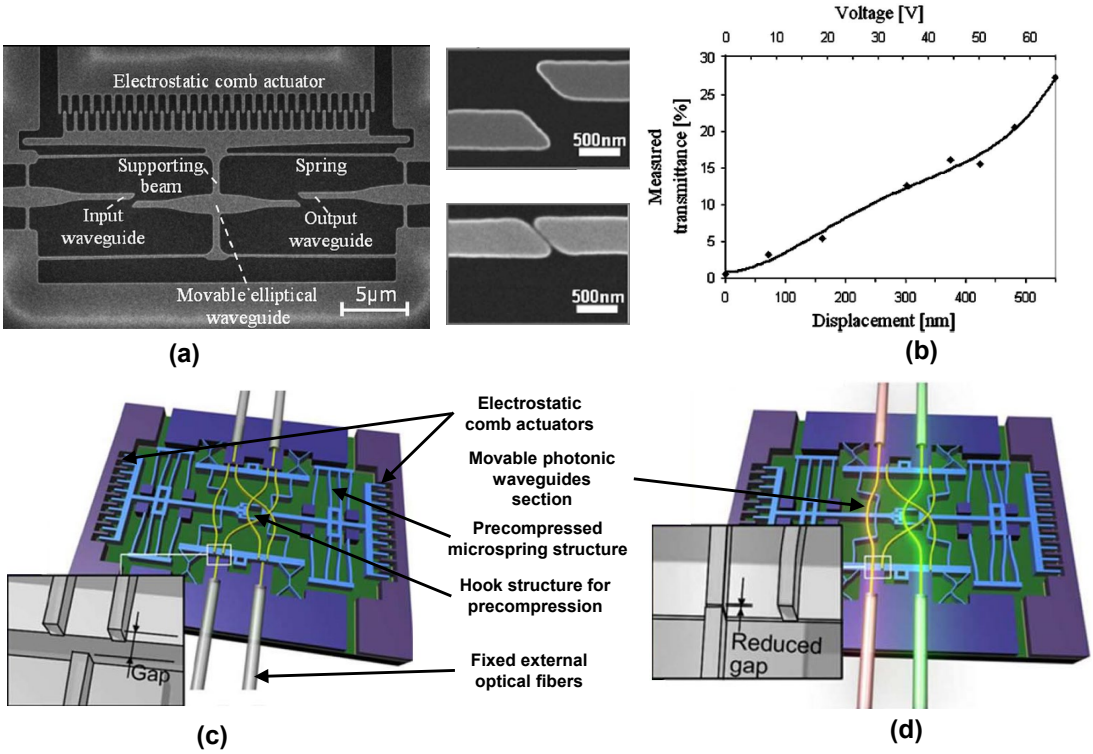

Fig. 2.5. **(a)** SEM image of optical switch driven by an electrostatic comb actuator. Optical switching with volatile performance is based on the displacement of a central movable waveguide with respect to the input/output fixed waveguides, as shown in the two smaller SEM images at the right. **(b)** Measured optical transmittance as a function of the applied voltage and induced displacement [143]. **(c)** Non-volatile optical switch based on a precompressed microspring structure driven by two electrostatic comb actuators. **(d)** The central movable photonic waveguide section is moved to the right position after the precompressed microspring structure is switched. The insets show a gap between the movable and fixed sections during the movement that is minimized when the switching process has finished. Adapted from [144].

ing force of the movable waveguide structure.

A full demonstration of non-volatile optical switching has not yet been reported, and only the mechanical parts have been designed and experimentally characterized. However, the optical switching performance of the vertical coupler structure has been demonstrated in previous devices [146]. The switch device and principle of operation are depicted in Fig. 2.6c. In this case, the elec-

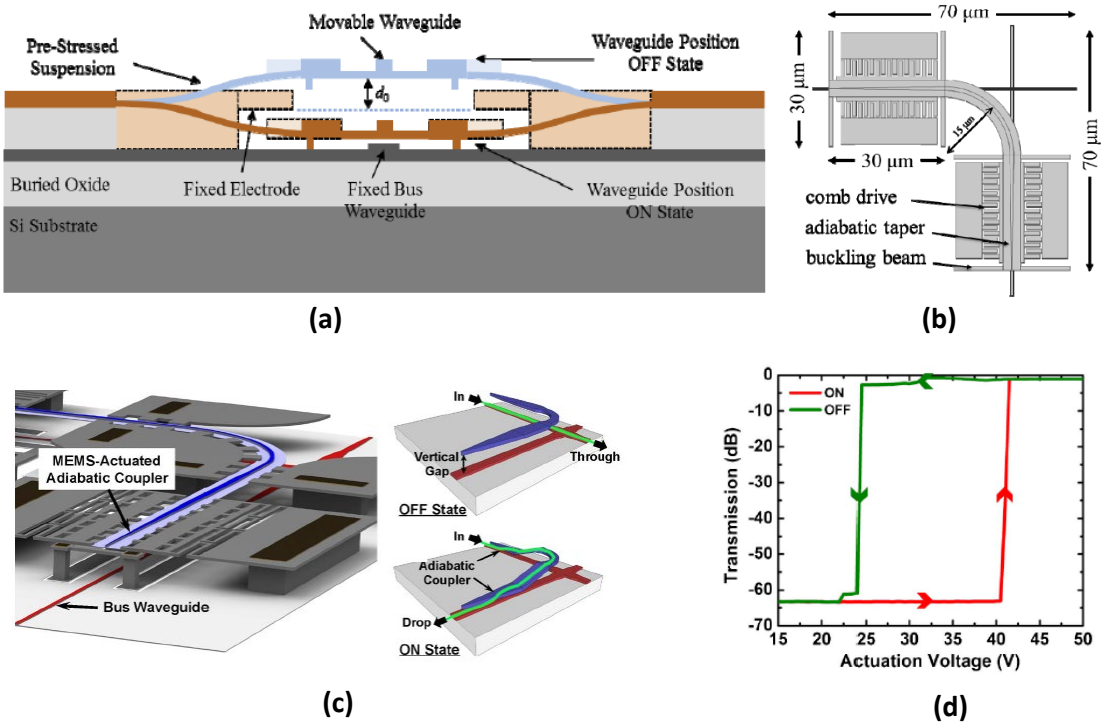

Fig. 2.6. **(a)** Cross-section of coupler structure proposed for non-volatile optical switching performance with movable waveguides in the vertical direction driven by **(b)** two vertical comb electrostatic actuators [145]. **(c)** Silicon switch based on the same coupler structure but driven by a volatile bistable actuator. **(d)** Measured optical transmission response as a function of the actuation voltage [146].

trostatic actuator was based on a parallel-plate arrangement with volatile performance. Hence, the movable waveguide is pulled down to the fixed bus waveguide when the voltage is applied to the actuator. The optical transmission response as a function of the actuation voltage is shown in Fig. 2.6d. It can be seen that the optical switching performance is volatile. However, an optical bistable operation is achieved due to the non-linear behavior of the electrostatic force applied by the actuator. Insertion losses as low as 0.47 dB and ultra-large extinction ratios above 60 dB were demonstrated. Moreover, switching times down to 300 ns and switching operations over 10 billion cycles were also reported. One of the main challenges is that the fabrication requires additional process steps to enable the suspended waveguide structures and MEMS actuators, which require tighter control and increase the complexity of the overall manufacturing. How-

ever, their potential for large-scale integration has been proved with success. Recently, a large switching matrix with 240×240 elements and maximum insertion losses below 10 dB has been demonstrated [147].

2.1.4 Non-volatile switching enabled by materials integration

The integration of materials with a refractive index that can be switched between bistable states upon an external excitation represents another promising strategy for enabling a non-volatile optical switching performance on silicon waveguide devices.

Chalcogenide compounds

Chalcogenide compounds are currently used to develop non-volatile memories for removable optical data storage, such as rewritable DVDs [148]. The main benefits are the possibility of enabling simple memory cells with small energy consumption, long data retention, and multi-level storage capability. However, their use for photonic applications has only been recently addressed [149–151]. Until now, the most promising results have been achieved by using germanium-antimony-tellurides and, in particular, $Ge_2Sb_2Te_5$, usually named GST [152]. The material can be switched between an amorphous and crystalline state in a reversible and non-volatile way. The refractive index drastically changes between the two states with possible intermediate values by partial crystallization. A refractive index of $4.69 + j0.19$ (amorphous) and $8.03 + j1.88$ (crystalline) has been reported at 1.55 μm [153]. Thereby, ultra-compact devices may be accomplished, making GST one of the most attractive candidates for enabling non-volatile silicon photonic devices with a multi-level operation. However, it should be highlighted that, while maintaining the large variation between both states, different refractive index values can be found in the literature [154]. Therefore, the refractive indices should ideally be measured for an optimal device design because they can vary significantly due to fabrication and deposition processes [155].

Hybrid GST/Si waveguides can be simply made by depositing a small and thin layer of GST on top of the silicon waveguide as depicted in Fig. 2.7a. The GST layer must be covered to avoid oxidation from the air since the phase state is triggered by heat. On one hand, the crystalline state is achieved by heating the material above the crystallization temperature (~160 ºC), typically with val-

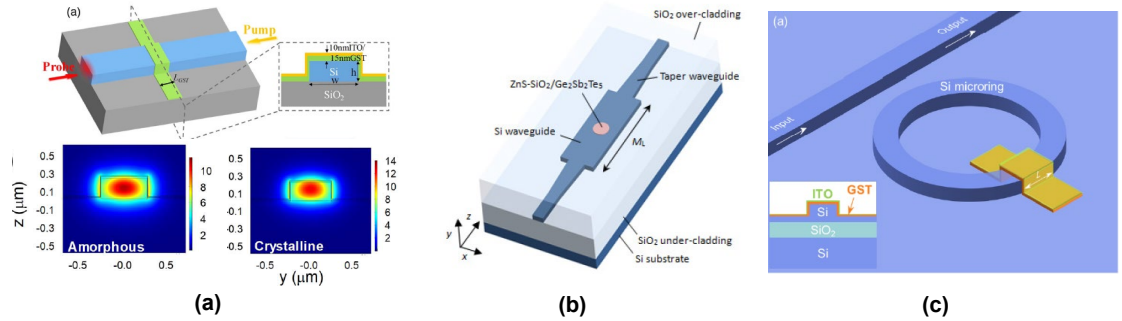

Fig. 2.7. **(a)** Hybrid GST/Si waveguide optically activated with an in-plane optical pumping [156]. **(b)** Hybrid device based on a silicon multimode interference to reduce insertion losses and increase switching speed [157]. **(c)** Hybrid ring resonator to increase extinction ratio and reduce energy consumption [158]. Non-volatile optical switching in **(b)** and **(c)** was triggered with an out-of-plane optical pumping.

ues around 180 - 250 ºC. On the other hand, the material needs to be heated above the melting temperature (~600 ºC) and then quenched by rapid cooling (~ns) for amorphization. The reach of such high temperatures increases energy consumption. On the other hand, the switching time between states is generally slower for crystallization and physically limited to hundreds of picoseconds [159]. However, the operation speed will depend on the excitation used for driving the thermally-mediated phase change and the influence of the generated heat on the photonic structure [154]. Optical pumping has been the dominant approach until now for analyzing the non-volatile switching performance in hybrid waveguide devices. Out-of-plane optical pumping was used in the first demonstration of a hybrid GST/Si waveguide device [160]. The switching speed and insertion losses were further improved by designing a silicon multimode interference waveguide, shown in Fig. 2.7b, with optical light concentrated on a 1 μm-diameter circular-shaped GST-film deposited on top [157]. Hybrid GST/Si waveguides with a few micrometer lengths and GST thicknesses of 20 nm have also been integrated on silicon ring resonators, as depicted in Fig. 2.7c, for achieving extinction ratios of 12 dB [36] and even larger than 30 dB [158]. However, the switching performance in cavities and multimode structures is influenced by undesired variations of the silicon refractive index due to heat and free carriers, which may also be induced by the strong optical absorption [157, 36].

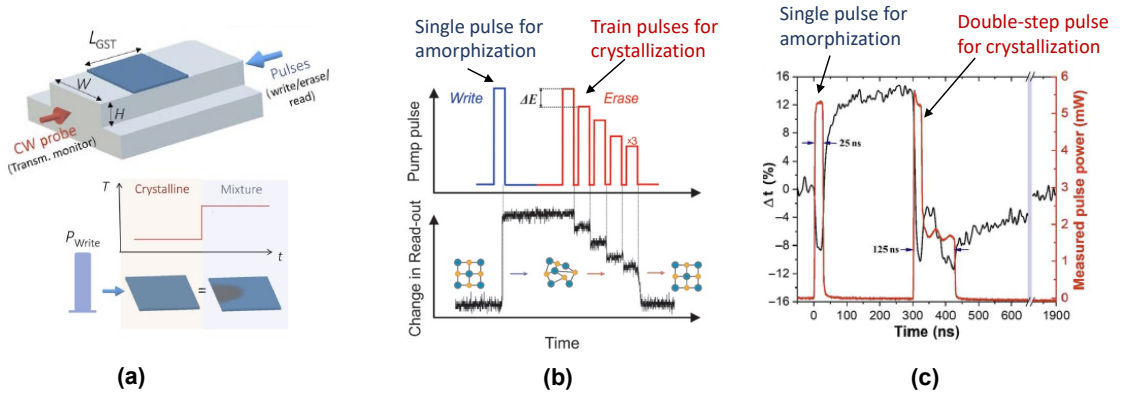

Fig. 2.8. **(a)** Non-volatile switching with in-plane optical pumping was first demonstrated with SiN waveguides. Non-uniform heating of the GST layer occurs with this kind of excitation [161]. **(b)** Optical pulses for driving the GST phase change. A single optical pulse is sufficient for amorphization, while a train of optical pulses with decreasing energy has been proposed for crystallization [162]. **(c)** Energy consumption and operation speed were improved by using a double-step optical pulse for crystallization [161].

On the other hand, in-plane optical pumping was first demonstrated with SiN waveguides, as shown in Fig. 2.8a. Optical pulses with switching energies of 533 pJ were required to achieve an optical contrast of 21% in a 5 µm-long hybrid waveguide [162]. However, non-uniform heating of the GST layer occurs with an in-plane optical pumping excitation, as depicted in Fig. 9 2.8a. Hence, switching to the crystalline state with a single optical pulse is challenging due to the rapid increase of optical absorption, which could lead to reamorphization if the phase transition occurs before the end of the optical pulse [163]. A train of optical pulses with decreasing energy has been proposed to avoid reamorphization of already crystallized regions, as shown in Fig. 2.8b, which could also be exploited for enabling a non-volatile multi-state operation. However, the switching time response and energy consumption will notably increase. More recently, a double-step optical pulse approach, depicted in Fig. 2.8c, has been demonstrated to reduce energy consumption and increase the overall speed during the crystallization process [161, 164]. On the other hand, in-plane optical pumping with hybrid GST/Si waveguides has been only reported in a few works [156, 165]. A switching energy of ~1 nJ was required for non-volatile optical switching on a 2 µm-long

hybrid GST/Si waveguide with 5 dB extinction ratio [156]. On the other hand, a switching energy of 9.5 nJ and switching time of 3.8 µs were employed to obtain a maximum optical contrast of 12% in a 4 µm-long hybrid GST/Si rib waveguide [165]. In general, higher energy but faster speed is achieved compared with hybrid GST/SiN waveguides due to the higher thermal conductivity of silicon and lower confinement of the optical mode in the GST layer.

Non-volatile optical switching has also been electrically demonstrated in a hybrid GST/Si waveguide by means of Joule heating applied with ITO heaters [166]. The use of ITO as a heater reduces optical losses and may reduce power consumption [167]. The hybrid waveguide structure is shown in Fig. 2.9a. The GST is placed on top of a silicon-wide waveguide. The extinction ratio was only 1.2 dB due to the small active region and weak interaction with the optical mode. Moreover, high switching energies of 14.4 and 4.2 mJ for the amorphization and crystallization, respectively, were required. Recently, non-volatile optical switching in a similar hybrid GST/Si waveguide device has also been demonstrated by means of electrical excitation but heating the silicon below the GST layer [168]. The hybrid GST/Si waveguide structure is shown in Fig. 2.9b. The silicon was highly doped below the GST to optimize the heat transfer and achieve an ohmic contact with the metallic electrodes. However, high insertion losses of 7.5 dB were reported due to a non-amorphization of the whole active region.

By using electrical excitation, a single voltage pulse could be used for both crystallization and amorphization, as can be seen in Fig. 2.9c. However, as a difference from optical excitation, the amorphization process could now be more critical because efficient heat dissipation or electrical pulses with fast fall times are required to avoid recrystallization when switching from the crystalline to the amorphous state. In further work, the GST region was optimized with a small circular geometry (Fig. 2.9d) for a more efficient amorphization process, thereby reducing insertion losses [169]. Moreover, parameters such as the electrical pulse duration, voltage, and GST size were analyzed. Non-volatile optical switching and multi-level operation were demonstrated with switching energies of around 10 nJ and switching times above 100 ns. A plasmonic structure, shown in Fig. 2.9e, has also been proposed to exploit both the electrical and optical changes in the GST layer [170]. The stronger light-matter interaction allows for the reduction of the footprint drastically. The non-volatile switching performance was characterized by driving the device with both optical and electrical excitations.

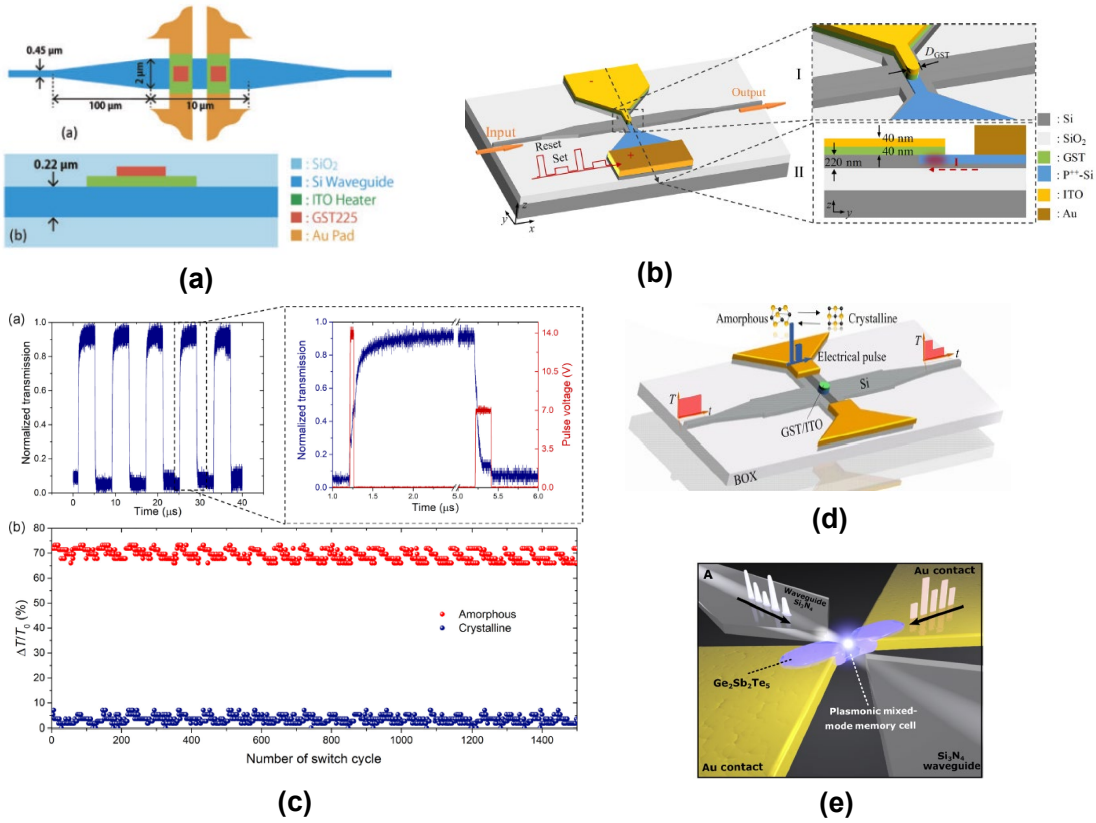

Fig. 2.9. **(a)** Hybrid GST/Si waveguide device electrically activated by means of Joule heating applied with ITO heaters [166]. **(b)** Similar device but based on heating the silicon below the GST layer and **(c)** measured non-volatile optical switching response triggered by single voltage pulses [168]. **(d)** Improved hybrid GST/Si waveguide device to reduce insertion losses [169]. **(e)** Plasmonic structure for exploiting both the electrical and optical changes in the GST layer and reducing energy consumption [170].

The switching energy with optical excitation was reduced by 6 (around tens of picojoules) compared to previous works [162]. On the other hand, sub-volt voltages were sufficient for electrically driving the GST state. However, in this case, the optical contrast was only around 0.6 %.

One challenge of GST is that the optical absorption is relatively high (between 1 and 4 dB/μm) at the amorphous state, which increases the insertion losses of the final device. A possible solution is to engineer the photonic structure cleverly. By following this strategy, a 1×2 switch with insertion losses lower than

1 dB has been recently demonstrated by patterning and encapsulating the GST into subwavelength structures [171]. Furthermore, the subwavelength patterning allowed GST to be switched more efficiently, i.e., with lower energy consumption and faster speeds. On the other hand, the use of other GST alloys, such as $Ge_2Sb_2Se_4Te_1$ (GSST) [82–84] [172–174] or $Ge_2Sb_2Se_5$(GSS) [20], with smaller optical losses at both phase states in the telecom wavelength range has also been proposed to implement non-volatile photonic devices with lower insertion losses.

Vanadium dioxide

Vanadium dioxid also stands out as a promising material for photonics [81, 83]. The key feature of this material is a reversible phase transition between an insulating and metallic state. The refractive index drastically changes between both states at telecom wavelengths, as shown in Fig. 2.10a. For VO_2 thin film deposited on silicon, at 1.55 μm, the value changes from $3.21 + j0.17$ (insulating) to $2.15 + j2.79$ (metallic) [35]. Therefore, ultra-compact devices with a broad response can be developed. However, it should be noted that variations of those values are also found in the literature [82]. Like in GST, the typical hybrid VO_2/Si waveguide is comprised of a standard silicon waveguide with a thin VO_2 layer on top, as illustrated in Fig. 2.10b. The interaction between the optical mode and the VO_2 at both states leads to a change in the effective refractive index that translates into both an optical phase and optical loss variation that can be exploited for optical switching. Ultra-compact (< 20 μm) VO_2/Si waveguides with large extinction ratios between the insulating and metallic state for TE (∼25 dB) and TM (> 40 dB) polarization either using a straight waveguide [96, 95] or in a Mach-Zehnder interferometer or microring resonator [92] have been demonstrated. On the other hand, competitive insertion loss below 0.05 dB/μm for TE polarization and 0.3 dB/μm for TM polarization has been achieved by engineering the morphology of the VO_2 layer [96].

The dominant mechanism for triggering the VO_2 phase transition has been temperature. The variation of the imaginary part of the refractive index, or extinction coefficient, as a function of temperature and at a wavelength of 1550 nm is depicted in Fig. 2.10c. The extinction coefficient shows a hysteretic response but is centered around 65 ºC. Therefore, holding power is required to exploit the bistability induced by the hysteresis loop. However, thermal requirements are more relaxed than chalcogenides as the phase change occurs near room tem-

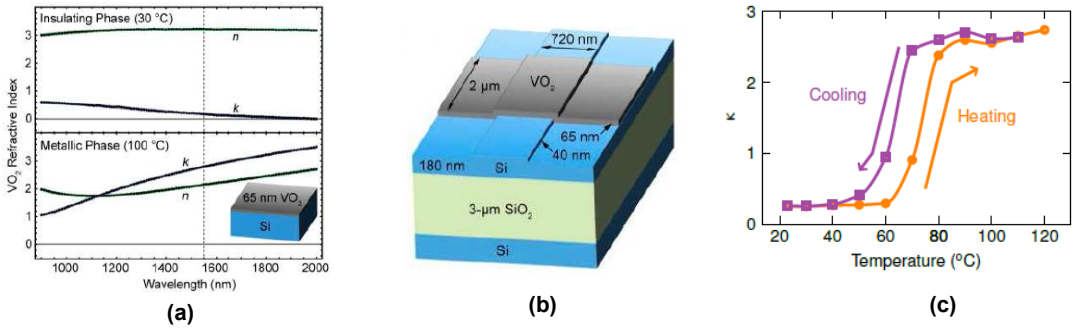

Fig. 2.10. **(a)** VO_2 refractive index at the insulating and metal states for telecom wavelengths and **(b)** typical hybrid VO_2/Si waveguide [35]. **(c)** Hysteretic variation of the imaginary part of the refractive index as a function of temperature at a wavelength of 1550 nm [175].

perature and is not restricted by a minimum cooling rate. Localized heating on the hybrid VO_2/Si waveguide can be achieved by means of Joule heating with a metallic microheater. Figures 2.11a-2.11b show a waveguide device with a lateral microheater optimized with two metals to reduce the energy consumption [96]. The optical power variation for transverse-magnetic (TM) polarization as a function of the applied electric power is depicted in Fig. 2.11c. The optical loss significantly increases when the VO_2 is switched to the metallic state. Optical switching between the two optical states was carried out by applying short electrical pulses while using a static electrical power of around 25 mW. Switching energies between 200-300 nJ and switching speeds around 3-4 µs were reported for this kind of heater-based device [95].

However, the physics across the VO_2 phase transition is complex, resulting in a subject of intense research. Intermediate metastable states and interplayed electronic and structural material aspects are involved [83]. In such a way, one of the main open questions is how to control them to enable a non-volatile optical switching performance with fast speed operation. In comparison with the heat-driven devices, an electric field gating approach has been demonstrated to reach lower consumptions (few nJ) and faster switching speeds (down to ~1 ns) but at the expense of higher optical losses and lower extinction ratios [93, 176]. Figures 2.11d -2.11e show an electrical gated hybrid VO_2/Si waveguide device and Fig. 2.11f the measured optical transmission versus applied voltage for different lengths [93]. The switching response is volatile. However, electrical gating with

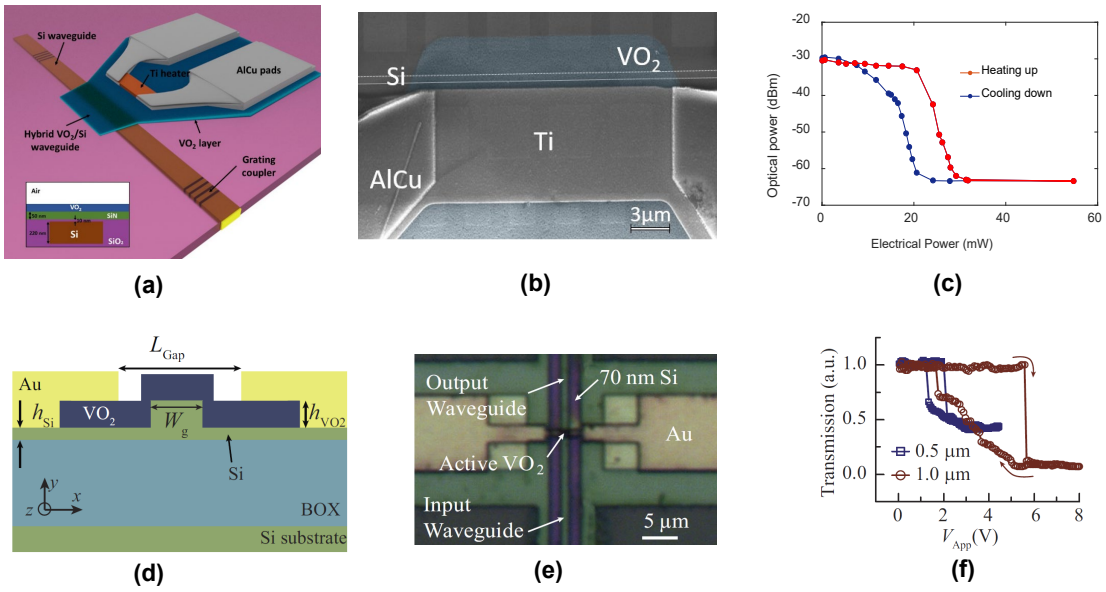

Fig. 2.11. **(a)** Hybrid VO_2/Si waveguide controlled by a lateral microheater, **(b)** SEM image of the active region, and **(c)** measured optical power variation as a function of the applied electrical power to the heater [96]. **(d)** Hybrid VO_2/Si waveguide controlled by electrical gating, **(e)** optical image of the fabricated device, and **(f)** measured optical power variation as a function of the applied voltage to the electrodes [93].

a non-volatile response has been demonstrated by including an ionic material like an electrolyte between the VO_2 and the electrode [177, 178]. The electrolyte is used to inject/extract ions from the VO_2, stabilizing the VO_2 phase transition at room temperature. Nevertheless, the experimental demonstration of such an approach in a waveguide structure has not been reported and is still an open challenge.

On the other hand, optical excitation has been proved the fastest way to induce the VO_2 phase transition with timescales in the femtosecond range [179–181] that would open a path to developing ultra-fast all-optical bistable devices. However, until now, switching times from several seconds to hundreds of picoseconds have been achieved for hybrid photonic waveguide devices driven by optical pumping [175, 90, 91, 99, 182]. Only very recently, sub-ps switching times with switching energies between 6 nJ to 360 nJ have been reported for a hybrid VO_2/Si photonic waveguide with out-of-plane optical pumping [100].

Therefore, a photo-thermal mechanism is still primarily dominant, and the difference in the timescales may be explained by the different characteristics of the control light source as well as the size of the VO_2 patch. Furthermore, the all-optical switching response remains volatile. Further work is required to elucidate if ultra-fast switching speeds down to the femtosecond are feasible on integrated waveguide devices and if non-volatility could be enabled. In the latter, the two main research directions are the reduction of the transition temperature by doping the VO_2 layer [183–185] or the control and stabilization of intermediate states by strain [186, 187].

Ferroelectrics

The utilization of ferroelectric materials such as lithium niobate [188], barium titanate (BTO) [40] or lead zirconate titanate (PZT) [189] on various PIC platforms has generated intense research activities mostly due to the demand of high-performance modulators for datacom applications. The key feature of ferroelectrics is their Pockels effects which enable electro-optical phase switching at ultra-fast speeds without an optical loss variation. Furthermore, a hysteretic response in the variation of the relative permittivity (refractive index) can be achieved by exploiting the ferroelectric domain structure and the change of the Pockels coefficients depending on such domain structure. The hysteretic curve typically has a butterfly shape, as depicted in the upper plot of Fig. 2.12a, that depends on the polling process of the ferroelectric domains and the coercive electric field of material. However, a non-volatile switching performance can be achieved by shifting the hysteric curve, as seen in the lower plot of Fig. 2.12a, by means of a permanent internal electric field induced across the ferroelectric film [190].

Among the ferroelectric materials, BTO exhibits one of the largest Pockels coefficients, and a value as high as 923 pm/V has been demonstrated in hybrid BTO/Si waveguide devices (see Fig. 2.12b) [40]. The measured hysteresis in the electro-optical phase response in a similar BTO/Si waveguide is depicted in Fig. 2.12c [191]. The hysteresis originates from the ferroelectric domain switching driven by the electric field applied across the BTO layer, as described in the schematics below. Furthermore, the preservation of the hysteresis has been proved at fast speeds (RF frequencies up to 60 GHz) [40] and, more recently, even at cryogenic temperatures (4 K), which could find application for quantum photonics [193]. Nevertheless, the key challenge for non-volatile switching is that the

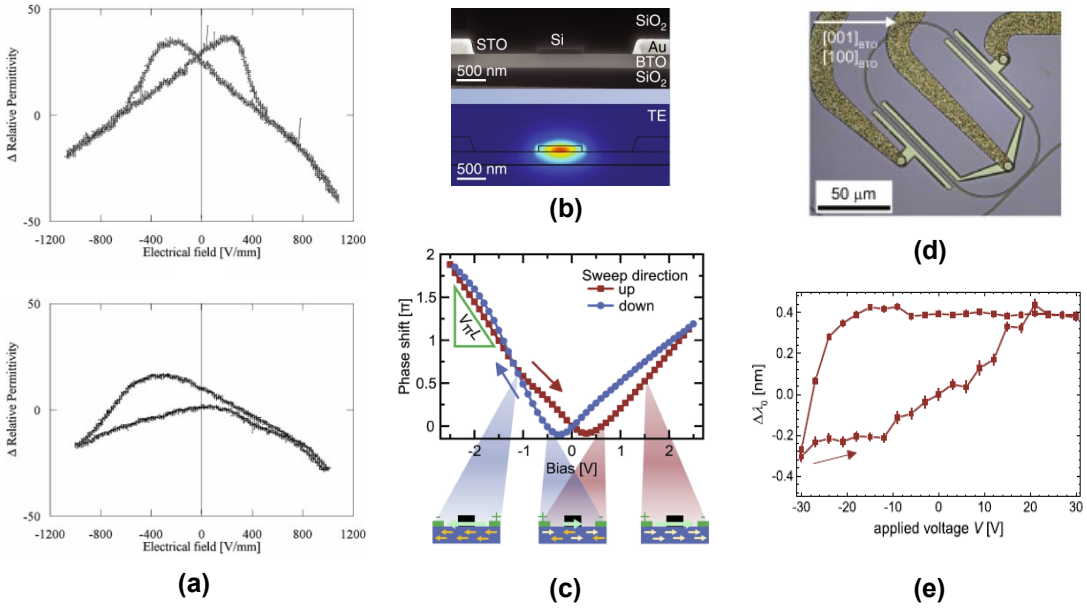

Fig. 2.12. **(a)** Butterfly-shaped variation of the relative permittivity at a wavelength of 633 nm with the applied electric field in the ferroelectric material of PLZT (lead lanthanum zirconate titanate). In the lower plot, the response is shifted by inducing an internal electrical field to enable non-volatility [190]. **(b)** Hybrid BTO/Si waveguide and optical mode for TE polarization [40]. **(c)** Measured hysteresis in the electro-optical phase response around 1550 nm in a similar BTO/Si waveguide [191]. The schematics below describe the ferroelectric domain switching under the influence of the applied voltage. **(d)** Ring resonator based on a hybrid BTO/Si waveguide and **(e)** non-volatility observed in the wavelength shift variation versus applied voltage [192].

best approach to induce the internal electric field to shift the hysteretic response is still unknown and will depend on the ferroelectric material and waveguide structure. For instance, a non-volatile electro-optical response was observed in a ring resonator based on a hybrid BTO/Si waveguide (see Fig. 2.12d) [192]. Figure 2.12e shows the wavelength shift of the resonance as a function of the applied voltage. The origin of the non-volatility was attributed to an internal electric field induced by the redistribution of free charges at the layer interfaces. On the other hand, stability over time is also a major challenge (see supplement of [40]).

Multi-state electro-optical switching has been reported but with retention times of only 6 minutes [194]. Recently, a multi-level non-volatile phase shifter

based on a hybrid BTO/Si waveguide has been demonstrated to address the stability issues [195]. Non-volatility is based on stabilizing different ferroelectric domains in BTO thin films employing electrical control pulses, which change the effective Pockels coefficient and hence the refractive index under an applied bias. The phase shifter exhibits ultra-low insertion loss (0.07 dB), eight distinct states, and stable operation with more than 10 h retention time and 300 switching cycles. Yet, the maximum achievable non-volatile phase shift of the 150-μm-long device is equal to 0.15π. This value corresponds to a 1-mm-long phase shifter to achieve a π phase shift. In this sense, further device engineering and materials quality development can help reduce this length.

Liquids

The use of liquids on silicon devices has also been proposed and demonstrated for enabling non-volatile photonic switching with an optical broadband operation [196, 197]. The switching performance relies on electrowetting actuation, which allows two liquids exhibiting different refractive indices to be moved and deposited on top of a photonic device. Non-volatility stems from the remaining liquid when the actuation voltage is removed. Optical switching has been achieved using a liquid-controlled switch device based on a directional coupler [198]. The cross-section of the coupler and a SEM image of the fabricated device are shown in Fig. 2.13a-2.13b. The oxide cladding lying on top of one of the coupler waveguides is locally removed to maximize the overlap between the optical mode and the liquid. The refractive indices of the two liquids were 1.43 and 1.63 to provide a large enough index difference. However, long switching lengths of 0.6 mm and 1.4 mm were required following an adiabatic design for achieving a broadband operation with an extinction ratio above 11 and 38 dB, respectively.

An additional experiment was reported to improve the switch performance by substituting the high-index liquid with air in order to achieve a larger refractive index change. As a result, the extinction ratio was improved above 20 dB for the shortest length, although using air instead of liquid increased the actuation voltage. On the other hand, insertion losses below 1 dB were reported, while a value lower than 0.02 dB was predicted to be achievable through design optimizations. A 16×16 switching matrix based on the liquid-controlled coupler switch has also been successfully demonstrated [199]. However, the required voltages or switching energies have not been provided, and switching times are limited to

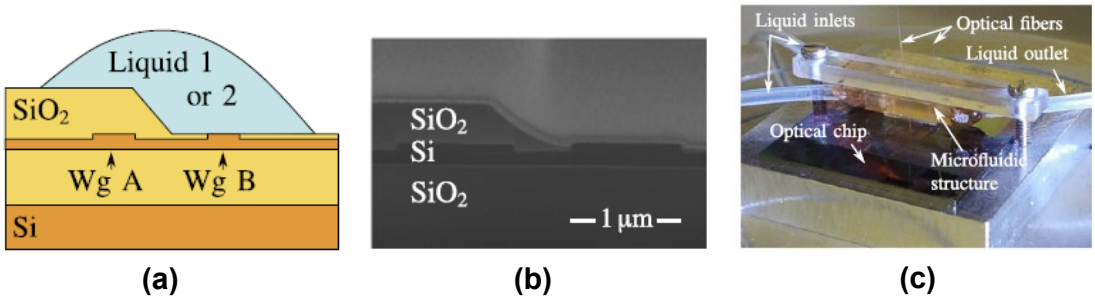

Fig. 2.13. **(a)** Cross-section of a liquid-controlled switch device based on a directional coupler and **(b)** SEM image of the fabricated device. **(c)** Required a microfluidic system to guide the liquid onto the chip [198].

the millisecond range. Furthermore, a microfluidic system is required to guide the liquid onto the chip, as depicted in Fig. 2.13c. The long-term stability and potential switching degradation at high temperatures also remain challenging.

2.1.5 Conclusions and perspectives

Optical bistability with ultra-low holding power can be simply achieved in silicon by using a photonic structure that provides optical feedback. However, non-volatility is impossible because the optical bistability is driven by the optical power of the pumping signal. Hence, several diverse approaches have been proposed for enabling non-volatile photonic switching in silicon waveguide devices.

Table 2.1: Qualitative comparison of the approaches for enabling non-volatile photonic switching in silicon-based devices.

Approach	Phase actuator	Intensity actuator	Excitation	Switching energy	Switching speed	Footprint	Manufacturing process
GST/Si	–	++	O/E	+	+	++	++
Flash memory	+	+	E	+	–	+	++
Resistive switching	–	++	E	++	+	++	+
Liquid/Si	++	–	E	+	–	–	+

++ Excellent
+ Medium
– Limited
O/E = Optical/Electrical.

Table 2.1 summarizes the main approaches where non-volatile switching has

been demonstrated in silicon waveguide devices. Nowadays, the dominant approach is based on the integration of GST since it provides a large and non-volatile multi-level change on its refractive index at room temperature that gives rise to ultra-compact devices. However, GST exhibits a relatively high optical absorption at telecom wavelengths, which makes it difficult to induce phase shifts with low optical loss. Hence, although GST has been mostly proved for optical memory cells, it is not the best candidate for phase actuators. Other chalcogenides, such as GSST may provide lower optical losses, but experimental demonstrations are needed. On the other hand, the temperature-driven switching process limits the switching speed and energy. Switching speeds in the nanosecond range and switching energies around a few nanojoules have typically been demonstrated in GST/Si waveguides with a few micrometers in length and triggered by optical and electrical excitations. Nevertheless, switching energy as small as 16 pJ has been recently demonstrated by using plasmonic waveguide structures, but at the expense of a low extinction ratio (< 1 dB) [170].

Electronic approaches could be used to remove the temperature mechanism. In this way, flash-like devices may be an option. One of the main advantages is that the fabrication is based on standard CMOS process steps. However, current experimental demonstrations rely on the weak plasma-dispersion effect of silicon and show slow switching speeds and high driving voltages. A switching time of 600 ms with voltages up to 20 V has been required for achieving extinction ratios above 20 dB in a ring device [119]. Larger phase shifts and absorption changes are predicted using alternative materials with superior properties, such as graphene. Yet, although several works have shown promising results, there is no experimental demonstration to date. On the other hand, resistive switching is another alternative to achieve ultra-compact footprints, fast switching, and low driving voltages but only for intensity actuators. However, this research field is still incipient, with few demonstrations with relatively large insertion losses and many open questions about the optimal active materials and waveguide structure, as well as control of the underlying physics to ensure reproducibility. Switching energies as low as 12.5 fJ with an extinction ratio up to 9.2 dB have been demonstrated but with a non-volatile plasmonic device and switching speeds in the microsecond range [131].

Following a different approach, liquid/Si devices have been developed to provide a non-volatile phase shift with low optical losses and without the need for

extra processing steps. In this case, switching speeds are slower (in the millisecond range) due to the underlying actuation mechanism. Its utilization may be restricted due to the necessity of a microfluidic system. However, high extinction ratios above 20 dB with insertion losses below 1 dB have been demonstrated employing a directional coupler device [199].

Table 2.2: Qualitative comparison of the approaches for enabling optical bistable switching in silicon devices but where non-volatility is still under progress.

Approach	Phase actuator	Intensity actuator	Excitation	Switching energy	Switching speed	Footprint	Manufacturing process
Si MEMS	++	++	E	+	+	–	+
VO_2/Si	–	++	O/E	+	++	++	++
Ferroelectrics/Si	++	–	E	++	++	+	+

++ Excellent
+ Medium
– Limited
O/E = Optical/Electrical.

Table 2.2 summarizes the solutions for optical switching with bistability but where non-volatility is still in progress. Silicon MEMS devices have emerged as a strong solution for implementing photonic switching devices in the last year. The mechanical displacement of photonic waveguides allows for obtaining very low insertion losses (< 0.5 dB) and ultra-large extinction ratio (> 60 dB) with switching times of 300 ns [146]. Long-term stability and high scalability have also been demonstrated. However, non-volatility still needs development, large footprints are required, and the fabrication process requires additional steps that increase the complexity and cost of the final device. On the other hand, VO_2 could be an alternative material for GST by providing a large optical contrast but with faster speeds and lower switching energies. This feature could allow optical memory cells of a few micrometers long with switching times potentially in the femtosecond range. Recently, sub-picosecond switching times with switching energies down to 6 nJ have been demonstrated for VO_2/Si photonic waveguides by using out-of-plane optical excitation [100]. However, the material change is volatile, and the strategies for enabling a non-volatility switching performance have not yet been demonstrated in waveguide devices. In addition, VO_2 is also not favorable for developing phase actuators due to the large optical loss in the metallic state.

A wide range of applications, from programmable photonics and LIDAR sys-

tems to neuromorphic computing, could benefit from non-volatile phase actuators. Ferroelectrics provide an optical phase shift without loss variation, due to the electro-optical Pockels effect, together with fast speeds and ultra-low energy consumption. BTO is an excellent choice due to its high Pockels coefficient and CMOS compatibility. Switching speeds in the picosecond range have been demonstrated in BTO/Si devices with estimated switching energy as low as 96 fJ [40]. However, the optimal route for enabling a reproducible and long-term non-volatile switching performance is still in progress.

In conclusion, to date, the optimal non-volatile approach will probably be different depending on the target application. On the one hand, the best performance metrics, such as switching energy, speed, extinction ratio, or insertion loss, show trade-offs among the proposed approaches. Non-volatile intensity actuators with high performance have been demonstrated. However, the best option for enabling non-volatile phase actuators is still an open issue. On the other hand, integration into the silicon photonics platform with the lowest complexity and high scalability might be an essential requirement. In addition, critical issues such as long-term stability or retention times have not been demonstrated in most of the devices reported so far. Nevertheless, despite all these challenges, it seems clear that non-volatile elements will be progressively integrated into the silicon platform in the next few years.

2.2 Non-volatile epsilon-near-zero readout memory

In this section, we propose to employ ITO as a floating gate in a flash-like electronic structure to achieve a non-volatile electro-optic readout memory. The memory acts as an electro-absorption switch at telecommunication wavelengths by electrically driving the ITO floating gate between a low and high loss optical state, being this latter in the ENZ regime. Hence, the memory is electronically written/erased and optically read. The main results of this section correspond to [Paper B].

2.2.1 Memory architecture and working principle

The structure of the photonic memory is depicted in Fig. 2.14, which is comprised of a stack of metal-oxide-metal-oxide-semiconductor (MOMOS). On top of the stack, a 10-nm-thick low-doped ITO layer acts as the control gate to electrically contact the memory. Conversely, the 500 nm × 220 nm silicon waveguide is electrically grounded. The floating gate is another low-doped ITO layer to minimize optical losses and is sandwiched between the two oxide layers. The oxide between the semiconductor and the floating gate is known as the tunneling oxide since it enables an electron flow between the floating gate and the semiconductor when a voltage pulse is applied to the control gate ($\pm V_{CG}$). On the other hand, the oxide between the floating and the control gates acts as a blocking layer to keep the electrons within the floating gate and avoid any leakage from the floating to the control gate.

The switching mechanism of the tunneling oxide between an insulating and a conducting state is based on the Fowler-Nordheim (FN) quantum mechanical tunneling [200]. The energy band diagram of the tunneling oxide lowers and becomes trapezoidal in the presence of a sufficiently high electric field induced by the control gate voltage. This reduction of the potential barrier enables a current between the semiconductor and the floating gate. Conversely, when the control voltage is released, the tunneling oxide turns back to insulating, and the accumulated carriers inside the floating gate become trapped. The FN current density (J_{FN}) through the tunneling oxide is given by:

$$J_{FN} = \frac{q^3}{8\pi^2 h \phi_b} E_T^2 \exp\left(-\frac{8\pi\sqrt{2m^*}\phi_b^{3/2}}{3hq}\frac{1}{E_T}\right) \tag{2.1}$$

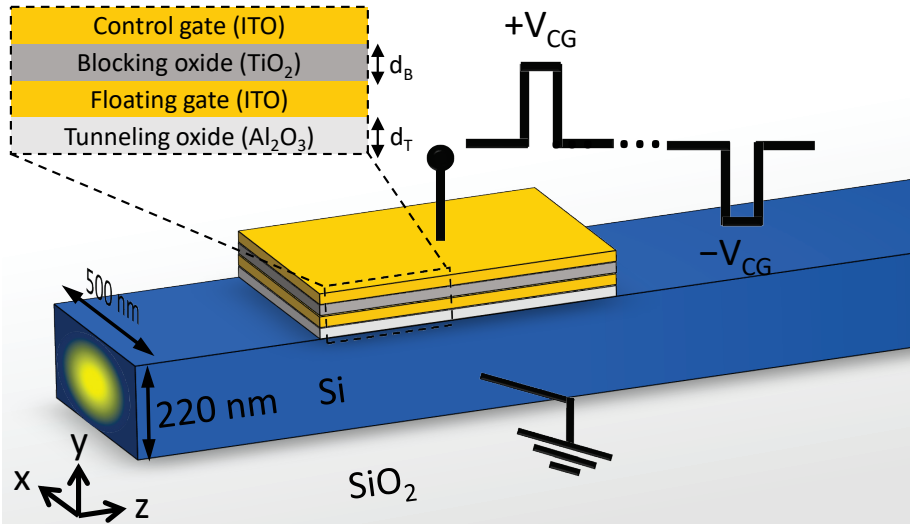

Fig. 2.14. Schematic illustration of the proposed memory based on a MOMOS structure. The ITO floating gate is driven between a low and high loss state with a non-volatile effect by applying electrical pulses.

where q is the fundamental charge, h is the Planck constant, ϕ_b is the energy difference between the tunneling oxide and the interfaced material, m^* is the electron effective mass, and E_T is the electric field within the tunneling oxide. It has to be noted that depending on whether the floating gate is written (charged) or erased (discharged), the ϕ_b should be calculated for the oxide/Si interface and the oxide/ITO interface, respectively.

2.2.2 Selection of the tunneling and blocking oxides

The ENZ regime of ITO is found for carrier densities around 6.5×10^{20} cm^{-3} at $\lambda = 1.55$ µm. This fact means that the tunneling oxide must support an E-field higher than ~ 10 MV/cm, which is a value above the dielectric breakdown of SiO_2. Therefore, we choose Al_2O_3 for the tunneling oxide since it can handle up to 30 MV/cm [201]. The FN current density as a function of the E-field inside the tunneling oxide for the Si/Al_2O_3 and the ITO/Al_2O_3 interfaces is shown in Fig. 2.15a. It can be noticed that J_{FN} for the ITO/Al_2O_3 interface is shifted to higher E-field intensities due to the higher ϕ_b than the Si/Al_2O_3 interface as it is depicted in Fig. 2.15b. Moreover, the utilization of Al_2O_3 instead of SiO_2 allows increasing the FN current density from 10^{-5} to 10^4 A/cm^2, which supposes an

increment of around ten orders of magnitude. On the other hand, utilizing a high-κ dielectric for the blocking oxide helps reduce both the control voltage and the current leakage induced by the accumulated charge in the floating gate. Hence, we choose TiO_2 as the blocking oxide, which exhibits a static permittivity of 80 [202].

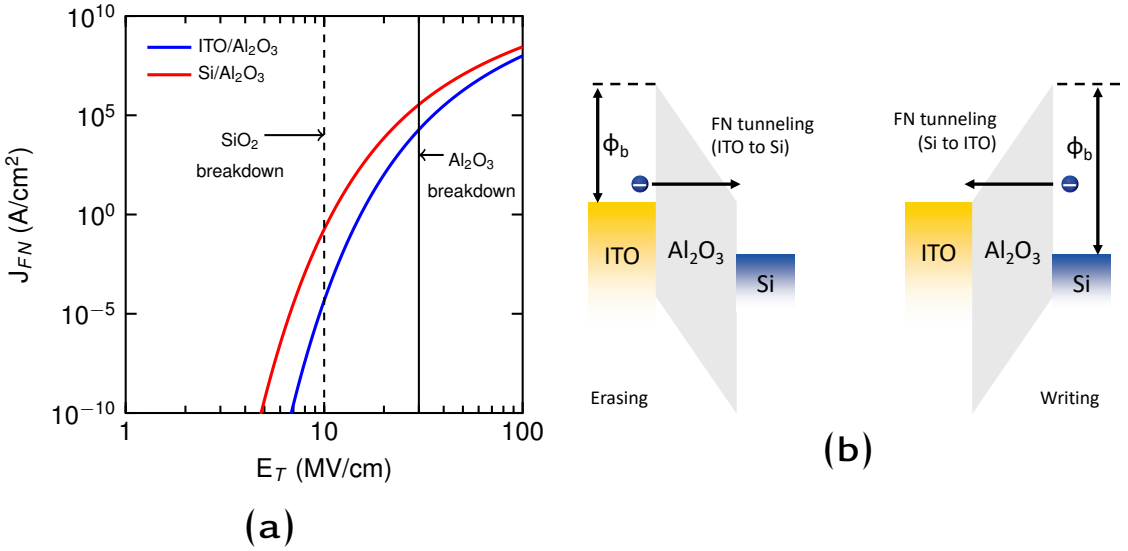

Fig. 2.15. **(a)** Fowler-Nordheim current density as a function of the E-field in the tunneling oxide for the ITO/Al_2O_3 and Si/Al_2O_3 interfaces. **(b)** Band diagram schematic during the memory erasing and writing processes.

2.2.3 Electrical modeling and retention time

From the electrical point of view, the memory can be seen as a superposition of series and parallel capacitors. On one hand, the series configuration (see Fig. 2.16a) occurs when a writing/erasing electrical pulse is applied to the control gate. On the other hand, the parallel configuration exists (see Fig. 2.16a) due to the accumulated carriers in the floating gate, which induce an electric potential ($-V_{FG}$) between the floating gate and the semiconductor/control gate (see Fig. 2.16b). By developing the electrostatics equations of the circuit model, we obtain:

$$E_T = \frac{V_{CG}}{d_T + d_B \frac{\varepsilon_T}{\varepsilon_B}} - \frac{\rho_{FG}}{\varepsilon_T + \varepsilon_B \frac{d_T}{d_B}}, \tag{2.2}$$

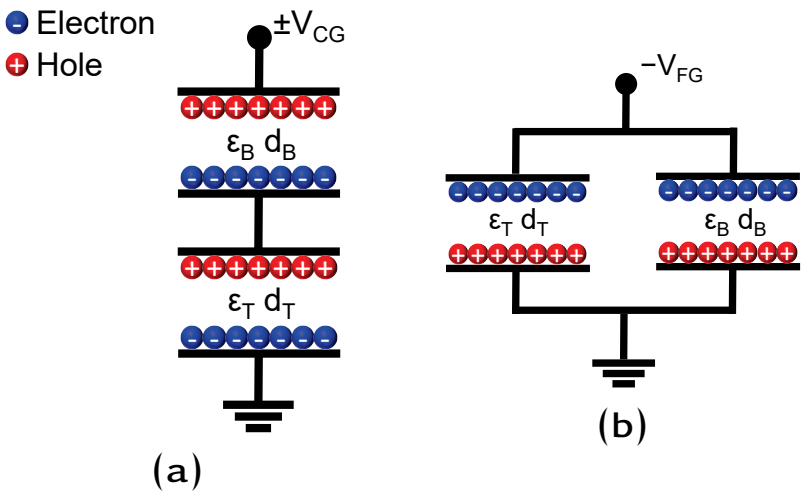

Fig. 2.16. Equivalent circuit model **(a)** during and **(b)** after a voltage pulse is applied to write/erase the memory.

where the under-scripts T and B stand for the tunneling and blocking oxide layer, d_{i} the thickness, and ε_{i} the static permittivity. The surface charge density in the floating gate (ρ_{FG}) is calculated as:

$$\rho_{\mathrm{FG}} = \int J_{\mathrm{FN}} \cdot dt. \tag{2.3}$$

Consequently, the electrical time-domain response of the MOMOS structure is obtained by combining Eqs. (2.1)-(2.3).

A 5-nm-thick ITO layer is used for the floating gate. Two accumulating layers are formed in both ITO interfaces, and thereby an overlap between them can be expected. Hence, the ITO carrier concentration (N) is estimated with uniform shape and by averaging ρ_{FG} to the floating gate thickness. Several works have utilized the Thomas-Fermi screening theory [203], Drift-Diffusion [204], or Quantum Hydrodynamic [205] models to explain the carrier distribution inside the ITO layer. However, experimental results utilizing ITO in a MOS structure do not fully agree with simulation results based on the models mentioned above [206].

The thicknesses of the tunneling and blocking oxides play an important role in terms of memory retention time. The voltage needed to drive the ITO to/from the ENZ state and the duration of the write and erase electrical pulses. In or-

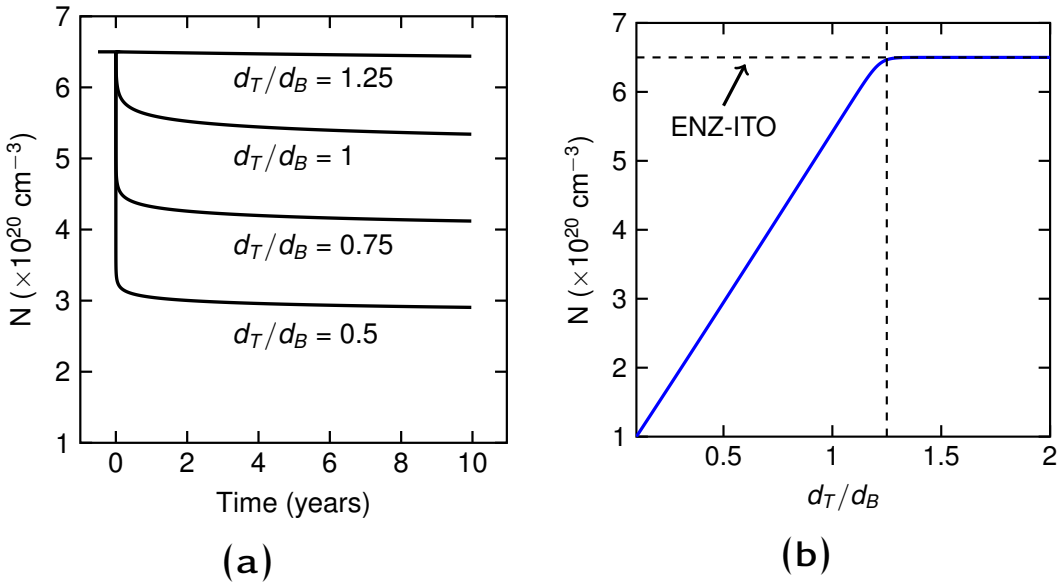

Fig. 2.17. Accumulated carriers in the floating gate as a function of **(a)** time for different oxide thicknesses relation and **(b)** after 5 years.

der to fix the thicknesses of the oxides, we first analyze the retention time after the write pulse is applied, and then, the ITO floating gate is driven to the ENZ regime. By inspecting Eq. 2.2, it can be noticed that the leakage current induced by the accumulated carriers depends on the relation between the tunneling and oxide thicknesses. The time evolution of the carrier density for different oxides thickness relations is shown in Fig. 2.17a. Initially, the floating gate experiences a rapid drop in its carrier concentration due to the self-induced FN current by the accumulated carriers. This rapid discharge reduces the E-field; hence, the leakage current is reduced to almost negligible values. Fig. 2.17b depicts the carrier concentration as a function of the oxides thickness relation after 5 years. In order to achieve long retention times and avoid degradation of the ENZ regime of ITO, the relation between the oxide thicknesses must be greater than 1.25.

2.2.4 Writing/erasing power consumption and speed

Thereby, the relation between the tunneling and blocking oxide thicknesses is set to 1.25, and the influence of the electric parameters, such as the amplitude and duration (t_p) of the control voltage pulse is investigated. Figs. 2.18a and 2.18b show the contour maps of the control gate voltage that is necessary to drive the

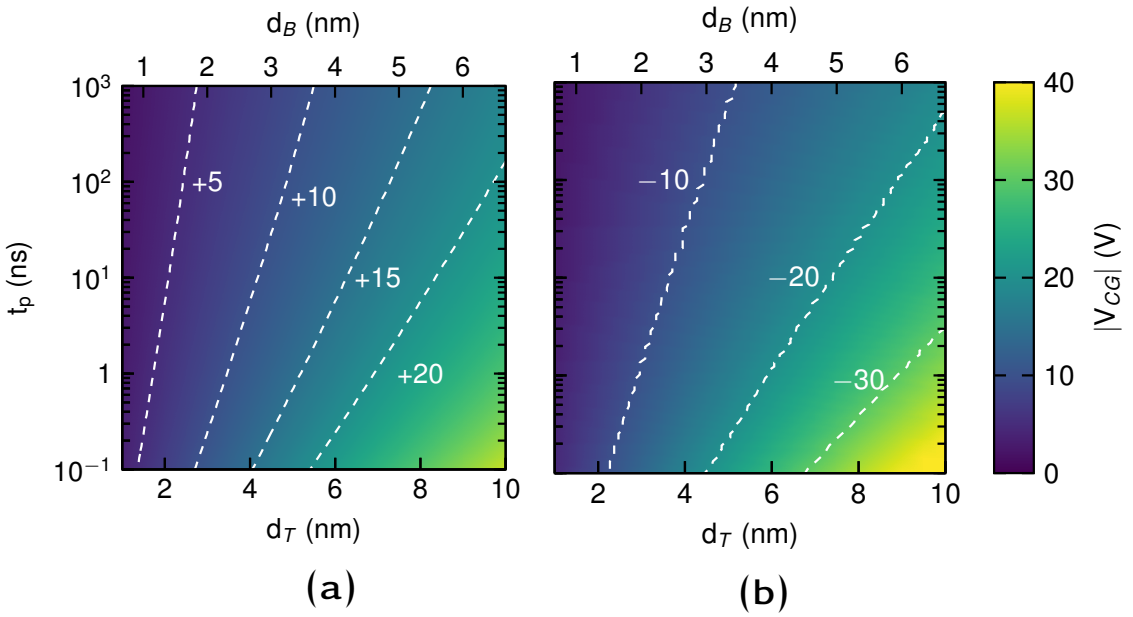

Fig. 2.18. Voltage needed to drive the ITO floating gate to/from the ENZ regime as a function of the electrical pulse duration and thicknesses of the oxides for the memory **(a)** writing and **(b)** erasing processes.

ITO in the ENZ regime (writing process) and to fully discharge the ITO from this state (erasing process), respectively. For both processes, the lower the oxide thickness, the lower the control voltage needed, since $E_{\mathrm{T}} \propto 1/d$. On the other hand, the control voltage can be reduced for a fixed thickness at the expense of applying longer control pulses and vice versa because the accumulated charge can be obtained by either applying a high voltage in a short time or a lower voltage in a longer time, taking into account that $E_{\mathrm{T}} \propto \mathrm{V_{CG}}$. Finally, the erasing process shows slightly higher power consumption for the same pulse duration because of the different ϕ_{b} between both processes, which imposes higher control voltage to erase than write the memory because of the higher band energy of ITO/Al_2O_3, as mentioned before.

The power consumption to write/erase the memory is given by

$$P_{\mathrm{switch}} = \frac{1}{4}\frac{C V_{\mathrm{CG}}^2}{t_{\mathrm{p}}} \tag{2.4}$$

where C is the equivalent capacitance of the two series capacitors formed by the tunneling and blocking oxide layers (see Fig. 2.16a). Figs. 2.19a and 2.19b show

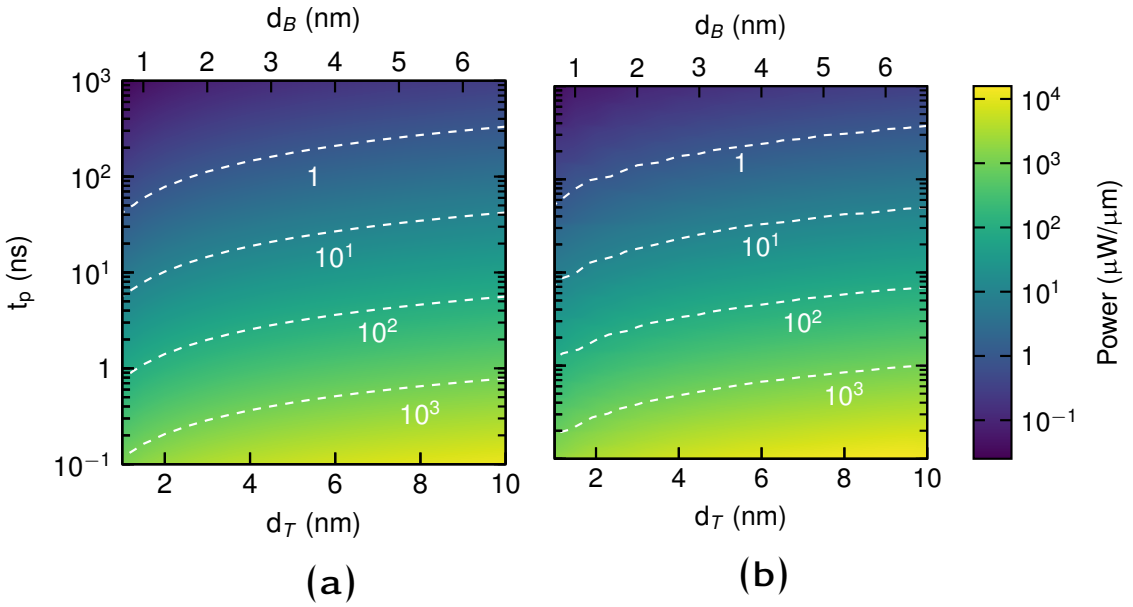

Fig. 2.19. Power consumption per length to switch the ITO floating gate to/from the ENZ regime as a function of the electrical pulse duration and thicknesses of the oxides. **(a)** Writing and **(b)** erasing process.

the power consumption per length for the written and erased processes, respectively, in order to charge and discharge the ITO floating gate to/from the ENZ regime as a function of the oxides thickness and the control voltage pulse. As can be noticed, the power consumption does not show a sharp variation with the oxide thicknesses, unlike the control voltage. This fact is caused by the reduction of the control voltage with the oxides' thicknesses is counteracted by an increase in the total capacitance. Hence, the power consumption is mainly determined by the duration of the control voltage pulse. Power consumption lower than the microwatt could be achieved for pulse durations below the microsecond range with memory lengths of a few micrometers.

2.2.5 Optical performance

In order to analyze the optical response of the memory after the writing and erasing processes, the thicknesses of the tunneling and oxide layers are fixed to 6 and 4 nm, respectively, which are feasible values to achieve by atomic layer deposition (ALD) [207, 201]. The ITO carrier density is mapped to the refractive index by applying the Drude model [Eq. (1.2)]. We take $\varepsilon_\infty = 3.9$, $\Gamma = 1.8 \times 10^{14}$

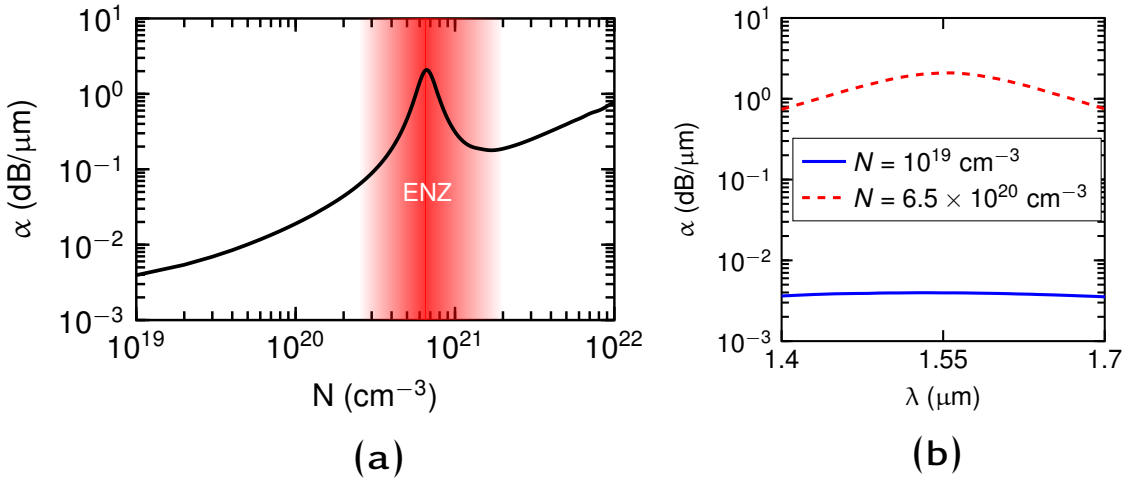

Fig. 2.20. Propagation losses for the TM-like mode as a function of the **(a)** ITO carrier concentration at $\lambda = 1.55$ µm and **(b)** the wavelength in the low-loss ($N = 10^{19}$ cm^{-3}) and ENZ ($N = 6.5 \times 10^{20}$ cm^{-3}) states.

rad/s, and $m^* = 0.35 m_e$ [208].

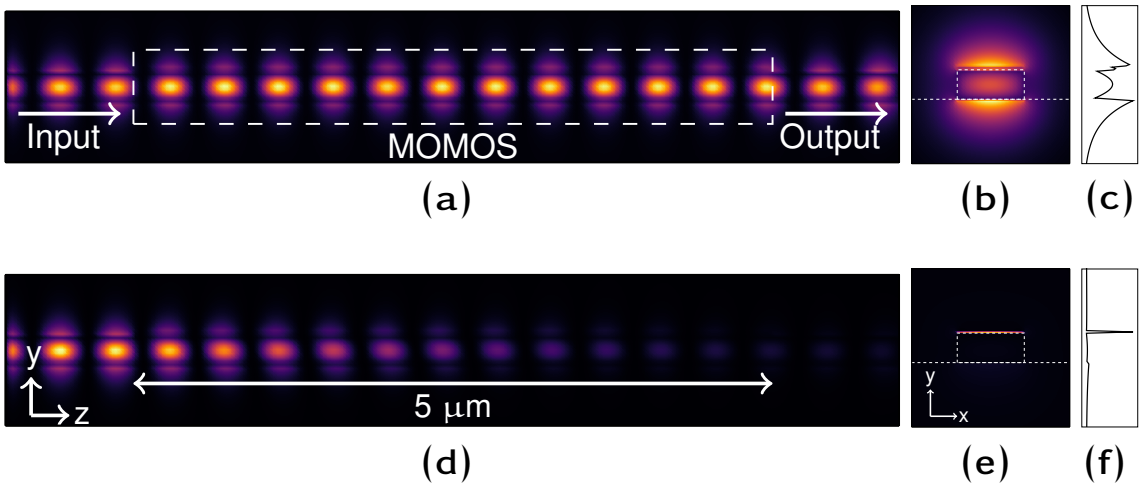

Fig. 2.21. 3D-FDTD simulations of the optical mode propagation for the memory state after the (a) erasing and (d) writing processes. Mode profiles (E_y) and y-cut of the mode profile after the (b, c) erasing and (e, f) writing processes. Simulations were carried out at $\lambda = 1.55$ µm.

Because the MOMOS structure is vertically stacked, the memory works for TM polarization. The mode profiles and effective indices are calculated using a FEM solver (see Appendix A.1.2 for simulation details). Fig. 2.20a depicts the

propagation losses as a function of the ITO floating gate carrier concentration. The peak loss is found when the ITO is in the ENZ regime, and it is enabled by the combination of the lossy ITO and the high confinement of the optical mode within the floating gate ITO layer because of the drastic reduction of the ITO $|\varepsilon|$ in the ENZ regime as shown in Figs. 2.21e and 2.21f. In the low-loss state ($N = 10^{19}$ cm^{-3}) the propagation loss is below 0.02 dB/μm and increases up to 2.1 dB/μm when the ITO is driven to the ENZ state ($N = 6.5 \times 10^{20}$ cm^{-3}). Thus, propagation losses between both states show a difference of more than two orders of magnitude. Moreover, the memory exhibits a broadband optical response, as shown in Fig. 2.20b. An ultra-high optical bandwidth far beyond 100 nm is achieved thanks to using a non-resonant structure and low wavelength dependence of ITO.

Figs. 2.21a and 2.21d show the 3D-FDTD optical simulations of a 5-μm-long memory for both memory states (see Appendix A.1.2 for simulation details). The memory exhibits 0.2 dB and 10.6 dB of losses after the erasing and writing processes, respectively, which agree with FEM propagation loss simulations. Moreover, power consumption of around 1 μW could be achieved for voltage control pulses of 11 V (writing) and 12 V (erasing) with a pulse duration of ~ 1 μs.

2.3 Ultra-compact non-volatile Mach-Zehnder switch enabled by a high-mobility TCO

In this section, we replace ITO with CdO as the material used for the floating gate to reduce the optical loss and, thus, enable low-loss non-volatile phase shifters. Based on this phase shifter, we propose a non-volatile Mach-Zehnder interferometer (NVMZI) for ultra-low power switching applications. The main results of this section correspond to [Paper C].

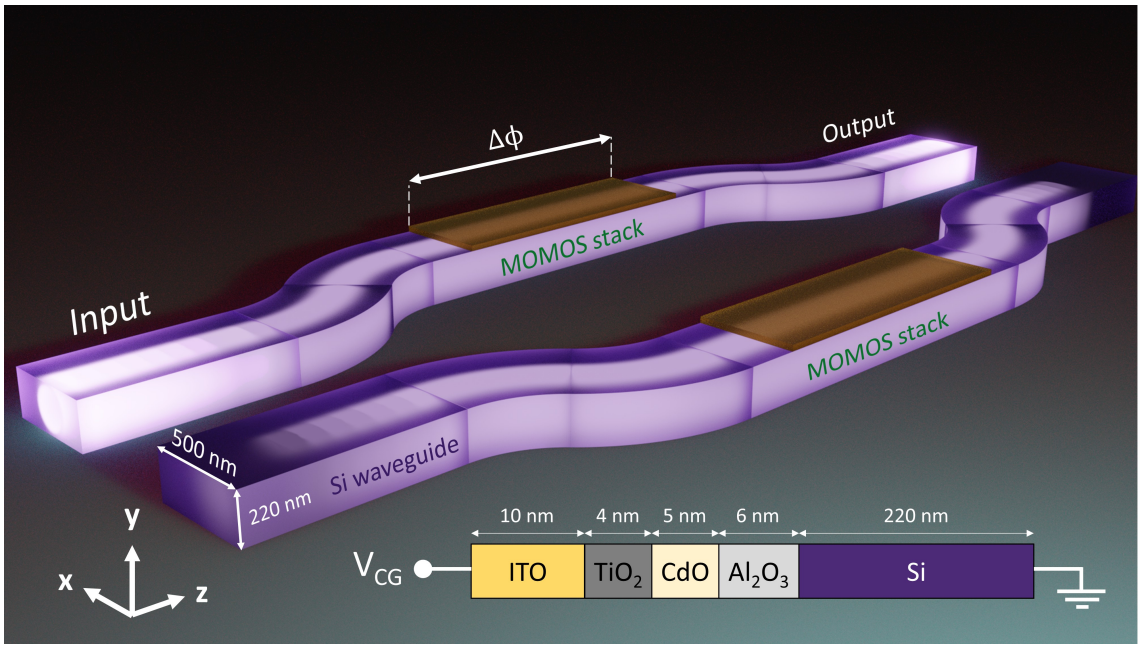

Fig. 2.22. Illustration of the proposed non-volatile Mach-Zehnder interferometer (NVMZI) switch. The NVMZI is comprised of a 500×220 nm^2 silicon waveguide fully surrounded by SiO_2. The phase shift is induced by one of the MOMOS arms. The materials and thickness used for the MOMOS layers are shown in the inset.

2.3.1 Non-volatile Mach-Zehnder switch concept

The proposed non-volatile switch is illustrated in Fig. 2.22. It is composed of a 2×2 symmetric NVMZI. Both branches have an electro-optic structure that induces a phase shift with a non-volatile effect. The electro-optic structure is comprised of a metal-oxide-metal-oxide-semiconductor (MOMOS) stack. A low-

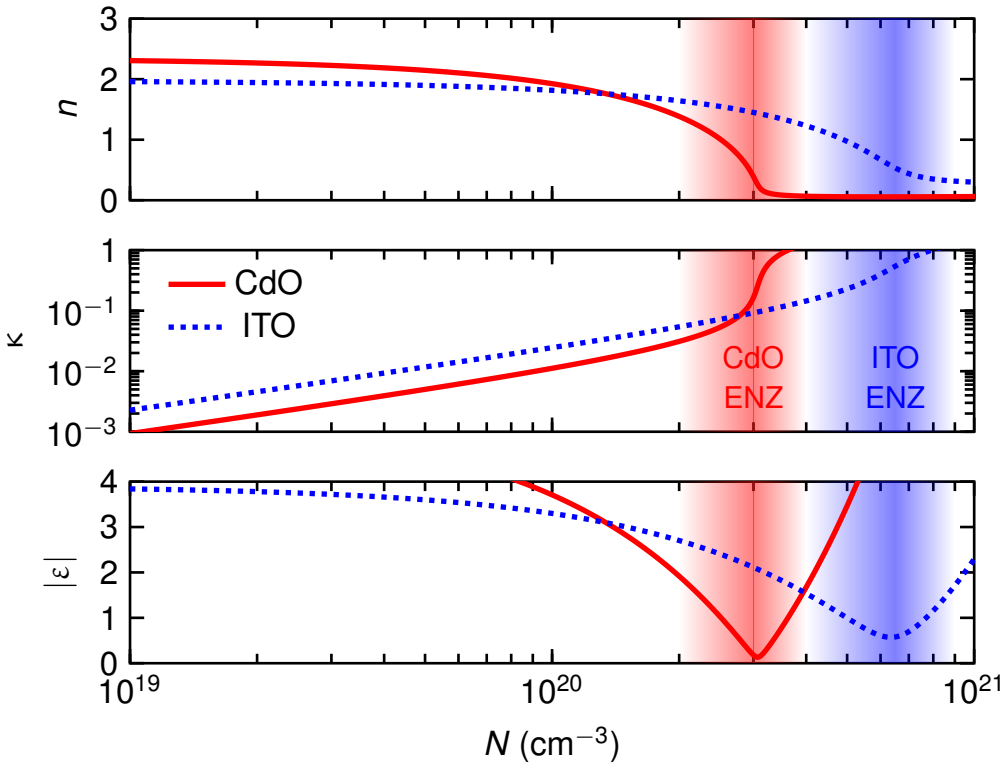

Fig. 2.23. Refractive index, $n + j\kappa$, and absolute value of the permittivity, $|\varepsilon|$, of CdO and ITO as a function of the free carrier concentration, N, at $\lambda = 1550$ nm. Optical properties were calculated using the Drude model and parameters from [209, 208].

doped ITO layer on top is electrically contacted, whereas the silicon waveguide is grounded. The floating gate, i.e., the sandwiched active layer, is either charged or discharged through the Al_2O_3 tunneling oxide by applying positive or negative voltage pulses. As a result, the free carrier dispersion effect of the floating gate changes its refractive index, thereby inducing a phase change in the optical mode. The materials and the thicknesses used for the MOMOS layers are depicted in the inset of Fig. 2.22. Further details of the MOMOS structure and methods can be found in the previous section 2.2.

2.3.2 CdO as an alternative to ITO for low-loss phase-based applications

The optical loss of materials is associated with ε''. From Eq. (1.2), the $\varepsilon''$of TCOs can be expressed as:

$$\varepsilon'' = \frac{\Gamma \varepsilon_\infty \omega_p^2}{\omega(\omega^2 + \Gamma^2)}, \tag{2.5}$$

which shows that losses are strongly correlated to Γ. The damping factor is inversely proportional to the mobility of the material ($\Gamma \propto 1/\mu$). Therefore, the mobility of the TCO should be as high as possible to obtain the minimum optical loss. Among the TCOs, CdO stands out with reported mobility values up to 1000 $cm^2\ V^{-1}\ s^{-1}$ [210]. Conversely, ITO exhibits mobilities of around 10 $cm^2\ V^{-1}\ s^{-1}$ [208]. Thus, CdO is as a better active material in the floating gate. In this work, we took the Drude parameters of the CdO from [209].

The complex refractive index, $n + j\kappa$, and the absolute value of permittivity, $|\varepsilon|$, as a function of N for both materials are shown in Fig. 2.23. The ENZ region of CdO is found around 3×10^{20} cm^{-3}, whereas ITO is at 6.5×10^{20} cm^{-3} due to the higher electron effective mass. The smaller value of Γ in CdO impacts both real (n) and imaginary (κ) parts of the complex refractive index as well as in the $|\varepsilon|$ value. On one hand, the real part for CdO presents a stepper and larger change compared with ITO in the ENZ regime. Additionally, the imaginary part is one order of magnitude smaller than ITO when the ENZ state begins to undergo. On the other hand, CdO presents higher LMI since the minimum value of ε is five-fold reduced with respect to ITO. As a result, this combination enables CdO to be used as the material for the floating gate to achieve low-loss and compact non-volatile phase shifters.

2.3.3 Optimal carrier concentration of CdO floating gate

FEM-based simulations were carried out for the cross-section of the MOMOS structure (see Appendix A.1.2 for simulation details). The effective refractive index was obtained by sweeping the free carrier concentration of the CdO floating gate between 10^{19} cm^{-3} and 10^{21} cm^{-3}. Then, the length to obtain a π phase

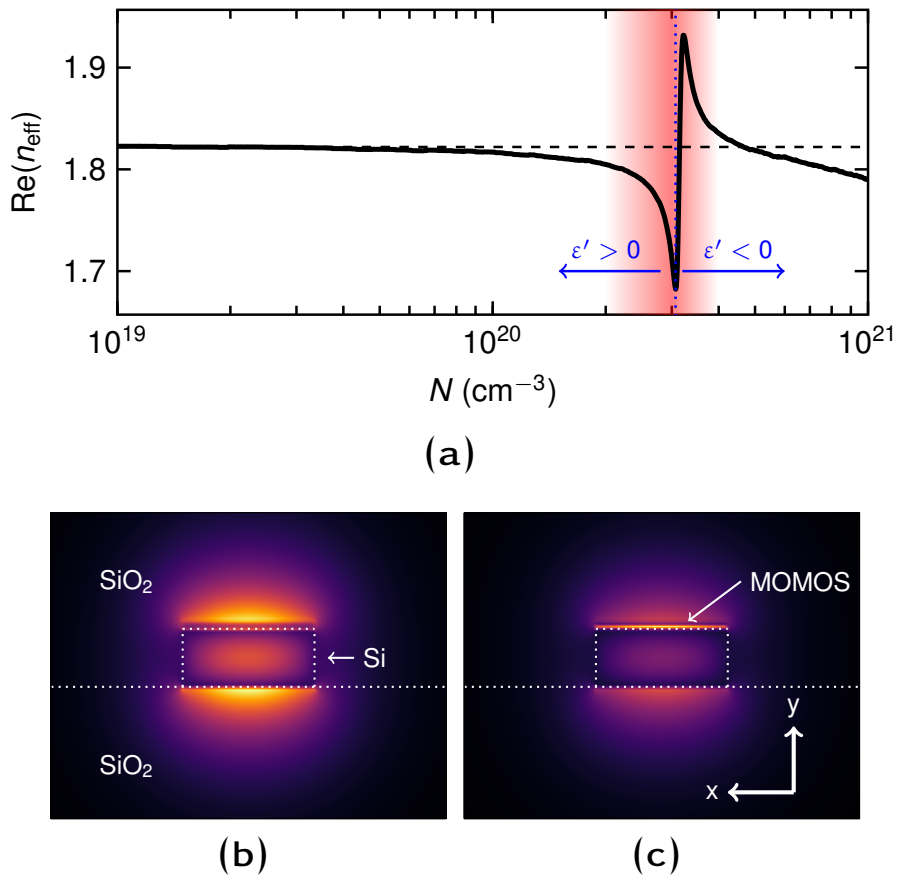

Fig. 2.24. **(a)** Real part of the effective refractive index, n_{eff}, for TM polarization as a function of the CdO floating gate free carrier concentration, N. The dashed line stands for the reference n_{eff} and the dotted line for $\varepsilon' = 0$ of CdO. **(b,c)** Electric field profile, $|E_y|$, of the MOMOS cross-section for different carrier concentration in the CdO floating gate: **(b)** 2×10^{19} cm^{-3} and **(c)** 2.3×10^{20} cm^{-3}.

shift, L_π, and the associated loss were calculated. The value of L_π is calculated as:

$$L_\pi = \frac{\lambda}{2|\Delta n_{\text{eff}}|}, \tag{2.6}$$

where λ is the working wavelength and Δn_{eff} is the increment in the real part of the effective refractive index taking as a reference value the obtained for $N = 2\times10^{19}$ cm^{-3}.

The variation of the real part of the effective refractive index with N is depicted in Fig. 2.24a. The Fano-like shape is induced by the change in the sign of

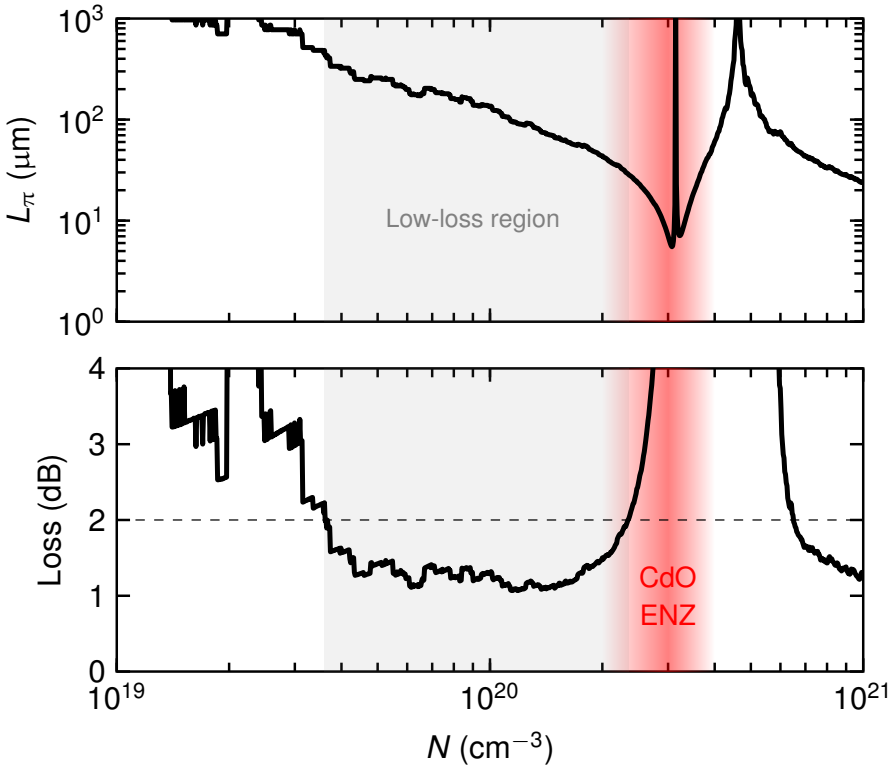

Fig. 2.25. MOMOS length to achieve a π phase shift, L_π, and associated optical loss as a function of the CdO floating gate free carrier concentration (N) at λ = 1550 nm.

the real part of the permittivity [211]. Both minimum and maximum values are found in the ENZ region. The minimum corresponds to a photonic mode since ε' of CdO is positive, whereas the maximum is a hybrid-plasmonic mode due to $\varepsilon' < 0$. For low values of N, the typical TM mode profile of a silicon waveguide is obtained (Fig. 2.24b). However, as the CdO approximates the ENZ regime, the light shifts to the floating gate and confines mostly within it (Fig. 2.24c). Ultimately, for higher values of N, CdO behaves as a metal, and a plasmonic mode is obtained.

Fig. 2.25 shows L_π and the optical loss as a function of N. As the free carrier concentration is increased from low values to the ENZ region, the greater the difference in the effective refractive index and, thus, the lower the value of L_π. Two ideal infinity values for L_π are achieved because of the Fano-like shape of $Re(n_{\text{eff}})$. The first one is during the transition of CdO from dielectric ($\varepsilon' < 0$) to

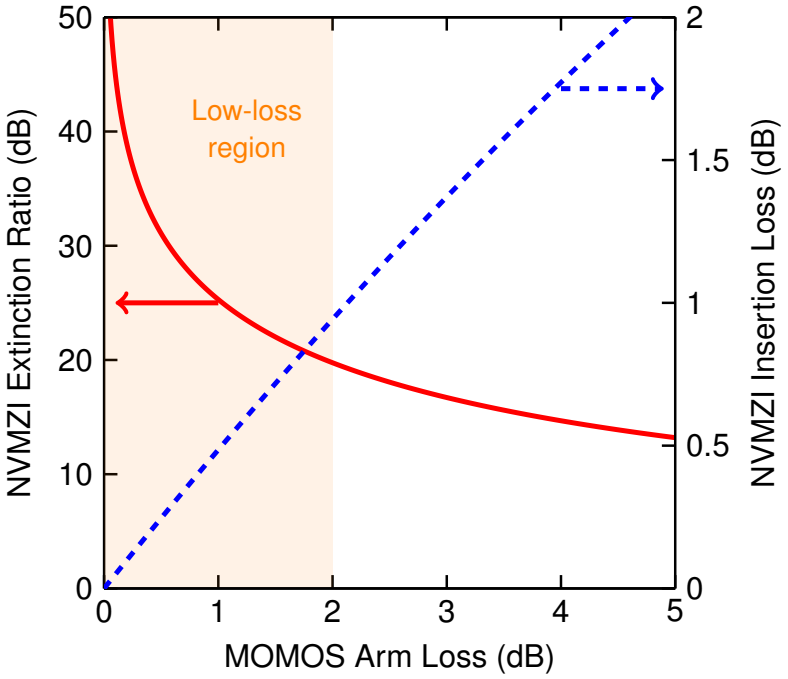

Fig. 2.26. Extinction ratio and insertion loss of the NVMZI by changing the losses of the MOMOS at $\lambda = 1550$ nm.

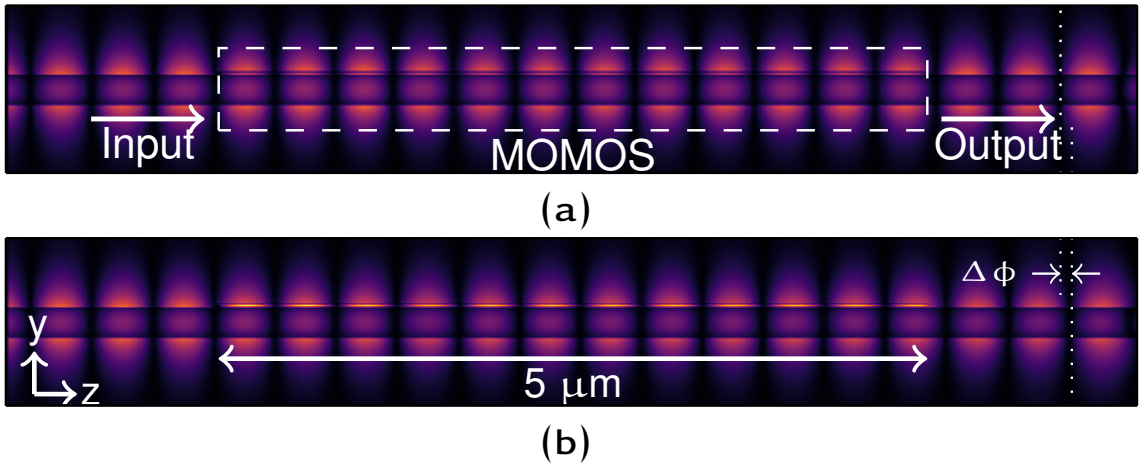

Fig. 2.27. Normalized TM electric field profile, $|E_y|$, obtained by 3D finite-difference time-domain (3D-FDTD) simulation at $\lambda = 1550$ nm. Simulations were carried out for a 5-μm-long MOMOS structure and a CdO floating gate carrier concentration of: (a) $N = 2 \times 10^{19}$ cm^{-3} and (b) $N = 2.3 \times 10^{20}$ cm^{-3}.

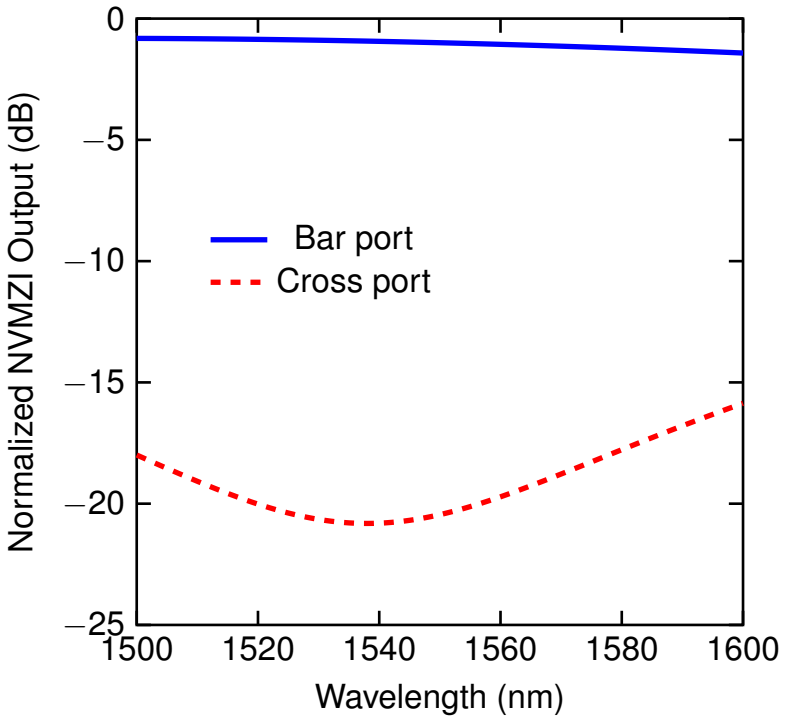

Fig. 2.28. Spectrum of the NVMZI when the floating gate of MOMOS bar arm is charged to $N = 2.3 \times 10^{20}$ cm^{-3}. The MOMOS length is L_π, and the power input is at the bar port.

metallic ($\varepsilon' > 0$), and the second one is in the CdO metallic region. The value of L_π diminishes for higher values of N with low losses. However, accumulating such high carrier concentrations is not feasible. The minimum value of L_π is found for $N \approx 3 \times 10^{20}$ cm^{-3}, obtaining an L_π below 10 µm. However, optical losses are extremely large (> 100 dB) to be used as a phase shifter.

The threshold loss of the MOMOS is determined by setting the values of the extinction ratio and insertion loss of the NVMZI. These are shown in Fig. 2.26 as a function of the MOMOS losses at $\lambda = 1550$ nm. In order to obtain more than 20 dB of extinction ratio with insertion loss lower than 1 dB, the MOMOS must exhibit losses lower than 2 dB. This criterion suffices from around $4{\times}10^{19}$ cm^{-3} to $2.3{\times}10^{20}$ cm^{-3} (see Fig. 2.25) in which the value of L_π diminishes from ~ 500 µm to 31.75 µm, respectively. Therefore, since the device footprint is highly reduced for N values near the ENZ regime, a target value of 2.3×10^{20} cm^{-3} is chosen to charge the floating gate.

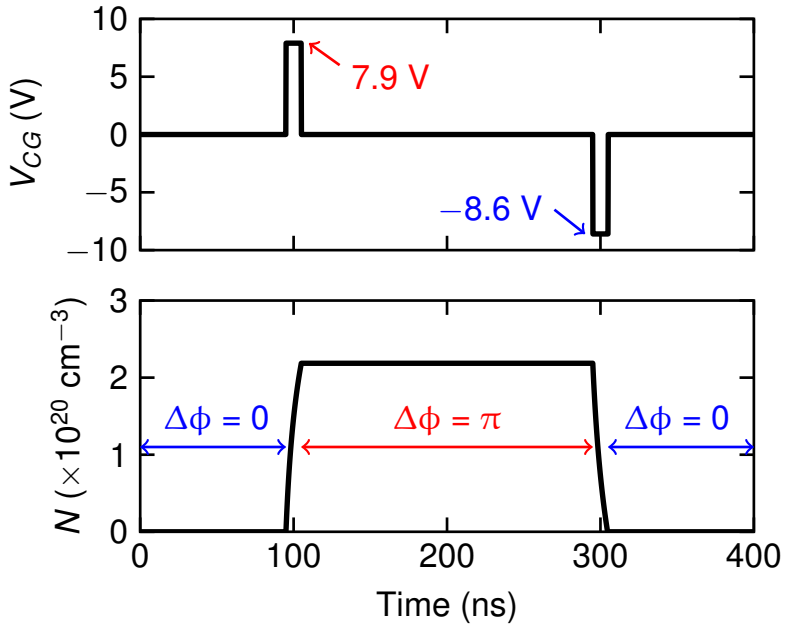

Fig. 2.29. Time-domain evolution of N as when both 10 ns wide charge and discharge electrical pulses are applied to the control gate.

2.3.4 Electro-optic performance

These results were confirmed by 3D-FDTD simulations (see Appendix A.1.2 for simulation details). A Si-MOMOS-Si waveguide with a short MOMOS structure was used in order to vary optical losses and the phase difference between both states. Fig. 2.27 shows the x-cut of the TM optical mode for a 5-µm-long MOMOS and when the CdO is discharged and charged to the values mentioned above. For the first case, optical losses are negligible (Fig. 2.27a). On the other hand, when the floating gate is charged (Fig. 2.27b, the optical mode is mostly confined within the CdO in the MOMOS structure, and thus, a phase shift is induced at the output. The phase increment is $\sim \pi/6$, which agrees with the theory since the MOMOS length is six times shorter than L_π. Furthermore, optical losses are equal to 0.31 dB in agreement with those obtained by FEM simulations, thereby obtaining negligible coupling losses for the Si-MOMOS interface.

Finally, Fig. 2.28 shows the spectrum of the NVMZI when the floating gate of one of the arms is charged to $N = 2.3 \times 10^{20}$ cm^{-3} and the MOMOS length is L_π ($\Delta\phi = \pi$). The device shows an extinction ratio higher than 15 dB and insertion loss lower than 1.5 dB in a 100 nm range. When the floating gate is discharged,

the insertion loss remains negligible.

Concerning the electrical performance, Fig. 2.29 shows the time-domain evolution of N when both charge and discharge pulses are applied. On one hand, for a 10-ns-wide pulse, a control voltage of 7.9 V is required to charge the floating gate. Notice that when the pulse is removed, the induced charge remains and, thus, behaves with a non-volatile effect. On the other hand, a negative pulse is needed to discharge the floating gate. In this case, the required voltage value is a bit higher than in the charging process. This is due to the Si/Al_2O_3 interface, which presents a lower energy band difference than the CdO/Al_2O_3. These voltages give a power consumption per switch event of around 300 μW. The switching energy is ~ 3 pJ, comparable to silicon switches based on the plasma dispersion effect [212]. However, it should be noted that the power consumption in the steady state is negligible in the proposed device. Finally, the time in which the device can maintain a $\Delta\phi = \pi$ is given by the retention time of the floating gate, which is predicted in the order of decades as in section 2.2.

2.4 Discussion

In conclusion, in sections 2.2 and 2.3 we have proposed intensity and phase-based electro-optic non-volatile devices, respectively, mimicking flash-like electronic structures. In this manner, the non-volatile actuators are electrically written and optically read. Retention times of about a decade have been predicted for both devices. The main benefit of these structures relies on utilizing TCOs (ITO and CdO) as active materials for the floating gate. Dramatic changes in the real and imaginary part of the effective refractive index can be achieved by combining such materials' large free-carrier dispersion effect with the high light-matter interaction stemming from the ENZ regime. Therefore, yielding electro-optic non-volatile devices with ultra-compact footprints of just a few micrometers.

Table 2.3: Comparison of non-volatile intensity actuators mimicking electronic memories and working around $\lambda = 1550$ nm.

Ref.	Device	Active material	Exp. / Sim.	Switching energy	Switching speed	Insertion loss (dB)	Extinction ratio (dB)	Optical bandwidth (nm)	Footprint (μm^2)
[120]	MRR	p-Si	Sim.	~pJ	~s	< 0.5	10	~ 0.2	~ 150
[122]	MRR	p-Si	Exp.	N/A	~ 100 ms	N/A	20	~ 0.1	~ 700
[119]	MRR	p-Si	Exp.	~pJ	~ 500 ms	~ 8	20	~ 0.1	~ 700
[124]	WG	Graphene	Sim.	~ 50 pJ	~ µs	~ 1.5	20	N/A	~ 150
[121]	MRR	p-Si	Exp.	N/A	N/A	N/A	< 1	~ 0.1	~ 700
[73]	WG	Graphene	Sim.	~ µJ	~ µs	~ 1.5	20	> 100	~ 10
[123]	MRR	p-Si	Sim.	~ 300 pJ	~ 100 µs	< 1	15	< 0.1	~ 1250
Our work (Sec. 2.2)	WG	ITO	Sim.	~ 1 pJ	~ µs	< 0.5	10	> 100	2.5

N/A = Not available; MRR = Microring resonator; WG = Waveguide.

Table 2.3 compares the main specification of similar flash-like-based non-volatile intensity devices reported in the literature with our device based on an ITO floating gate. Most of them rely on the weak silicon plasma-dispersion effect (PDE) to induce a change in the effective refractive index [119–123], thereby requiring resonant structures such as microring resonators to provide acceptable extinction ratios with low switching energies. However, this fact comes with a significant penalty on the optical bandwidth and the stability of the device. This latter might be caused by thermal fluctuations, considering the strong thermo-

optic coefficient of silicon. To circumvent such trade-offs, advanced optoelectronic materials such as graphene have been proposed to be used for the floating gate [124, 126]. In this manner, the need for resonant structures is prevented; thus, such devices are spectrally broadband. However, despite the superior electro-optic properties of graphene compared to silicon, the atomic thickness of graphene results in a very weak interaction with the optical mode. Therefore, considerable long devices are required to operate with low switching energies. In this context, our proposal has better electro-optic specifications by featuring switching energies as low as $\sim$ 1 pJ with switching speeds in the microsecond range. Moreover, the insertion loss is as low as 0.2 dB with a large extinction ratio above 10 dB in more than 100 nm bandwidth for an ultra-compact hybrid waveguide being only 5 µm long.

Table 2.4: Comparison of non-volatile phase actuators mimicking electronic memories and working around $\lambda = 1550$ nm.

Ref.	Device	Active material	Exp. / Sim.	Switching energy ($\Delta\phi = \pi$)	Switching speed	Insertion loss (dB)	Optical bandwidth (nm)	Footprint (μm^2)
[124]	WG	Graphene	Sim.	$\sim$ 100 pJ	$\sim$ µs	$\sim$ 3	N/A	$\sim$ 300
[125]	MZI	Graphene	Sim.	$\sim$ 50 pJ	$\sim$ 500 ns	$\sim$ 1.7	N/A	$\sim$ 35
[126]	WG	Graphene	Sim.	$\sim$ 36 µJ	$\sim$ µs	$\sim$ 1.5	> 100	$\sim$ 10
Our work (Sec. 2.3)	WG	CdO	Sim.	$\sim$ 3 pJ	$\sim$ 10 ns	$\sim$ 2	> 100	$\sim$ 15

N/A = Not available; MZI = Mach-Zehnder interferometer; WG = Waveguide.

Regarding phase-based non-volatile devices, Table 2.4 surveys similar works reported in the literature and compares their main specification with our device using a CdO floating gate. For this case, using other active materials instead of silicon is required since its refractive index variation due to free carriers occurs both in the real and imaginary parts. Hence, previous work has relied on the integration of graphene to attain a π phase shift with moderate insertion loss [124–126]. However, similarly to the intensity actuators, the change in the effective refractive index is not as efficient as in TCOs. Thus, our device can provide lower switching energies for a more compact footprint. Moreover, by integrating our non-volatile phase shifter in a symmetric Mach-Zehnder interferometer (MZI), a broadband non-volatile electro-optic switch can be achieved with extinction ratios as high as 20 dB and an insertion loss of only 1 dB.

3

Power-efficient thermo-optic phase shifters using TCO-based transparent heaters

3.1 Review of thermo-optic phase shifters in silicon

In this section, we introduce the topic of optical phase shifters in silicon photonics by briefly reviewing the well-known mainstream and main emerging technologies. Afterward, we focus on the thermo-optic technology and review its current state of the art to place in proper context our work on electro-optic and all-optical phase shifters using TCO-based transparent heaters.

3.1.1 Introduction

Phase shifters are devices able to manipulate the phase of the light (real part of the effective refractive index) with minimal –ideally zero– optical loss (imaginary part of the effective refractive index). Phase shifters are a vital building block in integrated photonics and are present in most applications, such as optical communications, LiDAR, and computing, to name a few. An ideal phase shifter should enable large-scale integration. Hence, a phase shifter should be CMOS-compatible, low loss, energy-efficient, fast, and compact. These requirements are challenging to meet simultaneously, giving rise to different trade-offs tried to solve by the technologies we comment on hereunder.

Figure 3.1 summarizes the mainstream and emerging electro-optic phase shifter technologies for the silicon photonics platforms. A comparison of their main specifications and typical values is surveyed in Table 3.1.

Silicon thermo-optic effect The most common way to implement phase shifters in the silicon photonics platform is to exploit the silicon thermo-optic effect. Although thermal effect are not very fast and power-efficient, localized heating can be easily implemented by using metallic microheaters standard CMOS fabrication processes [213–227] (see Fig. 3.1a). This approach can achieve negligible optical loss with metallic heaters by choosing a proper distance between the silicon waveguide and the high-loss microheater. However, this fact yields a trade-off between the optical loss and the power consumption and switching speed of the phase shifter. Therefore, common thermo-optic phase shifters using metallic microheaters are power-hungry (dozens of milliwatts) and slow (several microseconds). These parameters can be optimized by using doped silicon heaters or using the silicon waveguide as the heater itself [228–235, 227, 236, 237]. In the

Table 3.1: Comparison of the mainstream and emerging electro-optic technologies for implementing phase shifters in silicon photonics.

Specifications	Si TOE	Si PDE	Plasmonics	Ferroelectrics	2D materials	MEMS
Insertion loss	Ultra low (< 1 dB)	High (> 3 dB)	High (> 3 dB)	Ultra low (< 1 dB)	Low (~ 1 dB)	Low (~ 1 dB)
Power consumption	Very high (> mW)	Moderate (~mW)	Ultra low (~nW)	Ultra low (~nW)	Ultra low (~nW)	Ultra low (~nW)
Switching time	Slow (> µs)	Very fast (~ns)	Ultra fast (~ps)	Ultra fast (~ps)	Very fast (~ns)	Slow (~ µs)
Footprint	Large (> 100 µm)	Very large (~mm)	Ultra compact (~ µm)	Compact (~ 100 µm)	Very large (~mm)	Compact (~ 100 µm)
Manufacturability	Excellent	Excellent	Complex	Good	Complex	Good

TOE = Thermo-optic effect; PDE = Plasma-dispersion effect.

latter, there is no heat loss since the heating occurs inside the waveguide. However, the main limitation of this approach is the unavoidable optical loss arising from the presence of free carriers. To circumvent such limitations, transparent conducting materials have been proposed to replace metallic heaters [238–244]. Also, advanced configuration based on folded waveguides [245–248] and mode multiplexing [17] have been proposed.

Silicon plasma-dispersion effect The plasma-dispersion effect of silicon can be leveraged to implement phase shifters. The underlying physical effect is very fast (hundreds of picoseconds) and can be implemented by n-/p-doping the silicon waveguide using the same fabrication process found in microelectronic CMOS foundries [249, 250] (see Fig. 3.1b). Morevoer, the power consumption of such phase shifters is moderate (microwatts). However, two main limitations are present for such devices. The first is that the plasma-dispersion effect changes the real and imaginary parts of the silicon refractive index [251]. Therefore, those phase shifters usually have relatively high optical losses (> 3 dB). The second is that the change in the refractive index is very small ($\sim 10^{-3}$), requiring thus large footprints (~mm) [252–257] that limit the chip density, or compact but narrow-band and thermal sensitive devices by using resonant structures [258–263].

Plasmonics The combination of nonlinear polymers and high optical confinement given by plasmonics stands as a promising solution for achieving high energy efficient, ultrafast, and ultra-compact phase shifters [264–267] (see Fig. 3.1c). However, the high optical loss ($> 5-10$ dB) can be considered the main limitation of this approach. Using non-CMOS-compatible metals like gold also prevents the mass-production of these plasmonics devices. Moreover, the long-term reliability and stability of the organic polymer require further verification [268]. To circumvent these issues, transparent conducting oxides are promising candidates as new low-loss, and CMOS-compatible plasmonic devices [269, 42, 48]. In this sense, the large free-carrier dispersion effect of ITO has been harnessed to achieve sub-wavelength long phase shifters with sub-nanosecond speeds by electrostatic tuning the ITO carrier concentration close to but not at the high-loss ENZ plasmonic region [70]. Despite this fact, further optimization of these structures is required because the insertion loss of the device was very high (~ 7 dB).

Ferroelectrics Silicon has no electro-optic (Pockels) effects due to its inversion symmetry. Hence, in order to provide integrated electro-optic phase shifters, different platforms have been raised in recent years. Lithium niobate (LN) is a well-known ferroelectric material used for developing commercial fiber-based electro-optic modulators. Recently, LN-integrated photonics has emerged as a new and promising platform [188, 270]. In the context of phase-shifting devices, both ultra-low loss and ultra-fast standalone LN [271], and hybrid LN/Si phase shifters [39] can be achieved while being highly energy efficient ($<$ pJ). Hybrid LN/Si phase shifters are achieved by employing two layers of hybrid integrated waveguides and vertical adiabatic couplers (VACs) (see Fig. 3.1d). The LN layer is transferred onto the photonic chip using benzocyclobuten (BCB) adhesive die-to-wafer bonding. The VACs transfer the optical power fully, rather than partially, between the silicon waveguide and the LN membrane waveguide. To this end, the width of the silicon waveguide is tapered along hundreds of micrometers, whereas the width of the LN waveguide remains constant. On the other hand, barium titanate (BTO) is an alternative CMOS-compatible ferroelectric material. The main benefit of BTO compared to LN is its higher Pockels coefficient (923 vs. $\sim$ 30 pm/V) [272, 273], which would result in devices with better specifications. The BTO layer is usually grown by MBE on SOI substrate and then transferred onto another silicon wafer covered with SiO_2 via direct wafer bond-

ing and substrate back etching, using Al_2O_3 as the bonding interface (see Fig. 3.1e). In such a way, several BTO/Si phase-based devices have been demonstrated. [274, 192, 191, 275, 40, 193]. However, although these two platforms hold promise due to the possibility of building high-performance pure phase shifters, the mass production of the LN/Si and BTO/Si photonic technology still needs to be demonstrated.

2D materials Integrating advanced materials featuring unique optoelectronic properties can also provide high-performance phase shifters. In this context, 2D materials such as graphene and transition-metal dichalcogenides (TMDs) have attracted tremendous attention for integrated photonics [276, 277]. In particular, for phase-based devices, graphene can provide a unique combination of strong electro-refractive effect and optical transparency when operated in the Pauli blocking regime. By exploiting this fact, hybrid graphene-silicon phase shifters have been demonstrated energy-efficient at gigahertz speeds [278, 279]. However, one of the main problems is that the optical loss is highly dependent on the quality of the graphene layer. For a 300-μm-long phase shifter, the optical is estimated to be around 7 dB [279]. Recently, a monolayer of a TMD material like WS_2 has been integrated on a silicon nitride waveguide to develop a low-loss photonic platform [280] (see Fig. 3.1f). WS_2 can feature a change in the real part of the refractive index as large as $\Delta n = 0.53$, with only a minimal change in the imaginary part $\Delta\kappa = 0.004$. Such properties give rise to $|\Delta n/\Delta\kappa| = 125$ together with propagation losses due to the WS_2 monolayer less than 1.5 dB/cm. These results outperform previous 2D-material-based phase shifters and classical silicon phase modulators based on the plasma dispersion effect. However, there are some remaining issues to address, such as the quality of the monolayers, the long-term reliability and stability, and high-yield wafer-scale production.

Silicon MEMS Turning to mechanical devices, silicon MEMS technology has reached maturity over the past decades. MEM-based phase shifters exhibit low optical loss ($<\sim$ 1 dB), are energy-efficient, and have compact footprints [281–283, 145, 265, 284–286]. Such mechanical device rely on geometrical modification of the modal cross section of a suspended silicon waveguide, achieved with a MEM actuator (see Fig. 3.1g). A voltage bias is applied between the movable shuttle and the fixed anchored electrode. The bias induces an attractive force

in the actuator, reducing the distance between both sets of teeth and displacing the free-hanging shuttle. Thus, a phase shift is obtained due to the change in the effective refractive index of the guided mode induced by the geometrical tuning. Thereby, only small optical losses stem from optical mismatch due to the transitions of the structure. The main limitation comes from the switching speed ($\sim 0.1-1$ MHz) and the fabrication side. Although MEMS are compatible with the manufacturing technologies of the microelectronics industry, the involved fabrication steps are complex, and non-foundry compatible metals such as gold are required to achieve fast speeds.

All in all, the silicon thermo-optic effect is currently the best technology for implementing phase-based devices. Their fabrication easiness and the possibility to achieve near-zero losses are critical specifications in most current applications using phase shifters. The plasma dispersion effect can offer very fast speeds and excellent manufacturability, but the insertion loss is high as well as have large footprints. This latter can be dramatically reduced by using plasmonics, but the optical loss remains together with increased complexity on the fabrication side. Integrating high-performance optoelectronic materials such as ferroelectrics and 2D materials is a promising option but requires further verification and optimization of the fabrication processes. Finally, MEMS has risen recently as a very interesting solution with good manufacturability where fast switching speeds are not required.

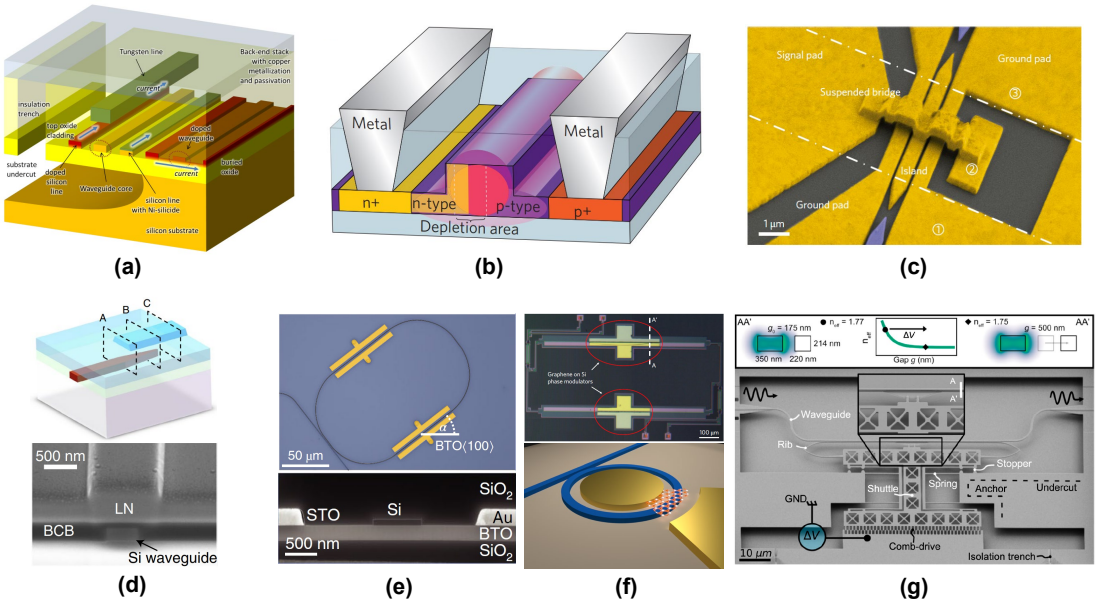

Fig. 3.1. Summary of the **(a,b)** mainstream and **(c)-(g)** emerging electro-optic technologies to develop phase shifters in silicon photonics. **(a)** Silicon thermo-optic effect with different heat architectures such as metals, doped silicon or undercut [224]. **(b)** Cross-section of typical phase shifters implementing carrier depletion mechanism, lightly doped p- and n-type regions are built in the waveguide to form a p-n diode, commonly used to manipulate the free-carrier concentrations in plasma-dispersion-based silicon structures electrically. [249]. **(c)** Plasmonic phase shifter with an organic polymer [265]. **(d)** Hybrid LN/Si phase shifter [39]. Schematic of the vertical adiabatic coupler (VAC, top image) and SEM image of the cross-sections of the VAC. **(e)** Hybrid BTO/Si phase shifter [40]. Optical micrograph of the photonic phase shifter (top image) and SEM cross-sectional image of the phase shifter. **(f)** Phase shifters using 2D materials such as graphene (top image) [279] and WS_2 (bottom image) [280]. **(g)** Silicon MEMS phase shifter. The inset shows the simulated E-field magnitude of the TE mode guided in the phase shifting cross-section at two actuation points and a graph of the simulated effective mode index with respect to gap width. [286].

3.1.2 Thermo-optic phase shifters: fundamentals and configurations

Fundamentals

Thermo-optic phase tuning in silicon waveguides is achieved by applying a localized heat and exploiting the large thermo-optic coefficient of silicon $\sim 1.8 - 1.9 \times 10^{-4}$ K^{-1} [287, 288]. The thermo-optic contribution of the SiO_2 is usually neglected since it is one order of magnitude lower than Si ($\sim 9 \times 10^{-6}$) [289]. Generally, the phase shift variation $\Delta\phi$ in a waveguide is expressed as:

$$\Delta\phi = \frac{2\pi}{\lambda}\Delta n_{\text{eff}} L \tag{3.1}$$

where λ is the wavelength, Δn_{eff} is the variation of the effective refractive index, and L is the path length. For the case the phase shift is caused by a variation in the waveguide temperature, we obtain:

$$\Delta\phi = \frac{2\pi}{\lambda}\frac{\partial n_{\text{eff}}}{\partial T}\Delta T L \tag{3.2}$$

where $\partial n_{\text{eff}}/\partial T$ is the thermo-optic coefficient of the optical mode, and ΔT is the temperature increase.

According to Joule heating, the temperature increase is proportional to the power consumed by the microheater $\Delta T \propto P_{\text{elec}}$. Therefore, the power consumption of thermo-optic phase shifters, i.e., the power required to induce a phase shift of π (P_π), can be expressed as:

$$P_\pi = \frac{\lambda}{2L}\left(\frac{\partial n_{\text{neff}}}{\partial P_{\text{elec}}}\right)^{-1} \tag{3.3}$$

where $\partial n_{\text{eff}}/\partial P_{\text{elec}}$ is the variation of the effective refractive index with the applied electrical power to the microheater. In thermo-optic phase shifters invariant in the propagation direction, such variation is proportional to the active length of the heater. Thus, in Eq. (3.3) the value P_π has no significant variation with the length of the phase shifter. In other words, the same phase shift can be achieved either using short but hot active heaters or long but mild heaters. The electrical power required to achieve the target temperature in both cases is the same. If the

phase shift architecture varies with the light propagation direction, this relationship is broken, so higher thermo-optic efficiencies can be achieved for the same active footprint.

To assess the performance of thermo-optic phase shifters, the following figure of merit (FOM) is usually employed to minimize its value:

$$\text{FOM} = P_\pi \tau \tag{3.4}$$

P_π is usually expressed in mW, and τ is the switching or reconfiguration time in microseconds. On the other hand, in order to experimentally determine the metrics of the phase shifters, these are usually embedded in interferometric structures such as MZIs, MRRs, or multimode interferometers (MMIs).

Basic configurations

The basic configuration of a thermo-optic phase shifter consists of a straight silicon waveguide with a parallel heater. Thus, the phase shifter is invariant in the propagation direction. The heater is usually made of an electrically conductive material to inject an electrical current and generate Joule heating $P_\text{h} = I_\text{h}^2 R_\text{h}$, where I_h is the current flowing through the heater, and R_h the heater resistance. Also, the heater can be the waveguide itself by doping the silicon.

For this configuration, the power consumption can be analytically approximated [227] as:

$$P_\pi \approx \Delta T_\pi G A \tag{3.5}$$

where G is the thermal conductance between the heated waveguide and surrounding materials, and A is the area traversed by the heat flow. Analogously, an analytical expression for the switching speed can also be derived [227]:

$$\tau \approx H/G \propto AL/G \tag{3.6}$$

where H is the heat capacity of the heated waveguide, in which $H \propto AL$.

In such a way, to reduce power consumption, we need to embed the waveguide with low thermal conductive materials and reduce the distance between the waveguide and the heater. However, this latter usually presents a trade-off with the optical loss induced by the heater absorption. On the other hand, a low thermally conductive material benefits power consumption but reduces the

switching speed. Hence, unless the distance between the heater and the waveguide is reduced, there is a clear trade-off between the power consumption and the switching speed. Based on Eqs. (3.5) and (3.6), a possible route to achieve faster speeds without increasing the power consumption is to reduce the heat capacity of the waveguide. This strategy implies using short active lengths. However, such an approach is not free of problems. By inspecting Eq. (3.2), one can observe that $L_\pi \propto 1/\Delta T_\pi$. Thus, short lengths can rise to very high temperatures, which can compromise the stability of the phase shifter and increase the crosstalk with close silicon waveguides or devices.

In such a way, several optimization approaches to improve power consumption, switching speed, or both, have been proposed in the literature, which we review hereinafter. The first focuses on utilizing metallic heaters and reducing power consumption by reducing the thermal conductance of the waveguide environment. However, this comes with an increase in the switching speed. Then, we review the utilization of transparent heaters to reduce the gap between the heater and the waveguide, i.e., the area A [see Eqs. (3.5) and (3.5)] traversed by the heat flow without penalizing the optical loss of the device. Finally, heating can be done directly in the silicon waveguide by doping it and using it as a resistor. Such an approach gives the best power consumption and switching speed since the value of A becomes minimal. However, the optical loss cannot be neglected due to the free carriers. Moreover, this approach is only valid for the silicon photonics platform and cannot be transferred to other emerging photonics platforms, such as silicon nitride. Unless otherwise stated, the results shown below are for transverse-electric (TE) polarization and around 1550 nm.

Metallic heaters and generic optimization strategies The most general approach to producing localized heating in a silicon waveguide or structure is using a metallic heater and Joule heating. Such resistive heaters are typically defined as metal wires on top of the silicon structure with an intermediate layer of a dielectric material such as SiO_2 to prevent optical loss. Their thickness is in the order of $\sim$ 100 nm and is usually defined by standard fabrication processes such as lift-off. Moreover, a wide variety of metals or metallic compounds that are compatible with the CMOS fabrication technology can be employed for the heaters, such as Cu, NiSi, Pt, Ti, TiN, or W.

Table 3.2 surveys the experimental works using a metallic heater and different

generic optimization strategies to implement phase shifters in straight silicon waveguides. Such optimization strategies are not limited to the utilization of metallic heaters but can be transferred to other approaches that we discuss below.

Table 3.2: Summary of basic experimental thermo-optic phase shifters using metallic heaters in silicon photonics.

Ref.	Structure / Heater metal	Optimization strategy	Loss (dB)	P_π (mW)	Switching time (µs)*	FOM (mW µs)	Length (µm)
[213]	MZI / CrAu	None	32^+	50	3.5	175	700
[214]	MZI / N/A	None	12^+	235	60	14×10^3	2500
[215]	MZI / N/A	None	22^+	90	100	9000	140
[221]	MRR / Ti	Air trenches	N/A	~10	~10	~100	~30
[220]	MZI / Pt	None	16^+	40	30	120	40
[216]	MRR / Ni	Pulse preemphasis	< 1	16	$4^\dagger$/ < $1^\ddagger$	$64^\dagger$/ < $16^\ddagger$	~ 60
[217]	MZI / Pt	Free-standing	2.8^+	0.54	141	76	100
[218]	MRR / Ti	Free-standing	< 1	1.2	170	204	50
[219]	MZI / NiSi	Close heater	< 1	20	3	60	200
[222]	MZI / TiN	Free-standing	< 1	0.49	144	71	1000
[223]	MRR / NiSi	Free-standing	< 1	2.9	358	1038	50
[225]	Microdisk NiCr	Close heater and pulse preemphasis	< 1	12	$2.9^\dagger$/ $0.085^\ddagger$	$35^\dagger$/ $1^\ddagger$	~ 60
[226]	MZI / W	None	< 1	22	45	990	200
[227]	MZI / TiN	Geometry	< 1	30	7	210	320

* We consider the limiting switching speed of the switch in the case that the value of the phase shifter is not reported, i.e., the highest value between the rise and fall time constants.
$^+$ The value corresponds to the entire switching device. The optical loss of the phase shifter is not reported.
† Without preemphasis. ‡ With preemphasis.
N/A = Not available; MZI = Mach-Zehnder interferometer; MRR = Microring resonator.

Espinola et al. reported one of the first experimental demonstrations of thermo-optic phase shifters on silicon almost two decades ago [213]. The phase shifter comprised a silicon waveguide with a 14-µm-wide and 100-nm-thick

Cr/Au heater on top. The length of the phase shifter was 700 μm. Between the waveguide and the heater, there was a 1-μm-thick SiO_2 layer. The phase shifter was embedded in an MZI, acting as a switch. The optical loss of the entire switch was very high (32 dB), and the authors attributed this result mainly to the scattering produced by the large sidewall roughness of the waveguide. On the other hand, the power consumption and the switching time were 50 mW and 3.5 μs, respectively, yielding a FOM of 175 mW μs. Despite being one of the first reported experimental works, later works reported similar or even worse performance [214, 215].

On the application side, the potential of these phase shifters has been employed for switching applications by implementing $1 \times N$ switches by cascading 1×2 MZI switches (see Fig. 3.2a) [215]. The main benefit of such switches was their compactness since the length of the phase shifter element was only 40 μm. However, both high power consumption and switching speeds were reported, 90 mW and 100 μs, respectively. The main reason for such low performance can be attributed to the large width used for the heaters ($\sim$ 20 μm), which increases the cross-section area A of the phase shifter [see Eqs. (3.5) and (3.6)]. In this regard, by reducing the width of the heater down to 5 μm, the power consumption and switching speed can be improved to 40 mW, and 30 μs with even a two-fold thick SiO_2 intermediate layer (see Fig. 3.2b) [220].

The heater width and the intermediate layer have been reported to have a high impact on the performance of phase shifters with metallic heaters on top of the waveguide [216]. On one hand, narrow heaters reconfigure faster ($\sim$ 4 mW) together with lower power consumption ($\sim$ 16 mW) as a result of smaller heating volume (see Fig. 3.2c). However, narrowing the heater below 2 μm does not represent a considerable improvement. This fact is mainly caused by the lateral diffusion of the heat ($\sim 1 - 2$ μm), which is comparable to the size of the microheater. On the other hand, the material utilized for the waveguide cladding affects both the power consumption and speed. There is a trade-off between these two features with the thermal conductivity of the cladding material. If its thermal conductivity is increased while its specific heat capacity is maintained, the phase shifter becomes faster but at the price of higher power consumption [Eqs. (3.5) and (3.6)]. To increase the speed, SiO_2 can be replaced by SiN. Additionally, the reconfiguration time can be reduced, even down to sub-microsecond timescales, by applying high-energy-pulsed drive signals [216]. In this manner, a

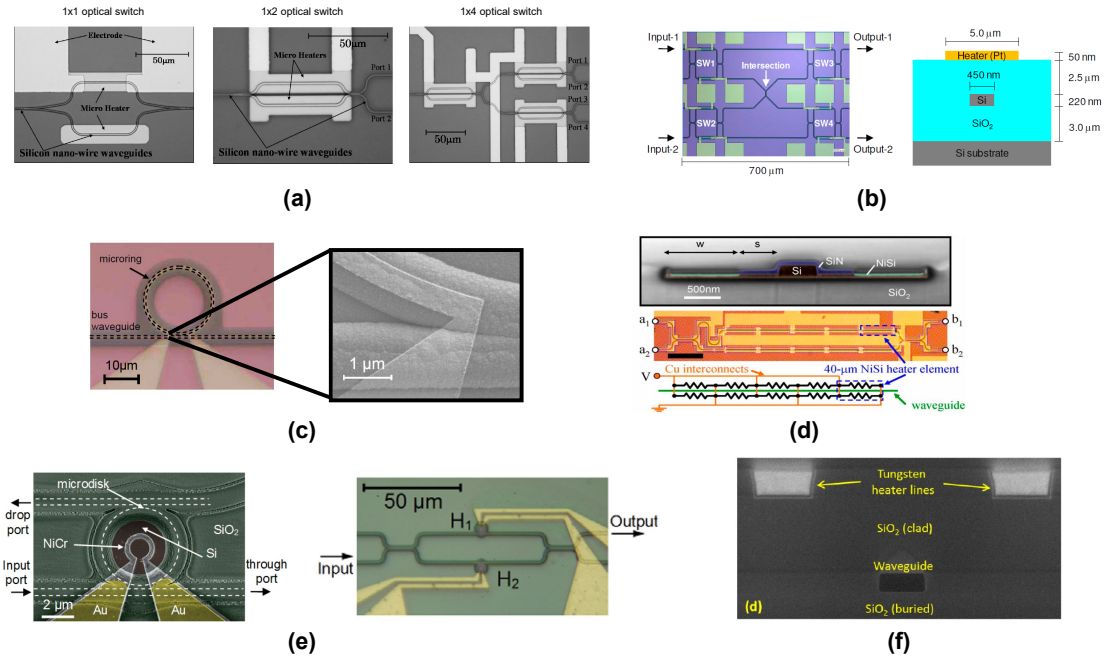

Fig. 3.2. Thermo-optic phase devices with basic configuration using metallic heaters without thermal isolation. **(a)** 1×N switch [215]. **(b)** Low-crosstalk 2×2 switch [220]. **(c)** Reconfigurable microring [216]. **(d)** 2×2 MZI with NiSi heaters [219]. **(e)** MZI with differential microdisk phase shifters [225]. **(f)** MZI using tungsten heaters [226].

preemphasis pulse can be employed to reach faster the steady step but bearing in mind that the minimum reconfiguration time is limited by the delay in the heat transfer from the heater to the silicon waveguide.

The utilization of parallel heaters to the silicon waveguide has been demonstrated to achieve low loss, energy-efficient, and fast phase shifters [219]. The phase shifter for this approach comprises a rib waveguide instead of the typical strip, and the heaters are defined on both sides of the thin bottom slab of the waveguide (see Fig. 3.2d). The heaters consist of a 20-nm-thick NiSi layer with a width ranging from 500 nm to 3 μm. It should be mentioned that for this approach, a SiN layer deposited on top of the silicon waveguide is required prior to the formation of the heater to prevent silica formation in the waveguide. The distance between the heaters and the waveguide was 500 nm to achieve low optical loss while obtaining a remarkable FOM. Thereby, although the propagation loss of the phase shifter was relatively high (25 dB/cm), their short length (40 μm)

yields an insertion loss of less than 1 dB. On the other hand, a FOM value as low as 60 mW μs was achieved with a power consumption of 20 mW and a switching time of 3 μs. Even lower FOM values have been reported by harnessing the silicon thermal conductivity and placing the metallic heater directly on top of the silicon structure [225]. In this manner, power consumption of only 12 mW and switching times of 2.9 μs are achieved. To prevent optical losses from the NiCr heaters, a small microdisk of 5 μm diameter is employed as a phase shifter instead of a straight waveguide (see Fig. 2e). In this structure, the optical mode evanesces toward the center of the device, so the interaction between the metal and the light is minimal (< 1 dB of loss). On the other hand, by using the pre-emphasis technique mentioned before from [216], the switching time associated with the heating can be reduced down to 85 ns (FOM ≈ 1 mW μs). One can use a differential architecture to achieve such low timescales in switching devices (see Fig. 3.2e). Consequently, the main limitation of this technique is in the wait time for cooling the heaters since the two arms should be cooled simultaneously before the next switching operation to avoid continuous heating of the device.

The choice of metal for the heaters may not be critical from the optical loss side. However, it is important to ensure that the electrical power is dissipated mainly in the heater and not in the interconnections and their availability when considering an industrial manufacturing environment. In this regard, conductors are used in the *middle-of-line* and *back-end-of-line* of the fabrication process flow. This fact limits the gamut of conductive materials to two main metals, copper and tungsten. The benefit of using tungsten over copper for heaters is its higher resistivity and melting point, which means that W heaters should provide better stability [226]. Also, the W heaters can be electrically connected by Cu wires, which will ensure that most heat dissipation occurs on the heater due to the higher resistivity of tungsten. W heaters on top of a silicon waveguide fabricated with a CMOS-like layer stack (see Fig. 3.2f) and without any further optimization have reported power consumptions of around 22 mW with switching times of ∼ 40 μs [226]. The optical loss was less than 1 dB, and good electrical stability was achieved for 750 switching cycles.

Thermal crosstalk should be considered in dense photonic integrated circuits. Long heaters reduce ΔT_π (see Eq. (3.2)) but increase the footprint and the optical loss. Therefore, judicious optimization is required to meet a good balance among the specifications. By using deep trenches between the aggressor and victim de-

vices, the parasitic thermal phase shift can be minimal even for short distances (~ 50 μm) between devices [227].

Thermal isolation of the phase shifter, either by using air trenches or releasing the structure from the substrate with an undercut, results in a dramatic reduction of power consumption because the thermal conductivity of air is almost two orders of magnitude lower than SiO_2 (~ 0.025 W m^{-1} K^{-1}). However, it should be highlighted that such an approach notably increases the switching time [see Eqs. (3.5) and (3.6)]. Nonetheless, this optimization solution is highly favorable for implementing many phase shifters with moderate total power consumption in applications that do not require fast speeds. The simplest way to achieve thermal isolation is to deep etch at both sides of the waveguide while maintaining the typical heater-waveguide configuration (see Fig. 3.3a). As a result, power consumption and switching speeds of around 10 mW and 10 μs, respectively, have been achieved [221]. Submilliwatt power consumptions (0.54 mW) can be attained by releasing the waveguide (see Fig. 3.3b) [217]. The free-standing phase shifter is mechanically stable using two SiO_2 struts in the 320-μm-long released waveguide. However, the switching time is increased from 39 μs in the unreleased version up to 141 μs. Similar values have been reported in recent work where the switching structure is released (see Figs. 3.3c-3.3e) [218, 222, 223].

Transparent heaters Transparent heaters, i.e., electrically conductive materials with low optical loss in the near infrared, can help to circumvent the trade-off between optical loss and power consumption and speed by reducing the distance between the silicon waveguide and the microheater. Carbon-based materials such as graphene and carbon nanotubes (CNTs) provide low optical loss thanks to their optical properties and atomically thickness while being electrically conductive. The fabrication of graphene heaters is not as easy as metals. Such heaters are usually fabricated by growing a monolayer sheet by CVD and then wet-transferred to the photonic chip with the subsequent patterning. Moreover, the optical and electrical properties are highly dependent on the quality of the sheet. Table 3.3 summarizes and compares the main specifications of experimental thermo-optic phase shifters in silicon using transparent materials.

Apart from being electrically conductive, graphene also features an exceptionally high thermal conductivity ~ 5000 W m^{-1} K^{-1} [290]. One of the first proposals using graphene in silicon waveguides for thermo-optic tuning was based

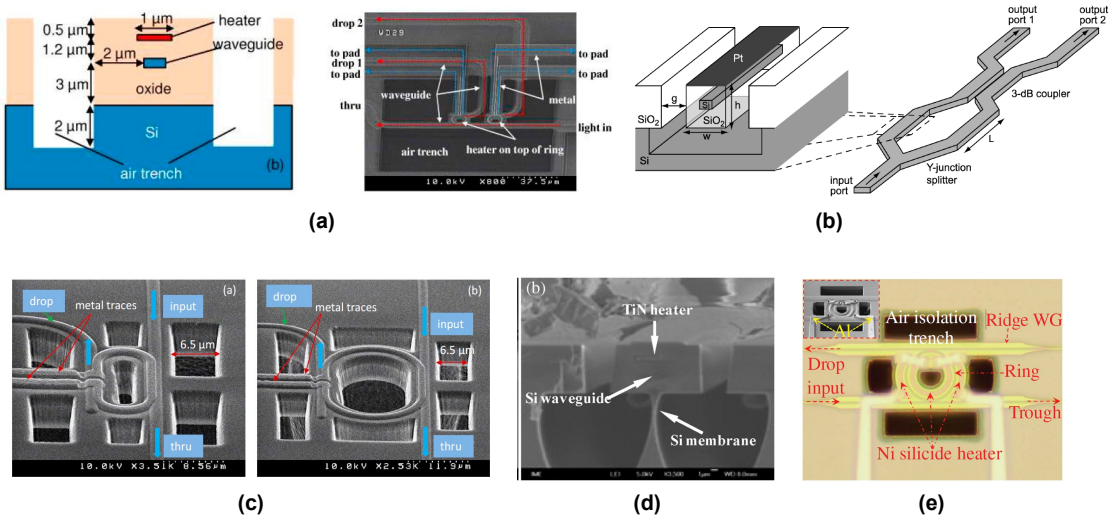

Fig. 3.3. Thermo-optic phase devices with basic configuration using metallic heaters and thermal isolation by using air trenches or undercut. **(a)** Reconfigurable ring resonator with air trenches and Ti heater[221]. **(b)** 1×2 MZI switch using a free-standing phase shifter using a Pt heater [217]. **(c)** Free-standing reconfigurable add-drop ring resonators with Ti heaters [218]. **(d)** Close view of the free-standing phase shifter using a TiN heater [222]. **(e)** Free-standing ring resonator filter with NiSi heaters [223].

on leveraging its thermal conductance. In this manner, the idea was to use a graphene layer connecting the metallic heater and the silicon waveguide to deliver the heat more efficiently (see Fig. 3.4a) [238]. However, the experimental results showed power consumptions higher than 50 mW and a moderate switching speed of 20 µs, which do not represent an improvement over the typical phase shifters using metals mentioned above. Moreover, the optical loss induced by the graphene layer obtained through numerical simulation was as high as ∼ 5 dB. More competitive results were obtained by using a similar silicon structure and approach as in [225] (see Fig. 3.1e). In this case, a graphene heater was employed on top of the silicon microdisk instead of a metallic one (see Fig. 3.4b top image) [241]. This device's power consumption and switching speed were 23.5 mW and around 10 µs, respectively. The insertion loss caused by the graphene heater was negligible ($< 2{\times}10^{-4}$ dB/µm) due to the very weak interaction between the heater and the optical mode of the microdisk resonator (see Fig. 3.4b bottom image). A

Table 3.3: Summary of basic experimental thermo-optic phase shifters using transparent heaters in silicon photonics.

Ref.	Structure / Heater material	Gap (nm)	Loss (dB)	P_π (mW)	Switching time (μm)*	FOM (mW μs)	Length (μm)
[238]	MZI / Metal + graphene	0	5+	> 50	20	> 1000	120
[241]	Microdisk / Graphene	0	< 1	23.5	13	305.5	~ 5
[240]	MRR / Graphene	240	< 1	11	3.5	38.5	~ 55
[242]	MZI-PhCW / Graphene	11	1.1	2	< 1	< 2	20
[243]	PhCC / Graphene	0	2	N/A	1.5	N/A	5
[244]	MRR / CNTs	0	N/A	14.5	4.5	65.3	~ 315

* We consider the limiting switching speed of the switch in the case that the value of the phase shifter is not reported, i.e., the highest value between the rise and fall time constants.
+ Value obtained through numerical simulation.
N/A = Not available; MZI = Mach-Zehnder interferometer; MRR = Microring resonator; PhCW = Photonic crystal waveguide; PhCC = Photonic crystal cavity; CNTs = Carbon nanotubes.

record FOM value with a value less than 40 mW μs (P_π = 11 mW and τ = 3.5 μs) has been reported using a graphene heater on top of a silicon waveguide [240]. Two intermediate layers comprised of HSQ and Al_2O_3 were used between the silicon waveguide and the graphene heater (see Fig. 3.4c). The gap was adjusted to 240 nm in order to deliver maximum performance while obtaining negligible optical loss. It is important to highlight that the power consumption was characterized at λ = 1310 nm and may suffer some variation at λ = 1550 mainly caused by the different confinement of the optical mode.

The combination of transparent heaters and enhancements of the light-matter interaction in silicon structures by means of slow light can lead to a dramatic improvement in both power consumption and speed. The slow light effect can enhance the tuning efficiency owing to the large group index that can be obtained in photonic crystal waveguides (PhCWs). Thereby, switching times below the microsecond together with power consumptions as low as 2 mW (FOM < 2 mW μs)

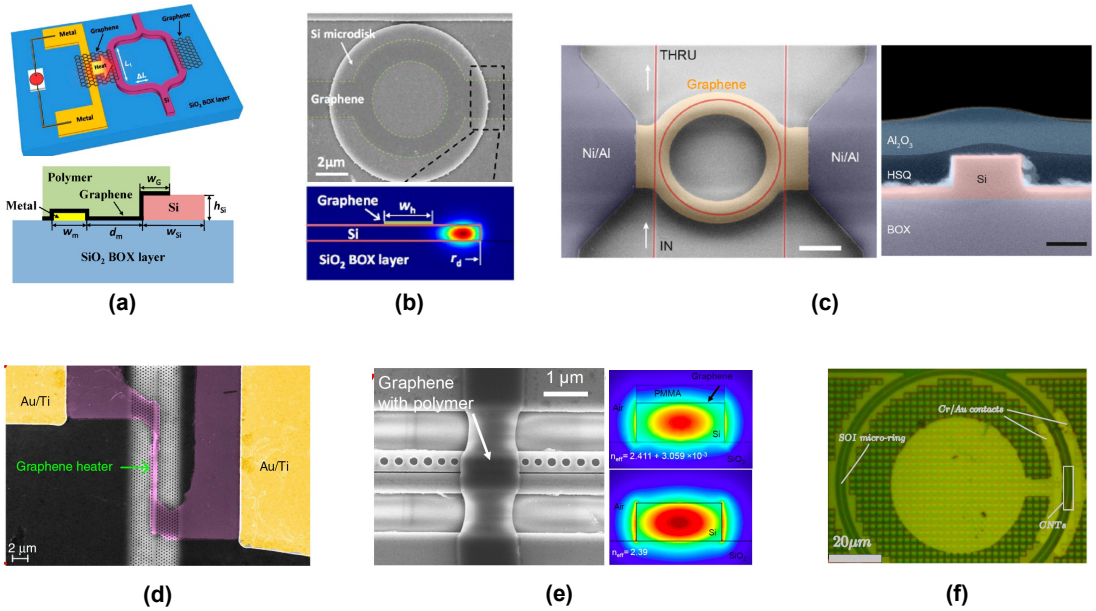

Fig. 3.4. Thermo-optic phase devices with basic configuration using transparent heaters. **(a)** MZI with a metallic heater. The graphene layer acts as a heat conductor between the metallic heater and the silicon waveguide [238]. **(b)** Silicon microdisk with a graphene nanoheater on top [241]. **(c)** Microring resonator with a graphene heater [240]. **(d)** Slow-light photonic crystal with a graphene heater [242]. **(e)** Photonic crystal cavity with a graphene heater [243]. **(f)** Microring resonator using CNT-based heater on top of the waveguide [244].

have been reported in ultra-compact phase shifters (20 μm) [242] based on a PhCW with a graphene heater on top (see Fig. 3.4d). The gap between the heater and the PhCW was only 11 nm. The optical loss corresponding to the graphene layer was 1.1 dB. Ultra-compact device switches can also be implemented similarly by creating a photonic crystal cavity (PhCC) (see Fig. 3.4e) [243]. In this regard, the switching power, i.e., the power required to change from a low loss to a high loss state, can be less than 2 mW together with a switching speed of ~ 1.5 μs in a device length of only 5 μm.

Apart from graphene, other carbon-based materials, such as CNTs have been proposed for achieving transparent heaters. In principle, the main benefit of CNTs compared to graphene is that has lower absorption in the near-infrared. CNTs directly on top of a silicon waveguide have been employed as a heater for thermo-optic tuning (see Fig. 3.4f) [244]. The main drawback of CNTs is that

their fabrication is not CMOS compatible. On the other hand, the reported power consumption values (14.5 mW) and switching speed (4.5 µs) do not represent an improvement over similar graphene-based works previously commented.

Doped silicon heaters Doped silicon can act as a standalone heater resistor or the silicon waveguide itself. Doping can be either n- or p-type by using different dopants such as arsenic (As), boron (B), or phosphorus (P). Optical loss is inherited from this approach due to free carriers, creating a trade-off between heaters' resistivity and absorption. To obtain low optical losses and resistance values compatible with electrical drivers and applications, silicon is usually doped with a carrier concentration around 10^{18} cm^{-3} and several heater resistors are employed in a parallel configuration to reduce the total resistance. On the other hand, it should be highlighted that doped silicon heaters are not holistic and thus compatible with other photonic platforms such as silicon nitride. Table 3.4 reports the experimental works using doped silicon as heater and main specifications.

Table 3.4: Summary of basic experimental thermo-optic phase shifters using doped silicon heaters in silicon photonics.

Ref.	Structure	Dopant / Concentration	Current injection	Loss (dB)	P_π (mW)	Switching time (µm)*	FOM (mW µs)	Length (µm)
[228]	MZI	p-type (B) / 10^{18} cm^{-3}	Direct	3	6	0.6	3.6	115
[229]	MZI	n-type (As) / 1.8×10^{18} cm^{-3}	Direct	0.5	12.7	2.4	30.5	~ 10
[230]	MZI	p-type (B) / 7×10^{17} cm^{-3}	Direct	~ 0.2	~ 25	~ 3	~ 75	61.6
[231]	MZI	n-type (N/A) / N/A	Parallel heaters	N/A	25	5	125	100
[232]	MRR	p and n-type (N/A) / 2×10^{18} and 4×10^{17} cm^{-3}	Direct with pn junction	N/A	19.5	0.45	7.8	~ 125
[233]	MRR	n-type (As) / 4×10^{13} cm^{-2}	Direct with pn junction	2.5	14	4	56	3.4
[234]	MZI	p and n-type (N/A) / N/A	Parallel heater with pn junction	1.6+	20.9	97.5	~ 2000	50
[227]	MZI	n-type (P) / 10^{20} cm^{-3}	Parallel heaters	< 0.4	22.8	2.2	50.2	320
[235]	MZI	p-type (P) / 10^{18} cm^{-3}	Direct	2	29	2	58	35
[237]	MZI	p-type (N/A) / 10^{18} cm^{-3}	Direct	0.24	22.6	0.5	11.3	~ 15

* We consider the limiting switching speed of the switch in the case that the value of the phase shifter is not reported, i.e., the highest value between the rise and fall time constants.
+ The value corresponds to the entire switching device. The optical loss of the phase shifter is not reported.
N/A = Not available; MZI = Mach-Zehnder interferometer; MRR = Microring resonator.

Doped silicon wires can replace metallic heaters without any inherent penalty. Typically, the employment of such resistors is made by doping the edges of a rib waveguide (see Fig. 3.5a) with a certain distance (< 1 μm) to prevent high optical loss. The center of the waveguide is kept undoped. Hence, the current of the resistors flows parallel to the waveguide. In such a way, similar values of power consumption can be attained with metallic heaters on top of the waveguide (~ 20 mW) but with faster switching speeds ($\sim 2-5$ μs) since the heat needs to propagate in a shorter distance [231, 227].

Direct current injection to the silicon waveguide mainly yields a significant reduction of the τ value compared to metallic heaters on top of the waveguide with an intermediate SiO_2 layer because the heat is generated inside the waveguide (see Fig. 3.5b left image). The power consumption is slightly reduced compared to parallel heaters placed close to the silicon waveguide since the surrounding materials mainly determine this. Rib waveguides are required to inject the electrical current in the waveguide. Usually, the waveguide edges are heavily doped, whereas the center is lightly doped (see Fig. 3.5b center image). These two doping profiles ensure maximum overlap between the thermal profile and the optical mode while minimizing the optical loss caused by free carriers. Additionally, the phase shifter can be implemented as a set of individual resistors in parallel (see Fig. 3.5b right image). Adding or removing unit cells makes it possible to tailor the device resistance and driving voltage/current while independently selecting its length. For such a strategy, insertion loss as low as 0.2 dB and power consumptions of around 25 mW with switching times of around 3 μs have been achieved [230]. Further improvement of the power consumption with minimal optical and switching speed variations can be attained by optimizing the geometry of the waveguide. In this regard, power consumption as low as 12.7 mW is achieved by inserting a compact doped-Si heater (~ 10 μm) directly into the waveguide with the help of an adiabatic bend (see Fig. 3.5c) [229]. The width of the waveguide is optimized to avoid scattering loss (narrow) or multimode loss (wide). The field pattern distribution in MMIs can be harnessed to achieve low insertion loss, compact footprints, and fast switching speeds. To this end, the electrical connections are placed at the positions where there are minima in the field pattern of the MMI (see Fig. 3.5d). For a 35-μm-long device, the power consumption and switching time are 29 mW and 2 μs, respectively [235]. In this case, the insertion loss was a moderate 2 dB value. To improve the inser-

tion loss below 1 dB, the number of electrical connections was reduced in recent work [237]. Moreover, the switching speed was improved to 500 ns by placing a heat sink made of a thin layer of Al.

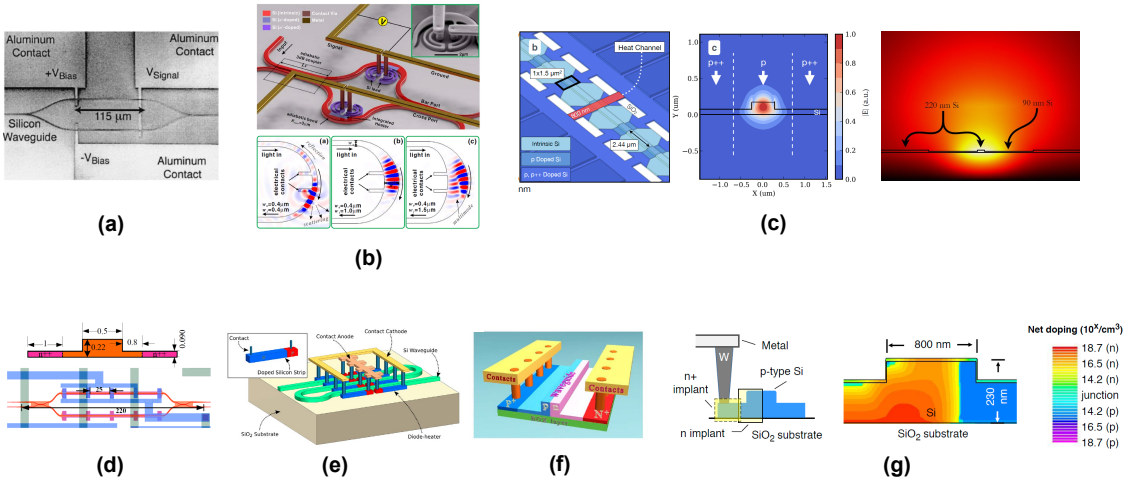

Fig. 3.5. Thermo-optic phase devices with basic configuration using doped silicon heaters. **(a)** Silicon phase shifter using side doped silicon wires as heaters [231]. **(b)** Phase shifter comprised of several doped silicon waveguides acting as heaters [230]. **(c)** MZI with an adiabatic waveguide acting as heater [229]. (d) MMI heated using silicon lead wires [235]. **(e)** Diode heater implemented as a side heater using a strip waveguide with a pn junction [234]. **(f,g)** Waveguide-heater based on pn junction [232, 233].

The saturated I-V response found in pn junctions can protect the phase shifter against runaways and a linear response between the phase shift and the applied voltage or current. Moreover, the diode-like response can be employed to drive multiple heaters independently with the same pads, thus reducing the number of electrical pads and saving space in the chip [234]. In this manner, two diode heaters are configured electrically in parallel. The cathode of one heater is connected to the anode of the other, and vice-versa (see Fig. 3.5e). Thus, one or another heater is selected by changing the polarity of the applied voltage. Power consumptions of ~ 21 mW and switching speeds of almost 100 µs have been reported with this configuration [234]. A total of 8 diode heaters were placed in parallel to reduce total resistance and, thereby, the driving voltage. Each heater was 50 µm long (8 µm p-doped) and 1.2-µm wide. The heaters were placed

0.75 μm far from the waveguide and in the same plane (see Fig. 3.5e). On the other hand, to circumvent the problem that the phase shift is highly nonlinear with the applied voltage in such heaters, the authors demonstrate a linear response by using pulse-width modulation (PWM). In this manner, the amplitude of the PWM signal is fixed at a value higher than the threshold voltage of the diode heater, and the delivered power is controlled and linearized by changing the signal's duty cycle. Recently, such diode heaters have been implemented for controlling large silicon photonics circuits [236]. Matrix topologies of N row and M column can be addressed by connecting $N \times M$ heaters. The heaters are digitally driven with PWM signals and time-multiplexed over different channels. This approach enables control of the circuit without employing digital-to-analog converters and using only $M + N$ wires. An experimental demonstration of this concept was a showcase to control a 3×5 matrix using 1×16 power splitter tree with 15 thermo-optic phase shifters connected through 8 bond pads [236]. To improve the switching speed, the pn junction can be directly created in the silicon waveguide (see Figs. 3.5f and 3.5g). Consequently, the speed can be enhanced to a few microseconds [233] or even to hundreds of nanoseconds [232]. However, this comes with a significant increase in the optical loss of the phase shifter ($\sim$ 2 dB) [233].

Advanced configurations

Other advanced configurations, reviewed hereinafter, aim to break the relationship between the heater and light path length found in basic phase shifters to reduce power consumption. To this end, the light path length is increased while maintaining the heater length, yielding thus a higher phase shift for the same power consumption. The main limitation of this approach is that large footprints are required to reduce power consumption significantly.

Folded waveguides Folded waveguides are an easy form of increasing the waveguide path length. The silicon waveguide is N-times folded under the heater. Fig. 3.6a shows an example of such configuration. Waveguide folding is achieved by means of a spiral with a total of 59 folds. The distance between adjacent waveguides was 2 μm to prevent coupling. A meander Cr/Au heater is placed on top of the photonic spiral with an intermediate 1.5-μm-thick SiO_2 layer. Thereby, a temperature change ΔT_π = 0.67 °C is required in an active

Table 3.5: Summary of advanced experimental thermo-optic phase shifters using folded waveguides and metallic heaters in silicon photonics.

Ref.	Structure	Number of folds	Loss (dB)	P_π (mW)	Switching time (µm)*	FOM (mW µs)	Length (µm)
[245]	MZI	59	~ 6+	~ 6.5	~ 14	~ 91	~ 13000
[246]	MZI	9	2.9+	4.2†/ 0.095‡	65†/ 1200‡	237†/ 114‡	2900
[247]	MZI	14	1.23	2.56	35	89.6	2300
[248]	MZI	22	0.9	3	11	33	1876

* We consider the limiting switching speed of the switch in the case that the value of the phase shifter is not reported, i.e., the highest value between the rise and fall time constants.
\+ The value corresponds to the entire switching device. The optical loss of the phase shifer is not reported.
† With air trenches. ‡ With undercut.
N/A = Not available; MZI = Mach-Zehnder interferometer.

length of 6.3 mm for the TM polarization, which yields a power consumption of ~ 6.5 mW [245]. Compared with a similar phase shifter using a straight waveguide, the power consumption of the folded phase shifter was five times less (36 mW). The switching time was 14 µs and limited by the thick SiO_2 waveguide cladding. Different widths between adjacent waveguides can be employed to avoid phase matching and thus coupling (see Fig. 3.6b) [246]. By releasing the entire phase shifter, the power consumption can be as low as 0.095 mW but at the expense of a slow switching time of ~ 1 ms.

Further optimization for such phase shifter has been made by employing non-circular Clothoid bends and optimizing the heater with and position (see Fig. 3.6c). This design enables more efficient utilization of the heat that is generated. Peripheral waveguides recollect the wasted heat energy and improve the phase shifter efficiency without using thermal isolation by means of air trenches or undercut. Thereby, this design reports a power consumption of 2.56 mW and a switching speed of around 35 µs. Recently, even better performance has been attained in recent work, reporting a P_π as low as 3 mW, and 11 µs fast [248]. Moreover, the optical loss of such a device is only 0.9 dB, minimized by the utilization of a small offset in the junction of the bend and straight waveguide (see

Fig. 3.6d) to prevent high-order mode excitation.

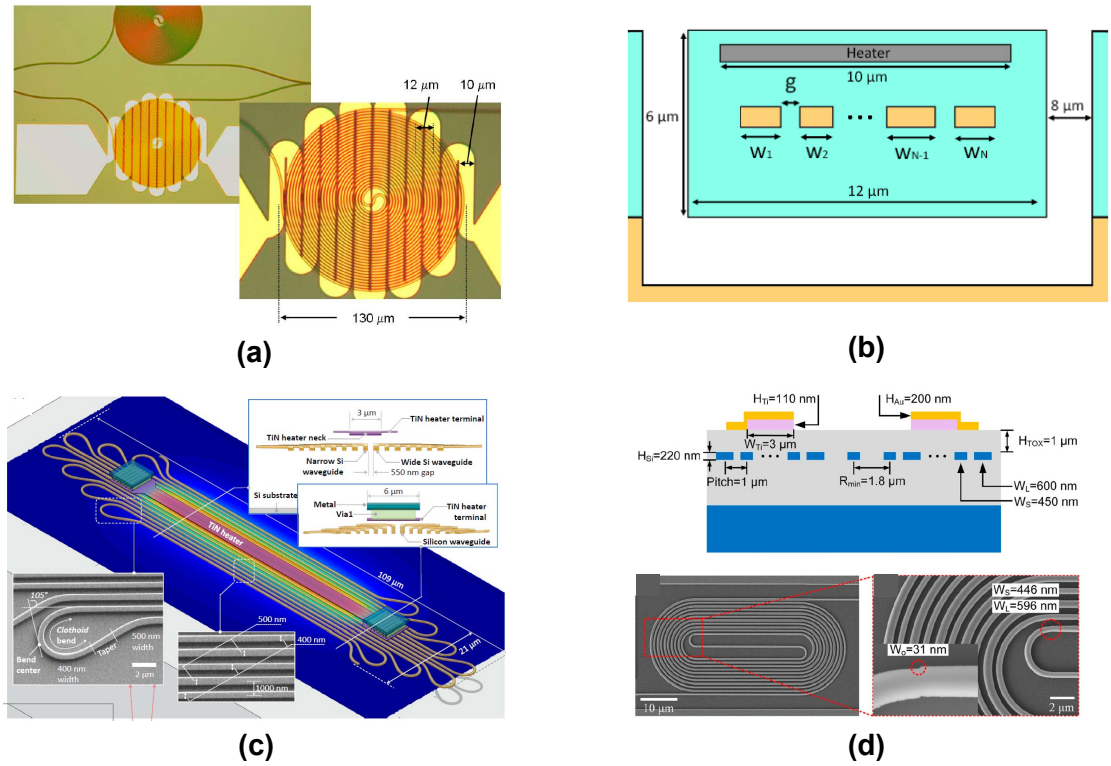

Fig. 3.6. Advanced experimental thermo-optic phase devices using folded waveguides and metallic heaters. **(a)** 59-folded spiral waveguide with Ti heater on top [245]. **(b)** Free-released phase-shifter using 9-folded waveguides with different widths between adjacent waveguides to avoid crosstalk [246]. **(c)** 14-folded waveguide with narrow Ti heater on top [247]. **(d)** 22-folded spiral waveguide with narrow Ti heater on top [248].

Multi-pass waveguides Another means to increase the effective path length is by using mode multiplexing [17]. The working principle is based on a recycled multimode waveguide, in which each pass is excited by an optical mode of a different order (see Fig. 3.7a). Light is input in the multi-pass structure in the TE_0 mode. Upon exiting the multimode waveguide, it is converted to the TE_1 mode via a mode converter and set back to the multimode waveguide in the opposite direction (see Fig. 3.7b). Upon exiting the multimode waveguide, light is then converted to the TE_2 mode and sent back to the multimode waveguide in the

forward direction, and so on. Finally, the fundamental mode is outputted. The mode converter consists of an adiabatic directional coupler (see Fig. 3.7c). Phase matching to the specific mode is achieved by tapering each of the waveguides in the opposite direction. The fabricated phase shifter is shown in Fig. 3.7d. A 360-μm-long Pt heater is placed on top of the multimode waveguide with an intermediate 1-μm-thick SiO_2 layer. The switching time of such a device is 6.5 μs, independent of the number of passes. Conversely, the power consumption and the optical loss are related to this parameter. The effective path length is increased with the number of passes, but so it makes the optical loss due to the higher number of adiabatic couplers. For a 3-pass phase shifter, the power consumption and the insertion loss are 4.6 mW and 1.2 dB, respectively. By using a 7-pass phase shifter, the power consumption is reduced down to 1.7 mW, but the loss is increased up to almost 5 dB. Finally, the potential of such a phase shifter for practical applications is demonstrated to achieve low-power (1.9 W) 2D beam steering using a silicon optical phased array with 512 actively controlled channels.

3.1.3 All-optical phase shifters

Silicon third-order nonlinear effects enable a variation of the silicon refractive index under an electric field. Although the change in the real part of the refractive index caused by the Kerr effect is ultra-fast (~ps), this is accompanied by a change in the imaginary part caused by TPA, which gives rise to optical loss [291]. In addition, TPA generates free carriers with a lifetime of ~ns that dominates over the Kerr effect, slowing down the device's speed. Additionally, the increased absorption in the silicon waveguide leads to self-induced heating, thereby leading to thermo-optic effects. Consequently, an interplay of different underlying physics hampers the implementation of low-loss all-optical phase shifters with a large phase tuning. In practice, the tiny achievable phase shift is usually employed to modulate the optical response of cavity structures that provide a large change in the transmission under small variations of the effective refractive index.

Two main types of cavities are usually employed: MRR and photonic crystal cavities. By using an MRR, a refractive index change as small as 10^{-3} can induce a large extinction ratio of 7 dB in an ultra-compact 20-μm-long structure (see Fig. 3.8a). In this manner, all-optical modulation with an extinction ratio higher than

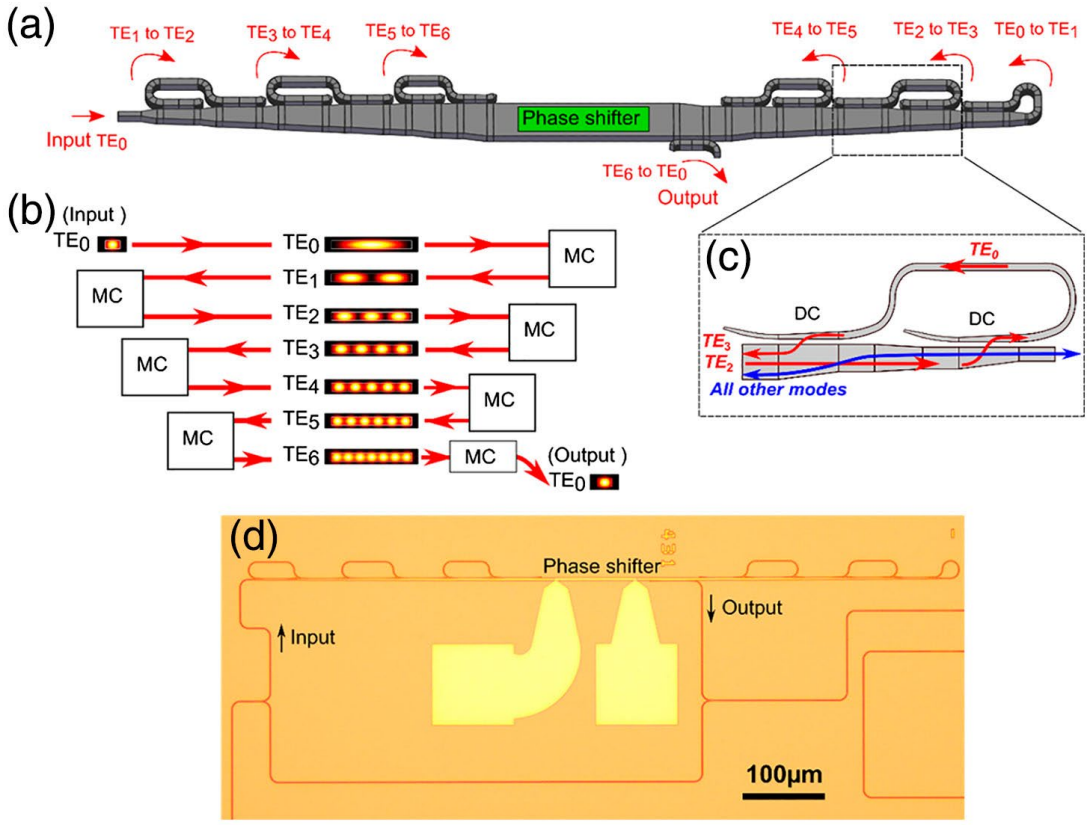

Fig. 3.7. Advanced experimental thermo-optic phase device using a multi-pass photonic structure based on mode multiplexing with a metallic heater [17]. **(a)** Sketch of a seven-pass structure that employs seven optical modes. **(b)** Illustration of the mode conversion at each pass. **(c)** Zoom-in of the structure that selects only the TE_2 mode and converts it to the TE_3 mode and reverses the propagation direction. **(d)** Optical micrograph of a seven-pass multi-pass structure embedded in an MZI. The metallic heater is on top of the wide part of the multi-pass structure. Between the waveguide and the heater, there is a 1-μm-thick SiO_2 layer.

10 dB has been demonstrated in less than 500 ps (see Fig. 3.8b) using light pulses energies as low as 25 pJ [30]. The effective index change under such pulses was -4.8×10^{-4}, which is equivalent to a refractive index change in the silicon core of -5.2×10^{-4}. This refractive index change is caused by a free-carrier concentration of 1.6×10^{17} cm^{-3}. Even lower switching times and energies can be attained by significantly increasing the light confinement by employing a photonic crystal

nanocavity [292] (see Fig. 3.8c). In this regard, a switch-on time as low as 17 ps has been demonstrated thanks to the ultra-fast TPA process. In contrast, a slower recovery time of ~ 200 ps is obtained and is determined by the relaxation time of TPA-generated carriers. Additionally, switching can be achieved using energies as low as 100 fJ approx.

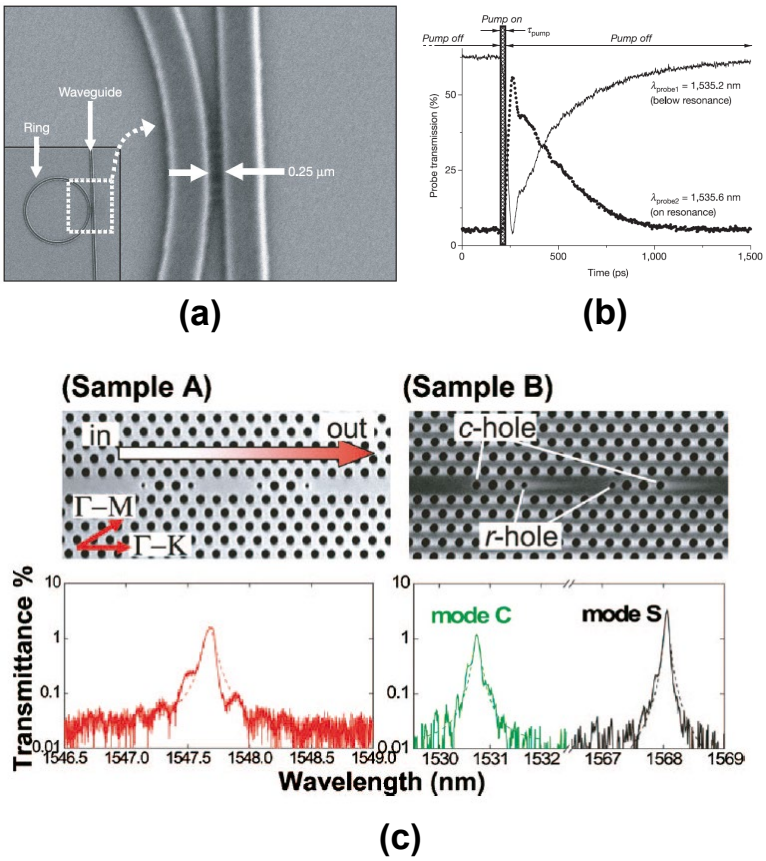

Fig. 3.8. **(a)** Scanning electron micrograph of a microring resonator used for all-optical switching, and **(b)** its temporal response under a pump signal excitation [30]. **(c)** Scanning electron micrographs and transmission spectra of photonic crystal nanocavities employed for all-optical switching [292].

The thermo-optic effect can also be leveraged to create all-optical integrated phase shifters. Heat can also turn up from optical absorption according to the radiative transport equation (RTE) and following the energy conservation law [293]. In such a case, the heat source corresponds to the energy deposited by the incident beam, i.e., $Q \propto \kappa I$, where κ is the absorption coefficient of the absorbing medium, and I the optical intensity impinging on it. Particularly, in an integrated

waveguide, κ and I correspond to the effective extinction coefficient, κ_{eff}, and the input power of the waveguide, P_{in}, respectively. Since a straight silicon waveguide is transparent at telecom wavelengths without nonlinear contributions, an efficient light-to-heat conversion requires including a lossy material in the waveguide. Thus, the higher the optical absorption, the more efficient will be the light-to-heat conversion.

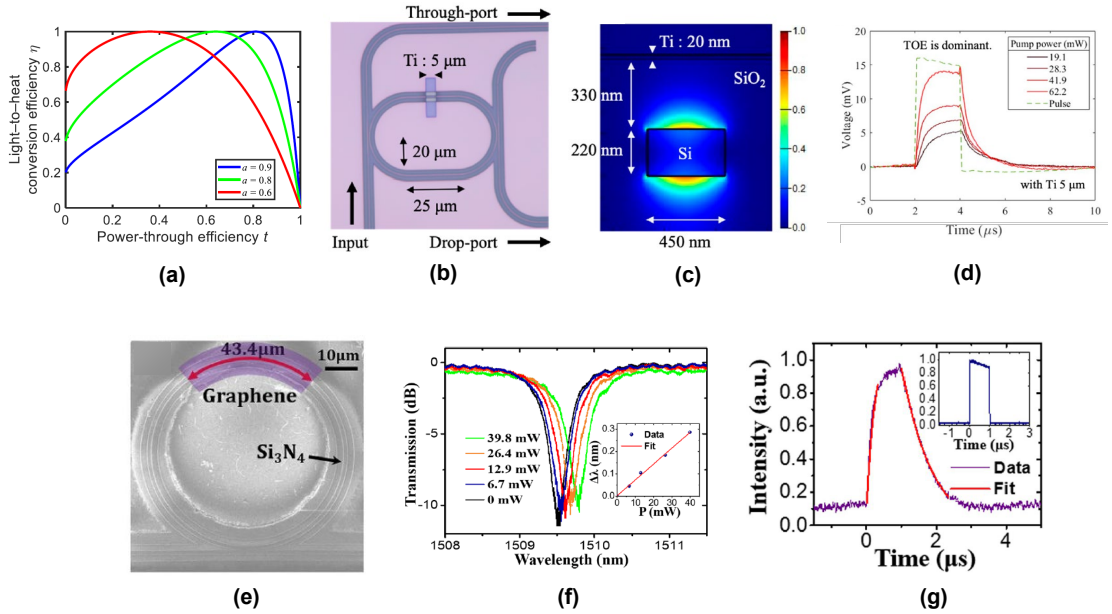

Fig. 3.9. **(a)** Light-to-heat conversion efficiencies of an all-pass MRR as a function of the self-coupling coefficient or power-through efficiency [294]. **(b)** Optical micrograph of an add-drop MRR with a 5-μm-long on top used for thermo-optic all-optical switching [295]. **(c)** Cross-section with the optical mode and **(d)** temporal response of the add-drop MRR. Scanning microscope micrograph of an all-pass SiN MRR with a graphene sheet directly on top of the waveguide for thermo-optic switching using an optical excitation [296]. **(f)** Spectrum response of the SiN MRR under a continuous-waveguide signal with different powers. **(g)** Temporal response of the SiN MRR when the probe signal is biased in a minimum of the device spectrum.

The most straightforward to achieve an optical heater is to use the same lossy metals as in electric thermo-optic phase shifters. However, it should be noted that this will give rise to optical loss in the phase shifter. To circumvent such a problem, the optical heater can be incorporated into an MRR to harness the recirculat-

ing light flow under the critical coupling condition (see Fig. 3.9a) [294]. Recently, an all-optical switching exploiting this concept has been reported [295]. The device is based on a silicon add-drop MRR resonator working for TM polarization with a 5-μm-long Ti patch on top (see Fig. 3.9b). The Ti layer is 20 nm thick. Between the silicon waveguide and the Ti patch, there is a 330-nm-thick SiO_2 layer (see Fig. 3.9c). The experimental propagation loss was 0.29 dB/μm. Notice that the maximum achievable light-to-heat efficiency conversion under the add-drop configuration is 0.5. Based on the modulation efficiency (0.04 nm/mW) and the FSR (∼ 2.5 nm), we estimate the power consumption of around 60 mW to achieve a phase shift of π. On the other hand, the switching times was around ∼ 1 μs (see Fig. 3.9d).

Two-dimensional materials such as graphene have also been employed for thermo-optic all-optical fiber and integrated devices [297]. Concerning integrated devices, all-optical phase control has been reported in SiN waveguides with graphene [296]. The device comprised a SiN MRR with a graphene sheet on top, acting as the optical heater. The length of the graphene heater was ∼ 43.4 μm (see Fig. 3.9e). The device worked for TE polarization. Therefore, part of the light is absorbed by the graphene monolayer and converted to heat. The heat is transferred by conduction directly to the SiN waveguide. The power consumption of the device was high (∼ 340 mW) and caused by the low tuning efficiency (0.00258π/mW) (see Fig. 3.9f). We attribute such poor values to the low thermo-optic coefficient of SiN and the moderate absorption of the hybrid waveguide (0.113 dB/μm). The switching time was characterized by setting the probe signal at a minimum of the spectrum. Upon a pump pulse, the SiN is heated, increasing the effective refractive index. Thereby, the spectrum of the ring is shifted, and the probe signal goes to a maximum. The rising and falling time constants were 253 ns and 888 ns, respectively (see Fig. 3.9g). The difference between both values is attributed to the nonlinear response of the ring [298].

Finally, it should be highlighted that although all the reviewed all-optical phase shifters can achieve a π phase shift, they employ an optical cavity to enhance the light-to-heat conversion efficiency and thus have limited bandwidth. Therefore, no all-optical phase shifters being at the same time broadband and power-efficient have been reported to the best of our knowledge.

3.2 Ultra-low loss hybrid ITO/Si thermo-optic phase shifter with optimized power consumption

In this section, we design and fabricate transparent ITO heaters for high-performance electro-optic phase tuning of silicon photonic structures. The ultra-low loss ITO heater is compared with a titanium-based one for different cladding configurations. The influence of the spacer between the waveguide and the microheater is analyzed. Additionally, the advantages of ITO against Ti are shown for TE and TM polarizations. Finally, ITO heaters are fabricated for a fully surrounded SiO_2 configuration and characterized for both polarizations using the optimal gaps found in the design section. The main results of this section correspond to [Paper D].

3.2.1 Design methodology

The heater/Si waveguide configuration that we use in this work is depicted in Fig. 3.10a. The heater is placed on top of the silicon waveguide in order to induce a phase shift from the combination of Joule heating and the silicon thermo-optic coefficient. Because heaters are usually lossy, an upper cladding is used to isolate the heater and the silicon waveguide optically (see Fig. 3.10b). However, large spacers may imply a downturn in the phase shifter performance, such as the power consumption and/or the switching speed.

As discussed in subsection 3.1.2, the performance of the phase shifter does not depend on the heater length. The heater length, L_h, neglects when both heat ($\Delta\phi \propto \Delta n_{eff} \propto \Delta T \propto 1/L_h$) and optical phase shift ($\Delta\phi \propto L_h$) equations are combined. Hence, the same phase shift is induced for a given power consumption regardless of the heater length [227]. Therefore, two strategies can be followed by either inducing a large change in the effective refractive index with a short heater and high temperatures or a low change using a long heater and low temperatures. By assuming the steady-state ($\partial T/\partial t = 0$), the power consumption can be reduced either by diminishing the thermal conductivity of the cladding, for instance, by using air trenches [217], or by narrowing and thinning the heater. However, both approaches have trade-offs. On one hand, reducing thermal conductivity can improve power consumption by orders of magnitude, but switching times usually worsen to the same degree. On the other hand, reducing the

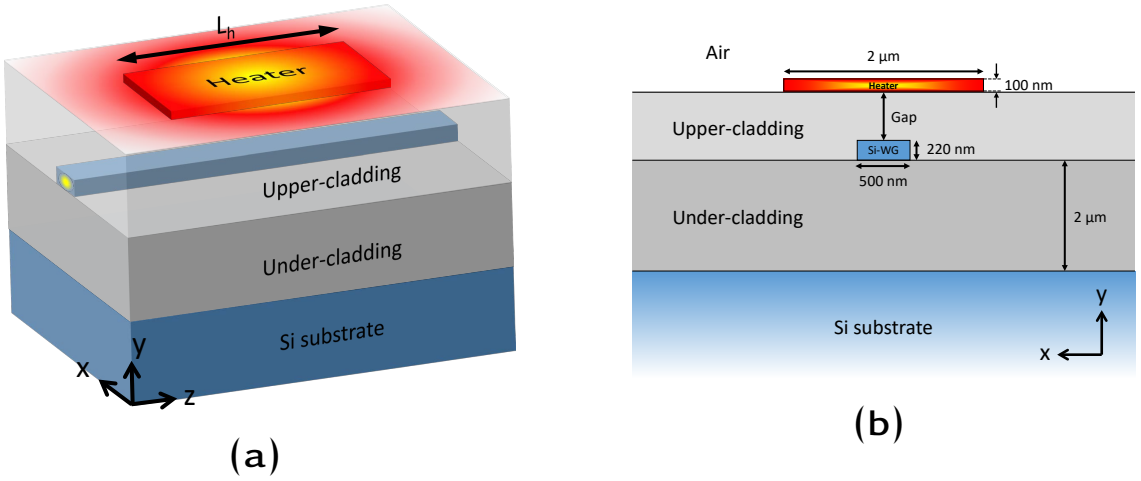

Fig. 3.10. **(a)** 3D view schematic and **(b)** cross-section of the analyzed heater/Si waveguide configuration.

heater cross-section may have some issues. A small cross-section will raise the current concentration and could melt the heater. Moreover, the driving voltage will also be higher, and a more stringent alignment will be required if the heater is narrowed to the same order as the waveguide width. Concerning the thickness, making homogeneous and high-quality thin films becomes hard for thicknesses lower than 100 nm. Consequently, in this work, the heater width and thickness are set to 2 µm and 100 nm, respectively.

In contrast to metals, in which both optical and electrical properties cannot be tuned, ITO has the advantage of tuning them during the fabrication steps such as deposition or post-annealing [50, 53, 299]. Figure 3.11 plots both permittivity (λ = 1550 nm) and resistivity of ITO as a function of the free carrier concentration. On one hand, a low-doped ITO ($N = 10^{19}$ cm^{-3}) provides both high-transparency ($\varepsilon'' \approx 0$) and high-resistivity properties. Below this value, ITO behaves as a Mott insulator and is no longer conducting [300]. On the other hand, the light-matter interaction is enhanced in the ENZ regime ($N = 6.5\times10^{20}$ cm^{-3}), where $\varepsilon' = 0$, $\varepsilon'' > 0$ and $|\varepsilon|$ achieves its minimum value ($|\varepsilon| = 0.57$). As a result, optical losses may be drastically increased, and thus, the transparency condition is lost.

Therefore, an ITO free carrier concentration of 10^{19} cm^{-3} is chosen, which provides a refractive index of $1.958 + j2.3\times10^{-3}$ and a resistivity of 2.24×10^{-2} Ω cm. Heat and optical properties used for simulations are summarized in Ap-

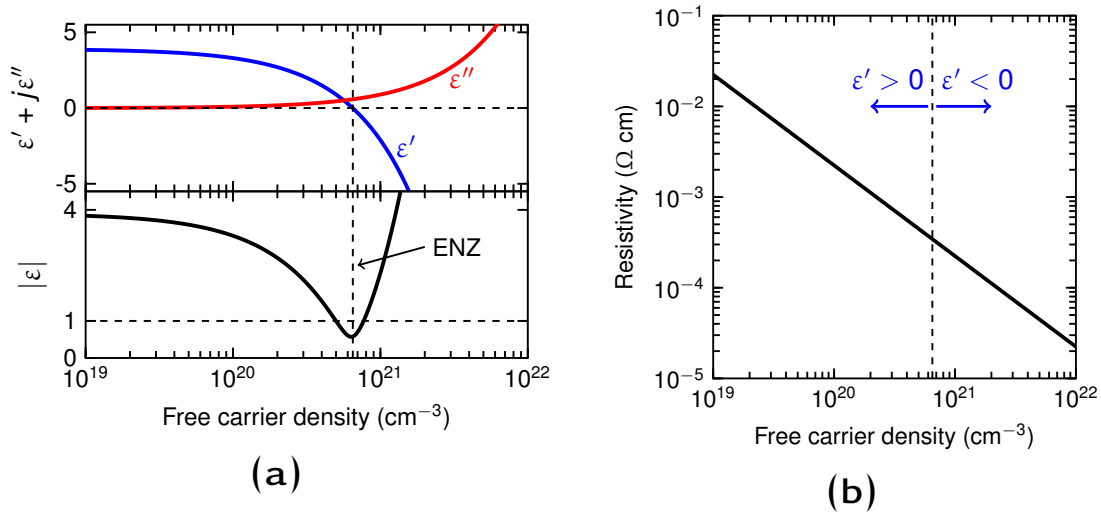

Fig. 3.11. **(a)** ITO permittivity and **(b)** resistivity as a function of the free carrier concentration. Permittivity is obtained by using the Drude model at $\lambda = 1550$ nm. Drude parameters are: $\varepsilon_\infty = 3.9$, $\Gamma = 1.8 \times 10^{14}$ rad/s and $m^*/m_e = 0.35$ [208].

pendix A.1.1. It is worth mentioning that the imaginary part of the ITO refractive index is almost three orders of magnitude lower than Ti. This difference enables an ultra-low loss heater, which could be exploited to reduce the spacer with the silicon waveguide and, thus, improve the performance of the phase shifter.

3.2.2 Influence of the spacer on the power consumption and switching speed

The influence of the gap for different under- and upper-claddings is hereinafter analyzed, comparing both Ti and ITO heaters. In this work, low and high thermal conductive materials such as SiO_2 and SiN are chosen for the claddings. Temperature distribution and optical modes for TE and TM polarization are obtained by using the finite element method. Details on optical and thermal simulations can be found in Appendices A.1.2 and A.1.3, respectively.

The temperature distribution for the cross-section of the phase shifter in the steady-state and different under- and upper-cladding configurations is shown in Fig. 3.12. The gap between the heater and the waveguide is 1 µm, and the heater temperature is set to the same temperature for all the cases. It is worth mentioning that the value of the heater's thermal conductivity has little impact on the

overall system.

When both claddings have the same thermal conductivity (see Figs. 3.12a and 3.12c), heat spreads across the claddings with negligible difference. However, for the SiN/SiO_2 configuration (see Fig. 3.12b), the SiO_2 under-cladding acts as a thermal wall for the SiN upper-cladding. Hence, heat distribution is almost constant and more homogeneous in the upper cladding for both y- and x-axis. Nonetheless, all configurations are robust to heater misalignment of several hundred nanometers.

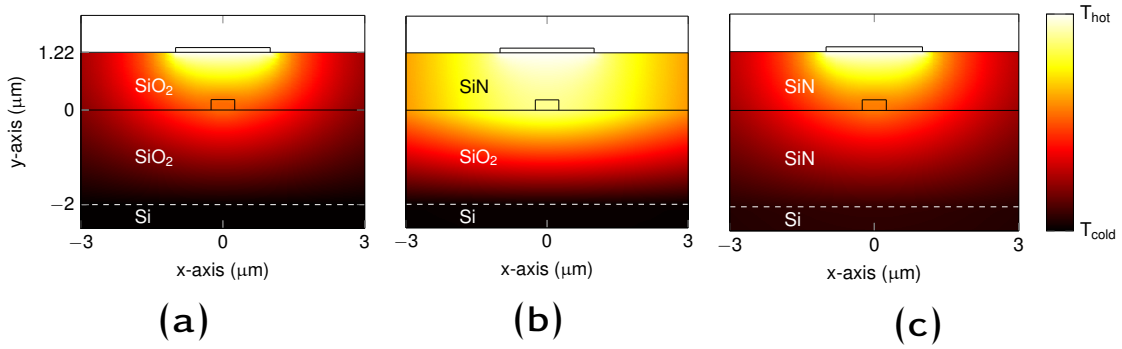

Fig. 3.12. Normalized steady-state temperature distribution for different upper- and under-claddings. **(a)** SiO_2/SiO_2, **(b)** SiN/SiO_2 and **(c)** SiN/SiN.

Then, we investigate the power consumption needed to achieve a phase shift of π rad (P_π). Fig. 3.13a shows P_π as a function of the gap for the different cladding configurations, heaters, and TM polarization. Differences between Ti- and ITO-based heaters are negligible for gaps larger than 500 nm. Below this value, hybrid-plasmonic modes begin to form for the Ti heater configuration, whereas the ITO heater remains photonic. For the SiN/SiO_2 claddings, the difference is more pronounced because of the asymmetric cladding. This behavior is depicted in Fig. 3.13b, where optical modes for a gap of 200 and 500 nm are compared for both heaters. When the spacer between the heater and the waveguide is sufficiently large (500 nm), a photonic mode is excited in both cases. However, if both structures are close enough (200 nm), a hybrid plasmonic mode is formed between the silicon waveguide and the Ti heater. Conversely, for the ITO heater, the optical mode remains photonic because ITO is optically dielectric. In the absence of a gap, a plasmonic mode is obtained for the Ti heater since the mode is confined at the Si/Ti interface, whereas the ITO heater remains guided within the silicon waveguide. This optical deconfinement from the silicon when the Ti

is used as a heater increases power consumption.

For TE polarization, power consumption ranges between 8-11 mW (SiO_2/SiO_2), 19-32 mW (SiN/SiO_2) and 120-165 mW (SiN/SiN) with a linear relation with the gap for all cladding configurations. The SiO_2/SiO_2 configuration remains the lowest power consumption, and dependence on the gap is also reduced. Moreover, P_π is smaller regardless of the configuration with respect to TM polarization because of the higher confinement of light in the silicon waveguide.

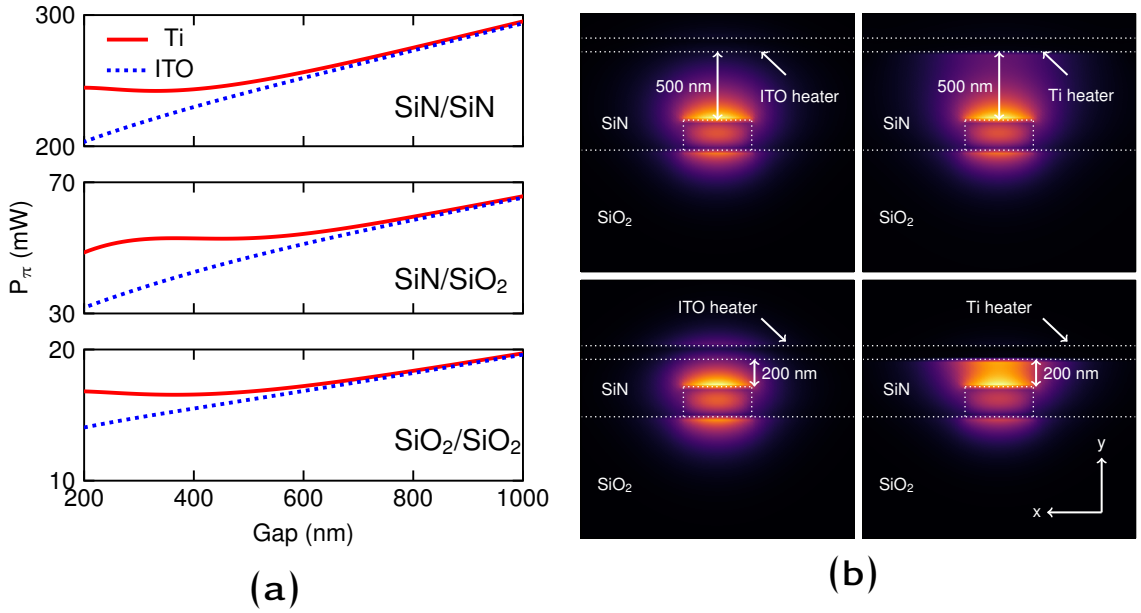

Fig. 3.13. **(a)** Power consumption (TM polarization) to achieve a phase shift of π rad (P_π) as a function of the gap for Ti (solid lines) and ITO (dashed lines) heaters and different under-/upper-cladding configuration: SiO_2/SiO_2, SiN/SiO_2 and SiN/SiN. **(b)** Mode profile ($|E_y|$) comparison between ITO and Ti heater for the SiN/SiO_2 configuration and gaps of 200 and 500 nm. Results are obtained at $\lambda = 1550$ nm.

Although a Si waveguide fully surrounded by SiO_2 provides the lowest power consumption, the low thermal conductivity of SiO_2 could be a switching speed drawback. The switching speed τ is evaluated by calculating the temporal response of the phase shifter when applying a step electrical signal to the heater. In the present work, τ is defined as the time difference between the amplitude from 10% ($\tau_{10\%}$) to 90% ($\tau_{90\%}$). Maximum switching speed can be calculated by obtaining either the rise or fall time of the phase shifter temporal response.

Fig. 3.14 shows the switching speed for the different cladding configurations. A SiN upper-cladding results in an independent behavior of the rise/fall times with the gap because of the SiN's high thermal conductivity. Moreover, the switching speed can be improved below the microsecond by using a complete SiN cladding and avoiding the SiO_2 thermal wall. Conversely, a full SiO_2 cladding shows a high dependence on the switching speed with the gap because of the low thermal conductivity of the SiO_2 upper cladding. Despite this, a full SiO_2 cladding is preferred due to the much lower power consumption, as shown in Fig. 3.13a. Moreover, low values of switching speed could also be attained if the gap is small enough, though optical losses induced by the heater impose a trade-off.

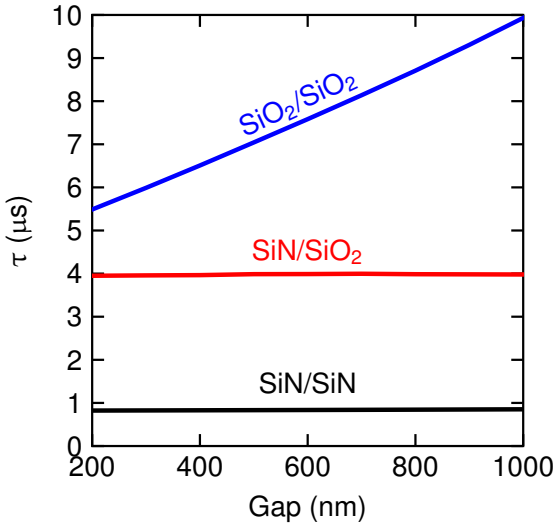

Fig. 3.14. Switching time as a function of the gap for the different under- and upper-claddings.

The minimum attainable gap is then imposed by the coupling losses that arise from the possible mismatch between the silicon waveguide and the phase shifter. Fig. 3.15a shows the total (input + output) coupling losses as a function of the gap for both polarizations and heaters. Coupling losses are obtained as the overlap of the optical modes with and without a heater. For TE polarization, gaps greater than 200 nm suffice for both materials ensuring coupling losses below 0.01 dB. Conversely, the minimum gap for TM polarization needs to be increased up to 330 nm (ITO) and 630 nm (Ti).

On the other hand, the heater length for a given gap is constrained between

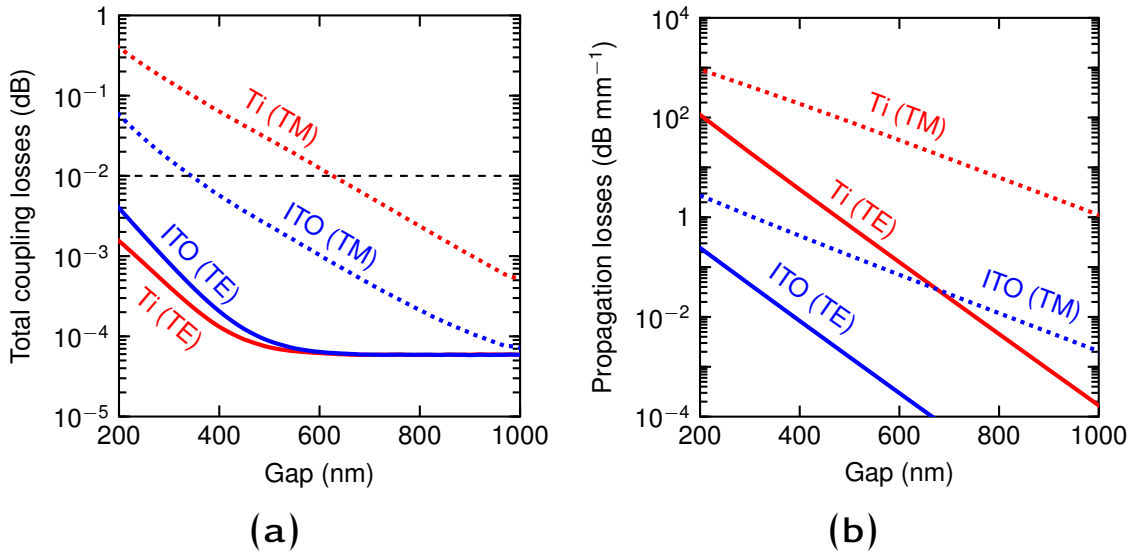

Fig. 3.15. **(a)** Coupling and **(b)** propagation losses as a function of the gap for a full SiO_2 cladding and for Ti and ITO heaters. Dashed line in **(a)** stands for the loss limit of 0.01 dB.

an under and upper limit. The first is associated with the maximum thermal cross-talk allowed between adjacent silicon structures, whereas the propagation losses determine the maximum length (see Fig. 3.15b). In this work, the thermal cross-talk is set by fixing the maximum heater temperature at 100 °C [298]. Table 3.6 summarizes the best results achieved for ensuring insertion losses below 0.01 dB. Such low insertion losses are mandatory to allow massive integration of phase shifters. The optimization of the phase shifter parameters was carried out to achieve the best performance and meet both optical and thermal requirements by minimizing the gap. It can be seen that smaller gaps can be achieved for ITO because propagation losses are three orders of magnitude lower than Ti, as depicted in Fig. 3.15b. Therefore, such smaller gaps benefit the power consumption and switching time of the phase shifter.

3.2.3 Experimental results

Fig. 3.16a shows an optical image of the fabricated structures used to validate the performance of the proposed hybrid ITO/Si phase shifter. The light was coupled to/from the optical fibers using grating couplers for TE and TM polarization. Asymmetric MZIs were used to extract the phase shift induced by the hybrid

Table 3.6: Main results of ITO and Ti heaters to obtain less than 0.01 dB of insertion losses for the SiO_2/SiO_2 cladding configuration.

	Polarization	Gap (nm)	P_π (mW)	τ (µs)	L_h (µm)
ITO	TE	320	8.5	6.1	70
ITO	TM	660	17.2	7.9	145
Ti	TE	700	9.9	8.1	85
Ti	TM	1500	23.1	13.3	225

ITO/Si waveguide. Moreover, 50 µm and 150 µm long ITO heaters were tested in order to investigate the influence of the heater length. Finally, ITO pads were also used to connect the heater to the electrical probes.

We fabricated optimal MZI/Si phase shifters on asymmetric Mach-Zehnder Interferometers to determine the power consumption and the switching speed of the phase shifter. Fabrication methods can be found in Appendix A.2. The experimental optical losses of the ITO/Si phase shifter were negligible in agreement with simulations (< 0.01 dB). Figure 3.17a shows the normalized measured spectrum of the TE MZI with 50 µm long heaters on-top for zero power consumption and P_π. During measurements, sharp resonances with extinction ratios larger than 20 dB were achieved, which allowed us to estimate the power consumption accurately.

Fig. 3.17b depicts the experimental phase shift $\Delta\phi$ as a function of the power consumption of the 150 µm long heater for TE and TM polarization. The P_π is then obtained by linearly fitting the experimental results. For both polarizations, the resulting experimental P_π is in very good agreement with simulations. TE polarization shows P_π = 9.7 mW, whereas for TM a P_π of 20.2 mW is obtained.

The influence of the heater length on the power consumption for TE polarization is shown in Fig. 3.17c. The same behavior was achieved for TM polarization. As it can be noticed, the influence of the heater length is negligible on the value of the P_π. The small differences between both heaters are attributed to the lower relation between the heater and pad resistance for the shortest heater, which leads to some power dissipation on the pads. Thus, the utilization of a shorter heater would permit to increase in the density of phase shifters in a PIC. On the other hand, the driving voltage is reduced, going from 14.5 V (150 µm) to

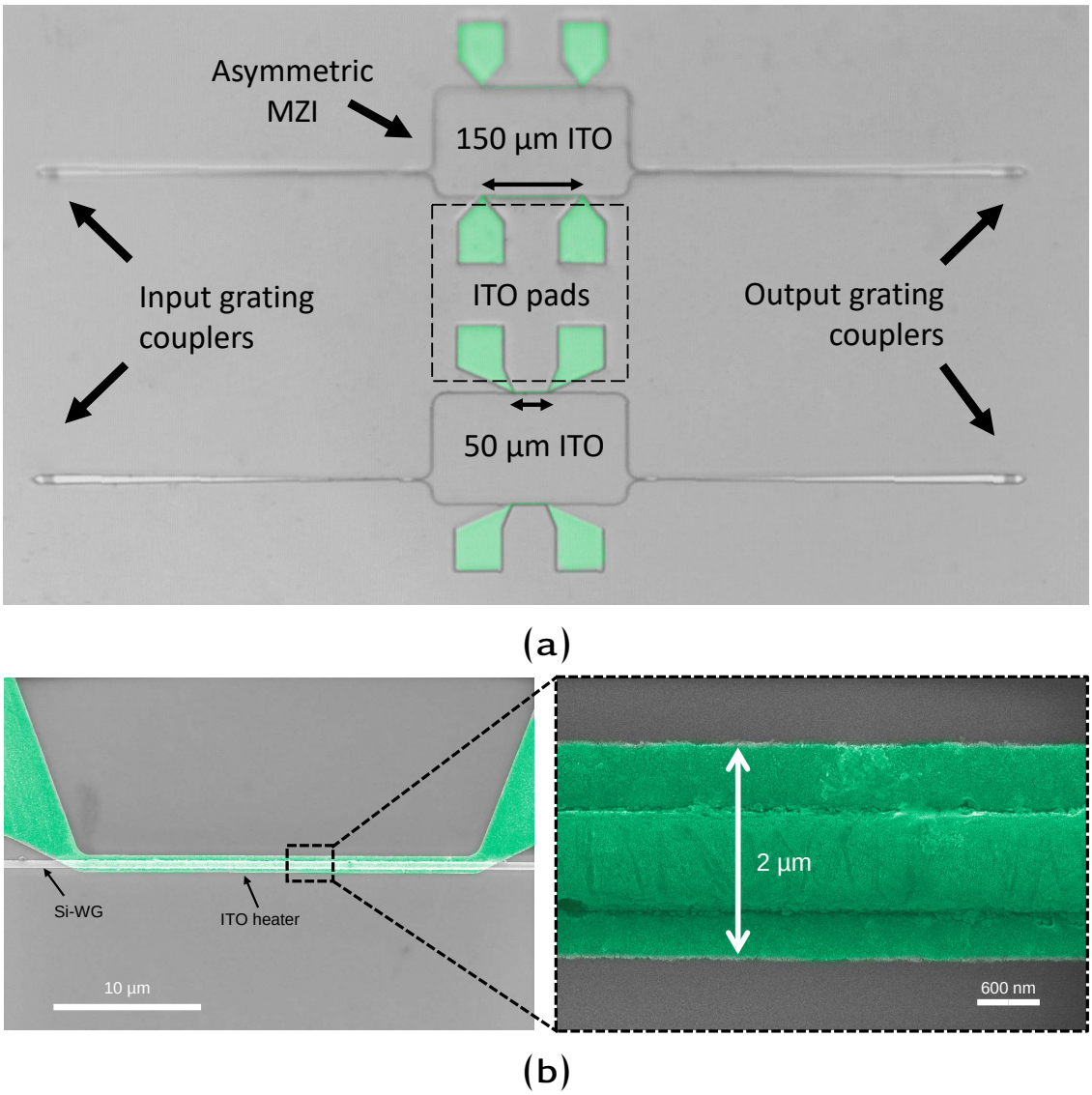

Fig. 3.16. **(a)** Optical image of the fabricated MZIs with ITO heaters on top. **(b)** False-color SEM images of the ITO/Si thermo-optic phase shifter structure. The silicon waveguide looks wider than 500 nm caused by the conformal PECVD deposition of the SiO_2 upper-cladding.

.

9.1 V (50 µm).

The switching times of the phase shifter were obtained by biasing the MZI in the linear region. Figure 3.18a depicts the recorded rise and fall times (312 nm upper-cladding) as a function of the applied power when a 10 kHz square sig-

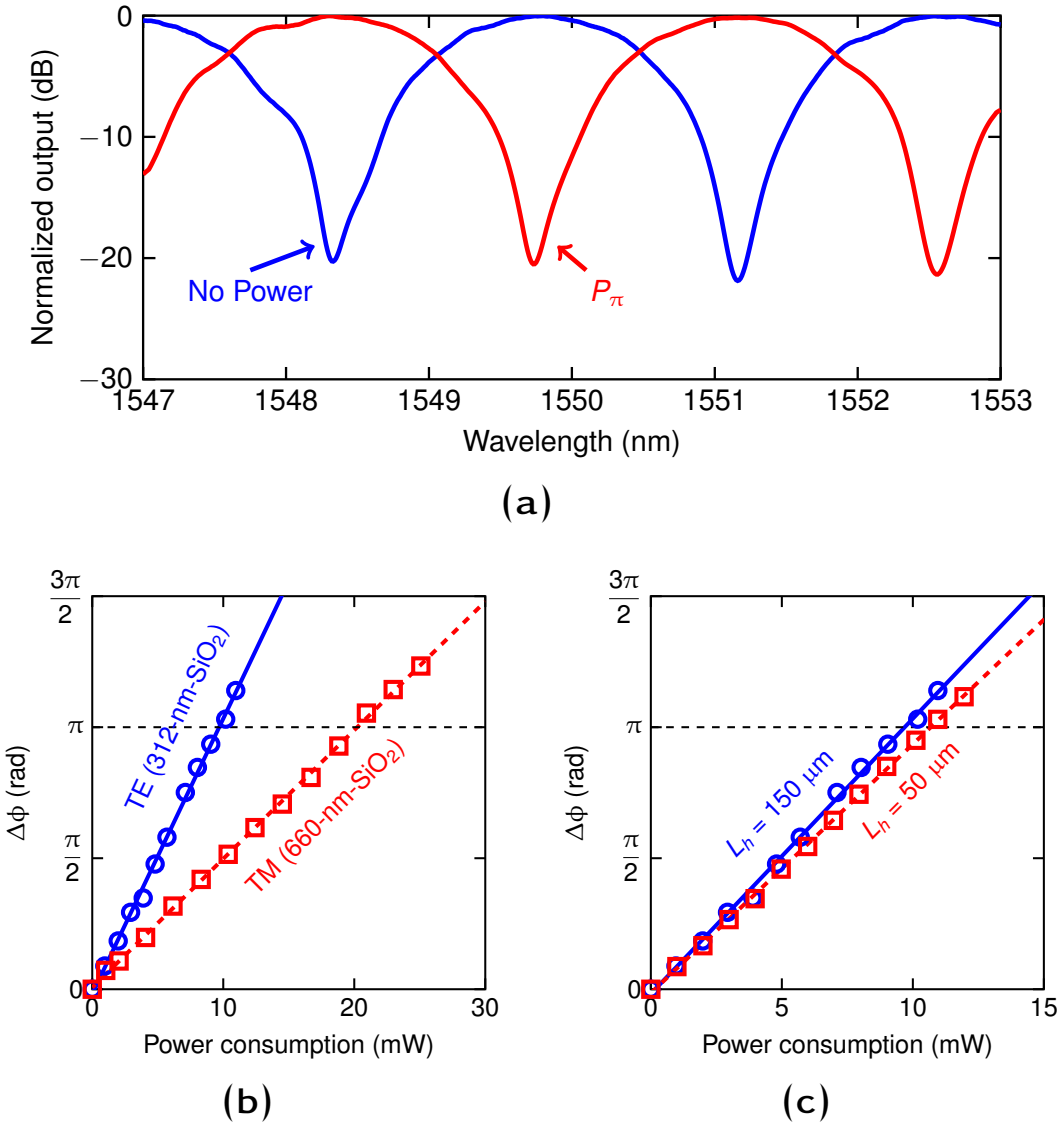

Fig. 3.17. **(a)** Normalized measured spectrum of the TE MZI with 50 μm long ITO heaters on-top for zero and P_π power applied to the heater on the long arm. Phase shift as a function of the ITO heater power consumption. **(b)** TE and TM polarization for a 150 μm long ITO heater. **(c)** TE polarization for a 150 μm and 50 μm long ITO heater.

nal was applied. For the 312-nm-thick upper-cladding (TE), a switching time of 5.2 μs was obtained, whereas the 660-nm-thick one (TM) was 6.8 μs. These differences between switching times are due to the different gap values (see Fig. 3.14) and are in good agreement with the values obtained in the simulation. For

small peak powers, both rise and fall times are equal in agreement with the heating/cooling behavior of a thermo-optic phase shifter. However, as the applied power is increased, the nonlinear regions of the MZI optical response affect the switching times [298]. Hence, both times diverge, and the resulting speed does not correspond to the hybrid ITO/Si phase shifter but to the entire MZI switching device. This effect can be seen in Figs. 3.18b and 3.18c. In the first case, a small amount of electrical power is applied, and thus, the MZI swings in the linear region leading to the equal rise and fall times. However, in Fig. 3.18c, the peak power falls within the nonlinear region of the MZI. Consequently, both rise and fall times do not correspond only to the phase shifter but the combinations of the nonlinear response of the MZI with the phase shifter.

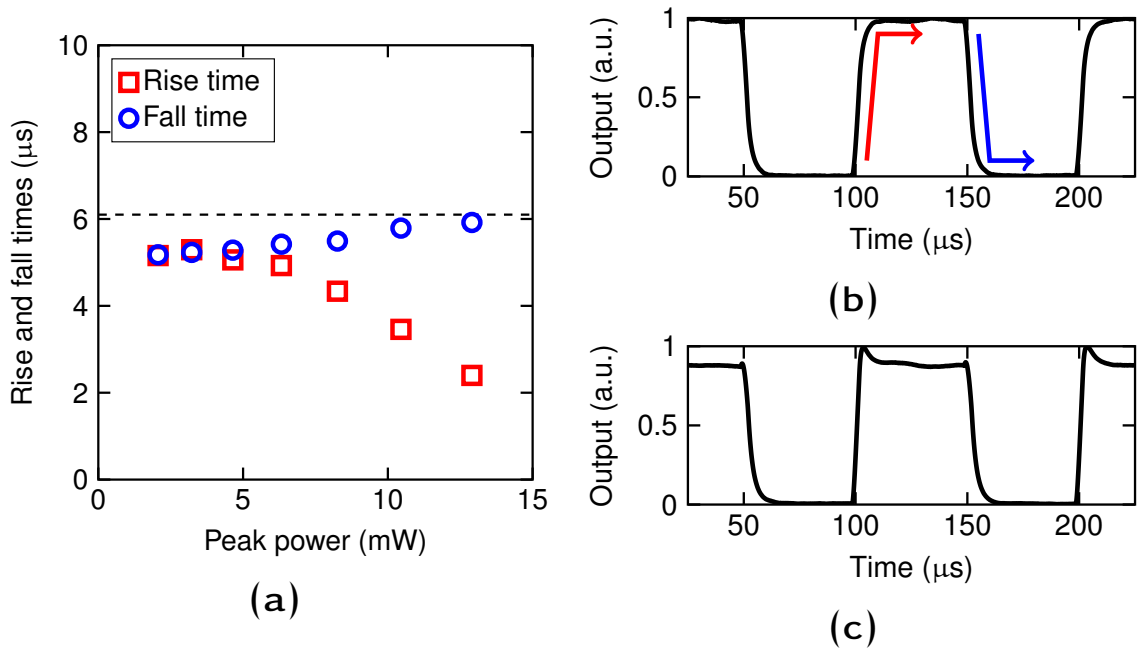

Fig. 3.18. **(a)** Recorded rise and fall times when a 10 kHz square signal is applied to the heater as a function of peak power applied to the heater. The dashed line stands for the simulation value. Normalized temporal response when **(a)** 4 mW and **(b)** 13 mW of peak power is applied to the heater. Measurements correspond for TE polarization and a 50 μm long ITO heater.

3.3 All-optical phase control in nanophotonic silicon waveguides with epsilon-near-zero nanoheaters

In this section, we investigate the utilization of an ENZ material to enable all-optical phase control in nanophotonic silicon waveguides. A phase shift for TE polarization is induced by exploiting the silicon thermo-optic coefficient. Such phase shift is optically controlled by means of a cross-polarized TM signal. The heat originates from a thin layer of ENZ material deposited on top of the waveguide, acting as an optical heat source. The pass polarizer behavior of the hybrid ENZ/Si waveguide provides low optical loss for TE phase-shifted signal but efficient optical-heat conversion for the TM one. The main results of this section correspond to [Paper E].

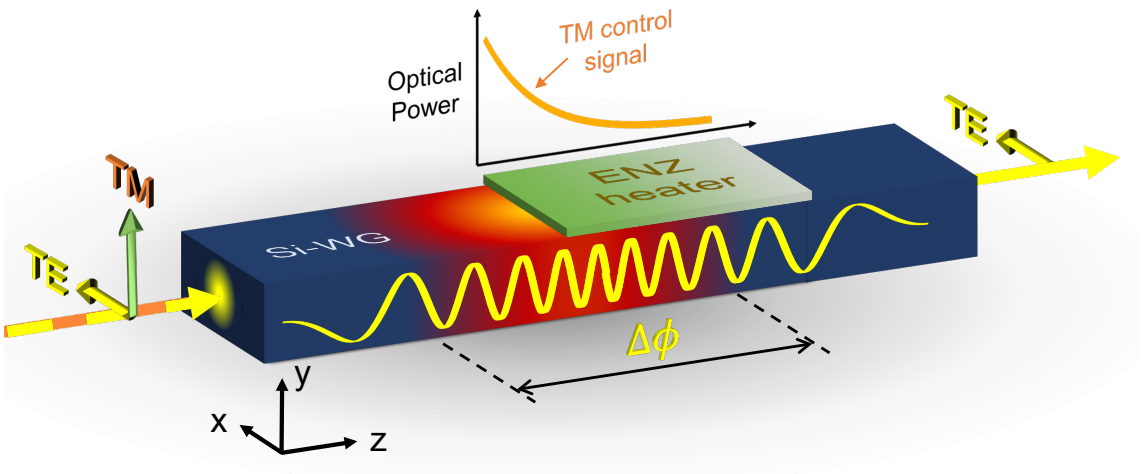

Fig. 3.19. Illustration of the proposed all-optical phase shifter. The optical heater is an ENZ material that heats up due to the absorbed optical power of the TM polarized mode. The phase shift is induced for TE polarization by exploiting the silicon thermo-optic coefficient and leads to low optical loss due to the pass polarizer operation of the hybrid waveguide section.

3.3.1 Working principle

Figure 3.19 shows a schematic of the proposed all-optical phase shifter. Here, the key challenge to achieving low optical loss for the phase-shifted mode in combination with a highly efficient optic-heat conversion would be to link the optical loss mainly to polarization and not to the intrinsic absorption of the heater. A polarization-dependent loss operation could be achieved by reducing the intrinsic loss of the heater and obtaining a strong LMI for TM polarization but weak for TE polarization. Such behavior can be reached by using a heater based on an ENZ material ($\varepsilon' = 0$) with relatively low optical loss, ε''. In that case, the difference in terms of LMI between both polarizations will be determined by the boundary conditions. For TM polarization, the major component of the electric field, E_y, is oriented normally to the interface between the ENZ heater and the silicon waveguide. Thus, giving the continuity of the displacement, the electric field at the interface of the ENZ material is $E_{ENZ} = |\varepsilon_{Si}|/|\varepsilon_{ENZ}|E_{Si}$. Note that, for $\varepsilon'_{ENZ} = 0$ and very low ε'' ($\varepsilon'' < 1$), the value of E_{ENZ} is greatly enhanced, thus giving rise to strong LMI. On the other hand, for TE polarization, most of the electric field, E_x, is tangential to the ENZ/Si interface. Then, the boundary condition for this case is $E_{ENZ} = E_{Si}$. Therefore, there is no electric-field enhancement, and thus, since most of the optical mode is confined within the silicon waveguide, there is a very weak LMI. We design an optimal ENZ layer for such purposes based on these considerations. The considered ENZ/Si waveguide comprises a standard 500 nm × 220 nm nanophotonic waveguide made from silicon-on-insulator (SOI) with a thin ENZ layer on top. We assume that the waveguide is covered with a 1-µm-thick SiO_2 upper-cladding as in typical silicon PICs to protect the environment. The materials properties used for this work can be found in Appendix A.1.1.

3.3.2 Optimal ENZ layer: thickness and loss

The optimal thickness and loss of the ENZ layer are obtained by assessing the figure of merit $FOM = \kappa_{eff}^{TM}/\kappa_{eff}^{TE}$. To this end, we obtained the complex effective index for the TE and TM mode of the hybrid waveguide by 2D FEM simulations (see Appendix A.1.2 for simulation methods details). Fig. 3.20 shows the values for different ε''_{ENZ} and layer thicknesses. For the analysis, the considered fundamental TM mode corresponds to the solution with the highest effective index when the ENZ/Si waveguide supports multiple propagation TM-polarized

modes. For TE polarization, the propagation loss increases with the thickness, and the intrinsic loss of the ENZ material is comparable to lossy dielectrics (Fig. 3.20a). In contrast, for TM polarization, we observe a maximum for the different thicknesses (Fig. 3.20b). This maximum is found in the region of $\varepsilon''_{\mathrm{ENZ}}$ values in which the loss is the result of strong coupling between $\varepsilon''_{\mathrm{ENZ}}$ and LMI since LMI is related to $1/|\varepsilon_{\mathrm{ENZ}}|$. For $\varepsilon''_{\mathrm{ENZ}}$ values beyond the maximum, the LMI reduces more than $\varepsilon''_{\mathrm{ENZ}}$ is increased, resulting in an overall reduction of the optical loss. On the other hand, for values of $\varepsilon''_{\mathrm{ENZ}} > 3$ approx., the intrinsic loss of the ENZ material becomes the dominant factor in the optical loss. As shown in Fig. 3.20c, the best FOM (~ 94) is achieved for $\varepsilon''_{\mathrm{ENZ}} = 0.17$ and 10-nm-thick layer, which corresponds to a propagation loss of 0.041 dB/μm and 3.84 dB/μm for TE and TM modes, respectively. Regarding the impact of the ENZ layer on the optical phase, the real part of the effective index for the TE mode is shown in Fig. 3.20d. The effective index of a silicon waveguide without ENZ material is kept as a reference value. We note that the impact of the ENZ material is very small in a wide range of $\varepsilon''_{\mathrm{ENZ}}$ values and for the different thicknesses due to the weak LMI.

3.3.3 Coupling loss and excitation of higher-order modes

Low-loss coupling between the photonic and ENZ/Si waveguide mode is also highly important to efficiently transform the optical power of the TM polarized signal into heat. We investigate the coupling loss between the silicon and the optimal ENZ/Si waveguide using 3D-FDTD simulations (see Appendix A.1.2 for simulation methods details). High coupling efficiency of $\sim 90\%$ (0.45 dB) was obtained for TM polarization. However, the absorbed power along the propagation direction (Fig. 3.21a) revealed the excitation of two TM modes, hereinafter ENZ modes, because the light is tightly confined in the ENZ layer. For the first mode (ENZ_0), the optical absorption is in good agreement with the propagation loss given in Fig. 3.20b until $z \approx 1.5$ μm. For larger values, the attenuation fits the second ENZ mode (ENZ_1) that features lower propagation loss (1.32 dB/μm). Their complex effective indices are $1.61 + j0.109$ and $1.499 + j0.038$, respectively. The E_y field component of the ENZ_0 mode (Fig. 3.21b) is very similar to the ENZ_1 (Fig. 3.21c), and we attribute this fact the reason to excite both modes in the hybrid waveguide. Despite the large similarity of the E_y, these modes are different as it can be noted by inspecting the E_z component (Figs. 3.21d and 3.21e).

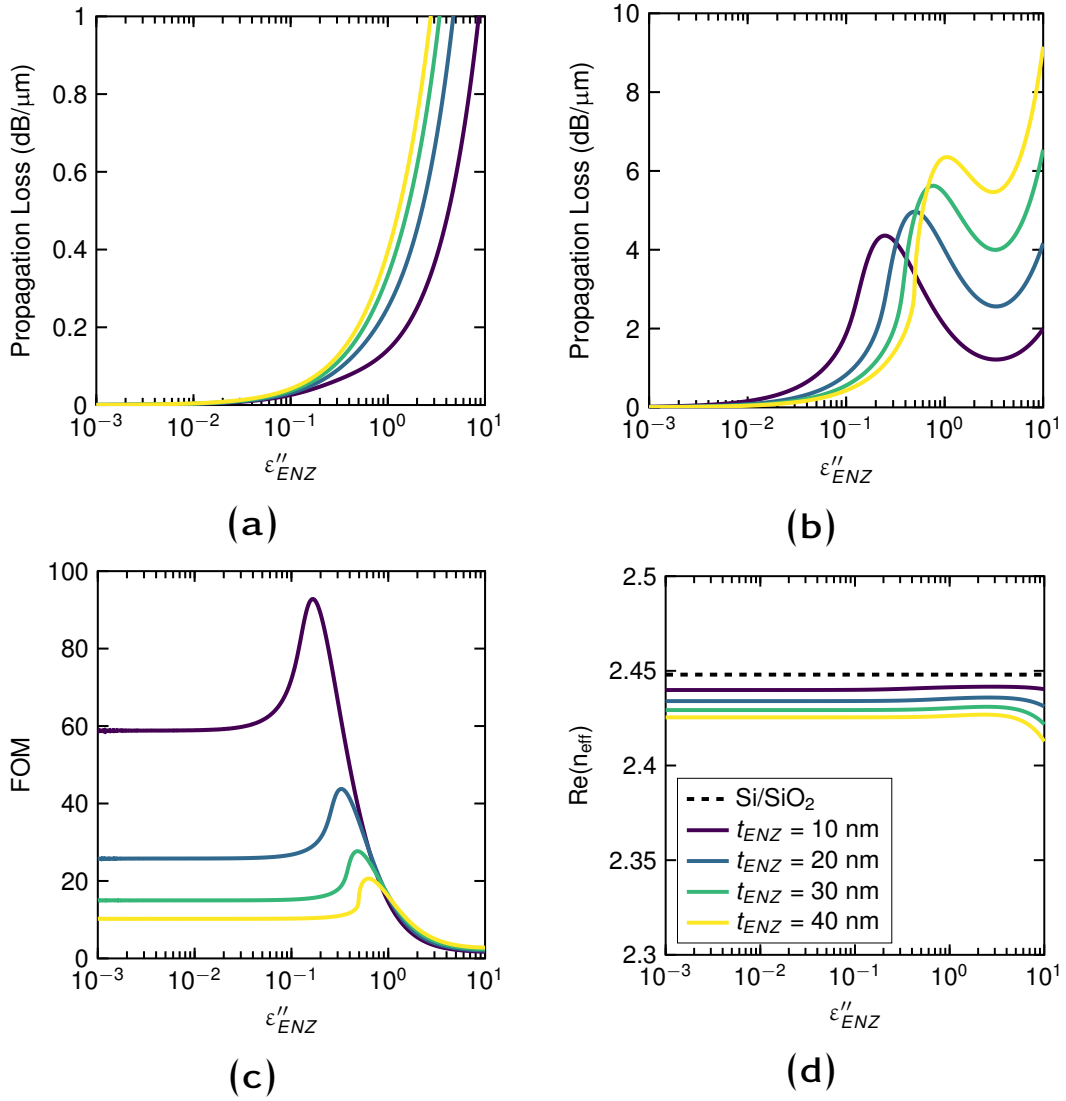

Fig. 3.20. Derived parameters from the complex effective index of TE and TM modes of the hybrid ENZ/Si waveguide as a function of the loss of the ENZ material, $\varepsilon''_{\mathrm{ENZ}}$, and for different ENZ layer thickness, t_{ENZ}. Propagation loss for **(a)** TE and **(b)** TM polarized modes. **(c)** Figure of merit. **(d)** Real part of the effective index for the TE mode. Values are given for $\lambda = 1550$ nm and imposing $\varepsilon'_{\mathrm{ENZ}} = 0$.

On the other hand, the nature of the ENZ modes is attributed to be similar to the so-called short-range surface plasmon-polariton (SR-SPP) waves, which can be found in very thin metallic layers ($\varepsilon' < 0$) surrounded by dielectric materials ($\varepsilon' > 0$) [301].

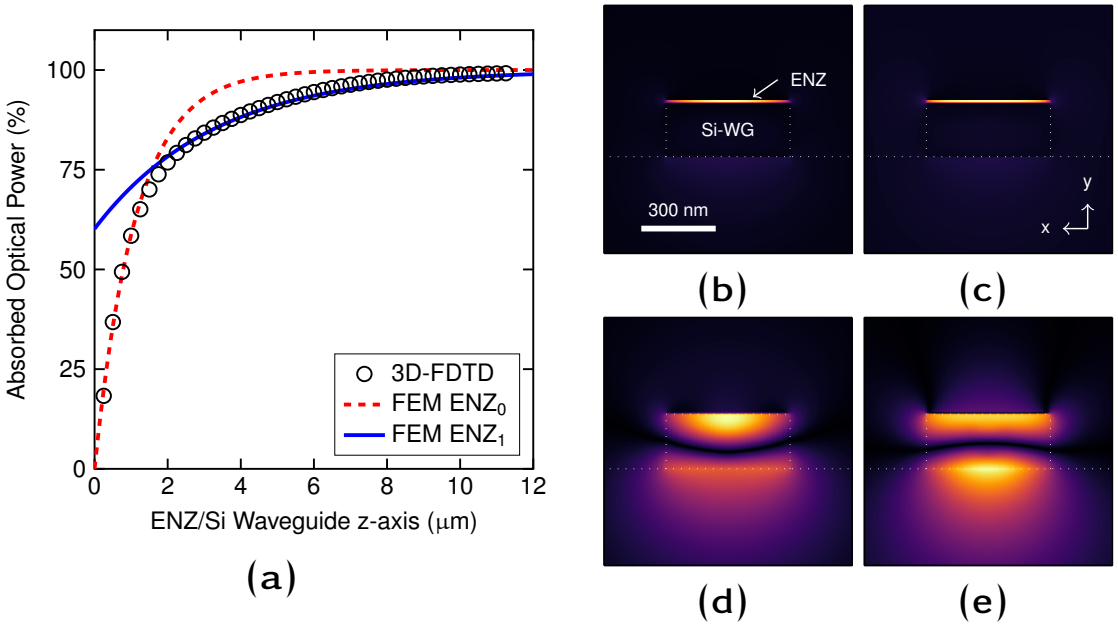

Fig. 3.21. **(a)** Absorbed optical power by the ENZ layer along the ENZ/Si waveguide obtained by 3D-FDTD and fitting with the values of ENZ modes given by FEM. Normalized **(b)** $|E_y|$ and **(d)** $|E_z|$ field components of the ENZ_0 mode. **(c,e)** Same as **(b,d)** but for the ENZ_1 mode. The complex effective index (propagation loss) is $1.61 + j0.109$ (3.84 dB/μm) and $1.499 + j0.038$ (1.32 dB/μm) for the ENZ_0 and ENZ_1 modes, respectively. Simulations were carried out at $\lambda = 1550$ nm and for a 10-nm-thick ENZ layer with $\varepsilon_{ENZ} = j0.17$.

Nevertheless, the impact of the higher-order ENZ mode is small. In order to absorb $\sim 99\%$ of the optical power, only 10 μm of length are required for the ENZ/Si waveguide. The coupling loss for TE polarization was also verified to be negligible by using 3D-FDTD simulations. Additionally, the insertion loss was in good agreement with the propagation loss calculated by FEM. The resulting overall loss for the TE mode is ~ 0.4 dB for such length.

3.3.4 Thermo-optic performance

The thermal response of such ENZ/Si phase shifter was obtained by modeling the ENZ as a heat source and solving the heat conduction equation (see Appendix A.1.3 for simulation methods). On the other hand, the phase shift induced to the optical mode, $\Delta\phi$, due to a temperature increment of the silicon waveguide, ΔT_{Si},

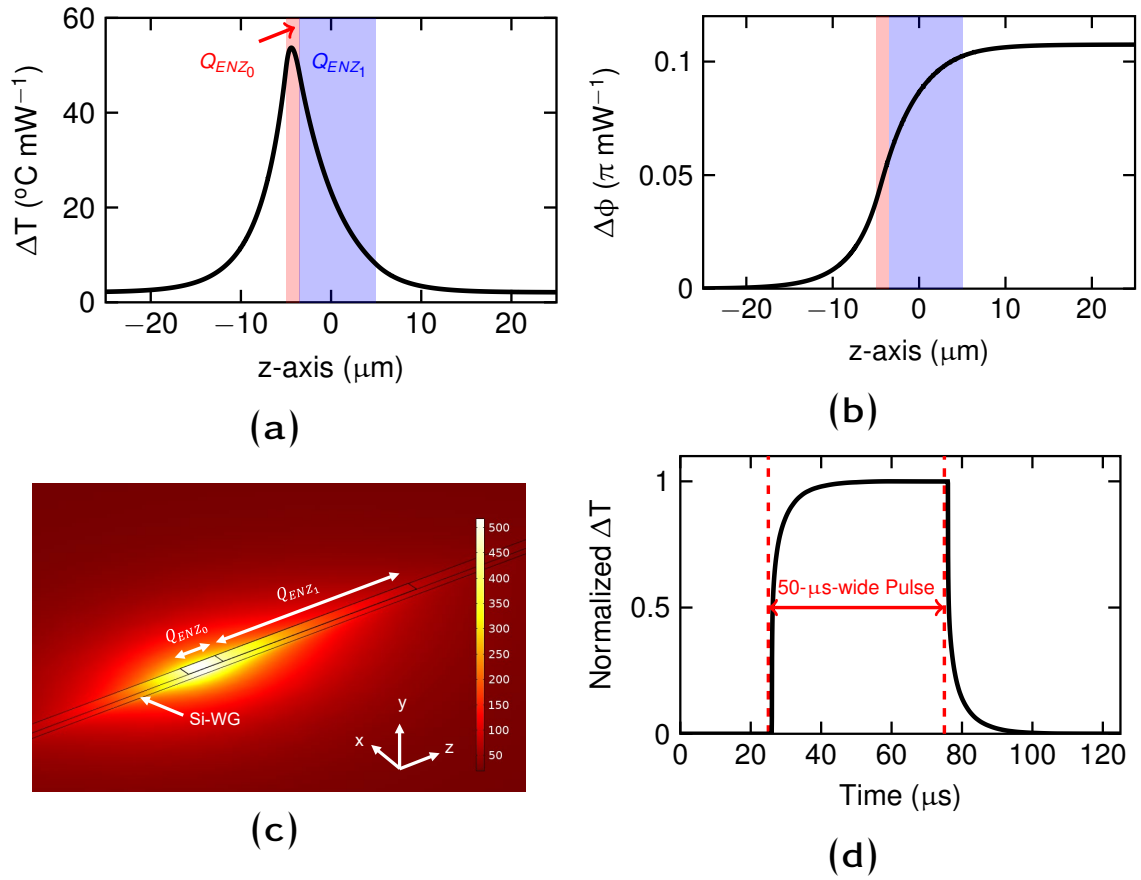

Fig. 3.22. **(a)** Normalized temperature increment in the silicon waveguide, ΔT, and **(b)** phase increment of the TE mode, $\Delta\phi$, along the z-axis (propagation direction). **(c)** Temperature distribution, in °C, for 9.5 mW in the TM polarized signal. The SiO_2 upper-cladding is hidden. **(d)** Time-domain response of the silicon waveguide peak temperature upon a 50-μs-wide square pulse.

and over a certain length, L, is obtained as:

$$\Delta\phi = \frac{2\pi}{\lambda}\frac{\partial n_{\text{eff}}}{\partial T}\int_0^L \Delta T_{\text{Si}}(z)dl \tag{3.7}$$

where $\partial n_{\text{eff}}/\partial T$ is the effective index dependence with the temperature due to the silicon thermo-optic coefficient. For a standard silicon waveguide surrounded by SiO_2 the value of $\partial n_{\text{neff}}/\partial T = 2\times10^{-4}$ K^{-1}. The same value was obtained for the ENZ/Si waveguide. As a result, the integral of Eq. (3.7) should be equal to 3875 K μm to obtain a π phase shift at $\lambda = 1550$ nm.

Figure 3.22a shows the normalized temperature increment in the silicon waveguide along the z-axis (light propagation direction). The accumulated phase shift of the TE mode along the waveguide is shown in Fig. 3.22b. Since there is a thermal gradient along the silicon waveguide, the phase shift begins to occur some microns before the ENZ/Si waveguide. On the other hand, the relation between the induced phase shift over the TE mode and the power of the TM polarized signal is $\sim 0.107\ \pi\ \mathrm{mW}^{-1}$, resulting in optical power for a π phase shift of around 9.5 mW. The temperature distribution for the whole structure for such optical power is depicted in Fig. 3.22c. Most of the heat is concentrated in the first micrometers around the ENZ/Si waveguide due to the high propagation loss of the ENZ_0 mode that leads to a rapid decay of the optical power. Moreover, this behavior is enhanced due to the high thermal conductivity of silicon, which generates a strong thermal gradient around the peak temperature. The temporal switching response was obtained from the evolution of the peak temperature within the silicon waveguide in the time domain upon a square pulse (Fig. 3.22d). The rise/fall time is around 5.3 µs using the 10-90% rule, in good agreement with heater-based thermo-optic phase shifters and limited by the low thermal diffusivity of the surrounding SiO_2.

3.3.5 Implementation with TCOs

For practical implementation, an ENZ heater exhibiting such optical properties at telecom wavelengths could be implemented utilizing TCOs or by forming a mixing media based on the effective medium theory formed by a host dielectric with metal nanoparticles [60]. However, TCOs provide a more practical and versatile way to obtain such ENZ heaters thanks to the different CMOS-compatible deposition techniques and the ability to precisely deposit thin films and tailor the optical properties during the deposition process or with a post-annealing treatment [50, 299, 53].

To meet the optimal condition $\varepsilon_{\mathrm{ENZ}} = j0.17$, the TCO should exhibit $\omega_p \approx 1.126 \times 10^{15}$ rad/s and $\Gamma \approx 0.045\omega_p$, considering a value of 3.8 for the ε_∞ [50]. In Ref. [50], the authors report $\omega_p = 1.2 \times 10^{15}$ rad/s and $\Gamma = 0.13\omega_p$ for ITO. Hence, it seems reasonable to accomplish such optimal material considering the rapid advances in the synthesis of TCOs [299, 53]. Moreover, ITO has already been experimentally demonstrated as a microheater with good thermal stability

for temperatures up to ~ 650 ºC [166].

3.4 Discussion

In sections 3.2 and 3.3 we have shown the potential of using TCOs as high-performance heaters to achieve low-loss and power-efficient electrical and all-optical, respectively, thermo-optic phase shifters.

In chapter 3.2, we have demonstrated through numerical simulation and experiment that it is possible to achieve low absorptive but electrically conducting ITO microheaters by tailoring the carrier concentration of ITO. Therefore, the main benefit of using ITO as a heater is that up to 3 orders of magnitude lower optical losses can be achieved compared to typical metals such as titanium. In such a way, the gap between the heater and waveguide can be reduced, which improves the performance of the phase shifter in terms of power consumption, switching speed, and footprint. Our results show that insertion loss less than 0.1 dB can be achieved for gaps as low as $\sim$ 310 nm and 660 nm for TE and TM polarizations, respectively. Our experimental results show power consumption as low as $\sim$ 10 mW and $\sim$ 20 mW for TE and TM polarization, respectively, together with switching times of $\sim$ 5 µs for a 50-µm-long ITO heater. Moreover, by embedding such phase shifters in an MZI, the device's turn-on time could be reduced to $\sim$ 2 µs due to the nonlinear response of the MZI, yielding a FOM of just only $\sim$ 20 for TE polarization.

In Table 3.7 we have selected the most representative experimental works based on the basic phase shifter configuration discussed in 3.1.2. The performance of our device is comparable to or outperforms most of the previous results. Compared with classical phase shifters based on metallic heaters, both power consumption and switching speed are benefited thanks to obtaining a smaller area A traversed by the heat flow (see Eqs. (3.5) and (3.6)) by thinning the SiO_2 intermediate layer. Graphene can also be used as a transparent heater with similar performance. However, the long-term stability of such phase shifters requires further verification since graphene is prone to fast oxidation with the ambient [302]. Finally, using the waveguide as the heater itself by doping the silicon waveguide may yield the best heat generation. However, optical losses are difficult to prevent since they are intrinsic to free carriers, and thus, more complex structures are required to minimize them. Additionally, doped silicon heaters cannot easily scale to other photonic-integrated platforms, and their potential cannot scale to other photonic-integrated platforms such as silicon nitride.

Table 3.7: Comparison of experimental electrically-driven thermo-optic phase shifters in silicon based on basic heater configurations.

Ref.	Heater / Polarization	Cladding / Undercut	Insertion loss (dB)	P_π (mW)	Switching time (µs)	FOM (mW µs)	Length (µm)
[217]	Metal (Pt) / TE	SiO_2 / Yes	N/A	0.54	141	~ 76	100
[219]	Metal (NiSi) / TE	SiN / No	~ 0.5	20	~ 3	~ 60	200
[216]	Metal (Ti) / TE	SiO_2 / No	< 1	16	~ 4	~ 64	~ 60
[230]	p-Si / TE	SiO_2 / No	~ 0.2	~ 25	~ 3	~ 75	~ 60
[240]	Graphene / TE	Al_2O_3-HSQ / No	< 0.1	11	~ 3	~ 33	~ 55
[227]	Metal (TiN) / TE	SiO_2 / No	< 0.4	~ 22	~ 5.5	~ 120	320
[227]	p-Si / TE	SiO_2 / No	< 0.4	~ 23	~ 2.2	~ 50	320
Our work (Ch. 3.2)	ITO / TE	SiO_2 / No	< 0.1	~ 10	~ 5	~ 50	50
Our work (Ch. 3.2)	ITO / TM	SiO_2 / No	< 0.1	~ 20	~ 7	~ 140	50

Regarding all-optical phase shifting, in chapter 3.3 we have shown the potential of utilizing ENZ materials for optical phase control in silicon waveguides with ultra-compact lengths and almost negligible insertion losses through numerical simulation. Our approach exploits the large change in terms of light-matter interaction between TE and TM polarized optical modes when using a thin ENZ layer (~ 10 nm) with relatively low optical loss ($\varepsilon''_{ENZ} \approx 0.17$). Under these conditions, the ENZ layer is almost transparent for TE but highly lossy for TM. Therefore, the ENZ layer acts as an efficient optical heat source and drives a thermo-optic phase shift of a TE polarized signal with an ENZ/Si waveguide of only 10 µm length and with an efficiency of $\sim 0.107\ \pi\ mW^{-1}$.

Table 3.8 surveys previous thermo-optic all-optical phase shifters that have been discussed in 3.1.3. Both works use an MRR to enhance the heat-to-light efficiency conversion by placing the control signal at a minimum of the ring spectral response. Therefore, the spectral operation of such devices is limited. Conversely, our device's building block comprises just a waveguide. Remarkably, its power consumption is much lower than the other works while maintaining an ultra-compact length.

Table 3.8: Comparison of optically-driven thermo-optic phase shifters in silicon based on basic heater configurations.

Ref.	Exp. / Sim.	Approach	Broadband operation	Insertion loss (dB)	P_π (mW)	Switching time (µs)	FOM (mW µs)	Length (µm)
[296]	Exp.	Graphene on SiN MRR	No	0.5	~ 340	~ 1	~ 340	~ 43.4
[295]	Exp.	Metal (Ti) on Si MRR	No	1.2	62.5	> 1	> 62.5	5
Our work (Ch. 3.3)	Sim.	ENZ (ITO) on Si wg	Yes	~ 0.4	9.5	~ 5	~ 50	10

Finally, our works can leverage most of the optimization strategies discussed in 3.1.2. For the electrical phase shifter using ITO microheaters, thermal isolation and pulse preemphasis can be applied to improve the power consumption or the switching time. In the case of the all-optical phase shifter, the underlying heat mechanism is the same as in thermo-optic phase shifters based on Joule heating. Therefore, similar approaches can be followed to improve power consumption or time response. The maximum temperature could be reduced by obtaining a longer but more uniform temperature increment according to Eq. (3.7). To this end, the value of κ_{eff} could be reduced [see Eqs. (A.5) and (A.6)] by using an ENZ material with lower ε'' or introducing a gap between the silicon waveguide and the heater. However, using the same surrounding materials would yield a turn-down in power consumption. A drastic reduction of the optical power could be obtained by creating air trenches around the ENZ/Si waveguide [217]. However, it should be noted that the time response would also be slowed down by a similar margin. On the other hand, one way to improve the time response would be to use a heat sink or engineer the shape of the excitation pulse [216]. However, both approaches will increase the peak optical power, leading to possible silicon nonlinearities. Therefore, the optimization process will depend on the target application.

Since our work is based on optimizing the materials used for the heater, such transparent heaters could also be leveraged in advanced configurations such as folded and multipass waveguides to reduce mainly the switching speeds of such phase shifters by reducing the gap. Therefore, by combining the optimization strategies and advanced configurations, we prospect submilliwatt power consumption and sub-microsecond switching speeds.

4 Ultra-compact and broadband nonlinear optical devices using VO_2

4.1 Review of nonlinear optical integrated devices

This section aims to contextualize our work on ultra-compact and broadband VO_2/Si nonlinear devices. Here, we cover the topic of nonlinear optics in the field of silicon photonics by first introducing the weak nonlinear properties of silicon. Afterward, we briefly review the integration of functional materials with

a larger nonlinear response and the current state-of-the-art on all-optical integrated photonic devices using VO_2. The main content of this last review is part of the work published in [Paper F].

4.1.1 Introduction

In the last decade, a plethora of applications encompasses nonlinear silicon photonic devices such as light sources and amplification, signal processing, optical memories, sensors, and quantum photonics, to name a few. For a thorough review of these applications and the specifications of those nonlinear silicon devices, we recommend the reader to read these reviews [291, 303, 304].

Put simply, nonlinear optical devices rely on modifying the optical properties of a medium with light. In other words, a change of the refractive index by the presence of light. Hence, nonlinear optics are in the sense that the response of the medium is not proportional to the strength of the light. Usually, the way to express the relation between the optical properties of a medium and the light is done by the definition of polarization $\mathcal{P}$, which depends on the strength of the electric field E. In a simplified form, the relationship between P and E can be expressed as a power of series as [305]

$$\mathcal{P} = \varepsilon_0 \left[\chi^{(1)} E + \chi^{(2)} E^2 + \chi^{(3)} E^3 + \ldots \right], \tag{4.1}$$

where ε_0 is the vacuum permittivity, $\chi^{(1)}$ is the linear susceptibility, and $\chi^{(2)}$ and $\chi^{(3)}$ are the nonlinear terms known as second- and third-order susceptibilities, respectively. In Eq. (4.1) we assume that all the terms are scalar and the medium is lossless and dispersionless. General and more specific expression of Eq. (4.1) can be found elsewhere [305]. The relationship between P and E becomes linear when the higher-order terms are negligible either because the higher-order susceptibilities of the medium are zero or the applied electric field is very weak. For condensed matter, $\chi^{(1)}$ is in the order of unity, $\chi^{(2)} \approx 10^{-12}$ m/V, and $\chi^{(3)} \approx 10^{-24}$ m^2/W [306]. On the other hand, second-order nonlinearities can occur only in noncentrosymmetric crystals, whereas third-order nonlinear optical interactions can occur in both centrosymmetric and noncentrosymmetric media.

Silicon presents inversion symmetry, i.e., it is a noncentrosymmetric crystal and, thus, only has third-order nonlinear effects. The second-order nonlinearity (Pockels effect) has been investigated in silicon waveguides by breaking the

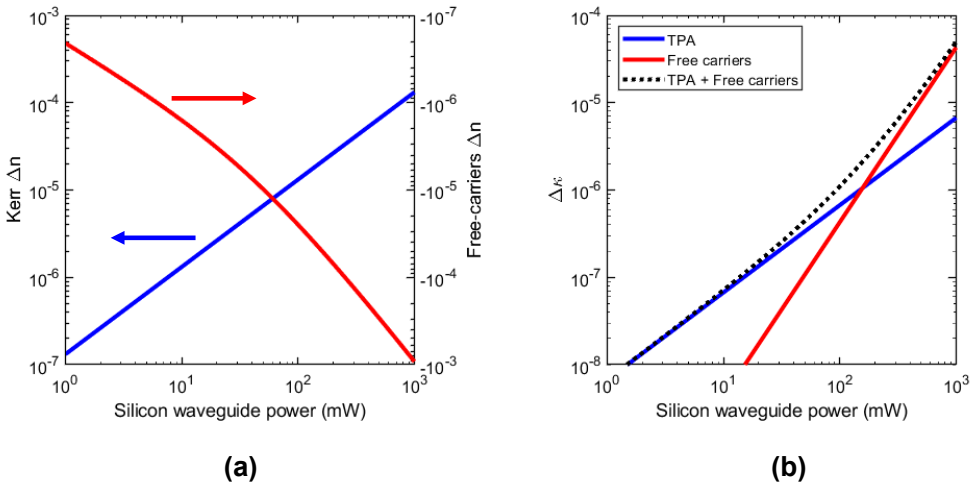

Fig. 4.1. Estimate of the variation in the **(a)** real and **(b)** imaginary part of the refractive index of silicon waveguide as a function of the optical power at $\lambda = 1550$ nm. We approximate the effective are by the dimensions of a standard silicon waveguide (500 nm × 220 nm). We consider changes from the third-order susceptibility (Kerr and TPA), and free-carriers effects from absorption due to TPA. For the Kerr and TPA coefficients, we consider $n_2 = 14.5 \times 10^{-18}$ m^2/W and $\beta = 0.6$ cm/GW [307]. The relationship between the generated free carriers N and the optical power P is $N(\text{cm}^{-3}) = 2.4 \times 10^{11} P^2$ [308]. The change in the silicon refractive index is obtained from the well-known equations given by Soref [251].

crystal symmetry with a highly stressed layer deposited on top [309–311]. Alternatively, the quadratic electro-optic or DC Kerr effect has been demonstrated using a p-i-n structure under reverse bias [312, 313]. However, the modulation efficiency is still low with both approaches. On the other hand, silicon $\chi^{(3)}$ has a complex value. This fact means that both the silicon refractive index's real (Kerr effect) and imaginary parts change under the electric field of light. The change in the imaginary part or absorption is caused by TPA, in which electrons in the valence band jump to the conduction band by absorbing photons. Consequently, TPA generates free carriers that also change the refractive index of silicon due to the plasma-dispersion effect. Silicon Kerr coefficient (n_2) is in the order of $10^{-18} - 10^{-19}$ m^2/W and TPA coefficient (β) is in the order of $0.5 - 1$ cm/GW [314]. Figure 4.1 shows the estimated variation of the complex refractive index

of a silicon waveguide as a function of the optical power. As can be seen, the change in both real and imaginary parts is very small, even for powers of hundreds of milliwatts. For the real part, free carries induce an opposite change to Kerr effect (see Fig. 4.1a), whereas for the imaginary part both effects increase the optical loss (see Fig. 4.1b) with a two distinct regions, in which either TPA (Power < 100 mW) or free carriers (Power > 100 mW) is clearly the dominant effect.

In such a way, resonant structures such as ring resonators or photonic crystal cavities are usually employed to enhance the light-matter interaction and implement practical all-optical devices regarding footprint and power consumption. Still, the operational spectral range of such nonlinear devices is very limited. Spectrally broadband devices are required in current trends to exploit dense wavelength-division multiplexing (DWDM) by using parallelism and capacity [315, 316]. Thus, it would be highly desirable to integrate other CMOS-compatible materials with a larger nonlinear optical response than silicon.

4.1.2 Nonlinear integrated devices with functional materials

Functional materials are generally characterized as engineered or advanced materials that possess particular native or tailored properties and functions of their own. In this part, we focus on those functional materials that are CMOS-compatible and feature a large nonlinear response at telecom wavelength, which has been harnessed for silicon-based photonic integrated devices. To date, four main groups of functional materials are the most appealing to integrating onto silicon waveguides: molecular organic materials, 2D materials, epsilon-near-zero materials, and phase-change materials.

Molecular-organic materials

Molecular-organic materials have been proposed for both electro-optic and all-optical nonlinear optics [317]. For all-optical applications, the main benefit of such molecular-organic materials is that they have a similar Kerr coefficient as silicon $n_2 \approx 2 \times 10^{-17}$ m^2/W. However, without suffering from TPA and the associated free-carrier absorption, [318]. Ultrafast all-optical silicon-organic hybrid (SOH) waveguides have been experimentally demonstrated [319]. The device consisted of a 4-mm-long silicon waveguide covered by a type of these organic

materials (DDMEBT). Since its linear refractive index (1.8) is lower than silicon, light can remain guided through the silicon waveguide. By using a slot waveguide instead of the typical strip configuration, higher light-matter interaction with the molecular materials is achieved (see Fig. 4.2a left image). Additionally, the TPA effects of silicon can be avoided [320], which results in a slowdown in the phase dynamics (see Fig. 4.2a right image). A practical application of such SOH waveguides was demonstrated in that case by performing four-wave mixing (FWM) and demultiplexing a 170.8 Gb/s return zero signal to a bit rate of 42.7 Gb/s. Still, although the absence of optical loss is a great advantage over silicon for implementing lossless nonlinear processes, long active lengths are required, which hampers the integration of such devices in dense photonic integrated circuits.

2D materials

2D materials, particularly graphene and TMDs, have been investigated for their utilization in all-optical hybrid 2D material-silicon waveguides. Graphene can behave as a nonlinear saturable absorption, i.e., graphene transforms from opaque to transparent with the increase of the light intensity as a result of Pauli blocking caused by photo-excited carriers [321]. In this regard, the saturable absorption response has been observed in a silicon waveguide with monolayer graphene on top and under in-plane light excitation [322]. However, such a response is followed by an increase in the absorption that lasts over several microseconds caused by graphene photo-excited carriers that transfer into the silicon waveguide. Therefore, eventually, free-carrier absorption dominates the optical loss. A maximum transmission loss of $\sim$ 13 dB for TE polarization was achieved for a 150-μm-long graphene-silicon waveguide with an incident optical power of 22.4 mW. In order to prevent the slow dynamics caused by free carriers, ultrafast all-optical switching has been recently demonstrated in graphene-loaded plasmonic waveguides that are connected to conventional silicon waveguides (see Fig. 4.2b left image) [323]. The combination of the suspended graphene with ultra-high confined plasmonic (see Fig. 4.2a right image) greatly enhances both switching time and energy. In this manner, the study reports for a 4-μm-long bilayer graphene device switching energies as low as 35 fJ together with an extinction ratio of 3.5 dB and a switching time of only 260 fs. However, the main drawback of this device was the high insertion loss of 19 dB.

Apart from all-optical modulation purposes, FWM wavelength conversion has also been demonstrated in highly p-doped graphene, which shifts the Fermi position deep into the valence band and thereby reduces the graphene optical absorption on a photonic crystal resonator [324]. On the other hand, TMD materials such as $MoSe_2$ have been employed in silicon waveguides to enhance second harmonic generation (SHG) [325]. $MoSe_2$ has a second-order coefficient $\chi^{(2)} \approx 5 \times 10^{-11}$ m/V. In that study, the authors demonstrated a 5-fold enhancement through excitation of the 2D material by the evanescent field of the guided mode. This enhancement is due to the increased interaction length limited in atomically-thin monolayer thicknesses under free-space excitation.

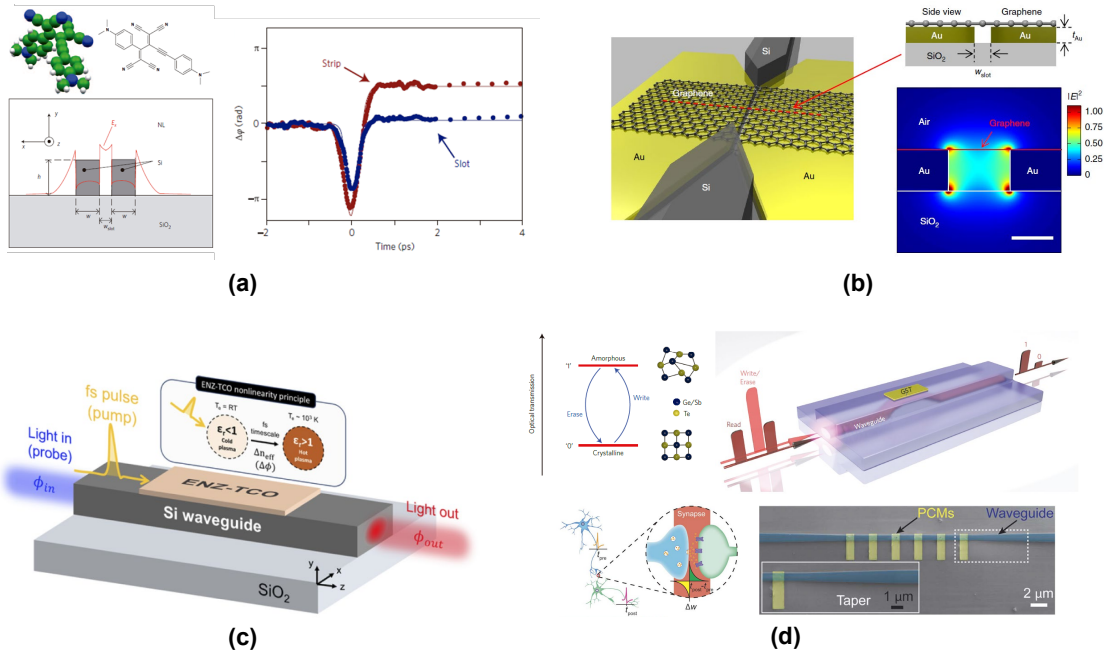

Fig. 4.2. Nonlinear silicon devices based on functional materials. **(a)** Slot waveguide covered and filled by a molecular organic material (left image), and its temporal response (right image) upon a pulsed optical signal with an on-chip average power of -1.2 dBm [319]. **(b)** All-optical graphene-plasmonic switch (left image) with femtojoule energy consumption by harnessing the ultra-confined plasmonic mode (right image) [323]. **(e)** Ultra-compact hybrid ENZ/Si waveguide acting as all-optical phase switch [326]. **(d)** Amorphous and crystalline phases of GST (top left image), non-volatile photonic memory (top right image) [162], and on-chip synapse (bottom image) [327].

Epsilon-near-zero materials

Epsilon-near-zero materials, and particularly TCOs in the near infrared, have been reported to exhibit unprecedented ultrafast nonlinear efficiencies within sub-wavelength propagation lengths [328]. TCOs' third-order susceptibility is in the same order of magnitude as silicon. Moreover, its value does not significantly enhance at the zero-permittivity wavelength. Therefore, the large nonlinear response should come from the dramatic increase of $|E|$ owing to the intrinsic field-enhancement mechanism of ENZ materials. In this regard, the magnitude of the normal component of the electric field E_t within a medium is proportional to the external field $E_{0,t}$ and to the inverse of its permittivity ($E_t \propto E_{0,t}/\varepsilon$). On the other hand, TCOs illuminated with energy smaller than their bandgap, for instance, near-infrared wavelength, incur electron heating that may cause a redistribution of electrons within the conduction band. This effect, together with the non-parabolicity of the conduction band, leads to an increase in electron effective mass and hence a variation of the plasma frequency and permittivity (see Eqs. (1.2) and (1.3)).

Changes in the real refractive index as large as 0.7 with a transient response below 200 fs have been reported in ITO thin films featuring the zero-permittivity wavelength at 1240 nm[329]. The nonlinearity was mainly attributed to a modification of the energy distribution of conduction-band electrons due to laser-induced electron heating. The enhancement in the ENZ spectral region was dependent on the incident angle of the light, suggesting that such large nonlinear values are caused by an enhancement of the electric field within the ITO film, as mentioned hereinbefore. Therefore, the main benefit of ITO against noble metals for nonlinearities is two-fold: first, the field enhancement caused by the ENZ regime; and second, the free-electron heat capacity of ITO is more than an order of magnitude smaller than that of noble metals. Thus, the increase in the free-electron temperature compared with the Fermi temperature and the consequent change in the refractive index in ITO is much large.

To the best of our knowledge, no experimental demonstration of all-optical ENZ/Si devices has been reported. However, there has recently been some proposal through numerical simulation using ENZ-loaded silicon waveguides (see Fig. 4.2c). Ultrafast and femtojoule all-optical absorption modulators could be achieved using hybrid ENZ/Si waveguides [73]. In that study, the authors prospect through numerical simulation a modulation strength as high as

15.9 dB/μm at telecom wavelengths and an ultrafast switching time as low as 230 fs at the cost of ultra-low switching energy of 13.5 fJ. A high-mobility TCO such as CdO is selected as the ENZ material for two main reasons. As discussed in our work of chapter 2.3, the imaginary part of the permittivity, which is associated with the optical loss, is proportional to the damping frequency ($\varepsilon'' \propto q/(\mu m_e)$). On the other hand, at the ENZ region, where $\varepsilon' = 0$, $|\varepsilon| = \varepsilon''$. Hence, the enhancement factor is proportional to the mobility of the TCO. Consequently, far from the ENZ regime, the material can be low loss, but high loss when it is close to, leading to dramatic extinction ratios.

A similar device but for phase, switching has been reported [326]. The authors investigate the best compromise between energy consumption, insertion losses, and phase change per unit length for enabling ultrafast switching times below 100 fs and compact active lengths in the order of several micrometers. An all-optical phase-switching device is designed based on a 6-μm-long TCO/Si waveguide with ultrafast switching times, as low as 75 fs, the energy consumption of a few picojoules and insertion losses around 4 dB.

Phase-change materials

Phase-change materials are a family of CMOS-compatible functional materials that undergo a structural change under certain external stimuli, typically when they are heated above the transition temperature. The phase change is accompanied by a dramatic variation in the electrical and optical properties of the material that are also spectrally broadband, thereby enabling ultra-compact and nonlinear broadband devices. In this regard, refractive index variations in the unity at telecom wavelength are obtained between the states of PCMs [151, 83]. For such materials, the origin of the nonlinear response of these materials comes from a variation of the linear refractive index caused by the structural change and not by second or third-order nonlinear coefficients. Chalcogenides and vanadium oxide compounds are the two leading families of PCMs used for photonics [330]. GST and VO_2 are the most famous PCMs in the field of integrated photonics [79]. GST changes between an amorphous (a-GST) and crystalline (c-GST) structure (see Fig. 4.2d top left image), whereas for VO_2 transition between the insulating (i-VO_2) monoclinic and metallic (m-VO_2) rutile phases. On the other hand, both materials have high values in the imaginary part of their refractive index, so most nonlinear devices are based on absorption. In this regard, the photoinduced

phase change usually relies on a self-heated mechanism enabled by the fact that the PCM is lossy. Therefore, such a process leads to a trade-off between the insertion loss of the device and the energy consumption. Low extinction coefficients result in low optical losses but high energy consumption, whereas high values for the extinction coefficient provide energy-efficient devices but with higher optical losses.

Although GST and VO_2 feature a drastic change in both electrical and optical properties, there are some essential differences between these PCMs. First, GST is nonvolatile at room temperature, whereas VO_2 is intrinsically volatile, despite there is some ongoing work trying to obtain such a feature (see section 2.1.4). Second, the transition temperatures and temporal requirements are different. The crystallization temperature of GST is between 180-250 ºC, whereas amorphization occurs at temperatures higher than 650 ºC. Additionally, a high-speed cooling rate is required > 1 ºC/ns during the cooling down of the amorphization in order to achieve the so-called melt-quench and thereby prevent recrystallization. Conversely, the insulator-metal transition of VO_2 is near room temperature ~ 68 ºC, and the metal-insulator transition is around 55 ºC. Therefore, VO_2-based devices would be more energy-efficient and easy to implement. Additionally, VO_2 does not require any particular heating or cooling rate to produce the phase transition. Finally, GST in the amorphous state is dielectric ($\varepsilon' > 0$) with high and moderate values in the real and imaginary parts of the refractive index. A unitary increase is achieved when the GST changes to crystalline but remains the material dielectric. Notably, the real part of the refractive of c-GST is much larger than silicon. Thereby, particular caution should be taken when choosing the thickness of the GST layer to achieve optimal optical switching by preventing the excitation of high-order optical modes [331]. On the other hand, VO_2 in the insulating state is also dielectric, with high and moderate values in the real and imaginary parts of the refractive index. However, VO_2 becomes metallic in the metallic state since $\varepsilon' < 0$.

Therefore, GST has been used mainly for developing optical nonlinear units with memory response [150] such as optical memories (see Fig. 4.2d bottom image) [162, 69, 165] or synapses (see Fig. 4.2d top right image) [327] that are appealing in emerging applications based on non-Von Neumman architecture such as in-memory computing [161], photonic tensor cores [23, 20], or neuromorphic computing [332]. By opposite, the volatile response of VO_2 has been mainly used

for developing all-optical switches, which are more thoroughly reviewed in the next section.

4.1.3 Optically switched silicon devices using VO_2

Recently, all-optical switching devices based on hybrid VO_2/Si waveguides have been reported. Notably, the switching timescale of the IMT triggered by optical excitation has been demonstrated down to the femtosecond [179] and would allow ultra-fast speed with seamless integration in PICs. However, such a type of ultra-fast device has not been demonstrated yet. Ryckman et al. demonstrated the first all-optical hybrid VO_2/Si device [90]. They integrated the hybrid VO_2/Si waveguide in a small ring resonator and induced the IMT of the VO_2 by pumping the patch out-of-plane with a pulsed laser in the visible. No switching times were reported, and the optical switching of the VO_2 was attributed to being photothermal. Afterward, the same authors investigated the timescale of such devices (see Fig. 4.3a) [91]. In this case, they used a pulsed laser of a few nanoseconds to excite the IMT of the VO_2. On one hand, dependence on the fluence in the completion of the IMT was observed. For this device, pump fluences above 12.7 pJ/μm^2 drove the VO_2 to metallic. On the other hand, the IMT occurred in a timescale similar to the pump-pulse width ($\sim$ 25 ns) with a minimum influence of the fluence. However, the switching time from metallic to insulating (relaxation time) showed a high dependence on the fluence and the VO_2 patch size. By increasing the pump fluence above the threshold up to $\sim$ 70 pJ/μm^2 and enlarging the VO_2 path from 500 nm to 1 μm, the relaxation time increased from $\sim$ 30 ns to $\sim$ 3 μs. Thus, the MIT dynamics were attributed to be a thermally mediated process dependent on the thermal diffusion of the monoclinic phase. Haglund et al. investigated the timescale of hybrid VO_2/Si waveguides by illuminating an out-of-plane device with a femtosecond laser acting as a pump and using an in-plane probe laser to record any change in the VO_2 [98]. For this case, a 900-nm-long VO_2 patch reported switching speeds lower than 2 ps for fluences between 50 and 100 pJ/μm^2. More recently, sub-picosecond switching times have also been demonstrated by optimizing the fluences and reducing the volume of VO_2 in the hybrid waveguide (see Fig. 4.3b) [100].

While these are promising results, the out-of-plane excitation is not the best approach for integration in PIC. Future all-optical schemes with both the pump

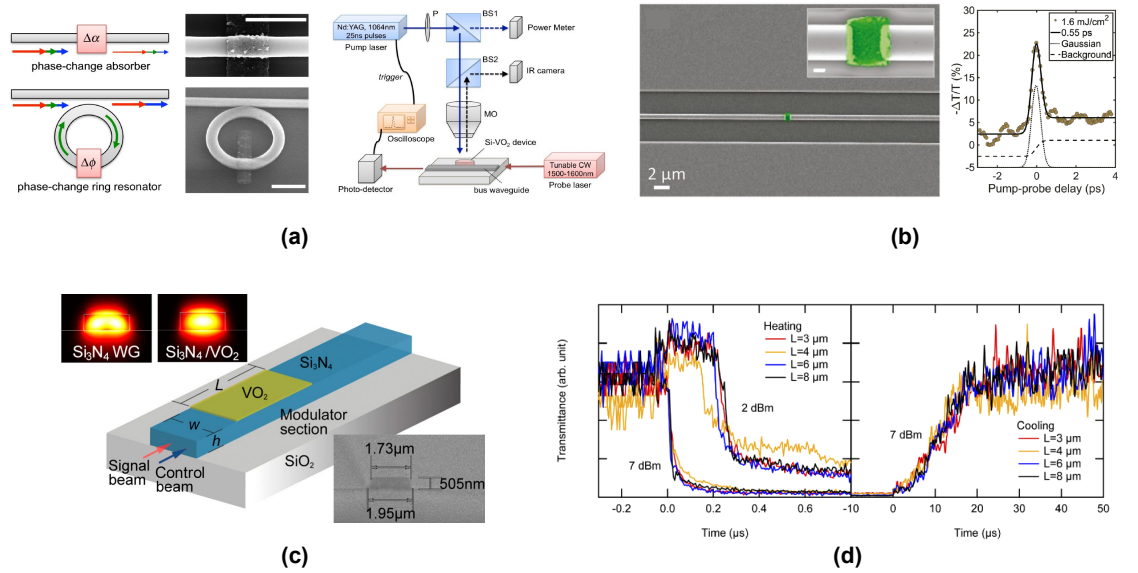

Fig. 4.3. **(a)** Illustration of a phase-change absorber where the IMT induces a broadband change in the absorption $\Delta\alpha$ and the phase $\Delta\phi$ (left image), SEM image of an ultra-compact VO_2/Si waveguide and ring resonator (scale bar is 1.5 µm, center image), and schematic of the experimental setup [91]. **(b)** False-color SEM image of a Si waveguide with a 700-nm-long VO_2 patch embedded (left image), and its temporal response (right image) under a pump fluence of 1.6 mJ/cm^2 with out-of-plane incidence [100]. **(c)** Schematic of an optically-driven SiN/VO_2 modulator with in-plane excitation. The top left image is the simulated TM optical modes at λ = 1550 nm. The bottom right image is an SEM image of the SiN waveguide cross-section [99]. **(d)** Temporal response of a VO_2/Si waveguide under in-plane excitation for different optical powers. The left image is the heating process, whereas the right image corresponds to the cooling [182].

and the probe guided within the waveguide would be more desirable. All-optical switching with hybrid waveguides using an in-plane approach has been recently reported [99]. In this case, SiN instead of Si was used for the hybrid waveguide to handle the pump between 700 and 1000 nm and the probe at 1550 nm (see Fig. 4.3c). An extinction ratio of 10 dB was achieved for a 5-µm-long hybrid waveguide with switching energy as low as 6.4 pJ. However, the timescale was not measured. Shibuya et al. have recently addressed this question using a similar in-plane approach in the telecom wavelength region with a hybrid VO_2/Si

waveguide [182]. They obtained switching times corresponding to the VO_2 heating process in the order of nanoseconds, whereas microseconds were obtained for the cooling process (see Fig. 4.3d). Moreover, such values depended on the optical power. Thus, their results revealed that the switching characteristics of the modulators driven by the photothermal effect are governed by heat transfer and thermal dissipation in the VO_2/Si waveguide.

4.2 All-optical VO_2/Si waveguide absorption switch at telecom wavelengths

This section demonstrates an all-optical absorption switch using a hybrid VO_2/Si waveguide. All-optical switching is achieved by an in-plane optical pumping excitation at telecom wavelengths, thus providing a device fully compatible with current silicon PICs. Moreover, a stable and long-term operation is expected by protecting the VO_2 from the external environment by using a SiO_2 cladding [333, 334]. The main results of this section correspond to [Paper G].

4.2.1 VO_2/Si waveguide and its transmission response

The fabricated hybrid VO_2/Si waveguide used in this section is shown in Fig. 4.4a. The device comprises a Si waveguide with a 20-µm-long VO_2 patch on top. A cross-section scheme is depicted in Fig. 4.4b. To work in the single-mode region, the Si waveguide is 480 nm × 220 nm. A 50-nm-thick SiN layer is used for the planarization of the silicon surface. Between the silicon waveguide and the SiN layer, there is a 10-nm-thick of SiO_2. A 40-nm-thick VO_2 layer is placed atop the SiN layer. Finally, the waveguide is protected with a 700-nm-thick SiO_2 upper cladding. Details about the fabrication process can be found in Appendix A.2.

Spectroscopic ellipsometry measurements were carried out on a dummy Si sample with the same 40-nm-thick VO_2 at room temperature (RT) and 100 ºC by using a hot plate to determine the VO_2 refractive index both in the insulating and metallic state. These measurements were performed before and after depositing the SiO_2 cladding to check for possible variations in the refractive index of the VO_2 caused by this processing step. The refractive index is almost not affected in the metallic state, as shown in Fig. 4.5a, whereas a small variation can be observed in the insulating state. Nevertheless, the hysteresis in the VO_2 phase transition is preserved as depicted in Fig. 4.5b, where the phase of the VO_2 refractive index with the temperature is shown during a heating-cooling cycle at $\lambda = 1550$ nm. For both claddings, the IMT begins around 60 ºC and the refractive index varied from $2.74 + j0.5$ (insulating) to $1.78 + j2.58$ (metallic) for the SiO_2 cladding.

Based on the aforementioned VO_2 refractive index values, FEM simulations

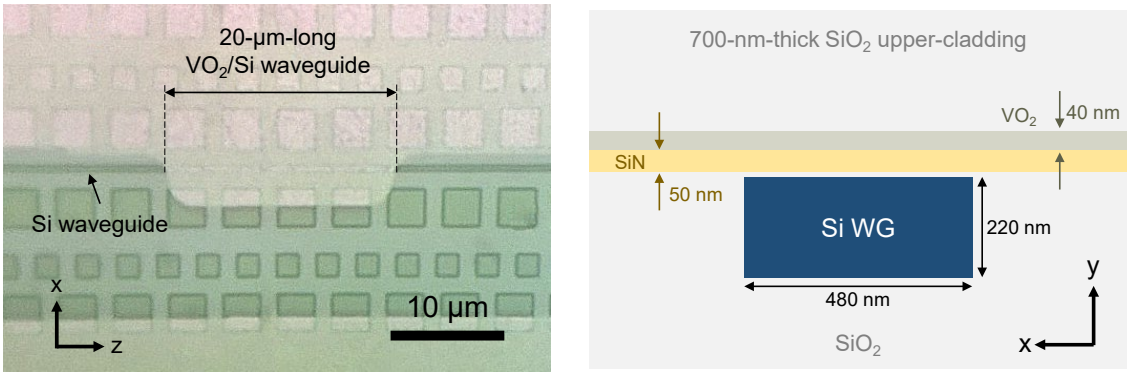

(a) (b)

Fig. 4.4. **(a)** Optical image of the fabricated hybrid 20-μm-long VO_2/Si waveguide before depositing the SiO_2 upper-cladding. The silicon squares shown in the image are used for the planarization process. **(b)** Cross-section scheme of the hybrid waveguide.

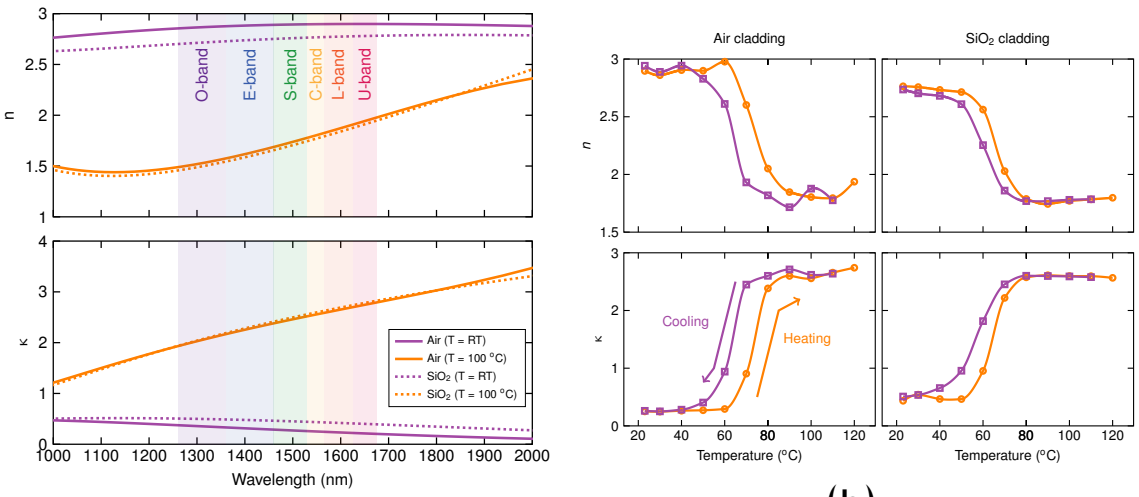

(a) (b)

Fig. 4.5. Refractive indices of VO_2 obtained by spectroscopic ellipsometry with an air and SiO_2 cladding: **(a)** as a function of the wavelength for the insulating (T = RT) and metallic (T = 100 ºC) states; and **(b)** at λ = 1550 nm as a function of the temperature during a heating-cooling cycle.

were performed to obtain the effective refractive index, $n_{\text{eff}} + j\kappa_{\text{eff}}$, of the guided modes for TE polarization (see Appendix A.1.2 for details). Due to the absorptive behavior of the switch, we will only work with the imaginary part. Hence, the

propagation loss, α, for both VO_2 states can be calculated following the well-known expression:

$$\alpha = 20\log_{10}(e)\frac{2\pi}{\lambda}\kappa_{\text{eff}}. \tag{4.2}$$

The calculated propagation losses are shown in Fig. 4.6a for wavelength values covering the C- and L-band. In the insulating state, propagation losses are around 0.7 dB/μm and remain independent of the wavelength due to the flat response of the VO_2 refractive index as shown in Fig. 4.5a. For the metallic state, propagation losses range from 1.2 dB/μm to almost 2 dB/μm from 1500 to 1650 nm, leading to an extinction ratio between 0.5 and 1.1 dB/μm. Nonetheless, a switch aiming to cover both bands and with a required minimum extinction ratio would be feasible since it would be designed only considering the C-band. Therefore, this kind of all-optical switch based on a non-resonant structure would be ultra-broadband. On the other hand, the optical mode of the silicon waveguide without the VO_2 capping (Fig. 4.6b) is very similar to those of the VO_2/Si waveguide in the insulating and metallic state as depicted in Figs. 4.6c and 4.6d, respectively. Therefore, optical losses due to mode mismatch between the silicon and the hybrid waveguide are expected to be much lower than propagation losses.

Larger extinction ratios could be obtained by using TM polarization and exploiting the formation of a high-lossy hybrid plasmonic mode in the metallic state [97]. Our simulations predict an increase of the extinction ratio up to 6.71 dB/μm at 1550 nm. However, the propagation loss in the insulating state increases to 1.45 dB/μm, and a higher mode mismatch could give rise to larger coupling losses.

The spectrum of the hybrid waveguide was measured with the VO_2 in the insulating and metallic state (Fig. 4.7a). To this end, the chip's temperature was set at 30 ºC and 90 ºC, respectively, using a Peltier device. The light was coupled to/from the chip by means of TE grating couplers. A reference waveguide without VO_2 was also measured to estimate grating and VO_2 losses. Experimental optical loss of VO_2 in the insulating and metallic state was 18.2 dB and 32.2 dB, respectively, which delivered an extinction ratio of 14 dB, in fair agreement with the values of propagation loss given by simulations. Moreover, these values would confirm the low losses due to the optical mode mismatch between the silicon waveguide and the device.

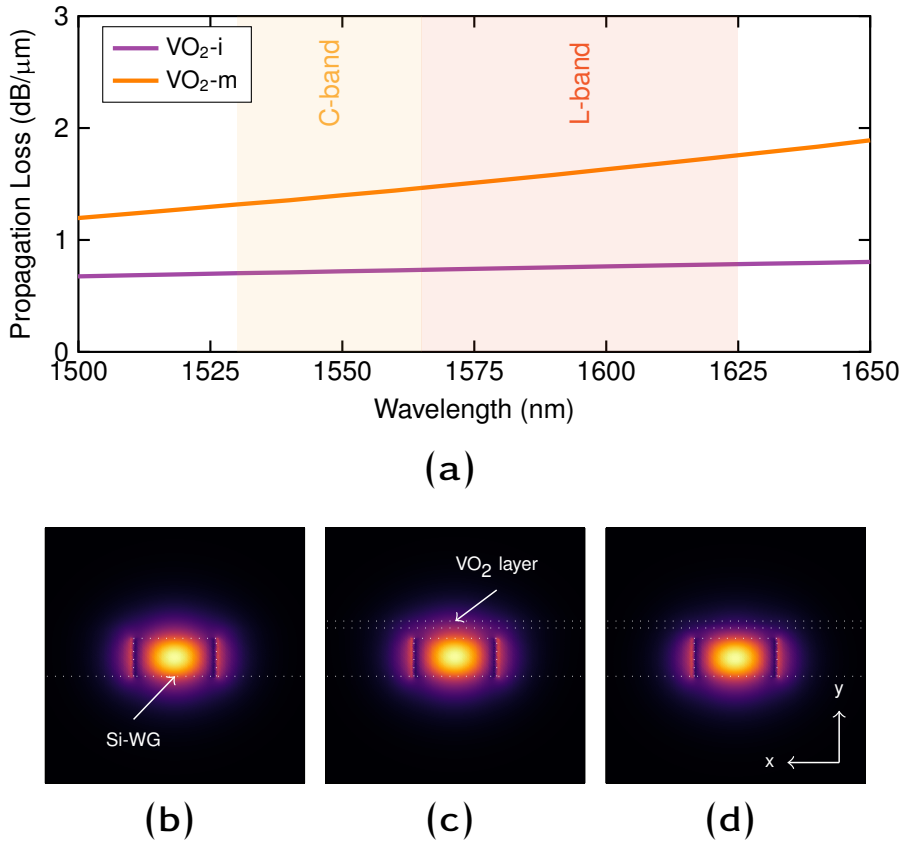

Fig. 4.6. **(a)** Simulated propagation loss as a function of the wavelength for the VO_2 in the insulating (VO_2-i) and metallic (VO_2-m) state. Normalized electric field (E_x) of the silicon waveguide **(b)** without VO_2 and with the VO_2 layer in the **(c)** insulating and **(d)** metallic state at $\lambda = 1550$ nm. Simulations were carried out for TE polarization and using the VO_2 refractive index values given in Fig. 4.5a.

The typical hysteretic response of VO_2 on its optical loss was obtained upon a heating-cooling cycle (Fig. 4.7b). On one hand, the IMT occurred around 58 ºC in a window between 55 ºC and 63 ºC. On the other hand, the MIT started at 60 ºC and finished around 30 ºC.

4.2.2 Experimental all-optical switching performance

Prior to temporal measurements, the all-optical static response of the hybrid waveguide was investigated. The waveguide's transmission was collected as a

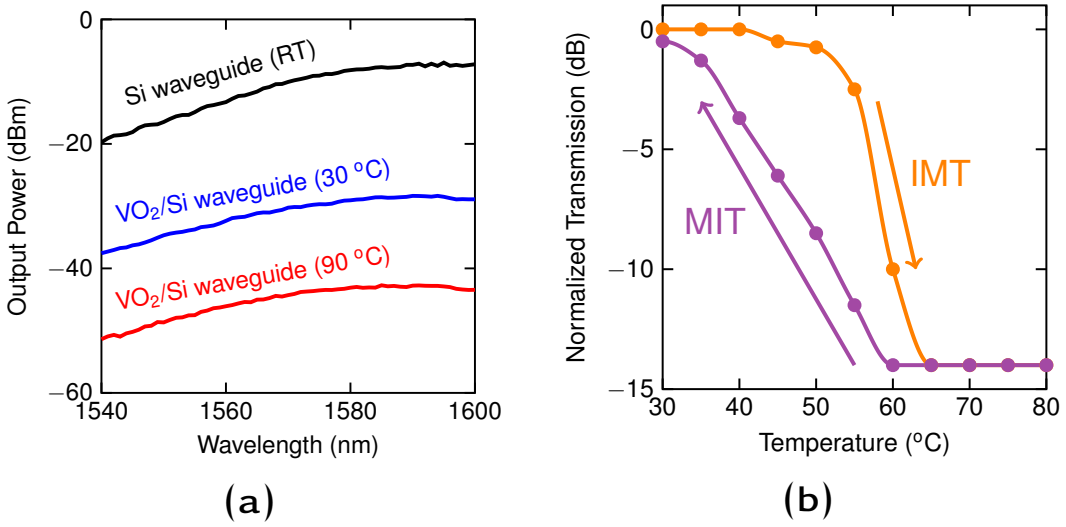

Fig. 4.7. **(a)** Spectra of a reference silicon waveguide and the hybrid waveguide in the insulating (T = 30 °C) and metallic (T = 90 °C) states. The laser output power was 0 dBm. **(b)** Normalized transmission of the hybrid waveguide as a function of the temperature for a heating-cooling cycle at $\lambda = 1550$ nm.

function of the input power. A tunable continuous-wave (CW) laser with an erbium-doped fiber amplifier (EDFA) was used to generate high-power optical signals to drive the VO_2 into the metallic state (see Appendix A.3 for more details). The normalized transmission as a function of the input power at the facet of the hybrid waveguide is shown in Fig. 4.8a. The power at the facet is calculated by subtracting the output power delivered by the EDFA from the grating estimated loss from the Si reference waveguide (see Fig. 4.7a). Several optical cycles were performed, varying the maximum power. On one hand, hysteresis is observed for all the cycles, which confirms that optical loss is due to the metallic/insulating change of the VO_2. On the other hand, the loss is proportional to the input power. This indicates that only a portion of the VO_2 patch becomes metallic, and it is attributed to the attenuation that experiences the optical signal due to the VO_2 absorption.

Based on these measurements and the simulated optical loss, the VO_2 underwent the metallic state with a rate of 1.06 μm/dBm for input powers higher than 3.5 dBm (Fig. 4.8b). To change the 20-μm-long VO_2 on top of the waveguide, an optical power of 22.4 dBm would be necessary at the facet. It is essential to bear in mind that in the static regime, the IMT is triggered by photo-thermal excita-

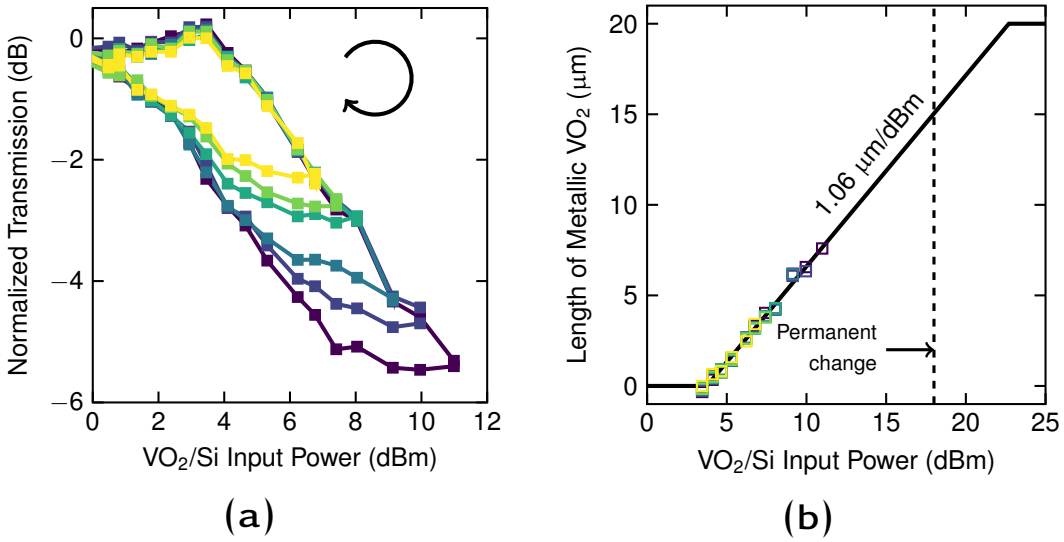

Fig. 4.8. **(a)** Normalized transmission as a function of the optical power. Different optical cycles were performed, varying the maximum power. The arrow indicates the direction of the cycle. **(b)** Fragment of VO_2 in the metallic state as a function of the optical power from experimental results (square markers) and fitting (solid line). For both figures, optical power is given at the facet of the hybrid waveguide and $\lambda = 1550$ nm.

tion [90]. Hence, the VO_2 could be damaged or permanently changed to another phase like V_2O_5 if this surpasses 600 °C [335]. In our hybrid waveguide, a permanent change was obtained when the input power was increased up to 18 dBm ($\sim$ 15 μm of metallic VO_2). Optical inspection observed a larger insertion loss, while a degradation in a fragment of the VO_2 layer was also observed. Furthermore, the response shown in Fig. 4.8a could not be reproduced using the same input powers.

The temporal dynamics of the hybrid waveguide were investigated based on the all-optical static measurements and constraints. To this end, the temporal characteristics were obtained from the hybrid waveguide transmission using a pump-probe technique in the telecom wavelength region. Small peak powers and short pulses were used to avoid damaging the VO_2 layer. Thus, a small fragment of VO_2 underwent the metallic state. Temporal measurements were stable during the entire characterization process.

The setup used for this work is based on a wavelength-multiplexed pump-probe experiment ($\lambda = 1550$ nm for the probe and $\lambda = 1560$ nm for the pump) and

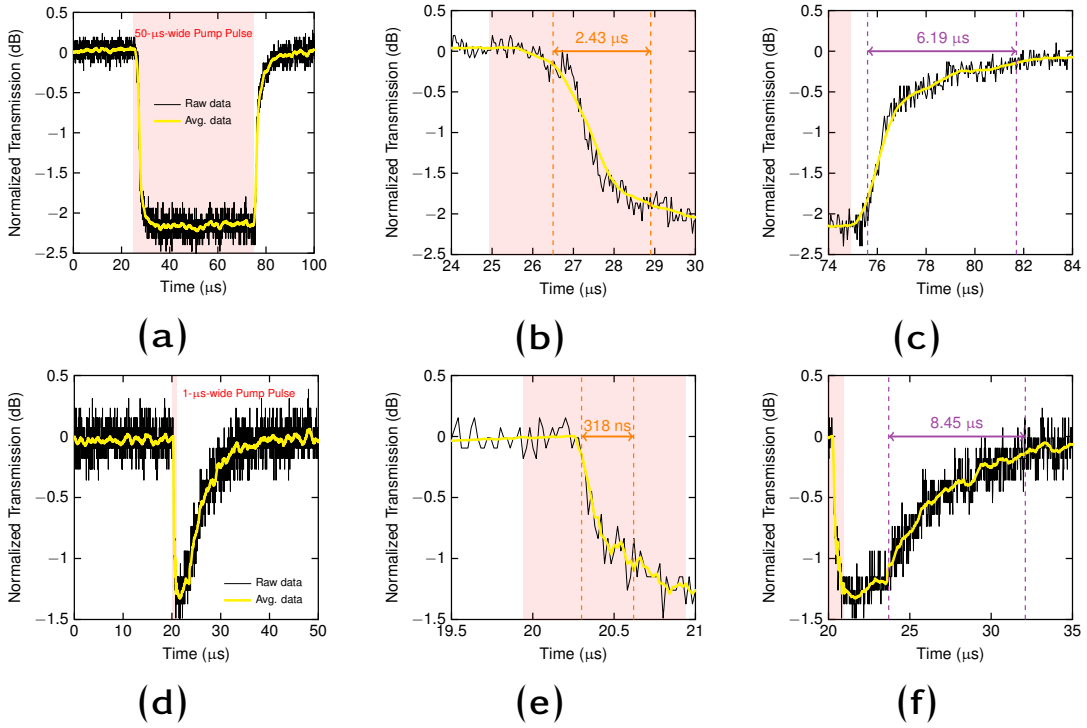

Fig. 4.9. Normalized output of the probe signal as a function of the time upon: **(a-c)** 50-μs-wide and 8 dBm rectangular pump pulse and **(d-f)** 1-μs-wide and 12 dBm rectangular pump pulse. **(b,c)** and **(e,f)** are the zooms of fall and rise times for **(a)** and **(d)**, respectively. Results are given at 1550 nm and 1560 nm for the probe and pump signals, respectively. The pump power values are at the facet of the hybrid waveguide. The time in which the pump signal is applied is highlighted in light red.

is explained in Appendix. A.3. A 50-μs-wide rectangular pulse with a repetition rate of 10 kHz was generated for the pump signal. Its amplitude was set to obtain around 8 dBm at the facet of the hybrid waveguide. This configuration led to energy consumption of 315 nJ. The normalized output is shown in Fig. 4.9a. Upon the pump signal, the probe suffered a drop in its power in good agreement with the results obtained in the static measurements (see Fig. 4.8a). The drop of the probe (OFF state) is associated with the high-loss metallic state of the VO_2, whereas the recovery (ON state) is linked to the low-loss insulating one. The switching times were obtained from the averaged data and following the 10%-90% rule. A value of 2.43 μs (Fig. 4.9b) and 6.19 μs (Fig. 4.9c) was obtained for the OFF and ON states, respectively. The difference between both values is

attributed to the thermal increment required to complete the IMT and MIT of the VO_2 (see Fig. 4.7b). The longer switch time of the ON state is because MIT needs a wider switching window compared to the IMT (OFF state) to complete the phase transition. This difference in the steepness between the IMT and MIT is the first more abrupt. It has also been reported in previous work [35], and it is attributed to different crystal grain sizes during the structural phase transition [336].

The timescales suggest a photo-thermal effect behind the VO_2. Notably, switching times are in the same order of magnitude as those reported using microheaters [95]. Therefore, the switching mechanism is attributed to be of thermal origin. On one hand, the insulating to metal switching (OFF switching) is due to heat arising from the VO_2 optical absorption. On the other hand, the metal to insulating switching (ON switching) involves a thermal dissipation process.

The surrounding materials thus condition the temporal response of the device as in thermo-optic phase shifters [216, 289, 167]. Nevertheless, the nonlinear thermal temporal response of VO_2 can be taken advantage of to reduce the insulating to metal switching times while maintaining the extinction ratio. To this end, higher optical pump powers should be used together with a drastic shortening of the pulse width. The first is to increase the heating rate, while the second is to avoid the VO_2 thermal damage threshold. To prove this point, the pulse width was 50 times decreased to 1 µs whereas the pump power was only increased 2.5 times up to 12 dBm. These values were chosen to achieve a similar extinction ratio. The normalized temporal response is shown in Fig. 4.9d. The switching time of insulating to metal was reduced one order of magnitude down to 318 ns (Fig. 4.9e). This reduction is attributed to the higher heating rate, which was confirmed by observing the delay between the pump and the actual switch of the probe. For this latter case, the delay was reduced from around 1.5 µs (Fig. 4.9b) to 300 ns (Fig. 4.9e). On the other hand, the metal-to-insulator switching time remained at a similar value (Fig. 4.9f), since it essentially depends on the thermal dissipation rate of the structure [92, 93]. Furthermore, the non-proportional shortening of the pulse width with the power increase leads to a reduction of the energy consumption, being, in this case, one order of magnitude lower and achieving 15.8 nJ.

Consequently, the all-optical hybrid VO_2/Si device using an in-plane approach is governed by thermal conductive dynamics. The switching time from

insulating to the metallic state could be reduced by increasing the pump power while reducing the pump pulse, which also benefits lower energy consumption values. On the other hand, reducing the size of the VO_2 patch [91] or including a heat sink, i.e., a high thermal conductive material close to the VO_2 layer, would reduce the heating/cooling time, thus yielding to faster switching speeds.

4.3 Low-threshold power and tunable integrated optical limiter based on an ultra-compact VO_2/Si waveguide

In this section, we experimentally demonstrate an ultra-compact VO_2/Si optical power limiter on silicon photonics featuring low-threshold power and tunability over a broad spectral response. The power limiting response is achieved by harnessing the large change in the absorption of VO_2 that accompanies the IMT and exploiting the gradual insulator to metal profile along the propagation direction under in-plane photothermal excitation. The main results of this section correspond to [Paper H].

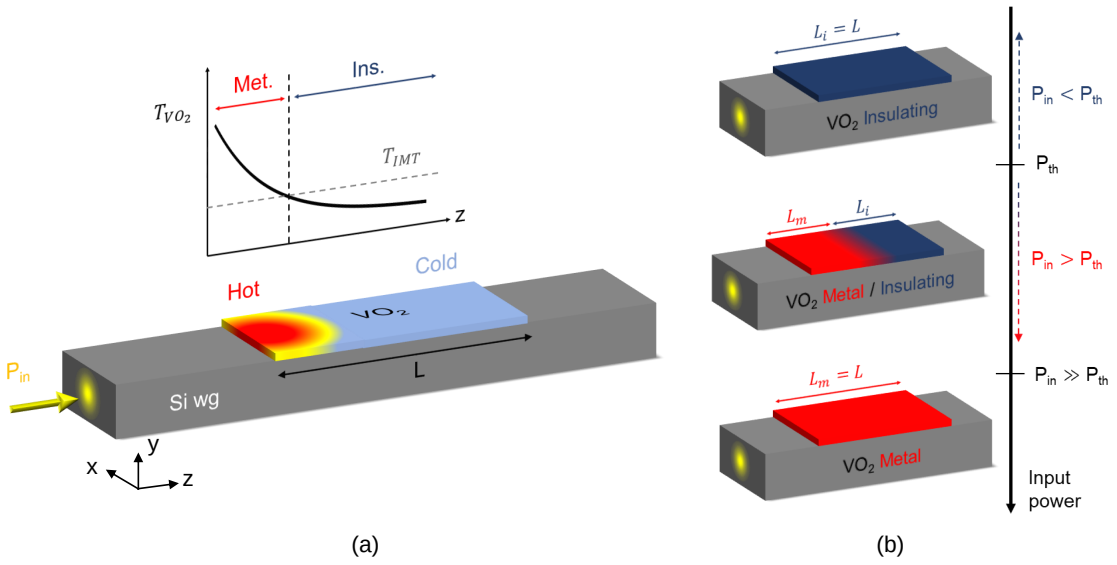

Fig. 4.10. **(a)** Illustration of the VO_2 heating in a hybrid VO_2/Si waveguide using an in-plane photothermal approach. **(b)** States of the VO_2 patch as the input power in the waveguide is increased.

4.3.1 In-plane photothermal response

Fig. 4.10a illustrates the photothermal behavior of a hybrid VO_2/Si waveguide fed by a high-power optical signal. We consider a standard Si waveguide with a thin VO_2 patch of length L on top. The IMT of the VO_2 is triggered by evanes-

cent coupling so that the absorbed optical power (P_{abs}) in the VO_2 acts as a heat source. Due to the in-plane approach, the value of the heat source is related to the absorption strength of the optical mode:

$$\frac{\partial P_{abs}}{\partial z} = P_{in}\alpha \exp(-\alpha z) \tag{4.3}$$

where P_{in} is the input power, and α is the propagation loss. Being this latter given by

$$\alpha = \frac{4\pi\kappa_{eff}}{\lambda} \tag{4.4}$$

where κ_{eff} is the effective extinction coefficient, and λ is the working wavelength. Because the absorption strength is not constant along the propagation direction (z axis), and thus the heat source, there is a temperature gradient in that direction. This temperature gradient translates into a phase-change gradient; the portion VO_2 material above the IMT temperature (T_{IMT}) will transition to metal, while the remaining portion of the patch will stay insulating.

According to previous experimental works [182, 175], the relation between the length of the metal fragment (L_m) and the optical power can be approximated as:

$$L_m \approx \eta \ln\left(\frac{P_{in}}{P_{th}}\right) \tag{4.5}$$

where η is a term relating to the thermo-optical efficiency of the structure and depends on both the optical and thermal properties of the hybrid waveguide.

The different states the hybrid waveguide can undergo are depicted in Fig. 4.10b. For low optical power below the threshold power, the VO_2 is insulating as the temperature in the patch is less than T_{IMT}. High optical power is required to obtain a full insulator-metal transition since the temperature profile in the whole VO_2 layer needs to be above the T_{IMT}. Nevertheless, in both cases, the output-input optical response of the hybrid waveguide is linear and is given by the propagation loss in the insulating (α_i) and metallic (α_m) cases, respectively.

On the other hand, for intermediate states comprised of a fraction of metal and insulator VO_2, the optical response can be described as

$$P_{out} = P_{in}\exp[-(\alpha_m - \alpha_i)L_m - \alpha_i L]. \tag{4.6}$$

Therefore, for such states, the optical response of the hybrid waveguide be-

comes nonlinear due to L_m and its dependence on the optical power (see Eq. (4.5)].

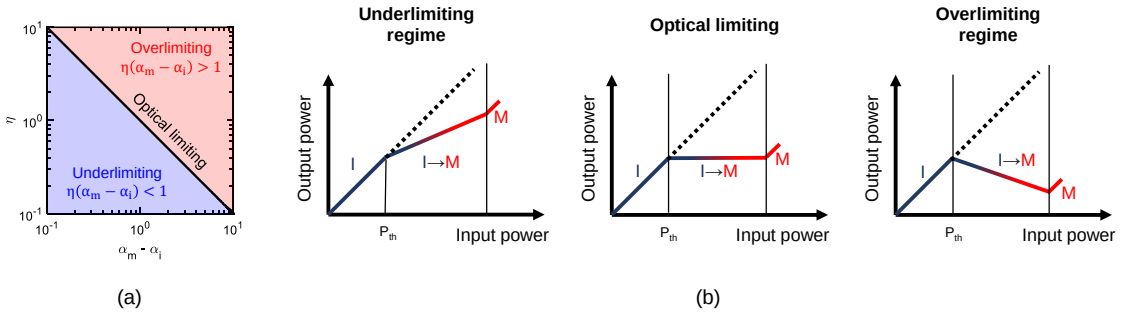

Fig. 4.11. (a) Optical limiting condition in a VO_2/Si waveguide using an in-plane photothermal approach. **(b)** Optical response of the hybrid waveguide for the different regimes.

4.3.2 Optical limiting condition

Optical limiting is achieved when the induced optical losses match the increase of the optical power when this exceeds the threshold power. In this case, the output is constant regardless of the input value. This response can be achieved by leveraging the nonlinear response of VO_2/Si found in the intermediate optical states (see Eq. (4.6)]. To this end, the following condition needs to be met

$$P_{th}\exp(-\alpha_i L) = P_{in}\exp[-(\alpha_m-\alpha_i)L_m - \alpha_i L]. \tag{4.7}$$

As a result, we obtain that the value of L_m fulfilling the optical limiting condition for a specific optical power is

$$L_{m,OL} = \frac{\ln(P_{in}/P_{th})}{\alpha_m - \alpha_i}. \tag{4.8}$$

Finally, by comparing Eqs. (3) and (6), we obtain that the photothermal efficiency term should be

$$\eta_{OL} = \frac{1}{\alpha_m - \alpha_i}. \tag{4.9}$$

Figure 4.11a shows the value of η with respect to $\alpha_m - \alpha_i$ in the different regimes. The optical limiting condition is comprised of overlimiting (red region)

and underlimiting (blue region) regimes. Such regimes arise when η does not match the value given by Eq. (4.9). The optical responses for the three regimes are plotted in Fig. 4.11b. When the VO_2 layer is mix of metal and insulator ($I \rightarrow M$), the output increases (underlimiting) or decreases (overlimiting) depending on whether the induced optical losses are lower $[\eta(\alpha_m - \alpha_i) < 1]$ or higher $[\eta(\alpha_m - \alpha_i) > 1]$, respectively, than the increase of the input power.

On the other hand, the photothermal efficiency is related to the light-matter interaction between the optical mode and the VO_2. Hence, different strategies can be followed to control the value of η in VO_2/Si waveguides to fulfill Eq. (4.9) such as changing the distance between the silicon waveguide and the VO_2 patch or varying the thickness of the VO_2. The photothermal efficiency will also depend on the polarization of the propagating mode.

4.3.3 Experimental results

Like in the previous section 4.2, our hybrid waveguide is based on a standard 480 nm × 220 nm Si waveguide with 40-nm-thick VO_2 layer on top separated by a 60 nm spacer formed by a 10-nm-thick silicon oxide layer plus a 50-nm-thick SiN hard mask. Further details regarding the fabrication process can be found in Appendix A.2. Fig. 4.12 shows an optical microscope image of the fabricated VO_2/Si waveguide. The refractive index of the deposited VO_2 at telecom wavelengths and for different temperatures is reported in Fig. 4.13. Film characterization was carried out by spectroscopy ellipsometry following the same deposition process.

The optical and photothermal parameters for that type of waveguide are: $\alpha_i \approx 0.91$ dB/μm, $\alpha_m \approx 1.61$ dB/μm, and $\eta \approx 1.06$ μm/dB at $\lambda = 1550$ nm and for TE polarization [175]. Therefore, our device was expected to be close to the optical limiting condition according to Eq. (4.9) with a small underlimiting response.

The power-limiting response was characterized by setting the wavelength of the laser and increasing the optical power. The experimental setup used for characterizing the optical limiter is described in Appendix A.3. Fig. 4.14 shows the power response of a reference silicon waveguide without VO_2 and the hybrid waveguide acting as an optical limiter at different temperatures. Input and output optical power values are given on-chip. The reference waveguide was characterized to discard a loss contribution from nonlinear silicon effects. In such a way,

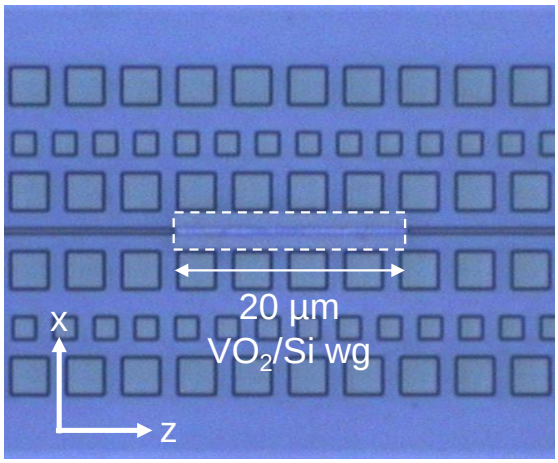

Fig. 4.12. Optical microscope image of the fabricated optical limiter.

a linear response was obtained (see Fig. 4.14a). Therefore, considering the optical power values, the nonlinear and limiting response of the hybrid waveguide owns to the photothermal induced IMT of VO_2 (Figs. 4.14b and 4.14c).

To fit the experimental values, we modeled the optical response by using Eqs. (4.5) and (4.6). A fair agreement is found between the experiment (dots) and the proposed model (solid lines). Therefore, optical saturation occurs due to the discussed relationship between the gradual metallic change of the VO_2 layer along the propagation direction and the optical power (see Eq. (4.8)). Our device features a low threshold power of ~ 3.5 mW near room temperature (see Fig. 4.14b] alongside a plateau in the response, which is indicative of being near the optical limiting condition (see Fig. 4.11b), for a range of input powers of around 7 dB.

Because the IMT is photothermally triggered, our optical limiter also provides the possibility of tuning its response. Biasing the temperature of the VO_2 near (far) the IMT reduces (increases) its threshold power. To prove this point, the chip's temperature was increased to 50 °C (Fig. 4.14c), near the IMT (~ 65 °C), with the Peltier device. In this manner, the threshold power was reduced down to ~ 2 mW since a smaller increase in temperature was required to trigger the IMT. Consequently, the input range, i.e., the input power values comprised between the threshold power and the maximum measured power (see Fig. 4.11b), increased up to ~ 10 dB. On the other hand, the photothermal efficiency was slightly improved ($\eta \approx 1.2$ µm/dB) because the difference between T_{IMT} and the background temperature was decreased.

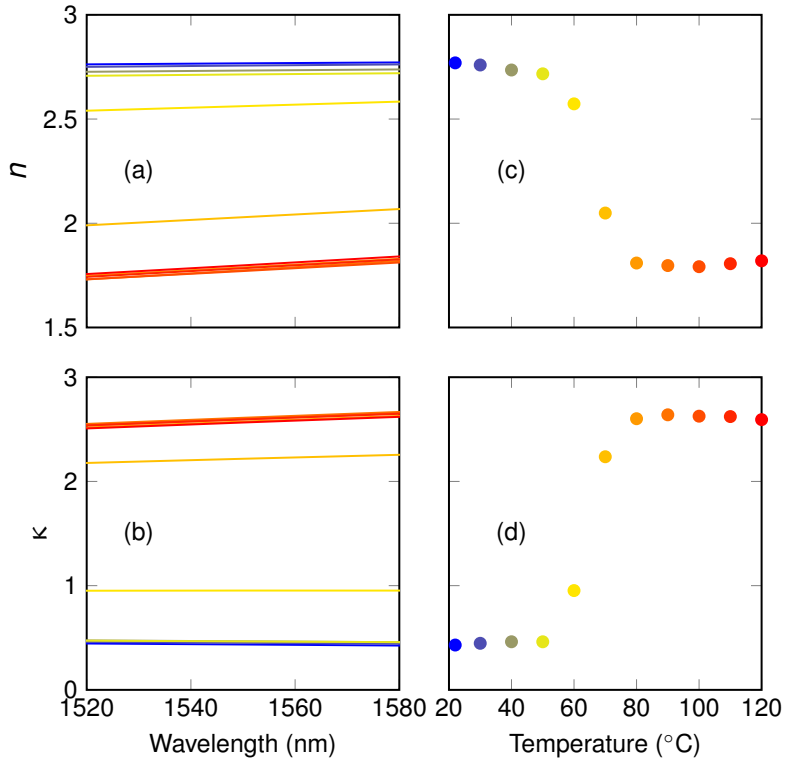

Fig. 4.13. Refractive index (n+$j\kappa$) of VO_2 thin film as a function of the wavelength and for different temperatures during a heating cycle. **(a)** Real and **(b)** imaginary parts of the refractive index spectrum. **(c)** Real and **(d)** imaginary parts of the refractive index at 1565 nm as a function of the temperature.

The spectral response of the proposed optical limiter is mainly restricted by the wavelength dependence of the propagation losses (see Eqs. (4.4) and (4.9)). In this regard, a remarkable advantage of the proposed optical limiter device is that it benefits from the low dispersion of VO_2 at telecom wavelengths (see Figs. 4.13a and 4.13b), providing thus a broadband response in VO_2/Si waveguides. To showcase this feature, we characterized the spectral response of our hybrid waveguide under low- and high-power signals as shown in Fig. 4.15, i.e., $P_{in} < P_{th}$ and $P_{in} \geq P_{th}$, respectively. The wavelength dependence of the input power is due to the EDFA. Our restricted bandwidth was around 15 nm. It should be highlighted that the measured spectral range was restricted by our EDFA and not by the bandwidth of the device, which should be larger due to the non-resonant operation. When the low-power signal at the input of the hybrid waveguide remains far below the threshold, the device works on the linear regime (full in-

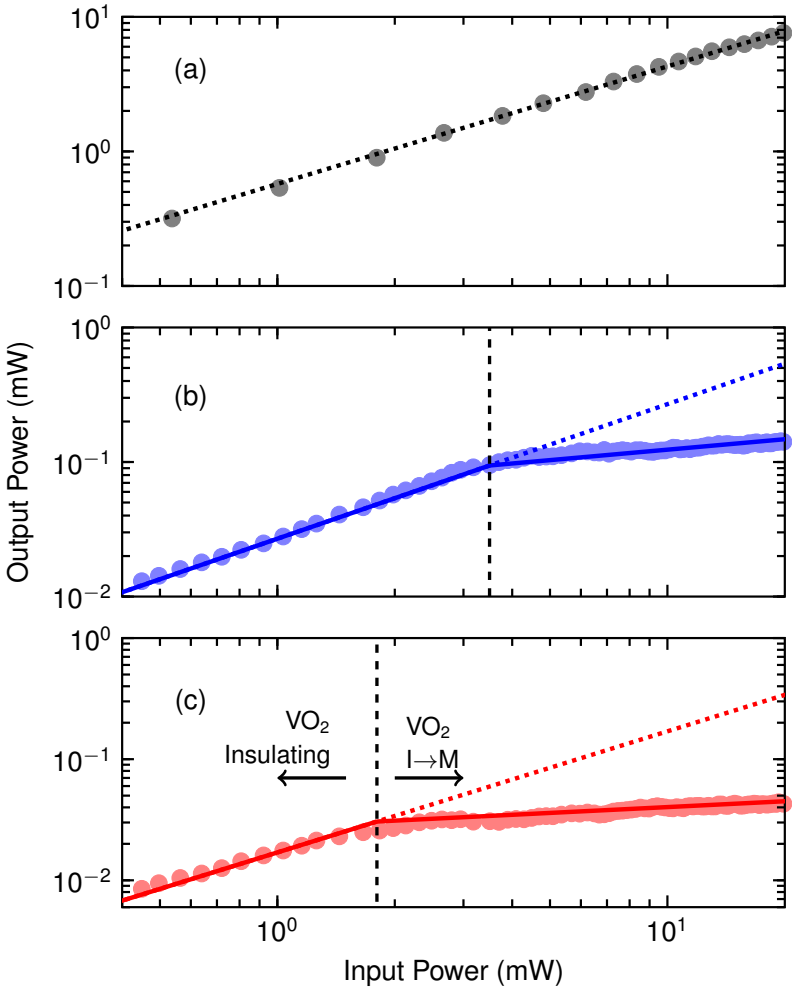

Fig. 4.14. Optical response of the **(a)** reference Si waveguide and **(b,c)** hybrid VO_2/Si waveguide setting the temperature of the chip at **(b)** 30 ºC and **(c)** 50 ºC. Experimental values (dots) are given on-chip at 1565 nm. Solid lines stand for fitted data. Dotted lines show the extrapolated behavior of the optical limiter if it had remained in the linear regime (full insulating VO_2).

sulating VO_2) and, therefore, the output is proportional to the input, and both responses have a similar shape. On the other hand, for the high-power signal, the hybrid waveguide is driven to the optical limiting condition (metal/insulator VO_2) because the input power exceeds the limiter threshold. Hence, the output is saturated, resulting in a flattening of the spectral response.

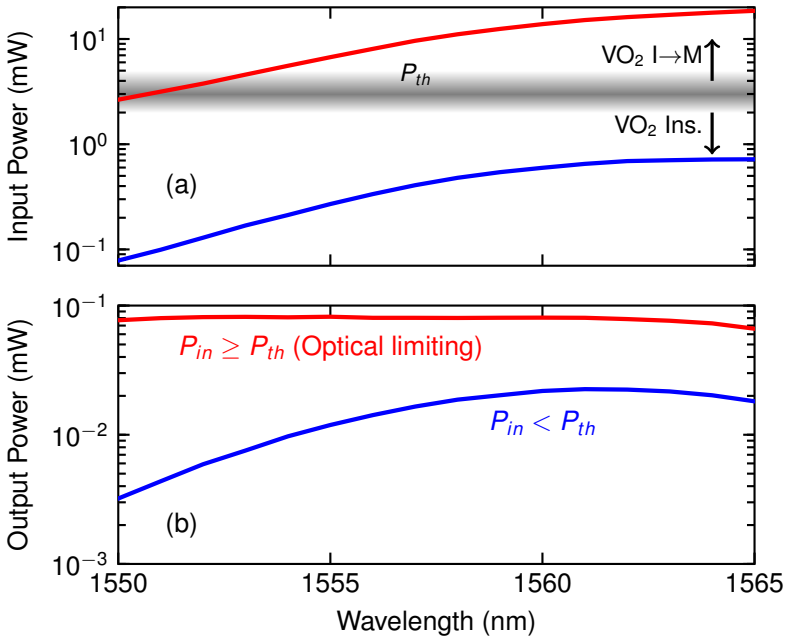

Fig. 4.15. Spectral response of the device under below-threshold (blue) and above-threshold (red) signals. **(a)** Input and **(b)** output power as a function of the wavelength. The shaded region in **(a)** stands for the threshold power. The device limits the power at the output for larger values and flattens the spectrum. Values are given on-chip and at 30 ºC.

4.4 Discussion

In summary, we have experimentally demonstrated two all-optical functionalities, switching and power limitation, using an ultra-compact hybrid VO_2/Si waveguide featuring broad spectral operation.

All-optical modulation has been demonstrated with an extinction ratio of 0.7 dB/μm and a maximum switchable length of 15 μm. This value is limited by the maximum temperature that can achieve the VO_2 without suffering a permanent and irreversible change. Temporal characterization showed that the dynamics of this device are mediated by a thermal process, in which the heat stems from the light absorbed by the VO_2. Switching values in the nano and microsecond range have been obtained with energy consumptions as low as nanojoules.

A comparison with previous experimental work is summarized in Table 4.1 in terms of key parameters such as wavelength, polarization, switching energy, and optical loss. Notice that, in previous work, the pump or control signal is not waveguided within the chip, but out-of-plane [91] and/or its wavelength is out of the transparent region of silicon (1.1–7 μm) [99]. In [99], Wong *et al.* obtained switching energies of a few picojoules using a SiN waveguide but at the expense of guiding a high peak power, which is unfeasible in silicon due to nonlinear effects because of TPA and the associated free carriers. By using an out-of-plane configuration, switching times less than picoseconds have been reported around telecom wavelengths using pulsed optical sources [99]. However, such an investigation has not been carried out using evanescent coupling with practical on-chip implementation. Finally, in [182] similar investigation was conducted as in our work and reported similar results but for TM polarization. That work and our work were published with a few months of difference. Actually, we were the first to report the temporal dynamics of such waveguides under in-plane excitation [337].

Regarding the utilization of VO_2/Si waveguides as power limiters, we have investigated three possible limiting regimes for such waveguides. We have demonstrated that the strong optical nonlinear response of VO_2 could be leveraged for achieving ultracompact and broadband optical limiters on silicon photonics with tunable performance. Threshold powers as low as 2 mW have been demonstrated with an optical bandwidth of 15 nm, restricted by our setup and not by the device. On-chip efficient thermal biasing could be easily achieved using low-loss

Table 4.1: Comparison of experimental all-optical absorption switches based on VO_2-waveguide configuration.

Ref.	Configuration / Pump wavelength	Polarization (Probe)	IL / ER (dB/μm)	Switching energy	Switching time	Optical bandwidth (nm)
[91]	Out-of-plane / 1064 nm	TE	~ 2 / ~ 4	~ 6 pJ	~ 25 ns	> 100
[99]	In-plane / 700-1000 nm	TM	0.98 / 1.68	6.4 pJ	N/A	> 100
[100]	Out-of-plane / 1670 nm	N/A	~ 10 / ~ 1	360 nJ	550 fs	N/A
[182]	In-plane / 1530-1610 nm	TM	~ 1.25 / ~ 2	~ 3 μJ	~ 10 – 100 ns	> 80
Our work (Ch. 4.2)	In-plane / 1560 nm	TE	0.91 / 0.7	15.8 nJ	~ 300 ns	> 60

microheaters that could be ITO-based like in Ch. 3.2, [241]. On the other hand, the threshold power of the device could be engineered by doping the VO_2 in order to modify the transition temperature [338–340]. Finally, the turn-on time of such a device under photothermal excitation is expected to be in the order of nano and microseconds, as demonstrated for all-optical switching.

Table 4.2: Comparison of experimental integrated optical limiters.

Ref.	Approach	Tunable	Threshold power (mW)	Optical bandwidth (nm)	Footprint (μm^2)
[341]	Silicon microrring resonator	Not demonstrated	~ 250	0.096	~ 450
[342]	Silicon photonic crystal cavity	Yes	0.023	0.062	~ 1
[308]	Silicon waveguide	No	~ 300	> 100	1080
Our work (Ch. 4.3)	VO_2/Si waveguide	Yes	~ 2	> 15	~ 10

A comparison with previous experimental work is summarized in Table 4.2 regarding the possibility of tuning the device, the threshold power, optical bandwidth, and footprint. Silicon waveguides exhibit such an optical limiting response stemming from TPA and free carriers when they are mm-long and work under high optical power of hundreds of milliwatts [308]. Thus, this is not practical. An attempt was made to reduce the threshold power, and footprint using a

ring resonator [341]. However, the reported threshold values were still ultrahigh ($\sim$ 250 mW) at the expense of reducing the optical bandwidth below 0.1 nm. Better results were obtained using a photonic crystal cavity with threshold powers of only 23 μW. Tunability was demonstrated by using the silicon thermo-optic effect. However, the optical bandwidth was remarkably small ($\sim$ 0.062 nm), which makes the device very sensitive to tiny fabrication deviations and temperature fluctuations. Therefore, our work is the only one gathering the key parameters with high performance.

5

Conclusions and future directions

In conclusion, in this thesis, we have significantly contributed to the field of silicon photonics by proposing and demonstrating both electro-optic and all-optical disruptive silicon photonic devices using the metal oxides TCOs and VO_2. In this regard, we have fulfilled our main goal by bringing new and enhancing current functionalities of silicon photonics. To this end, we have addressed the topics of non-volatility, phase shifting, and optical nonlinearities throughout this work by harnessing the unique optoelectronic properties of TCOs and VO_2. Figure 5.1 summarizes the hybrid devices presented in this thesis. The main benefits of our devices are their ultra-compact footprints of just a few micrometers together with a broad spectral operation since they rely on non-resonant structures. The main highlights of such devices are listed as follows:

- **Non-volatile ENZ electro-optic readout memory** (Fig. 5.1a, Section 2.2): We have proposed a non-volatile readout photonic memory through numerical simulation. The memory mimics the electronic counterparts. The memory employs ITO as a floating gate and exploits its ENZ regime and electro-optic activity. In this manner, we obtain extinction ratios higher than 10 dB in an optical bandwidth for a 5-μm-long memory. Moreover, switching energies of a few picojoules with retention times of about a decade are predicted.

- **Non-volatile MZI switch** (Fig. 5.1b, Section 2.3): We have proposed a non-volatile MZI electro-optic switch through numerical simulation. Phase-shifting operation is achieved by replacing the ITO floating gate with a high-mobility TCO such as CdO. Our results show an active length of only

30 μm to obtain a π phase shift for the switching device. Moreover, an extinction ratio of 20 dB and insertion loss as low as 1 dB could be attained. The device shows a broad spectral response and can be controlled with low-power pulses in the nanosecond range.

- **Ultra-low-loss ITO/Si thermo-optic phase shifter with optimized power consumption** (Fig. 5.1c, Section 3.2): We have demonstrated ultra-low loss thermo-optic phase shifters for TE and TM polarization using ITO as a transparent heater. The optimal gap and cladding configuration are investigated to achieve low power consumption. Our experimental results show power consumption to achieve a π phase shift as low as 10 mW and switching times of a few microseconds for a compact 50-μm-long ITO/Si phase shifter.

- **All-optical phase control in silicon waveguides with ENZ nanoheaters** (Fig. 5.1d, Section 3.3): We have investigated through numerical simulation the utilization of TCO in the ENZ regime as optical heaters for all-optical phase control in silicon waveguides. Optical phase tuning based on the silicon thermo-optic effect is achieved using an ENZ material as a compact, low-loss, and efficient optical heat source. Such a phase shift is induced on TE polarization and controlled by a cross-polarized TM signal. Our results show an insertion loss of less than 0.5 dB for TE polarization and high control efficiency of $\sim 0.107\ \pi\ \mathrm{mW}^{-1}$ for a 10-μm-long ENZ/Si waveguide.

- **All-optical hybrid VO_2/Si waveguide absorption switch** (Fig. 5.1e, Section 4.2): We have demonstrated an all-optical absorption switch using a hybrid VO_2/Si waveguide by harnessing the unitary change in the imaginary part of the VO_2 refractive index caused by the photoinduced MIT. Our results show an extinction ratio of 0.7 dB/μm for TE polarization with a maximum switchable length of 15 μm, switching speeds as low as 318 ns, and switching energy of 15.8 nJ. The device works under in-plane excitation and features broadband response caused by the non-resonant operation.

- **Low-threshold power and tunable optical limiter based on an ultra-compact VO_2/Si waveguide** (Fig. 5.1f, Section 4.3): We have demonstrated an integrated power limiter on silicon photonics-based on an ultra-compact VO_2/Si waveguide. The optical limiting response is engineered from the

gradual photoinduced IMT of the VO_2 layer caused by the evanescent field. Our experimental results show an on-chip thermal tunable threshold power of only ~ 3.5 mW with a broadband response for a 20-µm-long VO_2/Si waveguide.

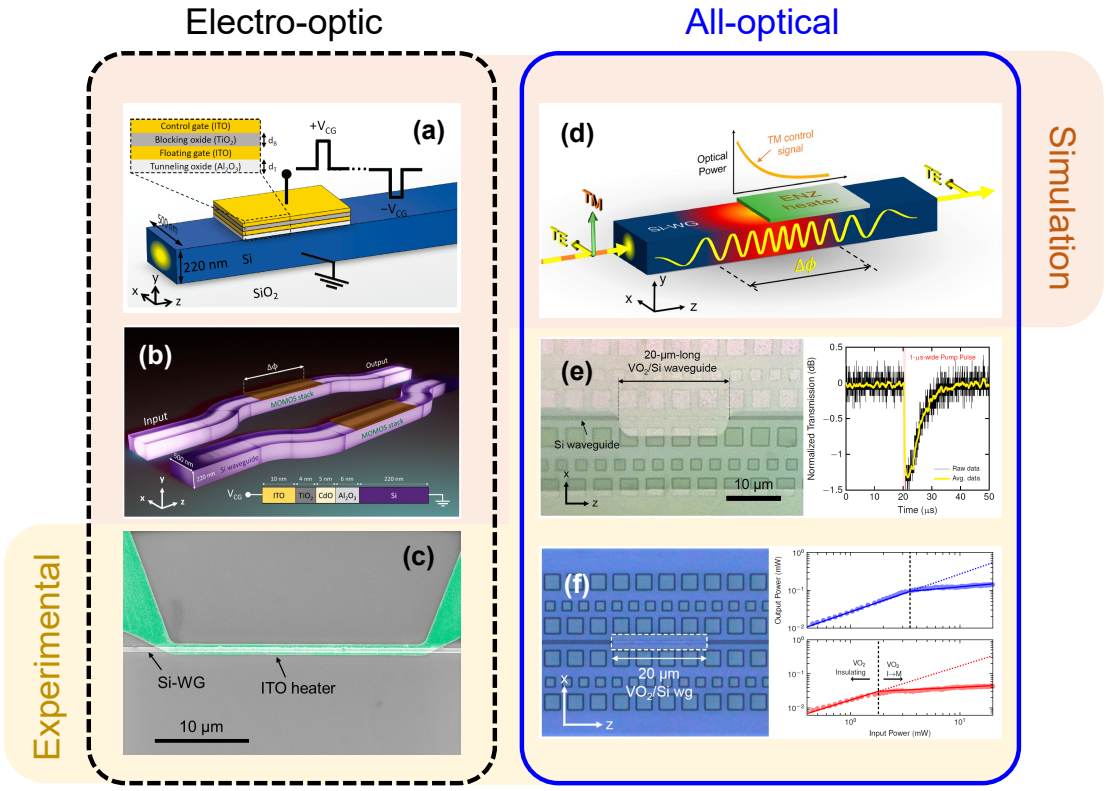

Fig. 5.1. Summary of the hybrid silicon photonic devices presented in this thesis. **(a)** Non-volatile ENZ electro-optic readout memory. **(b)** Non-volatile MZI switch. **(c)** Ultra-low loss ITO/Si phase shifter with optimized power consumption. **(d)** All-optical phase control in silicon waveguides with ENZ nanoheaters. **(e)** All-optical hybrid VO_2/Si waveguide absorption switch. **(f)** Low-threshold power and tunable power limiter based on an ultra-compact VO_2/Si waveguide.

Our devices may find potential utilization in a wide gamut of current and emerging PIC applications where such key features would be very appealing such as data centers, neural networks, neuromorphic computing, space communication systems, LiDAR, microwave photonics, photonic tensor cores, programmable photonics, quantum information processing, and many others.

Finally, the results directly derived from this thesis has been published in various peer-reviewed journal papers [Paper A] - [Paper H] and presented at diverse conferences [Conf. 1] - [Conf. 8]. The research framework of silicon photonics and integration of materials has also been applied to other devices and applications that have led to other contributions in journal papers [Paper 9] - [Paper 16] and conference proceedings [Conf. 9] - [Conf. 15].

Future directions

Several works and topics could be subject to further research beyond this thesis. First, it would be desirable to demonstrate the non-volatile devices and the all-optical phase shifter experimentally. In this regard, optimizing the TCO layers would be the main challenge, as well as preventing the formation of defects during the formation of the stacks in the non-volatile devices that could compromise the retention time. On the other hand, searching for and investigating other non-toxic and abundant TCOs in nature, such as AZO, would also be interesting. Meanwhile, we will outline hereinafter the guidelines to improve the characteristics of our devices and other interesting applications.

Current trends in photonic integrated circuits go toward co-packaging photonics and electronics in the same chip [2]. In this regard, microelectronic circuits employ voltage levels below 5 V. Hence, very short ITO heaters would be required, thereby raising the phase shifter temperature values that permanently damage the device. To circumvent this issue, we propose replacing a single ITO wire with a series of wires arranged in an electrical parallel configuration (see Fig. 5.2a) to make the driving voltage with CMOS-compatible values. To minimize optical loss, metallic contacts would connect ITO wires at a certain distance from the waveguide. Since the ITO resistivity is much higher than typical metals, Joule heating would mainly occur in the ITO heaters, even for ultra-short ITO microheaters. On the other hand, such an ITO resistor could be tapered to increase the heat dissipation in the silicon waveguide.

Our ENZ optical heaters could be used to build all-optical switches for optical routing. Thanks to relying on the cross-polarization for the control phase-shifted signal, this phase shifter could be embedded in a directional coupler or an MMI. In the first case, the routing would be applied to TE polarization. In contrast, TM polarization would efficiently drive the switch by neglecting its coupling to

the adjacent waveguide due to the large effective refractive index difference between both polarizations [343] (see Fig. 5.2b). Moreover, the design would not require different waveguide widths between both waveguides of the coupler because the effective refractive index of the TE polarization has a minimal variation in the ENZ/Si waveguide with respect to the waveguide without the ENZ cap. In the case of employing an MMI as an optical router, the ENZ heater would be deposited directly on top of the MMI (see Fig. 5.2c) [344]. Its position would be investigated to achieve the best performance.

Concerning VO_2/Si devices, the experimental demonstration of ultrafast switching times using an in-plane approach remains to be demonstrated. On the other hand, to reduce the insertion loss of all-optical VO_2 modulators, a similar approach as for the ENZ switches based on a directional coupler could be used while maintaining a high extinction ratio. In this way, the insertion loss would be minimized by designing the directional coupler to switch between the bar and cross states when the VO_2 changes from insulating to the metallic state, respectively.

The dramatic change in the refractive index with low optical powers could enable broadband non-reciprocal devices in silicon photonics without requiring power-hungry external bias using narrowband cavities [345–348], or non-CMOS-compatible magnetic materials [349]. Nonreciprocity can be achieved by combining nonlinear optical materials and asymmetric structures [350–352]. Notice that we do not use the term isolator since such VO_2-based non-reciprocal devices would not isolate the forward and backward signal when applied simultaneously. In this manner, we propose a possible guideline to achieve such non-reciprocal devices. Fig. 5.2d illustrates such a concept. A VO_2 patch is placed on top of a silicon structure exhibiting different optical power values at the position where the nonlinear material is placed depending on whether the light is injected forward or backward –not at the same time– [353]. Without the VO_2 layer, the silicon structure is reciprocal since the system is linear. Ideally, to achieve the best isolation ratio, the VO_2 patch must be placed where there is minimum power for the forward signal, whereas a maximum value for the backward. Thus, the forward signal is transmitted since the VO_2 remains in a low loss insulating state. In contrast, the backward signal is blocked because its optical power triggers the VO_2 phase transition and changes to the high-loss metallic state.

Finally, tailored activation functions for neural networks could be built by

replacing the uniform VO_2 layer of the optical limiter with a subwavelength pattern. Subwavelength structures are periodically arranged particles that can behave as artificial material with tailored optical properties [354–356]. The refractive index is usually engineered by tuning the duty cycle of the periodic subwavelength medium (see Fig. 5.2e). In this regard, one can obtain an extinction coefficient of VO_2/Si waveguides that vary with the propagation direction, which enables control of the absorption profile, and, thereby, the nonlinear response of the hybrid waveguide (see Fig. 5.2e inset).

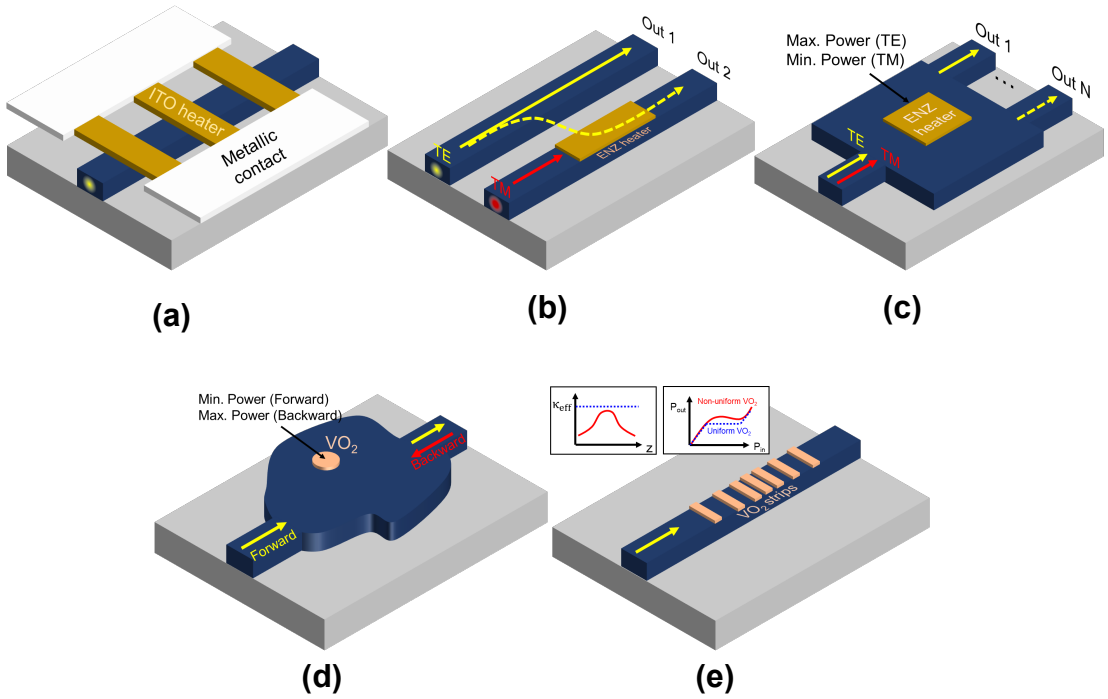

Fig. 5.2. Proposed silicon photonic devices using TCOs and VO_2 for future development. **(a)** Low-loss and CMOS-compatible voltage using ITO heaters in a parallel electrical configuration with high electrical conducting metallic contacts to minimize heat loss. **(b)** 1×2 all-optical thermo-optic switch based on a directional coupler. **(c)** $1 \times N$ all-optical thermo-optic switch based on a MMI. Ideally, the ENZ heater is placed in the MMI at the position where there is a maximum optical contrast between the TE and TM field distribution to minimize the insertion loss for TE while maximizing the energy consumption for TM. **(d)** Bias-free non-reciprocal device using an asymmetric silicon structure with a patch of VO_2 on top. Ideally, the VO_2 is placed in the asymmetric structure where exists maximum optical contrast between the field distribution of the forward (minimum power) and backward (maximum power) signal. **(e)** Optical nonlinear unit with tailored optical response for activation functionalities in photonic neural networks based on a silicon waveguide with a subwavelength patterned VO_2 layer on top.

Author's merits

Main contributions

Journal papers

[**Paper A**] **J. Parra**, I. Olivares, A. Brimont, and P. Sanchis, "Toward nonvolatile switching in silicon photonic devices," Laser & Photonics Reviews 6(15), 1-18 (2021).

[**Paper B**] **J. Parra**, I. Olivares, A. Brimont, and P. Sanchis, "Non-volatile epsilon-near-zero readout memory," Optics Letters 16(44), 3932 (2019). [Editors' Pick]

[**Paper C**] **J. Parra**, I. Olivares, F. Ramos, and P. Sanchis, "Ultra-compact non-volatile Mach-Zehnder switch enabled by a high-mobility transparent conducting oxide," Optics Letters 6(45), 1503 (2020).

[**Paper D**] **J. Parra**, J. Hurtado, A. Griol, and P. Sanchis, "Ultra-low loss hybrid ITO/Si thermo-optic phase shifter with optimized power consumption," Optics Express 7(28), 9393 (2020).

[**Paper E**] **J. Parra**, W. H. P. Pernice, and P. Sanchis, "All-optical phase control in nanophotonic silicon waveguides with epsilon-near-zero nanoheaters," Scientific Reports 9474(11), 1-9 (2021).

[Paper F] S. Cueff, J. John, Z. Zhang, **J. Parra**, J. Sun, R. Orobtchouk, S. Ramanathan, and P. Sanchis, "VO_2 nanophotonics," APL Photonics 11(5), 110901 (2020). [Featured Article]

[Paper G] **J. Parra**, T. Ivanova, M. Menghini, P. Homm, J.-P. Locquet, and P. Sanchis, "All-Optical Hybrid VO_2/Si Waveguide Absorption Switch at Telecommunication Wavelengths," IEEE Journal of Lightwave Technology 9(39), 2888 (2021).

[Paper H] **J. Parra**, J. Navarro-Arenas, M. Menghini, M. Recaman, J.-P. Locquet, and P. Sanchis, "Low-threshold power and tunable integrated optical limiter based on an ultracompact VO_2/Si waveguide," APL Photonics 12(6), 121301 (2021).

Conferences

[Conf. 1] **J. Parra**, J. Navarro-Arenas, J.-P. Locquet, and P. Sanchis, "Sub-milliwatt and tunable optical power limiters using vanadium dioxide in ultra-compact silicon waveguides," in *23^{nd} European Conference on Integrated Optics (ECIO 2022)*, 357-359, Milan (Italy), 2022.

[Conf. 2] **J. Parra**, T. Ivanova, M. Menghini, P. Homm, J.-P. Locquet, and P. Sanchis, "Integrated all-optical VO_2/Si waveguide switch" in *33^{rd} IEEE Photonics Conference (IPC 2020)*, 1-2, Online, 2020.

[Conf. 3] **J. Parra**, T. Ivanova, M. Menghini, P. Homm, J.-P. Locquet, and P. Sanchis, "Ultra-compact low-power hybrid VO_2/Si waveguide switch," in *22^{nd} European Conference on Integrated Optics (ECIO 2020)*, 1-3, Online, 2020.

[Conf. 4] **J. Parra**, S. Hernández, O. Blázquez, B. Garrido, and P. Sanchis, "Integration of transparent conducting oxides in photonic circuits for enabling high performance functionalities," in *E-MRS Fall Meeting 2019*, 1-2, Warsaw (Poland), 2019.

[Conf. 5] **J. Parra**, I. Olivares, A. Brimont, and P. Sanchis, "Non-volatile indium tin oxide electro-optic switch," in *16^{th} IEEE International Conference on Group IV Photonics (GFP 2019)*, 1-2, Singapore, 2019.

[Conf. 6] **J. Parra**, and P. Sanchis, "Indium tin oxide for a new generation of photonic devices," in *XXXVII Reunión Bienal de la Real Sociedad Española de Física*, Zaragoza (Spain), 2019. [Best poster award]

[Conf. 7] **J. Parra**, I. Olivares, A. Brimont, J. L. Frieiro, O. Blázquez, and P. Sanchis, "Non-Volatile and Ultra-Compact Photonic Memory," in *21st European Conference on Integrated Optics (ECIO 2019)*, 1-3, Ghent (Belgium), 2019.

[Conf. 8] **J. Parra**, I. Olivares, J. L. Frieiro, O. Blázquez, S. Hernández, B. Garrido, and P. Sanchis, "Transparent Conducting Oxides for Optoelectronics and Biosensing Applications," in *20th International Conference on Transparent Optical Networks (ICTON 2018)*, 1-4, Bucharest (Romania), 2018. [Invited]

Other contributions

Journal papers

[Paper 9] J. Navarro-Arenas, **J. Parra**, and P. Sanchis, "Comparative performance evaluation of transparent conducting oxides with different mobilities for all-optical switching in silicon," submitted.

[Paper 10] **J. Parra**, J. Navarro-Arenas, M. Kovylina, and P. Sanchis, "Impact of GST thickness on GST-loaded silicon waveguides for optimal switching," Scientific Reports 9774(12), 1-9 (2022).

[Paper 11] B. Chmielak, S. Suckow, **J. Parra**, V. C. Duarte, T. Mengual, M. A. Piqueras, A. L. Giesecke, M. Lemme, and P. Sanchis, "High-performance grating coupler for ultralow-loss Si_3N_4-based platform," Optics Letters 47(10), 2498 (2022).

[Paper 12] J. Navarro-Arenas, **J. Parra**, and P. Sanchis, "Ultrafast all-optical phase switching enabled by epsilon-near-zero materials in silicon," Optics Express 30(9), 14518 (2022).

[Paper 13] I. Olivares, **J. Parra**, and P. Sanchis, "Non-Volatile Photonic Memory Based on a SAHAS Configuration," IEEE Photonics Journal 2(13), 1-9

(2021).

[Paper 14] I. Olivares, **J. Parra**, A. Brimont, and P. Sanchis, "Enhancing Pockels effect in strained silicon waveguides," Optics Express 19(27), 26882 (2019).

[Paper 15] L. D. Sánchez, I. Olivares, **J. Parra**, M. Menghini, P. Homm, J.-P. Locquet, and P. Sanchis, "Experimental demonstration of a tunable transverse electric pass polarizer based on hybrid VO_2/silicon technology," Optics Letters 15(43), 3650 (2018).

[Paper 16] I. Olivares, L. Sánchez, **J. Parra**, R. Larrea, A. Griol. M. Menghini, P. Homm, L.-W. Jang, B. van Bilzen, J. W. Seo, J.-P. Locquet, and P. Sanchis, "Optical switching in hybrid VO_2/Si waveguides thermally triggered by lateral microheaters," Optics Express 10(26), 12387 (2018).

Conferences

[Conf. 9] S. Suckow, B. Chmielak, **J. Parra**, V. C. Duarte, T. Mengual, M. A. Piqueras, A. L. Giesecke, M. C. Lemme, and P. Sanchis, "Enhancing Si_2N_4 grating couplers on an ultralow-loss photonic platfom with self-aligned amorphous Si," in *48^{th} international conference on Micro and Nano Engineering - Eurosensors (MNE-ES2022)*, Leuven (Belgium), 2022.

[Conf. 10] E. Pinilla-Cienfuegos, A. Vicente, **J. Parra**, J. Navarro-Arenas, P. Sanchis, R. Sanchis-Gual, R. Torres-Cavanillas, M. Gimenez-Marques, and E. Coronado, "Optical bistability on the integration of a molecular nanomaterial in silicon photonics," in *XXXVIII Reunión Bienal de la Real Sociedad Española de Física*, Murcia (Spain), 2022.

[Conf. 11] J. Navarro-Arenas, **J. Parra**, and P. Sanchis, "Comparative performance evaluation of transparent conducting oxides with moderate mobility for all-optical switching in silicon," in *23^{rd} European Conference on Integrated Optics (ECIO 2022)*, 189-191, Milan (Italy), 2022. [Best poster award]

[Conf. 12] E. Pinilla-Cienfuegos, A. Vicente, **J. Parra**, J. Navarro-Arenas, P. Sanchis, R. Sanchis-Gual, R. Torres-Cavanillas, M. Gimenez-Marques, E.

Coronado, "Optical bistability based on the integration of a molecular nanomaterial in silicon photonics," in *APS March Meeting 2022*, 1-1, Chicago (USA), 2022.

[Conf. 13] **J. Parra**, A. Santomé, J. Navarro-Arenas, and P. Sanchis, "Fast volatile response in GST/Si waveguides for all-optical modulation," in *17th IEEE International Conference on Group IV Photonics (GFP 2021)*, 1-2, Online, 2021.

[Conf. 14] J. Navarro-Arenas, M. Ribera, **J. Parra**, and P. Sanchis, "Ultra-fast all-optical phase switch based on a CdO/Si waveguide," in *17th IEEE International Conference on Group IV Photonics (GFP 2021)*, 1-2, Online, 2021.

[Conf. 15] A. Santomé, H. Urgelles, **J. Parra**, and P. Sanchis, "High-performance optical switches based on GST/Si waveguides," in *1st Spintronics, Photonics, Phononics, and Magneto-Optics Online International Conference (SPPM 2021)*, 20-20, Online, 2021.

[Conf. 16] P. Sanchis, **J. Parra**, A. Santomé, M. Ribera, and J. Navarro-Arenas, "Optical switching in silicon photonics with phase change materials," in *1st Spintronics, Photonics, Phononics, and Magneto-Optics Online International Conference (SPPM 2021)*, 20-20, Online, 2021.

[Conf. 17] E. Pinilla-Cienfuegos, **J. Parra**, A. Brimont, I. Olivares, R. Sanchis-Gual, R. Torres-Cavanillas, and P. Sanchis, "New Molecular-Based Materials for Enabling Electro-Optical Bistability in the Silicon Photonics Platform," in *21st International Conference on Transparent Optical Networks (ICTON 2019)*, 1-3, Angers (France), 2019. [Invited]

A

Appendices

A.1 Simulations methods

A.1.1 Materials' properties

The refractive index and thermal constants used for optical and thermal simulations are shown in Tables A.1-A.3. For the silicon thermo-optic coefficient we used 1.86×10^{-4} K^{-1} [287].

Table A.1: Refractive index of the dielectric materials and metals used for optical simulations at $\lambda = 1550$ nm.

Air	Si	SiO_2	SiN	Al_2O_3	TiO_2	Ti
1	3.476	1.444	1.97	1.66	2.43	$4.04 + j3.82$

Table A.2: Refractive index of the active materials (TCOs and VO_2) used for optical simulations at $\lambda = 1550$ nm.

ITO (Chs. 2.2,2.3,3.2)		CdO (Ch. 2.3)		TCO-ENZ (Ch. 3.3)	VO_2 (Chs. 4.2,4.3)	
$N = 10^{19}$ cm^{-3}	$N = 6.5\times10^{20}$ cm^{-3}	$N = 2\times10^{19}$ cm^{-3}	$N = 2.3\times10^{20}$ cm^{-3}		Insulator (T = 30 °C)	Metal (T = 80 °C)
$1.958 + j0.002$	$0.537 + j0.537$	$2.268 + j0.002$	$1.179 + j0.042$	$0.291 + j0.291$	$2.758 + j0.451$	$1.788 + j2.574$

Table A.3: Thermal constants of the materials used for simulations.

Material	Thermal conductivity (W m^{-1} K^{-1})	Specific heat capacity (J kg^{-1} K^{-1})	Density (kg m^{-3})
Si	148	703	2230
SiO_2	1.38	709	2203
SiN	14	170	2500
ITO	11	1290	7100
Ti	23	523	4500

A.1.2 Optical simulations

Optical modes

The optical modes of the hybrid waveguides were obtained by 2D FEM simulations with RSoft FemSIM simulation tool. Fig. A.1 depicts the domain used for such simulations. This usually comprised a region from $x = -1$ to $+1$ µm and $y = -1$ to $+1$ µm (Fig. A.1a). To reduce the computational cost, for certain cases, symmetric boundary conditions were applied at $x = 0$ µm considering the symmetry in the x-axis of the waveguide (Fig. A.1b). The default grid size for the x-axis was set to 20 nm. A non-uniform mesh was used for the y-axis to obtain good accuracy within the remaining layers. In this case, the default grid size was set to 5 nm with a minimum subdivision of 10 points.

Coupling and insertion losses

3D-FDTD simulations using the RSoft FullWAVE simulation tool were conducted to investigate the coupling and insertion losses of the hybrid waveguides. Usually, the simulated structures comprised a silicon waveguide with the hybrid device embedded. Fig. A.2 shows the simulated domain in the YZ plane. The XZ plane is similar to Fig. A.1. To avoid reflections, perfectly matched layer (PML) boundary conditions were applied to all the boundaries. Each PML boundary was

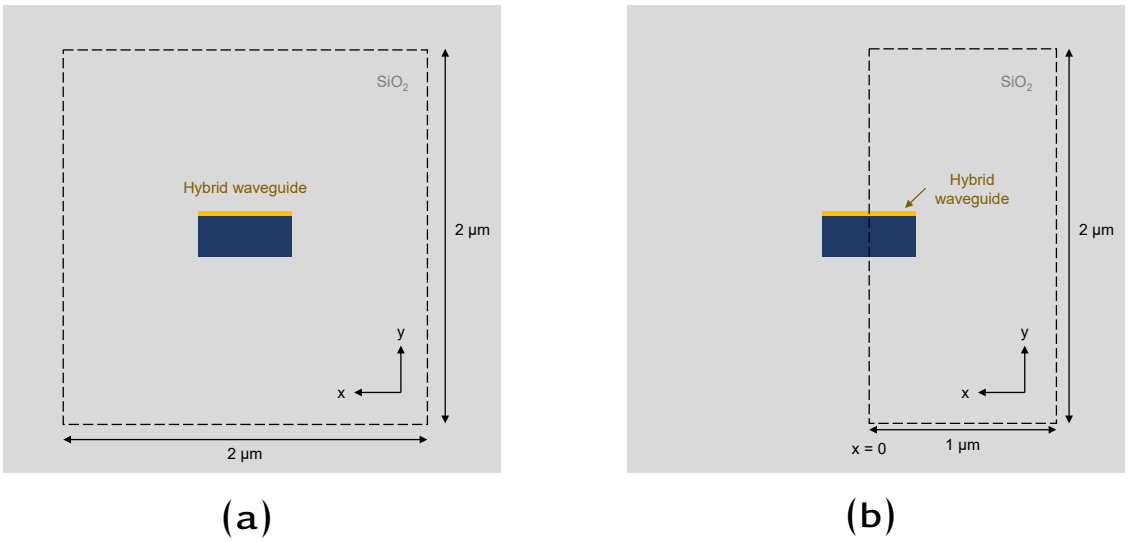

Fig. A.1. Illustration of the simulated region used in 2D-FEM to obtain the optical modes of the hybrid waveguides **(a)** without and **(b)** with symmetric boundary condition.

formed by 10 PML cells. In some cases, the symmetric boundary conditions were applied at $x = 0$ µ to reduce the computational memory and time. The structure was extended completely through the PML region to avoid any reflection. For the x-axis and z-axis, we used a grid size of 20 nm by default. Similar to FEM simulations, a non-uniform mesh was employed for the hybrid waveguide with a grid size of 5 nm and a minimum division of 10 points. A standard silicon waveguide's TE or TM polarized mode was used as optical excitation. The launch field was placed at a certain distance from the $-z$ boundary to avoid interacting with the PML. Finally, different monitors were usually employed along the z-axis to measure the optical. The monitors' size was 1 µm × 1 µm approx.

A.1.3 Thermal simulations

Electrical microheaters

Because the microheater does not vary in the propagation direction of the light, the temperature in the silicon waveguide can be obtained by solving the following

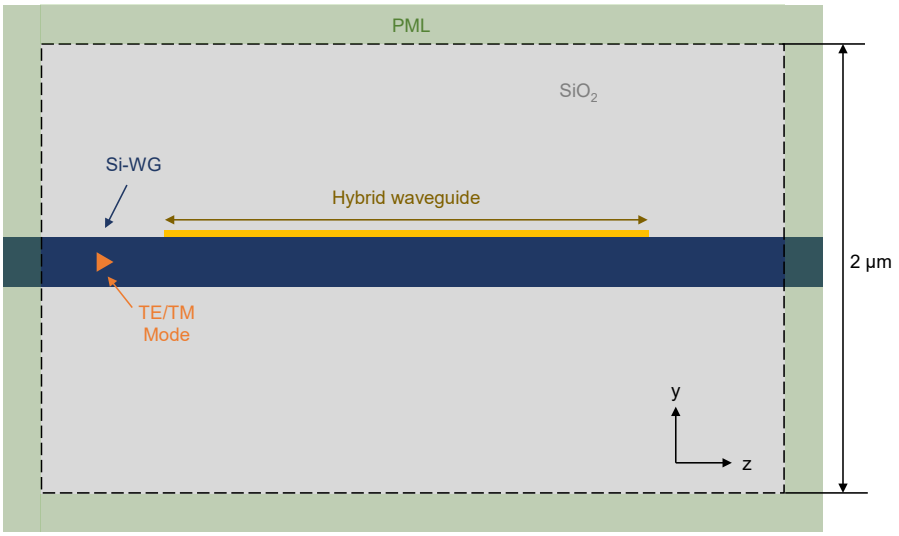

Fig. A.2. Illustration (not to scale) of the simulated region (YZ plane) used in 3D-FDTD to obtain the coupling and insertion losses of the hybrid waveguide. Monitors are not shown for better clarity.

conductive heat equation for the cross-section:

$$\nabla(-k\nabla T) + Dc\frac{\partial T}{\partial t} = Q \tag{A.1}$$

where k is the thermal conductivity, D is the density, c is the specific heat capacity, T is the temperature, t is the time, and Q is the heat source. This latter can be defined as:

$$Q = \frac{P_{\text{elec}}}{w_{\text{h}} t_{\text{h}} l_{\text{h}}} \tag{A.2}$$

where P_{elec} stands for the electrical power consumed by the heater, and w_{h}, t_{h} and l_{h} is the width, thickness, and length of the microheater, respectively.

2D thermal simulations were conducted by solving Eq. A.1 in the steady-state and the time-domain with COMSOL Multiphysics simulation tool. We used the materials' thermal properties shown in A.3. Fig. A.3 sketches the simulated structure. This comprised the silicon substrate (20 µm × 10 µm), a 2-µm-thick SiO_2 under-cladding, the standard silicon waveguide, the SiO_2/SiN upper-cladding, and the 2-µm-wide and 100-nm-thick microheater. A non-uniform tetrahedral mesh was used, comprising different element sizes. The microheater and silicon waveguide was discretized with sizes between 1 nm and 10 nm,

whereas the remaining domains were formed by elements between 100 nm and 500 nm. Convective heat flux was set as a boundary condition on the top boundary with a heat transfer coefficient $h = 15$ W m^{-2} K^{-1}. The temperature boundary condition for the remaining boundaries was used by setting $T = 293.15$ K (20 ºC). The heat source in the steady-state was defined following Eq. (A.2). For time-domain simulations, that value was used for the amplitude of a 200-µs-wide square pulse using a time step of 50 ns.

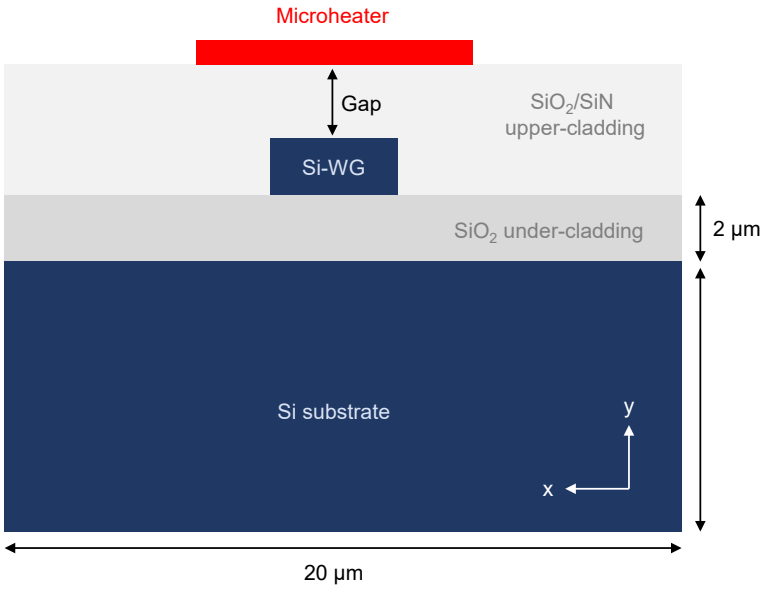

Fig. A.3. Illustration (not to scale) of the 2D simulated region to obtain the heat distribution using electrical microheaters.

ENZ optical heat source

Optical heat sources are self-heated materials caused by optical power that is absorbed. Under the assumption that there is only one lossy material in the hybrid waveguide and the field distribution (XY plane) within this material is almost uniform, the optical heat source (Q) can be approximated as:

$$Q = \frac{P\Gamma}{wt}\frac{\partial}{\partial z}\left[1 - P_{\mathrm{WG}}(z)\right] \tag{A.3}$$

where P is the optical power of the optical mode, Γ is the coupling efficiency between the silicon and hybrid waveguide, w and t are the width and thickness

of the lossy material, respectively, and $P_{WG}(z)$ is the normalized optical power within the hybrid waveguide along the propagation direction. Considering that $P_{WG}(z)$ can be described by a single optical mode, the value of Q is then

$$Q = \frac{P\Gamma}{wt}\frac{4\pi\kappa_{eff}}{\lambda}\exp\left[-\frac{4\pi\kappa_{eff}}{\lambda}(z-z_0)\right], \tag{A.4}$$

where κ_{eff} is the effective extinction coefficient of the propagated mode in the hybrid waveguide, and z_0 is the point at which the hybrid waveguide starts.

In the case of the ENZ/Si waveguide, we consider that $P_{WG}(z)$ fits the excitation of the ENZ modes 0 and 1 in the short and long region, respectively, then $Q_{ENZ} = Q_{ENZ_0} + Q_{ENZ_1}$. The value of $Q_{ENZ_{0/1}}$ is

$$Q_{ENZ_0} = \frac{P_{TM}\Gamma}{w_{ENZ}t_{ENZ}}\frac{4\pi\kappa_{eff}^{ENZ_0}}{\lambda}\exp\left[-\frac{4\pi\kappa_{eff}^{ENZ_0}}{\lambda}(z-z_0)\right] \tag{A.5}$$

and

$$Q_{ENZ_1} = P_{WG}(z_1)\frac{4\pi\kappa_{eff}^{ENZ_1}}{\lambda}\exp\left[-\frac{4\pi\kappa_{eff}^{ENZ_1}}{\lambda}(z-z_1)\right], \tag{A.6}$$

where z_1 is the point from which the optical attenuation is described by the ENZ_1 mode.

3D thermal simulations were conducted by solving the heat conduction equation in the steady-state and the time domain with COMSOL Multiphysics simulation tool. Contribution from radiation heat transfer was assumed to be negligible. Fig. A.4 illustrates the structure used for such simulations. The ENZ/Si waveguide was defined using a 10-nm-thick ITO layer with 10 µm of length. We used the materials' thermal properties shown in A.3. The hybrid waveguide was placed in the middle (z-axis) of the simulation region, and the length of the Si-only waveguide extended to 80 µm. The influence of the silicon substrate was taken into account, setting a size (width × height) of 40 µm × 20 µm. The height of the SiO_2 under- and upper-cladding was 3 µm and 1.22 µm (1 µm + Si waveguide height). A non-uniform tetrahedral mesh was used, comprising different element sizes. The ITO layer (heat source) was discretized with elements of sizes between 1 nm and 50 nm. The silicon waveguide utilized elements between 50 nm and 200 nm. Finally, the remaining domains (substrate, under-, and upper-cladding) were formed by elements of between 500 nm and 3 µm. Convective

heat flux was set as a boundary condition on top of the upper cladding with a heat transfer coefficient $h = 5$ W m^{-2} K^{-1}. The temperature boundary condition for the remaining boundaries was used by setting $T = 293.15$ K (20 °C). The heat source in the steady-state was defined following Eqs. (A.5) and (A.6). For time-domain simulations, that value was used for the amplitude of a 50-µs-wide square pulse using a time step of 25 ns.

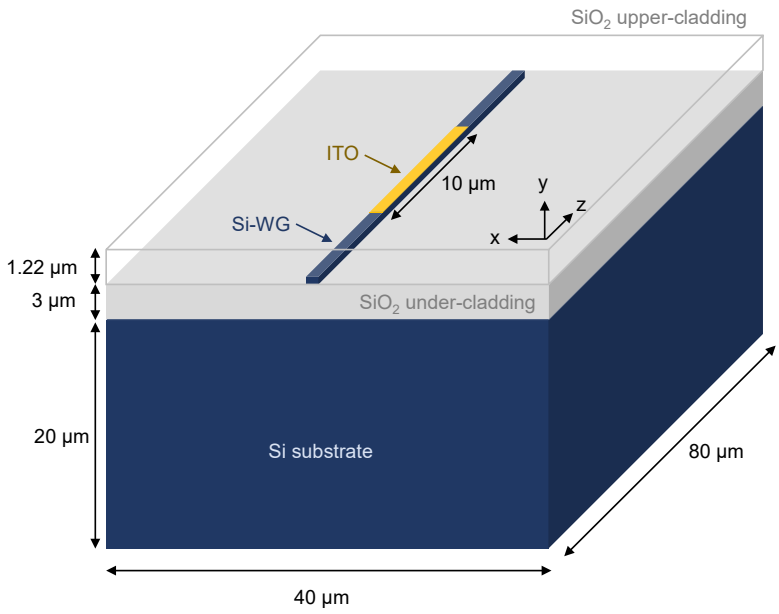

Fig. A.4. Illustration (not to scale) of the 3D simulated region to obtain the heat distribution using ITO as an optical heater.

A.2 Fabrication processes

ITO/Si thermo-optic phase shifter

The ITO/Si phase shifters were fabricated at NTC-UPV. The fabrication of the silicon waveguides was based on the use of standard SOI samples from SOITEC wafers with a top silicon layer thickness of 220 nm (resistivity $\rho \sim 1-10\ \Omega\ \mathrm{cm}^{-1}$, with a lightly p-type background doping of $\sim 10^{15}\ \mathrm{cm}^{-3}$). The fabrication is based on an electron beam direct writing process performed on a coated 100 nm hydrogen silsesquioxane (HSQ) resist film. The mentioned electron beam exposure, performed with a Raith 150 tool, was optimized in order to reach the required dimensions, employing an acceleration voltage of 30 keV and an aperture size of 30 μm. After developing the HSQ resist using tetramethylammonium hydroxide (TMAH) as the developer, the resist patterns were transferred into the SOI samples, employing an optimized inductively coupled plasma-reactive ion etching (ICP-RIE) process with fluoride gases (SF_6 and CF_4).

We fabricated two copies in different samples. Each one was covered with a target thickness of 320 nm and 660 nm of SiO_2. The SiO_2 upper-cladding was deposited atop the SOI samples by plasma-enhanced chemical vapor deposition (PECVD) performed with a Centura 5200 tool from Applied Materials.

Afterward, the ITO microheaters were patterned with a second e-beam lithography process. Alignment marks in the silicon level were utilized to ensure the right positioning of the microheaters. A 100-nm-thick target ITO layer was deposited from a In_2O_3/SnO_2 90/10 wt % target and using DC sputtering in a ArO_2 atmosphere, with a subsequent lift-off process. Finally, a post-annealing process was carried out for 30 minutes in a tubular oven in forming gas (4% H_2 in Ar) atmosphere at 600 ºC.

VO_2/Si waveguides

The described hybrid VO_2/Si waveguides have been fabricated on a SOI wafer with a buried oxide layer thickness of 2 μm. The silicon waveguide structures were first fabricated at IHP CMOS line by a standard process using deep UV (DUV) photolithography. The wafer was then polished by chemical mechanical planarization (CMP) and diced for VO_2 deposition. At KU Leuven, a 40-nm thick amorphous VO_x layer was grown by MBE. After the deposition, a lift-off pro-

cess was done to remove the VO_x deposited on the undesired regions. Finally, an ex-situ annealing process at 400 ºC in forming gas was carried out to form a polycrystalline VO_2 layer. Finally, at NTC-UPV, a 700-nm-thick SiO_2 upper-cladding was deposited by PECVD with a Centura 5200 tool from Applied Materials to avoid VO_2 deterioration.

A.3 Characterization setups

ITO/Si thermo-optic phase shifters

The experimental setup used to characterize the ITO/Si phase shifters is shown in Fig. A.5. A tunable CW laser [Photonetics ECL-1600] was used as a light source with an output power of 0 dBm. The polarization of the optical fiber was adjusted to TE or TM by using a 3-paddle polarization controller (PC) [Thorlabs FP032] before injecting the light into the chip. Fiber-to-chip coupling was achieved using standard TE and TM grating couplers with an incident angle of 10º, and fibers were aligned using 3-axes manual translation stages. On the other hand, square electrical pulses were generated using an arbitrary waveform generator (AWG) [Rigol DG1062Z] and connected to the ITO electrodes with DC probes. The output was amplified with an EDFA [Amonics 33-B-FA] working in the telecom C-band. The output signal was recorded by using a high-speed photodiode [u^{2}t XPDV2120R] and an oscilloscope [Rigol DS1000E].

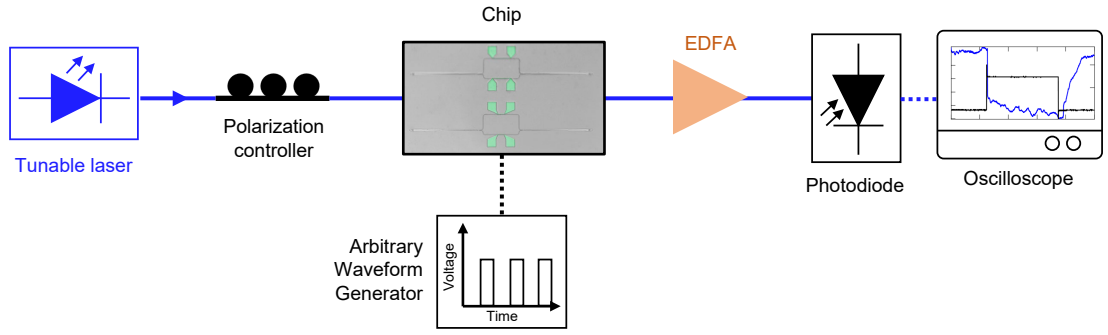

Fig. A.5. Setup employed for the characterization of ITO/Si phase shifters. Solid (dotted) lines stand for the optical fibers (electrical wires).

All-optical VO_2/Si waveguides

The experimental setup used for characterizing the power limiting response of the VO_2/Si waveguides is shown in Fig. A.6. As the light source, we use a tunable CW laser [Photonetics ECL-1600] with an output power of 0 dBm together with an EDFA [Amonics 33-B-FA] working in the telecom C-band. The polarization of the optical fiber was adjusted to TE by using a 3-paddle PC [Thorlabs FP032].

Fiber-to-chip coupling was achieved using standard TE grating couplers with an incident angle of 10º, and fibers were aligned using 3-axes manual translation stages. The chip temperature during the measurements was controlled using a Peltier device. Finally, the output power was recorded using a high-sensitivity photodiode [Thorlabs S155C] and a power meter [Thorlabs PM320].

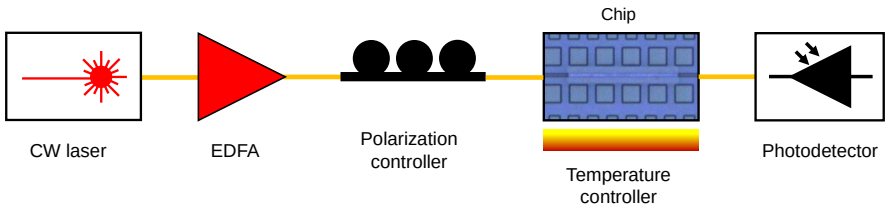

Fig. A.6. Setup employed for the characterization of the power limiting response of VO_2/Si waveguides.

To perform all-optical switching and characterize the temporal dynamics of VO_2/Si waveguides, we used a pump-probe scheme as shown in Fig. A.7. On one hand, the probe signal was generated by using a CW laser at 1550 nm [Photonetics ECL-1600] with an output power of 3 dBm and set to TE polarization with a 3-paddle manual polarization controller (PR) [Thorlabs FP032]. On the other hand, the pump pulses were generated from another CW laser [Agilent 81689A] at 1560 nm with an output power of 5 dBm together with an external electro-optic modulator (EOM) [Codeon Mach-40] and an arbitrary waveform generator [Rigol DG1062Z]. The output of the EOM was amplified with an EDFA [Amonics 33-B-FA]. Then, the high-power pump signal was TE-polarized with another PR and band-pass filtered using a 3-nm tunable filter [Tecos FC-1565B-2-3] in order to remove the noise introduced by the EDFA. Before injecting the probe and pump signals into the chip, both were combined using a 3 dB directional coupler [Thorlabs TW1550R5A1]. Like in the static characterization, fiber-to-chip coupling was achieved using standard TE grating couplers with an incident angle of 10º, and fibers were aligned using 3-axes manual translation stages. The output of the chip was band-pass filtered with a 1-nm tunable filter [Tecos FC-1565B-1-1] to remove the pump signal, amplified with a second EDFA [Photonetics EDFA C-17] to compensate for the chip optical loss, and filtered again with another 1-nm band-pass filter [Tecos FC-1565B-1-1] to remove the EDFA noise. Finally, the temporal response was recorded by using a high-speed photodiode

[u^{2}t XPDV2120R] and an oscilloscope [Rigol DS1000E].

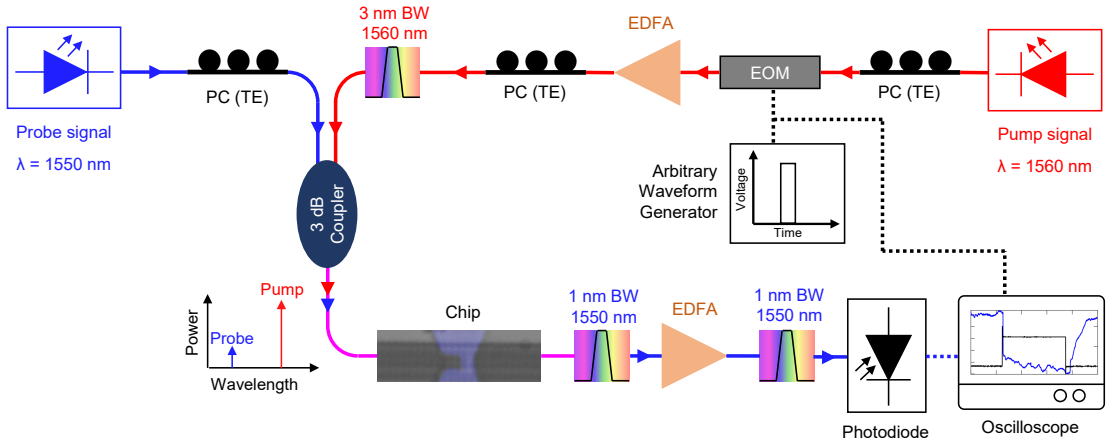

Fig. A.7. Setup employed to perform dynamic all-optical switching in VO_2/Si waveguides based on a pump-probe scheme. Solid (dotted) lines are the optical fibers (electrical wires).

Bibliography

[1] European Commission, *Re-finding Industry - Defining Innovation* (2018).

[2] N. Margalit, C. Xiang, S. M. Bowers, A. Bjorlin, R. Blum, and J. E. Bowers, "Perspective on the future of silicon photonics and electronics," Applied Physics Letters **118**, 220501 (2021).

[3] A. H. Atabaki, S. Moazeni, F. Pavanello, H. Gevorgyan, J. Notaros, L. Alloatti, M. T. Wade, C. Sun, S. A. Kruger, H. Meng, K. A. Qubaisi, I. Wang, B. Zhang, A. Khilo, C. V. Baiocco, M. A. Popović, V. M. Stojanović, and R. J. Ram, "Integrating photonics with silicon nanoelectronics for the next generation of systems on a chip," Nature **560** (2018).

[4] Q. Cheng, S. Rumley, M. Bahadori, and K. Bergman, "Photonic switching in high performance datacenters [Invited]," Optics Express **26**, 16022 (2018).

[5] IEA, "Data Centres and Data Transmission Networks," (2021).

[6] A. N. Tait, T. Ferreira de Lima, M. A. Nahmias, H. B. Miller, H.-T. Peng, B. J. Shastri, and P. R. Prucnal, "Silicon Photonic Modulator Neuron," Physical Review Applied **11**, 064043 (2019).

[7] Y. Shen, N. C. Harris, D. Englund, and M. Soljacic, "Deep learning with coherent nanophotonic circuits," Nature Photonics **11**, 441–447 (2017).

[8] B. J. Shastri, A. N. Tait, T. Ferreira de Lima, W. H. P. Pernice, H. Bhaskaran,

C. D. Wright, and P. R. Prucnal, "Photonics for artificial intelligence and neuromorphic computing," Nature Photonics **15**, 102–114 (2021).

[9] A. Radovic, M. Williams, D. Rousseau, M. Kagan, D. Bonacorsi, A. Himmel, A. Aurisano, K. Terao, and T. Wongjirad, "Machine learning at the energy and intensity frontiers of particle physics," Nature **560**, 41–48 (2018).

[10] J. Han, A. Jentzen, and W. E, "Solving high-dimensional partial differential equations using deep learning," Proceedings of the National Academy of Sciences **115**, 8505–8510 (2018).

[11] T. W. Hughes, M. Minkov, Y. Shi, and S. Fan, "Training of photonic neural networks through in situ backpropagation and gradient measurement," Optica **5**, 864 (2018).

[12] J. He, T. Dong, and Y. Xu, "Review of Photonic Integrated Optical Phased Arrays for Space Optical Communication," IEEE Access **8**, 188284–188298 (2020).

[13] X. Sun, L. Zhang, Q. Zhang, and W. Zhang, "Si Photonics for Practical LiDAR Solutions," Applied Sciences **9**, 4225 (2019).

[14] Y. Lim, H. Park, B. Kang, K. Kim, D. Yang, and S. Lee, "Holography, Fourier Optics, and Beyond Photonic Crystals: Holographic Fabrications for Weyl Points, Bound States in the Continuum, and Exceptional Points," Advanced Photonics Research **2**, 2100061 (2021).

[15] M. J. Heck, "Highly integrated optical phased arrays: photonic integrated circuits for optical beam shaping and beam steering," Nanophotonics **6**, 93–107 (2017).

[16] J. Sun, E. Timurdogan, A. Yaacobi, E. S. Hosseini, and M. R. Watts, "Large-scale nanophotonic phased array," Nature **493**, 195–199 (2013).

[17] S. A. Miller, Y.-C. Chang, C. T. Phare, M. C. Shin, M. Zadka, S. P. Roberts, B. Stern, X. Ji, A. Mohanty, O. A. Jimenez Gordillo, U. D. Dave, and M. Lipson, "Large-scale optical phased array using a low-power multi-pass silicon photonic platform," Optica **7**, 3 (2020).

[18] J. Yao, "Microwave Photonics," Journal of Lightwave Technology **27**, 314–335 (2009).

[19] D. Marpaung, J. Yao, and J. Capmany, "Integrated microwave photonics," Nature Photonics **13**, 80–90 (2019).

[20] M. Miscuglio and V. J. Sorger, "Photonic tensor cores for machine learning," Applied Physics Reviews **7**, 031404 (2020).

[21] W. Bogaerts and A. Rahim, "Programmable Photonics: An Opportunity for an Accessible Large-Volume PIC Ecosystem," IEEE Journal of Selected Topics in Quantum Electronics **26**, 1–17 (2020).

[22] N. C. Harris, G. R. Steinbrecher, M. Prabhu, Y. Lahini, J. Mower, D. Bunandar, C. Chen, F. N. C. Wong, T. Baehr-Jones, M. Hochberg, S. Lloyd, and D. Englund, "Quantum transport simulations in a programmable nanophotonic processor," Nature Photonics **11**, 447–452 (2017).

[23] J. Feldmann, N. Youngblood, M. Karpov, H. Gehring, X. Li, M. Stappers, M. Le Gallo, X. Fu, A. Lukashchuk, A. S. Raja, J. Liu, C. D. Wright, A. Sebastian, T. J. Kippenberg, W. H. P. Pernice, and H. Bhaskaran, "Parallel convolutional processing using an integrated photonic tensor core," Nature **589**, 52–58 (2021).

[24] W. Bogaerts, D. Pérez, J. Capmany, D. A. B. Miller, J. Poon, D. Englund, F. Morichetti, and A. Melloni, "Programmable photonic circuits," Nature **586**, 207–216 (2020).

[25] J. Wang, F. Sciarrino, A. Laing, and M. G. Thompson, "Integrated photonic quantum technologies," Nature Photonics **14**, 273–284 (2020).

[26] N. C. Harris, J. Carolan, D. Bunandar, M. Prabhu, M. Hochberg, T. Baehr-Jones, M. L. Fanto, A. M. Smith, C. C. Tison, P. M. Alsing, and D. Englund, "Linear programmable nanophotonic processors," Optica **5**, 1623 (2018).

[27] R. Soref, J. Schmidtchen, and K. Petermann, "Large single-mode rib waveguides in GeSi-Si and Si-on-SiO2," IEEE Journal of Quantum Electronics **27**, 1971–1974 (1991).

[28] D. Taillaert, W. Bogaerts, P. Bienstman, T. Krauss, P. Van Daele, I. Moerman, S. Verstuyft, K. De Mesel, and R. Baets, "An out-of-plane grating coupler for efficient butt-coupling between compact planar waveguides and single-mode fibers," IEEE Journal of Quantum Electronics **38**, 949–955 (2002).

[29] T. Shoji, T. Tsuchizawa, T. Watanabe, K. Yamada, and H. Morita, "Low loss mode size converter from 0.3 um square Si wire waveguides to singlemode fibres," Electronics Letters **38**, 1669 (2002).

[30] V. R. Almeida, C. A. Barrios, R. R. Panepucci, and M. Lipson, "All-optical control of light on a silicon chip," Nature **431**, 1081–1084 (2004).

[31] H. Rong, R. Jones, A. Liu, O. Cohen, D. Hak, A. Fang, and M. Paniccia, "A continuous-wave Raman silicon laser," Nature **433**, 725–728 (2005).

[32] A. Liu, R. Jones, L. Liao, D. Samara-Rubio, D. Rubin, O. Cohen, R. Nicolaescu, and M. Paniccia, "A high-speed silicon optical modulator based on a metal-oxide-semiconductor capacitor," Nature **427**, 615–618 (2004).

[33] A. W. Fang, H. Park, O. Cohen, R. Jones, M. J. Paniccia, and J. E. Bowers, "Electrically pumped hybrid AlGaInAs-silicon evanescent laser," Optics Express **14**, 9203 (2006).

[34] L. Vivien, M. Rouvière, J.-M. Fédéli, D. Marris-Morini, J. F. Damlencourt, J. Mangeney, P. Crozat, L. El Melhaoui, E. Cassan, X. Le Roux, D. Pascal, and S. Laval, "High speed and high responsivity germanium photodetector integrated in a Silicon-On-Insulator microwaveguide," Optics Express **15**, 9843 (2007).

[35] R. M. Briggs, I. M. Pryce, and H. A. Atwater, "Compact silicon photonic waveguide modulator based on the vanadium dioxide metal-insulator phase transition," Optics Express **18**, 11192 (2010).

[36] M. Rudé, J. Pello, R. E. Simpson, J. Osmond, G. Roelkens, J. J. G. M. van der Tol, and V. Pruneri, "Optical switching at 1.55 um in silicon racetrack resonators using phase change materials," Applied Physics Letters **103**, 141119 (2013).

[37] M. Liu, X. Yin, E. Ulin-Avila, B. Geng, T. Zentgraf, L. Ju, F. Wang, and X. Zhang, "A graphene-based broadband optical modulator," Nature **474**, 64–67 (2011).

[38] V. J. Sorger, N. D. Lanzillotti-Kimura, R.-M. Ma, and X. Zhang, "Ultra-compact silicon nanophotonic modulator with broadband response," Nanophotonics **1**, 17–22 (2012).

[39] M. He, M. Xu, Y. Ren, J. Jian, Z. Ruan, Y. Xu, S. Gao, S. Sun, X. Wen, L. Zhou, L. Liu, C. Guo, H. Chen, S. Yu, L. Liu, and X. Cai, "High-performance hybrid silicon and lithium niobate Mach-Zehnder modulators for 100 Gbit s-1 and beyond," Nature Photonics **13**, 359–364 (2019).

[40] S. Abel, F. Eltes, J. E. Ortmann, A. Messner, P. Castera, T. Wagner, D. Urbonas, A. Rosa, A. M. Gutierrez, D. Tulli, P. Ma, B. Baeuerle, A. Josten, W. Heni, D. Caimi, L. Czornomaz, A. A. Demkov, J. Leuthold, P. Sanchis, and J. Fompeyrine, "Large Pockels effect in micro- and nanostructured barium titanate integrated on silicon," Nature Materials **18**, 42–47 (2019).

[41] D. S. Ginley, *Handbook of Transparent Conductors* (Springer US, Boston, MA, 2011).

[42] G. V. Naik, V. M. Shalaev, and A. Boltasseva, "Alternative Plasmonic Materials: Beyond Gold and Silver," Advanced Materials **25**, 3264–3294 (2013).

[43] P. R. West, S. Ishii, G. V. Naik, N. K. Emani, V. M. Shalaev, and A. Boltasseva, "Searching for better plasmonic materials," Laser & Photonics Reviews **4**, 795–808 (2010).

[44] J. F. Wager, "Transparent Electronics," Science **300**, 1245–1246 (2003).

[45] C. Guillén and J. Herrero, "TCO/metal/TCO structures for energy and flexible electronics," Thin Solid Films **520**, 1–17 (2011).

[46] S. C. Dixon, D. O. Scanlon, C. J. Carmalt, and I. P. Parkin, "n-Type doped transparent conducting binary oxides: an overview," Journal of Materials Chemistry C **4**, 6946–6961 (2016).

[47] B. Yang, C. Yao, Y. Yu, Z. Li, and X. Wang, "Nature Degradable, Flexible, and Transparent Conductive Substrates from Green and Earth-Abundant Materials," Scientific Reports **7**, 4936 (2017).

[48] W. Jaffray, S. Saha, V. M. Shalaev, A. Boltasseva, and M. Ferrera, "Transparent conducting oxides: from all-dielectric plasmonics to a new paradigm in integrated photonics," Advances in Optics and Photonics **14**, 148 (2022).

[49] A. Klein, "Transparent Conducting Oxides: Electronic Structure-Property Relationship from Photoelectron Spectroscopy with in situ Sample Preparation," Journal of the American Ceramic Society **96**, 331–345 (2013).

[50] J. W. Cleary, E. M. Smith, K. D. Leedy, G. Grzybowski, and J. Guo, "Optical and electrical properties of ultra-thin indium tin oxide nanofilms on silicon for infrared photonics," Optical Materials Express **8**, 1231 (2018).

[51] J. Wu, Z. T. Xie, Y. Sha, H. Y. Fu, and Q. Li, "Epsilon-near-zero photonics: infinite potentials," Photonics Research **9**, 1616 (2021).

[52] V. E. Babicheva, A. Boltasseva, and A. V. Lavrinenko, "Transparent conducting oxides for electro-optical plasmonic modulators," Nanophotonics **4**, 165–185 (2015).

[53] Y. Gui, M. Miscuglio, Z. Ma, M. H. Tahersima, S. Sun, R. Amin, H. Dalir, and V. J. Sorger, "Towards integrated metatronics: a holistic approach on precise optical and electrical properties of Indium Tin Oxide," Scientific Reports **9**, 11279 (2019).

[54] D. Ashkenasi, G. Müller, A. Rosenfeld, R. Stoian, I. V. Hertel, N. M. Bulgakova, and E. E. B. Campbell, "Fundamentals and advantages of ultrafast micro-structuring of transparent materials," Applied Physics A **77**, 223–228 (2003).

[55] D. Fomra, K. Ding, V. Avrutin, Ü. Özgür, and N. Kinsey, "Al:ZnO as a platform for near-zero-index photonics: enhancing the doping efficiency of atomic layer deposition," Optical Materials Express **10**, 3060 (2020).

[56] L. Dong, G. S. Zhu, H. R. Xu, X. P. Jiang, X. Y. Zhang, Y. Y. Zhao, D. L. Yan, L. Yuan, and A. B. Yu, "Preparation of indium tin oxide (ITO) thin film

with (400) preferred orientation by sol–gel spin coating method," Journal of Materials Science: Materials in Electronics **30**, 8047–8054 (2019).

[57] I. Hamberg and C. G. Granqvist, "Evaporated Sn-doped In 2 O 3 films: Basic optical properties and applications to energy-efficient windows," Journal of Applied Physics **60**, R123—-R160 (1986).

[58] F. Lai, M. Li, H. Wang, H. Hu, X. Wang, J. G. Hou, Y. Song, and Y. Jiang, "Optical scattering characteristic of annealed niobium oxide films," Thin Solid Films **488**, 314–320 (2005).

[59] Y. Wang, A. C. Overvig, S. Shrestha, R. Zhang, R. Wang, N. Yu, and L. Dal Negro, "Tunability of indium tin oxide materials for mid-infrared plasmonics applications," Optical Materials Express **7**, 2727 (2017).

[60] X. Niu, X. Hu, S. Chu, and Q. Gong, "Epsilon-Near-Zero Photonics: A New Platform for Integrated Devices," Advanced Optical Materials **6**, 1701292 (2018).

[61] V. E. Babicheva, N. Kinsey, G. V. Naik, M. Ferrera, A. V. Lavrinenko, V. M. Shalaev, and A. Boltasseva, "Towards CMOS-compatible nanophotonics: Ultra-compact modulators using alternative plasmonic materials," Optics Express **21**, 27326 (2013).

[62] R. Amin, R. Maiti, C. Carfano, Z. Ma, M. H. Tahersima, Y. Lilach, D. Ratnayake, H. Dalir, and V. J. Sorger, "0.52 V mm ITO-based Mach-Zehnder modulator in silicon photonics," APL Photonics **3**, 126104 (2018).

[63] Q. Gao, E. Li, and A. X. Wang, "Ultra-compact and broadband electroabsorption modulator using an epsilon-near-zero conductive oxide," Photonics Research **6**, 277 (2018).

[64] E. Li, Q. Gao, R. T. Chen, and A. X. Wang, "Ultracompact Silicon-Conductive Oxide Nanocavity Modulator with 0.02 Lambda-Cubic Active Volume," Nano Letters **18**, 1075–1081 (2018).

[65] E. Li, Q. Gao, S. Liverman, and A. X. Wang, "One-volt silicon photonic crystal nanocavity modulator with indium oxide gate," Optics Letters **43**, 4429 (2018).

[66] K. Liu, S. Lee, S. Yang, O. Delaire, and J. Wu, "Recent progresses on physics and applications of vanadium dioxide," Materials Today **21**, 875–896 (2018).

[67] M. G. Wood, S. Campione, S. Parameswaran, T. S. Luk, J. R. Wendt, D. K. Serkland, and G. A. Keeler, "Gigahertz speed operation of epsilon-near-zero silicon photonic modulators," Optica **5**, 233 (2018).

[68] R. Amin, J. K. George, S. Sun, T. Ferreira de Lima, A. N. Tait, J. B. Khurgin, M. Miscuglio, B. J. Shastri, P. R. Prucnal, T. El-Ghazawi, and V. J. Sorger, "ITO-based electro-absorption modulator for photonic neural activation function," APL Materials **7**, 81112 (2019).

[69] E. Li, B. A. Nia, B. Zhou, and A. X. Wang, "Transparent conductive oxide-gated silicon microring with extreme resonance wavelength tunability," Photonics Research **7**, 473 (2019).

[70] R. Amin, R. Maiti, Y. Gui, C. Suer, M. Miscuglio, E. Heidari, R. T. Chen, H. Dalir, and V. J. Sorger, "Sub-wavelength GHz-fast broadband ITO Mach–Zehnder modulator on silicon photonics," Optica **7**, 333 (2020).

[71] B. Zhou, E. Li, Y. Bo, and A. X. Wang, "High-Speed Plasmonic-Silicon Modulator Driven by Epsilon-Near-zero Conductive Oxide," Journal of Lightwave Technology **38**, 3338–3345 (2020).

[72] L. Hsu and A. Ndao, "Diffraction-limited broadband optical meta-power-limiter," Optics Letters **46**, 1293 (2021).

[73] E. Li and A. X. Wang, "Femto-Joule All-Optical Switching Using Epsilon-Near-Zero High-Mobility Conductive Oxide," IEEE Journal of Selected Topics in Quantum Electronics **27**, 1–9 (2021).

[74] Y. Huang, J. Zheng, B. Pan, L. Song, K.-A. Chen, Z. Yu, H. Ye, and D. Dai, "High-bandwidth Si/In 2 O 3 hybrid plasmonic waveguide modulator," APL Photonics **7**, 51301 (2022).

[75] N. F. Mott, "Metal-insulator transitions," Pure and Applied Chemistry **52**, 65–72 (1980).

[76] Y. Ke, S. Wang, G. Liu, M. Li, T. J. White, and Y. Long, "Vanadium Dioxide: The Multistimuli Responsive Material and Its Applications," Small **14**, 1802025 (2018).

[77] Z. Yang, C. Ko, and S. Ramanathan, "Oxide Electronics Utilizing Ultrafast Metal-Insulator Transitions," Annual Review of Materials Research **41**, 337–367 (2011).

[78] F. J. Morin, "Oxides which show a metal-to-insulator transition at the neel temperature," Physical Review Letters **3**, 34–36 (1959).

[79] K. J. Miller, R. F. Haglund, and S. M. Weiss, "Optical phase change materials in integrated silicon photonic devices: review," Optical Materials Express **8**, 2415 (2018).

[80] R. Shi, N. Shen, J. Wang, W. Wang, A. Amini, N. Wang, and C. Cheng, "Recent advances in fabrication strategies, phase transition modulation, and advanced applications of vanadium dioxide," Applied Physics Reviews **6**, 011312 (2019).

[81] Z. Shao, X. Cao, H. Luo, and P. Jin, "Recent progress in the phase-transition mechanism and modulation of vanadium dioxide materials," NPG Asia Materials **10**, 581–605 (2018).

[82] M. Currie, M. A. Mastro, and V. D. Wheeler, "Characterizing the tunable refractive index of vanadium dioxide," Optical Materials Express **7**, 1697 (2017).

[83] S. Cueff, J. John, Z. Zhang, J. Parra, J. Sun, R. Orobtchouk, S. Ramanathan, and P. Sanchis, "VO2 nanophotonics," APL Photonics **5**, 110901 (2020).

[84] M. M. Qazilbash, M. Brehm, B.-G. Chae, P.-C. Ho, G. O. Andreev, B.-J. Kim, S. J. Yun, A. V. Balatsky, M. B. Maple, F. Keilmann, H.-T. Kim, and D. N. Basov, "Mott Transition in VO2 Revealed by Infrared Spectroscopy and Nano-Imaging," Science **318**, 1750–1753 (2007).

[85] T. Maruyama and Y. Ikuta, "Vanadium dioxide thin films prepared by chemical vapour deposition from vanadium(III) acetylacetonate," Journal of Materials Science **28**, 5073–5078 (1993).

[86] D. Brassard, S. Fourmaux, M. Jean-Jacques, J. C. Kieffer, and M. A. El Khakani, "Grain size effect on the semiconductor-metal phase transition characteristics of magnetron-sputtered VO2 thin films," Applied Physics Letters **87**, 051910 (2005).

[87] R. McGee, A. Goswami, B. Khorshidi, K. McGuire, K. Schofield, and T. Thundat, "Effect of process parameters on phase stability and metal-insulator transition of vanadium dioxide (VO2) thin films by pulsed laser deposition," Acta Materialia **137**, 12–21 (2017).

[88] B.-G. Chae, H.-T. Kim, S.-J. Yun, B.-J. Kim, Y.-W. Lee, D.-H. Youn, and K.-Y. Kang, "Highly Oriented VO2 Thin Films Prepared by Sol-Gel Deposition," Electrochemical and Solid-State Letters **9**, C12 (2006).

[89] L. L. Fan, S. Chen, Y. F. Wu, F. H. Chen, W. S. Chu, X. Chen, C. W. Zou, and Z. Y. Wu, "Growth and phase transition characteristics of pure M-phase VO2 epitaxial film prepared by oxide molecular beam epitaxy," Applied Physics Letters **103**, 131914 (2013).

[90] J. D. Ryckman, V. Diez-Blanco, J. Nag, R. E. Marvel, B. K. Choi, R. F. Haglund, and S. M. Weiss, "Photothermal optical modulation of ultra-compact hybrid Si-VO2 ring resonators," Optics Express **20**, 13215 (2012).

[91] J. D. Ryckman, K. A. Hallman, R. E. Marvel, R. F. Haglund, and S. M. Weiss, "Ultra-compact silicon photonic devices reconfigured by an optically induced semiconductor-to-metal transition," Optics Express **21**, 10753 (2013).

[92] P. Markov, R. E. Marvel, H. J. Conley, K. J. Miller, R. F. Haglund, and S. M. Weiss, "Optically Monitored Electrical Switching in VO2," ACS Photonics **2**, 1175–1182 (2015).

[93] A. Joushaghani, J. Jeong, S. Paradis, D. Alain, J. Stewart Aitchison, and J. K. S. Poon, "Wavelength-size hybrid Si-VO2 waveguide electroabsorption optical switches and photodetectors," Optics Express **23**, 3657 (2015).

[94] K. J. Miller, K. A. Hallman, R. F. Haglund, and S. M. Weiss, "Silicon waveguide optical switch with embedded phase change material," Optics Express **25**, 26527 (2017).

[95] L. D. Sánchez, I. Olivares, J. Parra, M. Menghini, P. Homm, J.-P. Locquet, and P. Sanchis, "Experimental demonstration of a tunable transverse electric pass polarizer based on hybrid VO2/silicon technology," Optics Letters **43**, 3650 (2018).

[96] I. Olivares, L. Sánchez, J. Parra, R. Larrea, A. Griol, M. Menghini, P. Homm, L.-W. Jang, B. van Bilzen, J. W. Seo, J.-P. Locquet, and P. Sanchis, "Optical switching in hybrid VO2/Si waveguides thermally triggered by lateral microheaters," Optics Express **26**, 12387 (2018).

[97] K. Shibuya, Y. Atsumi, T. Yoshida, Y. Sakakibara, M. Mori, and A. Sawa, "Silicon waveguide optical modulator driven by metal–insulator transition of vanadium dioxide cladding layer," Optics Express **27**, 4147 (2019).

[98] R. F. Haglund, K. A. Hallman, K. J. Miller, and S. M. Weiss, "Picosecond Optical Switching in Silicon Photonics Using Phase-Changing Vanadium Dioxide," Conference on Lasers and Electro-Optics **1**, STh4H.1 (2019).

[99] H. M. Wong, Z. Yan, K. A. Hallman, R. E. Marvel, R. P. Prasankumar, R. F. Haglund, and A. S. Helmy, "Broadband, Integrated, Micron-Scale, All-Optical Si3N4/VO2 Modulators with pJ Switching Energy," ACS Photonics **6**, 2734–2740 (2019).

[100] K. A. Hallman, K. J. Miller, A. Baydin, S. M. Weiss, and R. F. Haglund, "Sub-Picosecond Response Time of a Hybrid VO2:Silicon Waveguide at 1550 nm," Advanced Optical Materials **9**, 2001721 (2021).

[101] X. Chen, M. M. Milosevic, S. Stankovic, S. Reynolds, T. D. Bucio, K. Li, D. J. Thomson, F. Gardes, and G. T. Reed, "The Emergence of Silicon Photonics as a Flexible Technology Platform," Proceedings of the IEEE **106**, 2101–2116 (2018).

[102] A. Rahim, T. Spuesens, R. Baets, and W. Bogaerts, "Open-Access Silicon Photonics: Current Status and Emerging Initiatives," Proceedings of the IEEE **106**, 2313–2330 (2018).

[103] W. Bogaerts and L. Chrostowski, "Silicon Photonics Circuit Design: Methods, Tools and Challenges," Laser & Photonics Reviews **12**, 1700237 (2018).

[104] R. Soref, "Tutorial: Integrated-photonic switching structures," APL Photonics **3**, 021101 (2018).

[105] T. Alexoudi, G. T. Kanellos, and N. Pleros, "Optical RAM and integrated optical memories: a survey," Light: Science & Applications **9**, 91 (2020).

[106] Y. Zhai, J.-Q. Yang, Y. Zhou, J.-Y. Mao, Y. Ren, V. A. L. Roy, and S.-T. Han, "Toward non-volatile photonic memory: concept, material and design," Materials Horizons **5**, 641–654 (2018).

[107] T. Ferreira de Lima, B. J. Shastri, A. N. Tait, M. A. Nahmias, and P. R. Prucnal, "Progress in neuromorphic photonics," Nanophotonics **6**, 577–599 (2017).

[108] C. V. Poulton, M. J. Byrd, P. Russo, E. Timurdogan, M. Khandaker, D. Vermeulen, and M. R. Watts, "Long-Range LiDAR and Free-Space Data Communication With High-Performance Optical Phased Arrays," IEEE Journal of Selected Topics in Quantum Electronics **25**, 1–8 (2019).

[109] V. R. Almeida and M. Lipson, "Optical bistability on a silicon chip," Optics Letters **29**, 2387 (2004).

[110] G. Priem, P. Dumon, W. Bogaerts, D. Van Thourhout, G. Morthier, and R. Baets, "Optical bistability and pulsating behaviour in Silicon-On-Insulator ring resonator structures," Optics Express **13**, 9623 (2005).

[111] P. E. Barclay, K. Srinivasan, and O. Painter, "Nonlinear response of silicon photonic crystal micresonators excited via an integrated waveguide and fiber taper," Optics Express **13**, 801 (2005).

[112] X. Zheng, Y. Luo, G. Li, I. Shubin, H. Thacker, J. Yao, K. Raj, J. E. Cunningham, and A. V. Krishnamoorthy, "Enhanced optical bistability from self-heating due to free carrier absorption in substrate removed silicon ring modulators," Optics Express **20**, 11478 (2012).

[113] M. Notomi, A. Shinya, S. Mitsugi, G. Kira, E. Kuramochi, and T. Tanabe, "Optical bistable switching action of Si high-Q photonic-crystal nanocavities," Optics Express **13**, 2678 (2005).

[114] Q. Xu and M. Lipson, "Carrier-induced optical bistability in silicon ring resonators," Optics Letters **31**, 341 (2006).

[115] L.-W. Luo, G. S. Wiederhecker, K. Preston, and M. Lipson, "Power insensitive silicon microring resonators," Optics Letters **37**, 590 (2012).

[116] T. Tanabe, M. Notomi, S. Mitsugi, A. Shinya, and E. Kuramochi, "Fast bistable all-optical switch and memory on a silicon photonic crystal on-chip," Optics Letters **30**, 2575 (2005).

[117] E. Kuramochi, K. Nozaki, A. Shinya, K. Takeda, T. Sato, S. Matsuo, H. Taniyama, H. Sumikura, and M. Notomi, "Large-scale integration of wavelength-addressable all-optical memories on a photonic crystal chip," Nature Photonics **8**, 474–481 (2014).

[118] A. Majumdar and A. Rundquist, "Cavity-enabled self-electro-optic bistability in silicon photonics," Optics Letters **39**, 3864 (2014).

[119] J. F. Song, X. S. Luo, A. E. J. Lim, C. Li, Q. Fang, T. Y. Liow, L. X. Jia, X. G. Tu, Y. Huang, H. F. Zhou, and G. Q. Lo, "Integrated photonics with programmable non-volatile memory," Scientific Reports **6**, 1–7 (2016).

[120] C. Barrios and M. Lipson, "Silicon photonic read-only memory," Journal of Lightwave Technology **24**, 2898–2905 (2006).

[121] M. Grajower, N. Mazurski, J. Shappir, and U. Levy, "Non-Volatile Silicon Photonics Using Nanoscale Flash Memory Technology," Laser & Photonics Reviews **12**, 1–8 (2018).

[122] J.-F. Song, A. E. J. Lim, X. S. Luo, Q. Fang, C. Li, L. X. Jia, X. G. Tu, Y. Huang, H. F. Zhou, T. Y. Liow, and G. Q. Lo, "Silicon photonic integrated circuits with electrically programmable non-volatile memory functions," Optics Express **24**, 21744 (2016).

[123] I. Olivares, J. Parra, and P. Sanchis, "Non-Volatile Photonic Memory Based on a SAHAS Configuration," IEEE Photonics Journal **13**, 1–8 (2021).

[124] Y. Li, H. Yu, T. Dai, J. Jiang, G. Wang, L. Yang, W. Wang, J. Yang, and X. Jiang, "Graphene-Based Floating-Gate Nonvolatile Optical Switch," IEEE Photonics Technology Letters **28**, 284–287 (2016).

[125] Y. Li, W. Chen, T. Dai, and P. Wang, "Nonvolatile integrated optical phase shifter with flash memory technology," Applied Physics Express **12**, 102005 (2019).

[126] Y. Li, H. Ping, T. Dai, W. Chen, and P. Wang, "Nonvolatile silicon photonic switch with graphene based flash-memory cell," Optical Materials Express **11**, 766 (2021).

[127] B. Hwang and J.-S. Lee, "Recent Advances in Memory Devices with Hybrid Materials," Advanced Electronic Materials **5**, 1800519 (2019).

[128] R. Waser and M. Aono, "Nanoionics-based resistive switching memories," Nature Materials **6**, 833–840 (2007).

[129] H. Wang and X. Yan, "Overview of Resistive Random Access Memory (RRAM): Materials, Filament Mechanisms, Performance Optimization, and Prospects," physica status solidi (RRL) – Rapid Research Letters **13**, 1900073 (2019).

[130] U. Koch, C. Hoessbacher, A. Emboras, and J. Leuthold, "Optical memristive switches," Journal of Electroceramics **39**, 239–250 (2017).

[131] A. Emboras, I. Goykhman, B. Desiatov, N. Mazurski, L. Stern, J. Shappir, and U. Levy, "Nanoscale Plasmonic Memristor with Optical Readout Functionality," Nano Letters **13**, 6151–6155 (2013).

[132] A. Emboras, J. Niegemann, P. Ma, C. Haffner, A. Pedersen, M. Luisier, C. Hafner, T. Schimmel, and J. Leuthold, "Atomic Scale Plasmonic Switch," Nano Letters **16**, 709–714 (2016).

[133] C. Hoessbacher, Y. Fedoryshyn, A. Emboras, A. Melikyan, M. Kohl, D. Hillerkuss, C. Hafner, and J. Leuthold, "The plasmonic memristor: a latching optical switch," Optica **1**, 198 (2014).

[134] G. Vescio, A. Crespo-Yepes, D. Alonso, S. Claramunt, M. Porti, R. Rodriguez, A. Cornet, A. Cirera, M. Nafria, and X. Aymerich, "Inkjet Printed HfO2-Based ReRAMs: First Demonstration and Performance Characterization," IEEE Electron Device Letters **38**, 457–460 (2017).

[135] J. J. Yang, F. Miao, M. D. Pickett, D. A. A. Ohlberg, D. R. Stewart, C. N. Lau, and R. S. Williams, "Corrigendum on 'The mechanism of electroforming of metal oxide memristive switches'," Nanotechnology **21**, 339803–339803 (2010).

[136] O. Blázquez, J. L. Frieiro, J. López-Vidrier, C. Guillaume, X. Portier, C. Labbé, P. Sanchis, S. Hernández, and B. Garrido, "Resistive switching and charge transport mechanisms in ITO/ZnO/ p -Si devices," Applied Physics Letters **113**, 183502 (2018).

[137] A. Mehonic, S. Cueff, M. Wojdak, S. Hudziak, O. Jambois, C. Labbé, B. Garrido, R. Rizk, and A. J. Kenyon, "Resistive switching in silicon suboxide films," Journal of Applied Physics **111**, 074507 (2012).

[138] A. Mehonic, S. Cueff, M. Wojdak, S. Hudziak, C. Labbé, R. Rizk, and A. J. Kenyon, "Electrically tailored resistance switching in silicon oxide," Nanotechnology **23**, 455201 (2012).

[139] Y. Yang, P. Gao, S. Gaba, T. Chang, X. Pan, and W. Lu, "Observation of conducting filament growth in nanoscale resistive memories," Nature Communications **3**, 732 (2012).

[140] E. Battal, A. Ozcan, and A. K. Okyay, "Resistive Switching-based Electro-Optical Modulation," Advanced Optical Materials **2**, 1149–1154 (2014).

[141] W. Noell, P.-A. Clerc, L. Dellmann, B. Guldimann, H.-P. Herzig, O. Manzardo, C. Marxer, K. Weible, R. Dandliker, and N. de Rooij, "Applications of SOI-based optical MEMS," IEEE Journal of Selected Topics in Quantum Electronics **8**, 148–154 (2002).

[142] C. Errando-Herranz, A. Y. Takabayashi, P. Edinger, H. Sattari, K. B. Gylfason, and N. Quack, "MEMS for Photonic Integrated Circuits," IEEE Journal of Selected Topics in Quantum Electronics **26**, 1–16 (2020).

[143] E. Bulgan, Y. Kanamori, and K. Hane, "Submicron silicon waveguide optical switch driven by microelectromechanical actuator," Applied Physics Letters **92**, 101110 (2008).

[144] Hao-Bing Liu and F. Chollet, "Moving Polymer Waveguides and Latching Actuator for 2 × 2 MEMS Optical Switch," Journal of Microelectromechanical Systems **18**, 715–724 (2009).

[145] H. Sattari, T. Graziosi, M. Kiss, T. J. Seok, S. Han, M. C. Wu, and N. Quack, "Silicon Photonic MEMS Phase-Shifter," Optics Express **27**, 18959 (2019).

[146] T. J. Seok, N. Quack, S. Han, R. S. Muller, and M. C. Wu, "Large-scale broadband digital silicon photonic switches with vertical adiabatic couplers," Optica **3**, 64 (2016).

[147] T. J. Seok, K. Kwon, J. Henriksson, J. Luo, and M. C. Wu, "240×240 Wafer-Scale Silicon Photonic Switches," in "Optical Fiber Communication Conference (OFC) 2019," , vol. 1 (OSA, Washington, D.C., 2019), vol. 1, p. Th1E.5.

[148] M. Wuttig and N. Yamada, "Phase-change materials for rewriteable data storage," Nature Materials **6**, 824–832 (2007).

[149] W. H. P. Pernice and H. Bhaskaran, "Photonic non-volatile memories using phase change materials," Applied Physics Letters **101**, 171101 (2012).

[150] M. Wuttig, H. Bhaskaran, and T. Taubner, "Phase-change materials for non-volatile photonic applications," Nature Photonics **11**, 465–476 (2017).

[151] S. Abdollahramezani, O. Hemmatyar, H. Taghinejad, A. Krasnok, Y. Kiarashinejad, M. Zandehshahvar, A. Alù, and A. Adibi, "Tunable nanophotonics enabled by chalcogenide phase-change materials," Nanophotonics **9**, 1189–1241 (2020).

[152] K. Shportko, S. Kremers, M. Woda, D. Lencer, J. Robertson, and M. Wuttig, "Resonant bonding in crystalline phase-change materials," Nature Materials **7**, 653–658 (2008).

[153] Y. Zhang, J. B. Chou, J. Li, H. Li, Q. Du, A. Yadav, S. Zhou, M. Y. Shalaginov, Z. Fang, H. Zhong, C. Roberts, P. Robinson, B. Bohlin, C. Ríos, H. Lin, M. Kang, T. Gu, J. Warner, V. Liberman, K. Richardson, and J. Hu, "Broadband transparent optical phase change materials for high-performance nonvolatile photonics," Nature Communications **10**, 4279 (2019).

[154] M. Stegmaier, C. RÍos, H. Bhaskaran, and W. H. P. Pernice, "Thermo-optical Effect in Phase-Change Nanophotonics," ACS Photonics **3**, 828–835 (2016).

[155] E. Gemo, S. V. Kesava, C. Ruiz De Galarreta, L. Trimby, S. García-Cuevas Carrillo, M. Riede, A. Baldycheva, A. Alexeev, and C. D. Wright, "Simple technique for determining the refractive index of phase-change materials using near-infrared reflectometry," Optical Materials Express **10**, 1675 (2020).

[156] H. Zhang, L. Zhou, J. Xu, L. Lu, J. Chen, and B. M. A. Rahman, "All-optical non-volatile tuning of an AMZI-coupled ring resonator with GST phase-change material," Optics Letters **43**, 5539 (2018).

[157] D. Tanaka, Y. Shoji, M. Kuwahara, X. Wang, K. Kintaka, H. Kawashima, T. Toyosaki, Y. Ikuma, and H. Tsuda, "Ultra-small, self-holding, optical gate switch using Ge2Sb2Te5 with a multi-mode Si waveguide," Optics Express **20**, 10283 (2012).

[158] J. Zheng, A. Khanolkar, P. Xu, S. Colburn, S. Deshmukh, J. Myers, J. Frantz, E. Pop, J. Hendrickson, J. Doylend, N. Boechler, and A. Majumdar, "GST-on-silicon hybrid nanophotonic integrated circuits: a non-volatile quasi-continuously reprogrammable platform," Optical Materials Express **8**, 1551 (2018).

[159] D. Loke, T. H. Lee, W. J. Wang, L. P. Shi, R. Zhao, Y. C. Yeo, T. C. Chong, and S. R. Elliott, "Breaking the Speed Limits of Phase-Change Memory," Science **336**, 1566–1569 (2012).

[160] Y. Ikuma, Y. Shoji, M. Kuwahara, X. Wang, K. Kintaka, H. Kawashima, D. Tanaka, and H. Tsuda, "Small-sized optical gate switch using Ge2Sb2Te5 phase-change material integrated with silicon waveguide," Electronics Letters **46**, 368 (2010).

[161] C. Ríos, N. Youngblood, Z. Cheng, M. Le Gallo, W. H. P. Pernice, C. D. Wright, A. Sebastian, and H. Bhaskaran, "In-memory computing on a photonic platform," Science Advances **5**, eaau5759 (2019).

[162] C. Ríos, M. Stegmaier, P. Hosseini, D. Wang, T. Scherer, C. D. Wright, H. Bhaskaran, and W. H. P. Pernice, "Integrated all-photonic non-volatile multi-level memory," Nature Photonics **9**, 725–732 (2015).

[163] C. Rios, M. Stegmaier, Z. Cheng, N. Youngblood, C. D. Wright, W. H. P. Pernice, and H. Bhaskaran, "Controlled switching of phase-change materials by evanescent-field coupling in integrated photonics [Invited]," Optical Materials Express **8**, 2455 (2018).

[164] X. Li, N. Youngblood, C. Ríos, Z. Cheng, C. D. Wright, W. H. Pernice, and H. Bhaskaran, "Fast and reliable storage using a 5 bit, nonvolatile photonic memory cell," Optica **6**, 1 (2019).

[165] X. Li, N. Youngblood, Z. Cheng, S. G.-C. Carrillo, E. Gemo, W. H. P. Pernice, C. D. Wright, and H. Bhaskaran, "Experimental investigation of silicon and silicon nitride platforms for phase-change photonic in-memory computing," Optica **7**, 218 (2020).

[166] K. Kato, M. Kuwahara, H. Kawashima, T. Tsuruoka, and H. Tsuda, "Current-driven phase-change optical gate switch using indium-tin-oxide heater," Applied Physics Express **10**, 72201 (2017).

[167] J. Parra, J. Hurtado, A. Griol, and P. Sanchis, "Ultra-low loss hybrid ITO/Si thermo-optic phase shifter with optimized power consumption," Optics Express **28**, 9393 (2020).

[168] H. Zhang, L. Zhou, J. Xu, N. Wang, H. Hu, L. Lu, B. Rahman, and J. Chen, "Nonvolatile waveguide transmission tuning with electrically-driven ultra-small GST phase-change material," Science Bulletin **64**, 782–789 (2019).

[169] H. Zhang, L. Zhou, L. Lu, J. Xu, N. Wang, H. Hu, B. M. A. Rahman, Z. Zhou, and J. Chen, "Miniature Multilevel Optical Memristive Switch Using Phase Change Material," ACS Photonics **6**, 2205–2212 (2019).

[170] N. Farmakidis, N. Youngblood, X. Li, J. Tan, J. L. Swett, Z. Cheng, C. D. Wright, W. H. P. Pernice, and H. Bhaskaran, "Plasmonic nanogap enhanced phase-change devices with dual electrical-optical functionality," Science Advances **5**, 1–8 (2019).

[171] C. Wu, H. Yu, H. Li, X. Zhang, I. Takeuchi, and M. Li, "Low-Loss Integrated Photonic Switch Using Subwavelength Patterned Phase Change Material," ACS Photonics **6**, 87–92 (2019).

[172] M. Miscuglio, J. Meng, O. Yesiliurt, Y. Zhang, L. J. Prokopeva, A. Mehrabian, J. Hu, A. V. Kildishev, and V. J. Sorger, "GSST-based photonic memory multilevel perceptron," in "Conference on Lasers and Electro-Optics," (OSA, Washington, D.C., 2020), p. JF3A.2.

[173] Q. Zhang, Y. Zhang, J. Li, R. Soref, T. Gu, and J. Hu, "Broadband nonvolatile photonic switching based on optical phase change materials: beyond the classical figure-of-merit," Optics Letters **43**, 94 (2018).

[174] W. Jiang, "Nonvolatile and ultra-low-loss reconfigurable mode (De)multiplexer/switch using triple-waveguide coupler with Ge2Sb2Se4Te1 phase change material," Scientific Reports **8**, 15946 (2018).

[175] J. Parra, T. Ivanova, M. Menghini, P. Homm, J.-P. Locquet, and P. Sanchis, "All-Optical Hybrid VO_2/Si Waveguide Absorption Switch at Telecommunication Wavelengths," Journal of Lightwave Technology **39**, 2888–2894 (2021).

[176] P. Markov, K. Appavoo, R. F. Haglund, and S. M. Weiss, "Hybrid Si-VO2-Au optical modulator based on near-field plasmonic coupling," Optics Express **23**, 6878 (2015).

[177] S. Chen, Z. Wang, H. Ren, Y. Chen, W. Yan, C. Wang, B. Li, J. Jiang, and C. Zou, "Gate-controlled VO2 phase transition for high-performance smart windows," Science Advances **5**, 1–9 (2019).

[178] K. Liu, D. Fu, J. Cao, J. Suh, K. X. Wang, C. Cheng, D. F. Ogletree, H. Guo, S. Sengupta, A. Khan, C. W. Yeung, S. Salahuddin, M. M. Deshmukh, and J. Wu, "Dense Electron System from Gate-Controlled Surface Metal–Insulator Transition," Nano Letters **12**, 6272–6277 (2012).

[179] A. Cavalleri, C. Tóth, C. W. Siders, J. A. Squier, F. Ráksi, P. Forget, and J. C. Kieffer, "Femtosecond Structural Dynamics in VO2 during an Ul-

trafast Solid-Solid Phase Transition," Physical Review Letters **87**, 237401 (2001).

[180] A. Cavalleri, T. Dekorsy, H. H. W. Chong, J. C. Kieffer, and R. W. Schoenlein, "Evidence for a structurally-driven insulator-to-metal transition in VO2: A view from the ultrafast timescale," Physical Review B **70**, 161102 (2004).

[181] M. R. Otto, L. P. René de Cotret, D. A. Valverde-Chavez, K. L. Tiwari, N. Émond, M. Chaker, D. G. Cooke, and B. J. Siwick, "How optical excitation controls the structure and properties of vanadium dioxide," Proceedings of the National Academy of Sciences of the United States of America **116**, 450–455 (2019).

[182] K. Shibuya, K. Ishii, Y. Atsumi, T. Yoshida, Y. Sakakibara, M. Mori, and A. Sawa, "Switching dynamics of silicon waveguide optical modulator driven by photothermally induced metal-insulator transition of vanadium dioxide cladding layer," Optics Express **28**, 37188 (2020).

[183] X. Tan, T. Yao, R. Long, Z. Sun, Y. Feng, H. Cheng, X. Yuan, W. Zhang, Q. Liu, C. Wu, Y. Xie, and S. Wei, "Unraveling Metal-insulator Transition Mechanism of VO2Triggered by Tungsten Doping," Scientific Reports **2**, 466 (2012).

[184] Y. Zhao, G. Karaoglan-Bebek, X. Pan, M. Holtz, A. A. Bernussi, and Z. Fan, "Hydrogen-doping stabilized metallic VO 2 (R) thin films and their application to suppress Fabry-Perot resonances in the terahertz regime," Applied Physics Letters **104**, 241901 (2014).

[185] N. R. Mlyuka, G. A. Niklasson, and C. G. Granqvist, "Mg doping of thermochromic VO2 films enhances the optical transmittance and decreases the metal-insulator transition temperature," Applied Physics Letters **95**, 171909 (2009).

[186] J. Laverock, S. Kittiwatanakul, A. A. Zakharov, Y. R. Niu, B. Chen, S. A. Wolf, J. W. Lu, and K. E. Smith, "Direct observation of decoupled structural and electronic transitions and an ambient pressure monocliniclike metallic phase of VO2," Physical Review Letters **113**, 216402 (2014).

[187] N. F. Quackenbush, H. Paik, M. J. Wahila, S. Sallis, M. E. Holtz, X. Huang, A. Ganose, B. J. Morgan, D. O. Scanlon, Y. Gu, F. Xue, L.-Q. Chen, G. E. Sterbinsky, C. Schlueter, T.-L. Lee, J. C. Woicik, J.-H. Guo, J. D. Brock, D. A. Muller, D. A. Arena, D. G. Schlom, and L. F. J. Piper, "Stability of the M2 phase of vanadium dioxide induced by coherent epitaxial strain," Physical Review B **94**, 085105 (2016).

[188] Y. Qi and Y. Li, "Integrated lithium niobate photonics," Nanophotonics **9**, 1287–1320 (2020).

[189] K. Alexander, J. P. George, J. Verbist, K. Neyts, B. Kuyken, D. Van Thourhout, and J. Beeckman, "Nanophotonic Pockels modulators on a silicon nitride platform," Nature Communications **9**, 3444 (2018).

[190] T. Ohashi, H. Hosaka, and T. Morita, "Refractive Index Memory Effect of Ferroelectric Materials Induced by Electrical Imprint Field," Japanese Journal of Applied Physics **47**, 3985–3987 (2008).

[191] F. Eltes, C. Mai, D. Caimi, M. Kroh, Y. Popoff, G. Winzer, D. Petousi, S. Lischke, J. E. Ortmann, L. Czornomaz, L. Zimmermann, J. Fompeyrine, and S. Abel, "A BaTiO 3 -Based Electro-Optic Pockels Modulator Monolithically Integrated on an Advanced Silicon Photonics Platform," Journal of Lightwave Technology **37**, 1456–1462 (2019).

[192] S. Abel, T. Stoferle, C. Marchiori, D. Caimi, L. Czornomaz, M. Stuckelberger, M. Sousa, B. J. Offrein, and J. Fompeyrine, "A Hybrid Barium Titanate–Silicon Photonics Platform for Ultraefficient Electro-Optic Tuning," Journal of Lightwave Technology **34**, 1688–1693 (2016).

[193] F. Eltes, G. E. Villarreal-Garcia, D. Caimi, H. Siegwart, A. A. Gentile, A. Hart, P. Stark, G. D. Marshall, M. G. Thompson, J. Barreto, J. Fompeyrine, and S. Abel, "An integrated optical modulator operating at cryogenic temperatures," Nature Materials **19**, 1164–1168 (2020).

[194] P. Stark, J. G. Kremer, F. Eltes, D. Caimi, J. Fompeyrine, B. J. Offrein, and S. Abel, "Non-Volatile Photonic Weights and their Impact on Photonic Reservoir Computing Systems," in "2019 Conference on Lasers and Electro-Optics Europe & European Quantum Electronics Conference (CLEO/Europe-EQEC)," (IEEE, 2019), pp. 1–1.

[195] J. Geler-Kremer, F. Eltes, P. Stark, D. Stark, D. Caimi, H. Siegwart, B. Jan Offrein, J. Fompeyrine, and S. Abel, "A ferroelectric multilevel non-volatile photonic phase shifter," Nature Photonics (2022).

[196] K. Nakatsuhara, A. Kato, and Y. Hayama, "Latching operation in a tunable wavelength filter using Si sampled grating waveguide with ferroelectric liquid crystal cladding," Optics Express **22**, 9597 (2014).

[197] S. Gunther, C. Endrody, S. Si, S. Weinberger, R. Claes, Y. Justo, H. D'heer, A. Neft, and M. Hoffmann, "EWOD system designed for optical switching," in "2017 IEEE 30th International Conference on Micro Electro Mechanical Systems (MEMS)," (IEEE, 2017), pp. 1329–1332.

[198] H. Dheer, C. L. Arce, S. Vandewiele, J. Watte, K. Huybrechts, R. Baets, and D. Van Thourhout, "Nonvolatile Liquid Controlled Adiabatic Silicon Photonics Switch," Journal of Lightwave Technology **35**, 2948–2954 (2017).

[199] H. D'Heer, K. Saurav, C. Lerma Arce, M. Detalle, G. Lepage, P. Verheyen, J. Watte, and D. Van Thourhout, "A 16×16 Non-Volatile Silicon Photonic Switch Circuit," IEEE Photonics Technology Letters **30**, 1258–1261 (2018).

[200] R. H. Fowler and L. Nordheim, "Electron Emission in Intense Electric Fields," Semiconductor Devices: Pioneering Papers **119**, 683–691 (1991).

[201] H. C. Lin, P. D. Ye, and G. D. Wilk, "Leakage current and breakdown electric-field studies on ultrathin atomic-layer-deposited Al2O3 on GaAs," Applied Physics Letters **87**, 1–3 (2005).

[202] G. D. Wilk, R. M. Wallace, and J. M. Anthony, "High-κ gate dielectrics: Current status and materials properties considerations," Journal of Applied Physics **89**, 5243–5275 (2001).

[203] A. P. Vasudev, J.-H. Kang, J. Park, X. Liu, and M. L. Brongersma, "Electro-optical modulation of a silicon waveguide with an "epsilon-near-zero" material," Optics Express **21**, 26387 (2013).

[204] G. Sinatkas, A. Pitilakis, D. C. Zografopoulos, R. Beccherelli, and E. E. Kriezis, "Transparent conducting oxide electro-optic modulators on silicon platforms: A comprehensive study based on the drift-diffusion semiconductor model," Journal of Applied Physics **121** (2017).

[205] U. Koch, C. Hoessbacher, J. Niegemann, C. Hafner, and J. Leuthold, "Digital Plasmonic Absorption Modulator Exploiting Epsilon-Near-Zero in Transparent Conducting Oxides," IEEE Photonics Journal **8**, 1–13 (2016).

[206] Q. Gao, E. Li, and A. X. Wang, "Comparative analysis of transparent conductive oxide electro-absorption modulators [Invited]," Optical Materials Express **8**, 2850 (2018).

[207] J.-P. Niemelä, G. Marin, and M. Karppinen, "Titanium dioxide thin films by atomic layer deposition: a review," Semiconductor Science and Technology **32**, 093005 (2017).

[208] F. Michelotti, L. Dominici, E. Descrovi, N. Danz, and F. Menchini, "Thickness dependence of surface plasmon polariton dispersion in transparent conducting oxide films at 1.55 μm," Optics Letters **34**, 839 (2009).

[209] F. Hu, W. Jia, Y. Meng, M. Gong, and Y. Yang, "High-contrast optical switching using an epsilon-near-zero material coupled to a Bragg microcavity," Optics Express **27**, 26405 (2019).

[210] S. K. Vasheghani Farahani, T. D. Veal, P. D. C. King, J. Zúñiga-Pérez, V. Muñoz-Sanjosé, and C. F. McConville, "Electron mobility in CdO films," Journal of Applied Physics **109**, 073712 (2011).

[211] M. F. Limonov, M. V. Rybin, A. N. Poddubny, and Y. S. Kivshar, "Fano resonances in photonics," Nature Photonics **11**, 543–554 (2017).

[212] A. Zanzi, C. Vagionas, A. Griol, A. Rosa, S. Lechago, M. Moralis-Pegios, K. Vyrsokinos, N. Pleros, J. Kraft, V. Sidorov, B. Sirbu, T. Tekin, P. Sanchis, and A. Brimont, "Alignment tolerant, low voltage, 0.23 Vcm, push-pull silicon photonic switches based on a vertical pn junction," Optics Express **27**, 32409 (2019).

[213] R. L. Espinola, M. C. Tsai, J. T. Yardley, and R. M. Osgood, "Fast and low-power thermooptic switch on thin silicon-on-insulator," IEEE Photonics Technology Letters **15**, 1366–1368 (2003).

[214] J. Xia, J. Yu, Z. Wang, Z. Fan, and S. Chen, "Low power 2x2 thermo-optic SOI waveguide switch fabricated by anisotropy chemical etching," Optics Communications **232**, 223–228 (2004).

[215] T. Chu, H. Yamada, S. Ishida, and Y. Arakawa, "Compact 1 x N thermo-optic switches based on silicon photonic wire waveguides," Optics Express **13**, 10109 (2005).

[216] A. H. Atabaki, E. Shah Hosseini, A. A. Eftekhar, S. Yegnanarayanan, and A. Adibi, "Optimization of metallic microheaters for high-speed reconfigurable silicon photonics," Optics Express **18**, 18312 (2010).

[217] P. Sun and R. M. Reano, "Submilliwatt thermo-optic switches using free-standing silicon-on-insulator strip waveguides," Optics Express **18**, 8406 (2010).

[218] P. Dong, W. Qian, H. Liang, R. Shafiiha, D. Feng, G. Li, J. E. Cunningham, A. V. Krishnamoorthy, and M. Asghari, "Thermally tunable silicon racetrack resonators with ultralow tuning power," Optics Express **18**, 20298 (2010).

[219] J. Van Campenhout, W. M. J. Green, S. Assefa, and Y. A. Vlasov, "Integrated NiSi waveguide heaters for CMOS-compatible silicon thermo-optic devices," Optics Letters **35**, 1013 (2010).

[220] Y. Shoji, K. Kintaka, S. Suda, H. Kawashima, T. Hasama, and H. Ishikawa, "Low-crosstalk 2 x 2 thermo-optic switch with silicon wire waveguides," Optics Express **18**, 9071 (2010).

[221] P. Dong, W. Qian, H. Liang, R. Shafiiha, N.-N. Feng, D. Feng, X. Zheng, A. V. Krishnamoorthy, and M. Asghari, "Low power and compact reconfigurable multiplexing devices based on silicon microring resonators," Optics Express **18**, 9852 (2010).

[222] Q. Fang, J. F. Song, T.-Y. Liow, H. Cai, M. B. Yu, G. Q. Lo, and D.-L. Kwong, "Ultralow Power Silicon Photonics Thermo-Optic Switch With Suspended Phase Arms," IEEE Photonics Technology Letters **23**, 525–527 (2011).

[223] Q. Fang, J. Song, X. Luo, L. Jia, M. Yu, G. Lo, and Y. Liu, "High Efficiency Ring-Resonator Filter With NiSi Heater," IEEE Photonics Technology Letters **24**, 350–352 (2012).

[224] A. Masood, M. Pantouvaki, G. Lepage, P. Verheyen, J. Van Campenhout, P. Absil, D. Van Thourhout, and W. Bogaerts, "Comparison of heater architectures for thermal control of silicon photonic circuits," in "10th International Conference on Group IV Photonics," , vol. 2 (IEEE, 2013), vol. 2, pp. 83–84.

[225] A. H. Atabaki, A. A. Eftekhar, S. Yegnanarayanan, and A. Adibi, "Sub-100-nanosecond thermal reconfiguration of silicon photonic devices," Optics Express **21**, 15706 (2013).

[226] A. Masood, M. Pantouvaki, D. Goossens, G. Lepage, P. Verheyen, J. Van Campenhout, P. Absil, D. Van Thourhout, and W. Bogaerts, "Fabrication and characterization of CMOS-compatible integrated tungsten heaters for thermo-optic tuning in silicon photonics devices," Optical Materials Express **4**, 1383 (2014).

[227] M. Jacques, A. Samani, E. El-Fiky, D. Patel, Z. Xing, and D. V. Plant, "Optimization of thermo-optic phase-shifter design and mitigation of thermal crosstalk on the SOI platform," Optics Express **27**, 10456 (2019).

[228] M. Geis, S. Spector, R. Williamson, and T. Lyszczarz, "Submicrosecond Submilliwatt Silicon-on-Insulator Thermooptic Switch," IEEE Photonics Technology Letters **16**, 2514–2516 (2004).

[229] M. R. Watts, J. Sun, C. DeRose, D. C. Trotter, R. W. Young, and G. N. Nielson, "Adiabatic thermo-optic Mach-Zehnder switch," Optics Letters **38**, 733 (2013).

[230] N. C. Harris, Y. Ma, J. Mower, T. Baehr-Jones, D. Englund, M. Hochberg, and C. Galland, "Efficient, compact and low loss thermo-optic phase shifter in silicon," Optics Express **22**, 10487 (2014).

[231] D. Patel, V. Veerasubramanian, S. Ghosh, Wei Shi, A. Samani, Qiuhang Zhong, and D. V. Plant, "A 4x4 fully non-blocking switch on SOI based on interferometric thermo-optic phase shifters," in "2014 Optical Interconnects Conference," , vol. 5 (IEEE, 2014), vol. 5, pp. 104–105.

[232] X. Li, H. Xu, X. Xiao, Z. Li, Y. Yu, and J. Yu, "Fast and efficient silicon thermo-optic switching based on reverse breakdown of pn junction," Optics Letters **39**, 751 (2014).

[233] X. Wang, A. Lentine, C. DeRose, A. L. Starbuck, D. Trotter, A. Pomerene, and S. Mookherjea, "Wide-range and fast thermally-tunable silicon photonic microring resonators using the junction field effect," Optics Express **24**, 23081 (2016).

[234] A. Ribeiro and W. Bogaerts, "Digitally controlled multiplexed silicon photonics phase shifter using heaters with integrated diodes," Optics Express **25**, 29778 (2017).

[235] M. Mendez-Astudillo, M. Okamoto, Y. Ito, and T. Kita, "Compact thermo-optic MZI switch in silicon-on-insulator using direct carrier injection," Optics Express **27**, 899 (2019).

[236] A. Ribeiro, S. Declercq, U. Khan, M. Wang, L. V. Iseghem, and W. Bogaerts, "Column-Row Addressing of Thermo-Optic Phase Shifters for Controlling Large Silicon Photonic Circuits," IEEE Journal of Selected Topics in Quantum Electronics **26**, 1–8 (2020).

[237] T. Kita and M. Mendez-Astudillo, "Ultrafast Silicon MZI Optical Switch With Periodic Electrodes and Integrated Heat Sink," Journal of Lightwave Technology **39**, 5054–5060 (2021).

[238] L. Yu, D. Dai, and S. He, "Graphene-based transparent flexible heat conductor for thermally tuning nanophotonic integrated devices," Applied Physics Letters **105**, 251104 (2014).

[239] S. Gan, C. Cheng, Y. Zhan, B. Huang, X. Gan, S. Li, S. Lin, X. Li, J. Zhao, H. Chen, and Q. Bao, "A highly efficient thermo-optic microring modulator assisted by graphene," Nanoscale **7**, 20249–20255 (2015).

[240] D. Schall, M. Mohsin, A. A. Sagade, M. Otto, B. Chmielak, S. Suckow, A. L. Giesecke, D. Neumaier, and H. Kurz, "Infrared transparent graphene heater for silicon photonic integrated circuits," Optics Express **24**, 7871 (2016).

[241] L. Yu, Y. Yin, Y. Shi, D. Dai, and S. He, "Thermally tunable silicon photonic microdisk resonator with transparent graphene nanoheaters," Optica **3**, 159 (2016).

[242] S. Yan, X. Zhu, L. H. Frandsen, S. Xiao, N. A. Mortensen, J. Dong, and Y. Ding, "Slow-light-enhanced energy efficiency for graphene microheaters on silicon photonic crystal waveguides," Nature Communications **8**, 14411 (2017).

[243] Z. Xu, C. Qiu, Y. Yang, Q. Zhu, X. Jiang, Y. Zhang, W. Gao, and Y. Su, "Ultra-compact tunable silicon nanobeam cavity with an energy-efficient graphene micro-heater," Optics Express **25**, 19479 (2017).

[244] A. Dash, V. Mere, P. R. Y. Gangavarapu, S. R. Nambiar, S. K. Selvaraja, and A. K. Naik, "Carbon-nanotube-on-waveguide thermo-optic tuners," Optics Letters **43**, 5194 (2018).

[245] A. Densmore, S. Janz, R. Ma, J. H. Schmid, D.-X. Xu, A. Delâge, J. Lapointe, M. Vachon, and P. Cheben, "Compact and low power thermo-optic switch using folded silicon waveguides," Optics Express **17**, 10457 (2009).

[246] K. Murray, Z. Lu, H. Jayatilleka, and L. Chrostowski, "Dense dissimilar waveguide routing for highly efficient thermo-optic switches on silicon," Optics Express **23**, 19575 (2015).

[247] S. Chung, M. Nakai, and H. Hashemi, "Low-power thermo-optic silicon modulator for large-scale photonic integrated systems," Optics Express **27**, 13430 (2019).

[248] H. Qiu, Y. Liu, C. Luan, D. Kong, X. Guan, Y. Ding, and H. Hu, "Energy-efficient thermo-optic silicon phase shifter with well-balanced overall performance," Optics Letters **45**, 4806 (2020).

[249] G. T. Reed, G. Mashanovich, F. Y. Gardes, and D. J. Thomson, "Silicon optical modulators," Nature Photonics **4**, 518–526 (2010).

[250] A. Rahim, A. Hermans, B. Wohlfeil, D. Petousi, B. Kuyken, D. Van Thourhout, and R. Baets, "Taking silicon photonics modulators to a higher performance level: state-of-the-art and a review of new technologies," Advanced Photonics **3**, 1–23 (2021).

[251] R. Soref and B. Bennett, "Electrooptical effects in silicon," IEEE Journal of Quantum Electronics **23**, 123–129 (1987).

[252] A. Liu, L. Liao, D. Rubin, H. Nguyen, B. Ciftcioglu, Y. Chetrit, N. Izhaky, and M. Paniccia, "High-speed optical modulation based on carrier depletion in a silicon waveguide," Optics Express **15**, 660 (2007).

[253] D. Marris-Morini, L. Vivien, J. M. Fédéli, E. Cassan, P. Lyan, and S. Laval, "Low loss and high speed silicon optical modulator based on a lateral carrier depletion structure," Optics Express **16**, 334 (2008).

[254] F. Y. Gardes, D. J. Thomson, N. G. Emerson, and G. T. Reed, "40 Gb/s silicon photonics modulator for TE and TM polarisations," Optics Express **19**, 11804 (2011).

[255] T. Baehr-Jones, R. Ding, Y. Liu, A. Ayazi, T. Pinguet, N. C. Harris, M. Streshinsky, P. Lee, Y. Zhang, A. E.-J. Lim, T.-Y. Liow, S. H.-G. Teo, G.-Q. Lo, and M. Hochberg, "Ultralow drive voltage silicon traveling-wave modulator," Optics Express **20**, 12014 (2012).

[256] Jianfeng Ding, Ruiqiang Ji, Lei Zhang, and Lin Yang, "Electro-Optical Response Analysis of a 40 Gb/s Silicon Mach-Zehnder Optical Modulator," Journal of Lightwave Technology **31**, 2434–2440 (2013).

[257] X. Xiao, H. Xu, X. Li, Z. Li, T. Chu, Y. Yu, and J. Yu, "High-speed, low-loss silicon Mach–Zehnder modulators with doping optimization," Optics Express **21**, 4116 (2013).

[258] Q. Xu, B. Schmidt, S. Pradhan, and M. Lipson, "Micrometre-scale silicon electro-optic modulator," Nature **435**, 325–327 (2005).

[259] J. C. Rosenberg, W. M. J. Green, S. Assefa, D. M. Gill, T. Barwicz, M. Yang, S. M. Shank, and Y. A. Vlasov, "A 25 Gbps silicon microring modulator based on an interleaved junction," Optics Express **20**, 26411 (2012).

[260] D. Marris-Morini, C. Baudot, J.-M. Fédéli, G. Rasigade, N. Vulliet, A. Souhaité, M. Ziebell, P. Rivallin, S. Olivier, P. Crozat, X. Le Roux, D. Bouville, S. Menezo, F. Bœuf, and L. Vivien, "Low loss 40 Gbit/s silicon modulator based on interleaved junctions and fabricated on 300 mm SOI wafers," Optics Express **21**, 22471 (2013).

[261] S. Meister, H. Rhee, A. Al-Saadi, B. A. Franke, S. Kupijai, C. Theiss, H. J. Eichler, D. Stolarek, H. H. Richter, L. Zimmermann, B. Tillack, M. Lesny, C. Meuer, C. Schubert, and U. Woggon, "High-Speed Fabry–Pérot Optical Modulator in Silicon With 3-um Diode," Journal of Lightwave Technology **33**, 878–881 (2015).

[262] R. Dubé-Demers, S. LaRochelle, and W. Shi, "Ultrafast pulse-amplitude modulation with a femtojoule silicon photonic modulator," Optica **3**, 622 (2016).

[263] J. Sun, R. Kumar, M. Sakib, J. B. Driscoll, H. Jayatilleka, and H. Rong, "A 128 Gb/s PAM4 Silicon Microring Modulator With Integrated Thermo-Optic Resonance Tuning," Journal of Lightwave Technology **37**, 110–115 (2019).

[264] A. Melikyan, L. Alloatti, A. Muslija, D. Hillerkuss, P. C. Schindler, J. Li, R. Palmer, D. Korn, S. Muehlbrandt, D. Van Thourhout, B. Chen, R. Dinu, M. Sommer, C. Koos, M. Kohl, W. Freude, and J. Leuthold, "High-speed plasmonic phase modulators," Nature Photonics **8**, 229–233 (2014).

[265] C. Haffner, W. Heni, Y. Fedoryshyn, J. Niegemann, A. Melikyan, D. L. Elder, B. Baeuerle, Y. Salamin, A. Josten, U. Koch, C. Hoessbacher, F. Ducry, L. Juchli, A. Emboras, D. Hillerkuss, M. Kohl, L. R. Dalton, C. Hafner, and J. Leuthold, "All-plasmonic Mach-Zehnder modulator enabling optical high-speed communication at the microscale," Nature Photonics **9**, 525–528 (2015).

[266] C. Haffner, D. Chelladurai, Y. Fedoryshyn, A. Josten, B. Baeuerle, W. Heni, T. Watanabe, T. Cui, B. Cheng, S. Saha, D. L. Elder, L. R. Dalton, A. Boltasseva, V. M. Shalaev, N. Kinsey, and J. Leuthold, "Low-loss plasmon-assisted electro-optic modulator," Nature **556**, 483–486 (2018).

[267] W. Heni, Y. Fedoryshyn, B. Baeuerle, A. Josten, C. B. Hoessbacher, A. Messner, C. Haffner, T. Watanabe, Y. Salamin, U. Koch, D. L. Elder, L. R. Dalton, and J. Leuthold, "Plasmonic IQ modulators with attojoule per bit electrical energy consumption," Nature Communications **10**, 1694 (2019).

[268] M. Xu and X. Cai, "Advances in integrated ultra-wideband electro-optic modulators [Invited]," Optics Express **30**, 7253 (2022).

[269] G. V. Naik, J. Kim, and A. Boltasseva, "Oxides and nitrides as alternative plasmonic materials in the optical range [Invited]," Optical Materials Express **1**, 1090 (2011).

[270] D. Zhu, L. Shao, M. Yu, R. Cheng, B. Desiatov, C. J. Xin, Y. Hu, J. Holzgrafe, S. Ghosh, A. Shams-Ansari, E. Puma, N. Sinclair, C. Reimer, M. Zhang, and M. Lončar, "Integrated photonics on thin-film lithium niobate," Advances in Optics and Photonics **13**, 242 (2021).

[271] C. Wang, M. Zhang, B. Stern, M. Lipson, and M. Lončar, "Nanophotonic lithium niobate electro-optic modulators," Optics Express **26**, 1547 (2018).

[272] S. Abel, T. Stöferle, C. Marchiori, C. Rossel, M. D. Rossell, R. Erni, D. Caimi, M. Sousa, A. Chelnokov, B. J. Offrein, and J. Fompeyrine, "A strong electro-optically active lead-free ferroelectric integrated on silicon," Nature Communications **4**, 1671 (2013).

[273] K. J. Kormondy, Y. Popoff, M. Sousa, F. Eltes, D. Caimi, M. D. Rossell, M. Fiebig, P. Hoffmann, C. Marchiori, M. Reinke, M. Trassin, A. A. Demkov, J. Fompeyrine, and S. Abel, "Microstructure and ferroelectricity of BaTiO3 thin films on Si for integrated photonics," Nanotechnology **28**, 075706 (2017).

[274] P. Castera, D. Tulli, A. M. Gutierrez, and P. Sanchis, "Influence of BaTiO3 ferroelectric orientation for electro-optic modulation on silicon," Optics Express **23**, 15332 (2015).

[275] J. E. Ortmann, F. Eltes, D. Caimi, N. Meier, A. A. Demkov, L. Czornomaz, J. Fompeyrine, and S. Abel, "Ultra-Low-Power Tuning in Hybrid Barium Titanate-Silicon Nitride Electro-optic Devices on Silicon," ACS Photonics **6**, 2677–2684 (2019).

[276] M. Romagnoli, V. Sorianello, M. Midrio, F. H. L. Koppens, C. Huyghebaert, D. Neumaier, P. Galli, W. Templ, A. D'Errico, and A. C. Ferrari, "Graphene-based integrated photonics for next-generation datacom and telecom," Nature Reviews Materials **3**, 392–414 (2018).

[277] J. You, Y. Luo, J. Yang, J. Zhang, K. Yin, K. Wei, X. Zheng, and T. Jiang, "Hybrid/Integrated Silicon Photonics Based on 2D Materials in Optical

Communication Nanosystems," Laser & Photonics Reviews **14**, 2000239 (2020).

[278] C. T. Phare, Y.-H. Daniel Lee, J. Cardenas, and M. Lipson, "Graphene electro-optic modulator with 30 GHz bandwidth," Nature Photonics **9**, 511–514 (2015).

[279] V. Sorianello, M. Midrio, G. Contestabile, I. Asselberghs, J. Van Campenhout, C. Huyghebaert, I. Goykhman, A. K. Ott, A. C. Ferrari, and M. Romagnoli, "Graphene-silicon phase modulators with gigahertz bandwidth," Nature Photonics **12**, 40–44 (2018).

[280] I. Datta, S. H. Chae, G. R. Bhatt, M. A. Tadayon, B. Li, Y. Yu, C. Park, J. Park, L. Cao, D. N. Basov, J. Hone, and M. Lipson, "Low-loss composite photonic platform based on 2D semiconductor monolayers," Nature Photonics **14**, 256–262 (2020).

[281] H. M. Chu and K. Hane, "A Wide-Tuning Silicon Ring-Resonator Composed of Coupled Freestanding Waveguides," IEEE Photonics Technology Letters **26**, 1411–1413 (2014).

[282] C. Errando-Herranz, F. Niklaus, G. Stemme, and K. B. Gylfason, "Low-power microelectromechanically tunable silicon photonic ring resonator add-drop filter," Optics Letters **40**, 3556 (2015).

[283] M. W. Pruessner, D. Park, T. H. Stievater, D. A. Kozak, and W. S. Rabinovich, "Broadband opto-electro-mechanical effective refractive index tuning on a chip," Optics Express **24**, 13917 (2016).

[284] R. Baghdadi, M. Gould, S. Gupta, M. Tymchenko, D. Bunandar, C. Ramey, and N. C. Harris, "Dual slot-mode NOEM phase shifter," Optics Express **29**, 19113 (2021).

[285] T. Grottke, W. Hartmann, C. Schuck, and W. H. P. Pernice, "Optoelectromechanical phase shifter with low insertion loss and a 13π tuning range," Optics Express **29**, 5525 (2021).

[286] P. Edinger, A. Y. Takabayashi, C. Errando-Herranz, U. Khan, H. Sattari, P. Verheyen, W. Bogaerts, N. Quack, and K. B. Gylfason, "Silicon photonic

microelectromechanical phase shifters for scalable programmable photonics," Optics Letters **46**, 5671 (2021).

[287] G. Cocorullo and I. Rendina, "Thermo-optical modulation at 1.5 μm in silicon etalon," Electronics Letters **28**, 83–85 (1992).

[288] J. Komma, C. Schwarz, G. Hofmann, D. Heinert, and R. Nawrodt, "Thermo-optic coefficient of silicon at 1550 nm and cryogenic temperatures," Applied Physics Letters **101**, 41905 (2012).

[289] M. Bahadori, A. Gazman, N. Janosik, S. Rumley, Z. Zhu, R. Polster, Q. Cheng, and K. Bergman, "Thermal Rectification of Integrated Microheaters for Microring Resonators in Silicon Photonics Platform," Journal of Lightwave Technology **36**, 773–788 (2018).

[290] A. A. Balandin, S. Ghosh, W. Bao, I. Calizo, D. Teweldebrhan, F. Miao, and C. N. Lau, "Superior Thermal Conductivity of Single-Layer Graphene," Nano Letters **8**, 902–907 (2008).

[291] J. Leuthold, C. Koos, and W. Freude, "Nonlinear silicon photonics," Nature Photonics **4**, 535–544 (2010).

[292] T. Tanabe, M. Notomi, S. Mitsugi, A. Shinya, and E. Kuramochi, "All-optical switches on a silicon chip realized using photonic crystal nanocavities," Applied Physics Letters **87**, 151112 (2005).

[293] M. F. Modest, *Radiative Heat Transfer* (Elsevier, 2013), 3rd ed.

[294] T. Murai, Y. Shoji, and T. Mizumoto, "Efficient Light-to-Heat Conversion by Optical Absorption of a Metal on an Si Microring Resonator," Journal of Lightwave Technology **37**, 2223–2231 (2019).

[295] Y. Kondo, T. Murai, Y. Shoji, and T. Mizumoto, "All-Optical Switch by Light-to-Heat Conversion in Metal Deposited Si Ring Resonator," IEEE Photonics Technology Letters **32**, 807–810 (2020).

[296] C. Qiu, Y. Yang, C. Li, Y. Wang, K. Wu, and J. Chen, "All-optical control of light on a graphene-on-silicon nitride chip using thermo-optic effect," Scientific Reports **7**, 17046 (2017).

[297] K. Wu, Y. Wang, C. Qiu, and J. Chen, "Thermo-optic all-optical devices based on two-dimensional materials," Photonics Research **6**, C22 (2018).

[298] X. Fang and L. Yang, "Thermal effect analysis of silicon microring optical switch for on-chip interconnect," Journal of Semiconductors **38** (2017).

[299] S. Xian, L. Nie, J. Qin, T. Kang, C. Li, J. Xie, L. Deng, and L. Bi, "Effect of oxygen stoichiometry on the structure, optical and epsilon-near-zero properties of indium tin oxide films," Optics Express **27**, 28618 (2019).

[300] P. P. Edwards, A. Porch, M. O. Jones, D. V. Morgan, and R. M. Perks, "Basic materials physics of transparent conducting oxides," Dalton Transactions pp. 2995–3002 (2004).

[301] B. Sturlesi, M. Grajower, N. Mazurski, and U. Levy, "Integrated amorphous silicon-aluminum long-range surface plasmon polariton (LR-SPP) waveguides," APL Photonics **3**, 036103 (2018).

[302] V. Singh, D. Joung, L. Zhai, S. Das, S. I. Khondaker, and S. Seal, "Graphene based materials: Past, present and future," Progress in Materials Science **56**, 1178–1271 (2011).

[303] I. Rukhlenko, M. Premaratne, and G. Agrawal, "Nonlinear Silicon Photonics: Analytical Tools," IEEE Journal of Selected Topics in Quantum Electronics **16**, 200–215 (2010).

[304] M. Borghi, C. Castellan, S. Signorini, A. Trenti, and L. Pavesi, "Nonlinear silicon photonics," Journal of Optics **19**, 093002 (2017).

[305] R. W. Boyd, *Nonlinear Optics* (Elsevier, 2003).

[306] R. W. Boyd, "Order-of-magnitude estimates of the nonlinear optical susceptibility," Journal of Modern Optics **46**, 367–378 (1999).

[307] H. Yamada, M. Shirane, T. Chu, H. Yokoyama, S. Ishida, and Y. Arakawa, "Nonlinear-Optic Silicon-Nanowire Waveguides," Japanese Journal of Applied Physics **44**, 6541–6545 (2005).

[308] A. Gil-Molina, I. Aldaya, J. L. Pita, L. H. Gabrielli, H. L. Fragnito, and P. Dainese, "Optical free-carrier generation in silicon nano-waveguides at 1550 nm," Applied Physics Letters **112**, 251104 (2018).

[309] R. S. Jacobsen, K. N. Andersen, P. I. Borel, J. Fage-Pedersen, L. H. Frandsen, O. Hansen, M. Kristensen, A. V. Lavrinenko, G. Moulin, H. Ou, C. Peucheret, B. Zsigri, and A. Bjarklev, "Strained silicon as a new electro-optic material," Nature **441**, 199–202 (2006).

[310] M. Berciano, G. Marcaud, P. Damas, X. Le Roux, P. Crozat, C. Alonso Ramos, D. Pérez Galacho, D. Benedikovic, D. Marris-Morini, E. Cassan, and L. Vivien, "Fast linear electro-optic effect in a centrosymmetric semiconductor," Communications Physics **1**, 64 (2018).

[311] I. Olivares Sánchez-Mellado, "Development of Photonic Devices Based on the Strained Silicon Technology," Ph.D. thesis, Universitat Politècnica de València, Valencia (Spain) (2021).

[312] E. Timurdogan, C. V. Poulton, M. J. Byrd, and M. R. Watts, "Electric field-induced second-order nonlinear optical effects in silicon waveguides," Nature Photonics **11**, 200–206 (2017).

[313] C. Castellan, R. Franchi, S. Biasi, M. Bernard, M. Ghulinyan, and L. Pavesi, "Field-Induced Nonlinearities in Silicon Waveguides Embedded in Lateral p-n Junctions," Frontiers in Physics **7**, 1–9 (2019).

[314] H. K. Tsang and Y. Liu, "Nonlinear optical properties of silicon waveguides," Semiconductor Science and Technology **23** (2008).

[315] P. Dong, "Silicon Photonic Integrated Circuits for Wavelength-Division Multiplexing Applications," IEEE Journal of Selected Topics in Quantum Electronics **22**, 370–378 (2016).

[316] D. Kong, H. Xin, K. Kim, Y. Liu, L. K. Oxenlowe, P. Dong, and H. Hu, "Intra-Datacenter Interconnects With a Serialized Silicon Optical Frequency Comb Modulator," Journal of Lightwave Technology **38**, 4677–4682 (2020).

[317] J. Leuthold, W. Freude, J.-M. Brosi, R. Baets, P. Dumon, I. Biaggio, M. L. Scimeca, F. Diederich, B. Frank, and C. Koos, "Silicon Organic Hybrid Technology-A Platform for Practical Nonlinear Optics," Proceedings of the IEEE **97**, 1304–1316 (2009).

[318] B. Esembeson, M. L. Scimeca, T. Michinobu, F. Diederich, and I. Biaggio, "A High-Optical Quality Supramolecular Assembly for Third-Order Integrated Nonlinear Optics," Advanced Materials **20**, 4584–4587 (2008).

[319] C. Koos, P. Vorreau, T. Vallaitis, P. Dumon, W. Bogaerts, R. Baets, B. Esembeson, I. Biaggio, T. Michinobu, F. Diederich, W. Freude, and J. Leuthold, "All-optical high-speed signal processing with silicon-organic hybrid slot waveguides," Nature Photonics **3**, 216–219 (2009).

[320] T. Vallaitis, S. Bogatscher, L. Alloatti, P. Dumon, R. Baets, M. L. Scimeca, I. Biaggio, F. Diederich, C. Koos, W. Freude, and J. Leuthold, "Optical properties of highly nonlinear silicon-organic hybrid (SOH) waveguide geometries," Optics Express **17**, 17357 (2009).

[321] F. Bonaccorso, Z. Sun, T. Hasan, and A. C. Ferrari, "Graphene photonics and optoelectronics," Nature Photonics **4**, 611–622 (2010).

[322] Z. Cheng, H. K. Tsang, X. Wang, K. Xu, and J.-B. Xu, "In-Plane Optical Absorption and Free Carrier Absorption in Graphene-on-Silicon Waveguides," IEEE Journal of Selected Topics in Quantum Electronics **20**, 43–48 (2014).

[323] M. Ono, M. Hata, M. Tsunekawa, K. Nozaki, H. Sumikura, H. Chiba, and M. Notomi, "Ultrafast and energy-efficient all-optical switching with graphene-loaded deep-subwavelength plasmonic waveguides," Nature Photonics **14**, 37–43 (2020).

[324] T. Gu, N. Petrone, J. F. McMillan, A. van der Zande, M. Yu, G. Q. Lo, D. L. Kwong, J. Hone, and C. W. Wong, "Regenerative oscillation and four-wave mixing in graphene optoelectronics," Nature Photonics **6**, 554–559 (2012).

[325] H. Chen, V. Corboliou, A. S. Solntsev, D.-Y. Choi, M. A. Vincenti, D. de Ceglia, C. de Angelis, Y. Lu, and D. N. Neshev, "Enhanced second-harmonic generation from two-dimensional MoSe2 on a silicon waveguide," Light: Science & Applications **6**, e17060–e17060 (2017).

[326] J. Navarro-Arenas, J. Parra, and P. Sanchis, "Ultrafast all-optical phase switching enabled by epsilon-near-zero materials in silicon," Optics Express **30**, 14518 (2022).

[327] Z. Cheng, C. Ríos, W. H. P. Pernice, C. D. Wright, and H. Bhaskaran, "On-chip photonic synapse," Science Advances **3**, e1700160 (2017).

[328] O. Reshef, I. De Leon, M. Z. Alam, and R. W. Boyd, "Nonlinear optical effects in epsilon-near-zero media," Nature Reviews Materials **4**, 535–551 (2019).

[329] M. Z. Alam, M. Z. Alam, I. D. Leon, and R. W. Boyd, "Large optical nonlinearity of indium tin oxide in its epsilon-near-zero region," Science **0330**, 0–5 (2016).

[330] Z. Gong, F. Yang, L. Wang, R. Chen, J. Wu, C. P. Grigoropoulos, and J. Yao, "Phase change materials in photonic devices," Journal of Applied Physics **129**, 030902 (2021).

[331] J. Parra, J. Navarro-Arenas, M. Kovylina, and P. Sanchis, "Impact of GST thickness on GST-loaded silicon waveguides for optimal optical switching," Scientific Reports **12**, 9774 (2022).

[332] J. Feldmann, N. Youngblood, C. D. Wright, H. Bhaskaran, and W. H. P. Pernice, "All-optical spiking neurosynaptic networks with self-learning capabilities," Nature **569**, 208–214 (2019).

[333] Y. X. Ji, S. Y. Li, G. A. Niklasson, and C. G. Granqvist, "Durability of thermochromic VO2 thin films under heating and humidity: Effect of Al oxide top coatings," Thin Solid Films **562**, 568–573 (2014).

[334] T. Chang, X. Cao, N. Li, S. Long, Y. Zhu, J. Huang, H. Luo, and P. Jin, "Mitigating Deterioration of Vanadium Dioxide Thermochromic Films by Interfacial Encapsulation," Matter **1**, 734–744 (2019).

[335] Y. Liu, J. Liu, Y. Li, D. Wang, L. Ren, and K. Zou, "Effect of annealing temperature on the structure and properties of vanadium oxide films," Optical Materials Express **6**, 1552 (2016).

[336] J. Y. Suh, R. Lopez, L. C. Feldman, and R. F. Haglund, "Semiconductor to metal phase transition in the nucleation and growth of VO2 nanoparticles and thin films," Journal of Applied Physics **96**, 1209–1213 (2004).

[337] J. Parra, T. Ivanova, M. Menghini, P. Homm, J.-P. Locquet, and P. Sanchis, "Temporal dynamics of all-optical switching in hybrid VO2/Si waveguides," (2020).

[338] K. Shibuya, M. Kawasaki, and Y. Tokura, "Metal-insulator transition in epitaxial V1-xWxO2(0≤x≤0.33) thin films," Applied Physics Letters **96**, 022102 (2010).

[339] J. G. Ramirez, T. Saerbeck, S. Wang, J. Trastoy, M. Malnou, J. Lesueur, J.-P. Crocombette, J. E. Villegas, and I. K. Schuller, "Effect of disorder on the metal-insulator transition of vanadium oxides: Local versus global effects," Physical Review B **91**, 205123 (2015).

[340] K. Miyazaki, K. Shibuya, M. Suzuki, H. Wado, and A. Sawa, "Correlation between thermal hysteresis width and broadening of metal–insulator transition in Cr- and Nb-doped VO 2 films," Japanese Journal of Applied Physics **53**, 071102 (2014).

[341] S. Yan, J. Dong, A. Zheng, and X. Zhang, "Chip-integrated optical power limiter based on an all-passive micro-ring resonator," Scientific Reports **4**, 6676 (2015).

[342] Z. Wu, M. Ji, and Y. Wang, "Ultra low threshold optical power limiter based on a silicon photonic crystal cavity," in "2015 11th Conference on Lasers and Electro-Optics Pacific Rim (CLEO-PR)," , vol. 2 (IEEE, 2015), vol. 2, pp. 1–2.

[343] Y.-F. Ma and D.-W. Huang, "A Compact Silicon-on-Insulator MMI-based Polarization Splitter," in "2007 IEEE/LEOS International Conference on Optical MEMS and Nanophotonics," , vol. 17 (IEEE, 2007), vol. 17, pp. 121–122.

[344] Á. Rosa, A. Gutiérrez, A. Brimont, A. Griol, and P. Sanchis, "High performace silicon 2x2 optical switch based on a thermo-optically tunable multimode interference coupler and efficient electrodes," Optics Express **24**, 191 (2016).

[345] K. Y. Yang, J. Skarda, M. Cotrufo, A. Dutt, G. H. Ahn, M. Sawaby, D. Vercruysse, A. Arbabian, S. Fan, A. Alù, and J. Vučković, "Inverse-designed

non-reciprocal pulse router for chip-based LiDAR," Nature Photonics **14**, 369–374 (2020).

[346] A. Pandey, S. Dwivedi, T. Zhenzhou, S. Pan, and D. Van Thourhout, "Non-reciprocal Light Propagation in a Cascaded All-Silicon Microring Modulator," ACS Photonics **8**, 1997–2006 (2021).

[347] D. B. Sohn, O. E. Örsel, and G. Bahl, "Electrically driven optical isolation through phonon-mediated photonic Autler-Townes splitting," Nature Photonics **15**, 822–827 (2021).

[348] H. Tian, J. Liu, A. Siddharth, R. N. Wang, T. Blésin, J. He, T. J. Kippenberg, and S. A. Bhave, "Magnetic-free silicon nitride integrated optical isolator," Nature Photonics **15**, 828–836 (2021).

[349] L. Bi, J. Hu, P. Jiang, D. H. Kim, G. F. Dionne, L. C. Kimerling, and C. A. Ross, "On-chip optical isolation in monolithically integrated non-reciprocal optical resonators," Nature Photonics **5**, 758–762 (2011).

[350] D. Jalas, A. Petrov, M. Eich, W. Freude, S. Fan, Z. Yu, R. Baets, M. Popović, A. Melloni, J. D. Joannopoulos, M. Vanwolleghem, C. R. Doerr, and H. Renner, "What is -and what is not- an optical isolator," Nature Photonics **7**, 579–582 (2013).

[351] Y. Shi, Z. Yu, and S. Fan, "Limitations of nonlinear optical isolators due to dynamic reciprocity," Nature Photonics **9**, 388–392 (2015).

[352] J. B. Khurgin, "Non-reciprocal propagation versus non-reciprocal control," Nature Photonics **14**, 711–711 (2020).

[353] A. M. Mahmoud, A. R. Davoyan, and N. Engheta, "All-passive nonreciprocal metastructure," Nature Communications **6**, 8359 (2015).

[354] R. Halir, P. J. Bock, P. Cheben, A. Ortega-Moñux, C. Alonso-Ramos, J. H. Schmid, J. Lapointe, D. Xu, J. G. Wangüemert-Pérez, Í. Molina-Fernández, and S. Janz, "Waveguide sub-wavelength structures: a review of principles and applications," Laser & Photonics Reviews **9**, 25–49 (2015).

[355] R. Halir, A. Ortega-Monux, D. Benedikovic, G. Z. Mashanovich, J. G. Wanguemert-Perez, J. H. Schmid, I. Molina-Fernandez, and P. Cheben,

"Subwavelength-Grating Metamaterial Structures for Silicon Photonic Devices," Proceedings of the IEEE **106**, 2144–2157 (2018).

[356] P. Cheben, R. Halir, J. H. Schmid, H. A. Atwater, and D. R. Smith, "Subwavelength integrated photonics," Nature **560**, 565–572 (2018).